SANDIA REPORT

SAND2009-2282
Unlimited Release
Printed March 2009

KAYENTA: Theory and User's Guide

R.M. Brannon, A.F. Fossum, and O.E. Strack

Sandia National Laboratories

KAYENTA
Theory and User's Guide

Rebecca M. Brannon
University of Utah; Mechanical Engineering
2134 MEB; 50 S. Central Campus Dr.; Salt Lake City, UT 84112; USA

Arlo F. Fossum
BP America, Inc.;
PO BOX 3092; Houston, TX 77079-3092; USA

O. Erik Strack
Sandia National Laboratories; Computational Shock and Multiphysics
PO Box 5800; Albuquerque, NM 87185-0378; USA

Abstract

The physical foundations and domain of applicability of the Kayenta constitutive model are presented along with descriptions of the source code and user instructions. Kayenta, which is an outgrowth of the Sandia GeoModel, includes features and fitting functions appropriate to a broad class of materials including rocks, rock-like engineered materials (such as concretes and ceramics), and metals. Fundamentally, Kayenta is a computational framework for generalized plasticity models. As such, it includes a yield surface, but the term "yield" is generalized to include *any* form of inelastic material response including microcrack growth and pore collapse. Kayenta supports optional anisotropic elasticity associated with ubiquitous joint sets. Kayenta supports optional deformation-induced anisotropy through kinematic hardening (in which the initially isotropic yield surface is permitted to translate in deviatoric stress space to model Bauschinger effects). The governing equations are otherwise isotropic. Because Kayenta is a unification and generalization of simpler models, it can be run using as few as 2 parameters (for linear elasticity) to as many as 40 material and control parameters in the exceptionally rare case when all features are used. For high-strain-rate applications, Kayenta supports rate dependence through an overstress model. Isotropic damage is modeled through loss of stiffness and strength.

Intentionally Blank

Acknowledgements

Rebecca Brannon
Rebecca.Brannon@utah.edu

Arlo Fossum
Arlo.Fossum@bp.com

Erik Strack
oestrac@sandia.gov

February 23, 2009

Contents

REFERENCES

Figures

Intentionally Left Blank

KAYENTA
Theory and User's Guide

Figure 1.0.   *Kayenta continuous yield surface.*   *(a)* **three-dimensional view** in principal stress space with the high pressure "cap" shown as a wire frame, *(b)* **the meridional "side" view** **(thick line)** with the cap shown on the more compressive right-hand side of the plot using cylindrical coordinates in which $\bar{z}$ points along the compressive [111] direction, and *(c)* **the octahedral view**, which corresponds to looking down the hydrostat (onto planes perpendicular to the [111] direction); an option is available for a pressure-varying octahedral profile.

1. Introduction

Simulating deformation and failure of a variety of materials is at the core of a broad range of applications, including exploration and production activities for the petroleum industry, structural integrity assessment for civil engineering problems, and penetration resistance and debris field predictions for the defense community. Constitutive models are required for metals, natural geological materials (such as limestone, granite, and frozen soil), rock-like engineered materials (such as concrete [58] and ceramics [2]). A common feature is the presence of microscale flaws such as porosity (which permits inelasticity even in purely hydrostatic loading) and networks of microcracks (leading to low strength in the absence of confining pressure, non-negligible nonlinear elasticity, rate-sensitivity, and differences in material behavior under triaxial extension compared to triaxial compression). Kayenta was originally developed for rock mechanics [22], but it was later generalized to include other features common in metals models (such as classical Drucker-Prager yield with power-law hardening and a high-pressure equation of state).

For computational tractability, and to allow relatively straightforward model parameterization using standard laboratory tests, Kayenta strikes a balance between first-principals micromechanics and phenomenological, homogenized, and semi-empirical modeling strategies. The over-arching goal is to provide a unified general-purpose constitutive model that can be used for a broad range of materials over a wide range of porosities and strain rates. As a unified theory, Kayenta can simultaneously model *multiple* failure mechanisms, or (by using only a small subset of the available parameters) it can duplicate simpler idealized yield models such as classic Von Mises plasticity and Mohr-Coulomb failure. Thus, exercising this model can require as many as ~40 parameters for extremely complicated materials to only 2 or 3 parameters for idealized simplistic materials. The model parameters are defined in the nomenclature table (Appendix B). Appendix "A" gives step-by-step instructions for using experimental data to assign values to Kayenta parameters.

Kayenta overview

Kayenta adopts and extends numerous features from seminal work of Schwer and Murray [51]. For example, a Pelessone function [43] is used to generate a continuously differentiable "cap" yield function for porous media. Relatively new hardening functions are used to accurately predict the competition between dilatation from microcracking and compaction from pore collapse that is observed in standard triaxial testing (where compaction initially prevails, but then smoothly transitions to shear-induced dilatation). For stress paths that result in brittle deformation, failure is associated ultimately with the attainment of a peak stress and work-softening deformation. Tensile or extensile microcrack growth dominates the micromechanical processes that result in macroscopically dilatant (volume increasing) strains even when all principal stresses are compressive. At low pressure, porous brittle materials can fail by shear localization and exhibit strain-softening behavior. At higher pressures, they can undergo strain-hardening deformation associated with macroscopically compactive volumetric strain (i.e. void collapse). Features and limitations of Kayenta are summarized below.

Features of Kayenta

Because it is a unification of simpler models, Kayenta has a large number of material parameters and control parameters (See page B-2). However, only *subsets* of these parameters are used in any given simulation. For example, only two parameters (shear and bulk modulus) are needed to reduce Kayenta to linear elasticity. An additional parameter (yield strength) is needed for Kayenta to replicate the idealization of von Mises plasticity. Further parameters are needed to account for nonlinear elasticity, pressure dependence of strength, rate-dependence, porosity, and other advanced features. In other words, the number of parameters increases with the desired sophistication of the constitutive model. Where possible, reasonable default values are used for any material parameters that are unspecified by the user.

Depending on how the model parameters are set, Kayenta is capable of any of the following model features

- Linear and nonlinear, associative or non-associative Drucker-Prager plasticity.
- Linear and nonlinear, associative or non-associative Mohr-Coulomb plasticity.
- Linear or nonlinear, associative or non-associative Willam-Warnke plasticity.
- Von Mises perfect plasticity option as a special case.
- Tresca perfect plasticity option as a special case.
- Sandler-Rubin two-surface cap plasticity (approximated).
- Three-invariant, mixed hardening, continuous surface cap plasticity.
- Three Lode-Angle functions (i.e., non-circular or circular octahedral yield profile).
- The triaxial extension/compression strength ratio can be either a constant or it can be computed internally to vary realistically with pressure.
- Linear or non-linear elasticity.
- Rate-independent or strain-rate-sensitive yield surface.
- Linear or nonlinear peak shear failure threshold marking the onset of softening.
- Linear or nonlinear peak shear failure threshold for fully damaged material.
- Linear or nonlinear kinematic hardening accounting for a Baushinger effect. The nonlinear option is similar to a power law model in that the amount of hardening decreases with monotonic loading. The linear option is used in verification testing.
- Nonlinear compaction function (pressure-volume) with isotropic hardening.[*]
- Flexibility that permits reducing the model (and the number of required parameters). to classical failure models.
- Pressure- and shear-dependent compaction (similar to p-α models *hydrostatic* loading, but generalized to include shear effects in general loading).
- Ubiquitous jointing (i.e., elastic stiffness reduction caused by a network of pre-existing oriented faults). An isotropic option applies to joints of uniformly random orientations. An orthotropic option allows joints aligned with a rectangular grid. A general anisotropic option allows specification of four joint sets of user-specified orientations (strike and dip).

Limitations of Kayenta.

- Support for orthotropic or anisotropic jointing is available only as a compile option; the theory and implementation for anisotropic joints is discussed in a separate report. The Kayenta version described in this report treats the material as initially isotropic. Kinematic hardening is the only mechanism for deformation-induced anisotropy.
- The elasticity model is hypoelastic rather than hyperelastic.
- While the hydrostatic crush curve is quite general, only an elliptic cap function is available for modeling shear effects on pore collapse and other mechanisms of plastic volume reduction. Alternative cap models (such as the Gurson function) can be incorporated in future revisions if needed.

---

[*] Isotropic hardening does not imply a uniform expansion of a yield surface in stress space. Isotropic hardening means that the yield function evolves in such a manner that it continues to depend only on stress invariants. For example, the isotropic hardening associated with pore collapse leads to a "stretching" of the yield surface along the hydrostat in stress space.

- The host code is responsible for satisfying frame indifference (by calling Kayenta using conjugate *reference* stress and strain rate measures). See page 88.
- Kayenta is designed to be easily installed into a "host code," which refers to a finite element code or any other code that solves the partial differential equations of mass and momentum balance. Kayenta may be installed as a classical local model if it is to be applied in a limited capacity to predict material response up to the *onset* of softening. However, if Kayenta's damage response functions (loss of strength and stiffness) are to be used to predict post-peak softening, then the host code is responsible for handling the change in type of the governing equations to ensure mesh independence. This additional burden on the host code possibly includes calling Kayenta with appropriately perturbed statistical variations and scale effects in the material parameters [15]. See page 72.
- Kayenta is not extensively parameterized (or even tested) for tensile loading, though it is thoroughly validated in compression.
- Compared with simple idealized models (which are well known to give unsatisfactory results in non-trivial structural applications), Kayenta is computationally intensive, though less so than many other models of comparable complexity.
- Kayenta is limited to relatively small distortional (shape changing) strains, though large volume changes are permitted. Arbitrarily large rotations are permitted if the host code manages the reference stress and strain measures properly (see page 88).
- Although Kayenta supports a pore collapse curve having convexity that changes sign, such curves are allowed only under compaction, not pore growth (see page 60).

Kayenta predicts observed material response, without explicitly addressing *how* the material behaves as it does. Kayenta reflects subscale inelastic phenomena *en ensemble* by phenomenologically matching observed data to interpolation functions. Considerations guiding the structure of Kayenta's material response functions are (1) consistency with microscale theory, (2) computational tractability, (3) suitability to capture trends in characterization data, and (4) physics-based judgements about how a material should behave in application domains where controlled experimental data cannot be obtained.

Fundamentally, Kayenta is a *generalized* and *unified* plasticity model. Here, the term "plasticity" is defined very broadly to include any mechanism of inelastic deformation. Primarily, the source of inelastic deformation in geological materials (or in rock-like materials such as concrete and ceramics) is growth and coalescence of microcracks and pores. Under massive confining pressures, inelasticity could include plasticity in its traditional dislocation sense or, more generally, might result from other microphysical mechanisms (internal locking, phase transformation, twinning, etc.). Equations governing generalized plasticity a mathematical formalism, as well as solution methods and limitations in shock physics, are summarized in Reference [14].

Kayenta is phenomenological and semi-empirical because the physical *mechanisms* of inelastic material behavior are handled in an *ensemble* manner, without explicitly partitioning and modeling each possible contributor to the inelasticity. Kayenta makes no *explicit* reference to microscale properties such as porosity, grain size, or crack density. Instead, the overall combined effects of the microstructure are modeled by casting the

macroscale theory in terms of macroscale variables that are realistic to measure in the laboratory. For example, inelastic compaction followed by shear-enhanced dilatation has long been attributed to an initial phase of void collapse followed later by microcracks opening in shear. Kayenta is exceptionally capable of matching this type of observed compaction/dilatation data, and it does so without demanding that the user supply information about essentially unknowable porosity or microcrack distributions within the material.

Being a generalized plasticity model, Kayenta presumes that there exists a convex contiguous "**elastic domain**" of stress states for which the material response can be construed to be elastic. The boundary of the elastic domain is called the **yield surface**. When loading is severe enough that continuing to apply elasticity theory would produce a stress state lying outside the yield surface, the material response will instead be inelastic and a different set of equations must then be solved. Aside from supporting kinematic hardening, Kayenta is isotropic, which means that the criterion for the onset of plasticity depends only on the three principal values of the stress tensor, $(\sigma_1, \sigma_2, \sigma_3)$, but not on the principal directions. Consequently, as illustrated in Fig. 1.0 (page 1), the yield surface may be visualized as a 2D surface embedded in a 3D space where the axes are the principal stresses. The elastic domain is the interior of this surface. The **hydrostat** is the [111] direction, along which all three principal stresses are equal. Any plane that contains the hydrostat is called a **meridional plane**. Any "side view" cross-section of the yield surface on a meridional plane is called a **meridional profile**. Any plane perpendicular to the hydrostat is called an **octahedral plane**, and any cross-section of the yield surface on an octahedral plane is called an **octahedral profile**.

Mathematically, the yield surface may be expressed in terms of a **yield function** $f(\sigma_1, \sigma_2, \sigma_3)$. When hardening is permitted, the yield function additionally depends on **internal state variables** that quantify the underlying microstructure (e.g. porosity). Points on the yield surface satisfy $f = 0$ and therefore, because the equation $f(\sigma_1, \sigma_2, \sigma_3) = 0$ is phrased in terms of three independent variables, the yield surface may be visualized in the 3D Cartesian space, called **stress space***. When the yield function additionally depends on internal state variables, different values for the internal state variables result in different yield surfaces in stress space. Points within the elastic domain satisfy $f < 0$. Brittle materials are very weak in tension, but they can deform elastically under a much broader range of stress states in compression. Consequently, the elastic domain (and therefore its boundary, the yield surface) resides primarily in the compressive part of stress space where all three principal stresses are negative. Thus, the typical rock yield surface shown in Fig. 1.0(a) is actually being viewed from the *compressive* [111] direction. The "cap" part of that yield surface (shown as a wire frame in Fig. 1.0) reflects the fact that, unlike solid metals, inelasticity can occur in rocks even under purely hydrostatic compression as a consequence of void collapse.

---

* Some people prefer that this be called Haigh-Westergaard space [40] so that the phrase "stress-space" may be reserved for the higher-dimensional space defined by the set of all tensors that commute with the stress tensor.

A **yield surface** is the boundary of *elastically* obtainable stress states, whereas a **limit surface** is the boundary of stresses that are quasi-statically obtainable *by any quasi-static means*, elastic or plastic. Points *outside* the limit surface can be reached only transiently in dynamic loading via viscoplastic rate dependence. Points outside a yield surface might be attainable through a hardening process, but points outside the limit surface are not attainable via *any* quasistatic process.
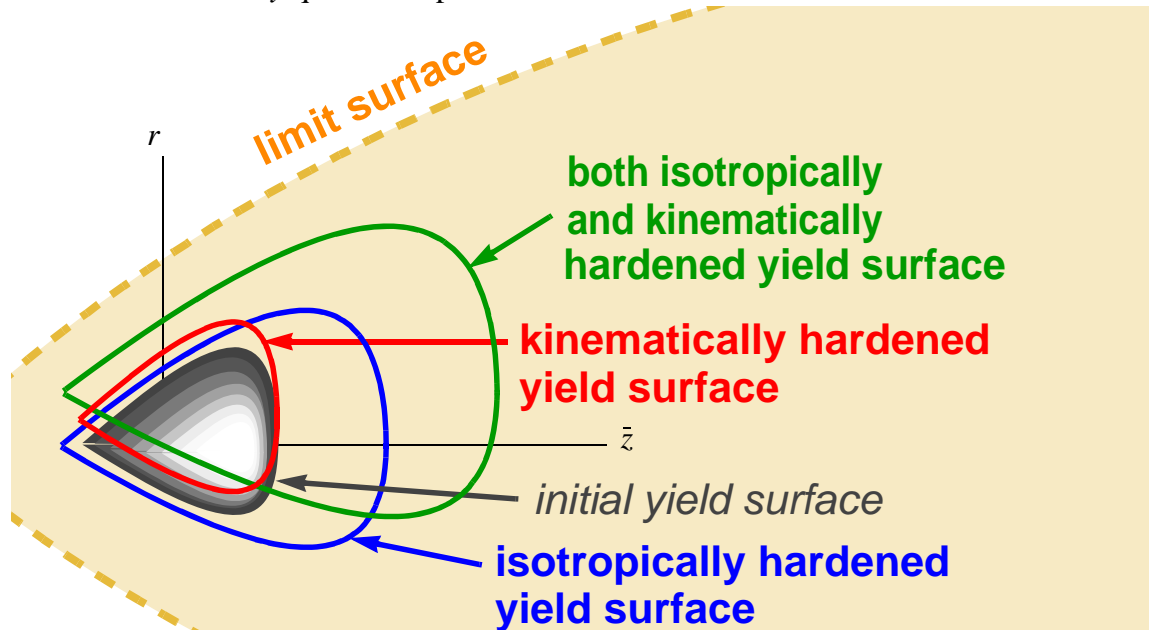
Figure 1.1.   Distinction between <u>a</u> yield surface and <u>the</u> limit surface.   This sketch shows meridional profiles of an initial yield surface along with hardened yield surfaces that might evolve from the initial surface. All achievable stress states (and therefore all possible yield surfaces) are contained within the limit surface. Fig. 1.0*(b)*, for example, depicts a family of yield surfaces, all bounded by the limit surface.

Points on the limit surface define the onset of material softening. Consequently, a state on the limit surface is attainable at least once, but might not be attainable thereafter. The Sandia GeoModel [23], which was the predecessor to Kayenta, allowed prediction of the material response only up to the limit state. The GeoModel did not simulate subsequent softening because softening induces a change in type of the partial differential equations for momentum balance, which therefore requires a response from the host code to alter its solution algorithm (perhaps by inserting void or by activating special elements that accommodate displacement discontinuities). Shortly after the documentation for the Geo-Model was released, a beta, research-only, revision (called BF1[*]) was developed to allow loss of strength and stiffness. This revision, which would have been nonphysical if applied in a local deterministic context, was used in combination with statistical uncertainty and scale effects to mitigate (not eliminate) mesh-dependencies as described on page 72.

---

* which stood for Brannon-Fossum model #1 and was so named to indicate that the aim was to mimic capabilities of the Johnson-Holmquist model [33] called JH1.

By definition, the initial limit surface is regarded as fixed — it does not evolve (i.e., move around in stress space) as a yield surface can. Since the limit surface contains all attainable stress states, it follows that the set of all possible yield surfaces is contained within the limit surface (see Fig. 1.1). Plasticity induces microstructural changes that permit the yield surface to evolve through time, effectively changing the initial material into a mechanically *different* material. A material can have an infinite number of yield surfaces generated via various path-dependent hardening processes, but it can have only one limit surface. Limit surface characterization is accomplished by performing numerous experiments all the way to the point of material rupture (catastrophic failure). Each such experiment can have only one peak stress state. Post-peak softening in a material might lead to a stress at rupture that is smaller than at the peak, but it is the collection of *peak* — not rupture — stress states that defines the limit surface. Of course, mapping out the limit surface for a given material requires using a *new sample* for every experiment, which itself introduces uncertainty regarding variability in material composition and microstructure. Presently, Kayenta treats the limit surface (and each yield surface) as a sharp threshold boundary. Work is underway to allow these boundaries in stress space to be "fuzzy" to better account for natural material variability.

The set of all possible *yield* surfaces is contained within the limit surface. Porous materials are capable of inelastic deformation even under purely hydrostatic loading. Consequently, porous materials tend to have *closed* convex yield surfaces. Once all pores are crushed out, however, a material can withstand an unlimited amount of pressure. Thus, as indicated in Fig. 1.1, the *limit* surface for any material will always be an *open* convex set.

Despite being originally developed for geological applications, Kayenta is truly a unification of many classical plasticity models. For example, by using only a small subset of available parameters, Kayenta can be instructed to behave precisely like a classical hardening or non-hardening Von Mises model, in which case the yield surface becomes a cylinder centered about the [111] direction. Other classical models such as Drucker-Prager plasticity, Tresca theory, maximum principal stress theory, and Mohr-Coulomb theory are also supported in Kayenta by using the simplified input sets summarized in Appendix B. Replicating analytical results from simplified theories is an important aspect of verification of Kayenta. However, full use of a majority of Kayenta features is often required to adequately *validate* the model for realistic rock-like materials.

To describe in greater detail how Kayenta supports its broad range of micromechanisms of failure in a mathematical and computational framework, Chapters 2 and 3 first summarize our notation and outline some important concepts and conventions about the nature of stress. Chapter 4 describes Kayenta theory (elasticity, yield surface definition and evolution, etc.). The computational algorithm, subroutines, and plotable output will be discussed in Chapter 7, followed by software quality assurance in Chapter 8. Chapters 9 and 10 summarize verification and validation tests that have been completed to date for a

variety of materials. Model parameters (as well as descriptions of internal state variables and other symbols used in this report) are defined in Appendix B, along with sample input sets for realistic and idealized materials. Instructions for determining appropriate model parameters from laboratory data are provided in Appendix A.

2. Notation

Typesetting conventions

Throughout this report, **blue variables** are user input parameters and **green variables** are internal state variables available for plotting in the numerical implementation. At the discretion of the host code in which Kayenta is run, several other field variables (e.g., stress) may be additionally available for plotting.

Vector and tensor equations will be presented using indicial Cartesian notation in which repeated indices within a term are understood to be summed from 1 to 3 while non-repeated indices are free and take values 1 through 3. Upon occasion, vectors and tensors will be written in symbolic or "direct" notation in which the number of "tildes" beneath a symbol equals the tensorial order of that variable. For example, s, $\underset{\sim}{v}$, and $\underset{\approx}{T}$ would denote a scalar, a vector, and a tensor, respectively.

Vector and Tensor notation

For this report, the following standard operations and definitions from vector and tensor analysis will be employed:

Dot product between two vectors: $\underset{\sim}{u} \bullet \underset{\sim}{v} \ = \ u_1 v_1 + u_2 v_2 + u_3 v_3 \ \ = \ u_k v_k.$ \hfill (2.1)

Dot product between a tensor and a vector: $\underset{\sim}{y} \ = \ \underset{\approx}{A} \bullet \underset{\sim}{x}$ means $y_i \ = \ A_{ik} x_k.$ \hfill (2.2)

Dot product between a tensor and a tensor: $\underset{\approx}{C} \ = \ \underset{\approx}{A} \bullet \underset{\approx}{B}$ means $C_{ij} \ = \ A_{ik} B_{kj}.$ \hfill (2.3)

Kronecker delta: $\delta_{ij} \ = \ \begin{cases} 1 & \text{if } i=j \\ 0 & \text{if } i \neq j \end{cases}.$ \hfill (2.4)

Identity tensor: $\underset{\approx}{I}$ is the tensor whose ij components are δ_{ij} and whose

component matrix is therefore the 3×3 identity matrix. \hfill (2.5)

Inner product between two tensors: $\underset{\approx}{A} : \underset{\approx}{B} \ = \ A_{ij} B_{ij}.$ \hfill (2.6)

Magnitude of a vector: $\|\underset{\sim}{v}\| \ = \ \sqrt{v_k v_k} \ = \ \sqrt{\sum_{k=1}^{3} v_k^2}.$ \hfill (2.7)

Magnitude of a tensor: $\left\|\underset{\approx}{A}\right\| \ = \ \sqrt{A_{ij} A_{ij}} \ = \ \sqrt{\sum_{i=1}^{3}\sum_{j=1}^{3} A_{ij}^2}.$ \hfill (2.8)

Trace of a tensor $\underset{\approx}{A}$: $\qquad$ $\mathrm{tr}\underset{\approx}{A} = A_{11} + A_{22} + A_{33} = A_{kk}$. $\hfill$ (2.9)

Deviatoric part of a tensor: $\underset{\approx}{A}^{\mathrm{dev}} = \underset{\approx}{A} - \frac{1}{3}(\mathrm{tr}\underset{\approx}{A})\underset{\approx}{I}$, or $A_{ij}^{\mathrm{dev}} = A_{ij} - \frac{1}{3}A_{kk}\delta_{ij}$. $\hfill$ (2.10)

First invariant (trace) of a tensor $\underset{\approx}{A}$: $\qquad$ $I_1^A = \mathrm{tr}\underset{\approx}{A} = A_{kk}$. $\hfill$ (2.11)

Second invariant of a tensor $\underset{\approx}{A}$: $\qquad$ $J_2^A = \frac{1}{2}\mathrm{tr}[(\underset{\approx}{A}^{\mathrm{dev}})^2]$. $\hfill$ (2.12)

Third invariant of a tensor $\underset{\approx}{A}$: $\qquad$ $J_3^A = \frac{1}{3}\mathrm{tr}[(\underset{\approx}{A}^{\mathrm{dev}})^3]$. $\hfill$ (2.13)

Throughout this report, invariants of the stress tensor $\underset{\approx}{\sigma}$ will be written without the superscript identifier. For example, J_2 means the same thing as J_2^σ. Kayenta supports kinematic hardening in which the **shifted stress tensor** $\underset{\approx}{\xi}$ is defined $\underset{\approx}{\xi} = \underset{\approx}{\sigma} - \underset{\approx}{\alpha}$, where $\underset{\approx}{\alpha}$ is the backstress tensor (defined later). The invariants I_1, J_2, J_3 in the non-hardening theory will become $I_1^\xi, J_2^\xi, J_3^\xi$ when kinematic hardening is used.

In materials modeling, tensors are often regarded as higher-dimensional vectors. The inner product between two tensors, $\underset{\approx}{A}$ and $\underset{\approx}{B}$, is isomorphic to (i.e., geometrically analogous to) the dot product between two vectors. This permits the "magnitude" of a tensor, the "direction" of a tensor, and the "angle" between two tensors to be defined in manners analogous to ordinary vector definitions. For example, the yield surface is a boundary in six-dimensional stress space, and the normal to this surface is a tensor found by differentiating the yield function with respect to stress. The angle between two tensors can be used to quantify non-normality (i.e., misalignment of the yield normal and flow direction tensor).

The derivatives of a scalar-valued function f that depends on a second-order tensor $\underset{\approx}{\sigma}$ as well as depending on a scalar κ are given by

$$\frac{\partial f}{\partial \underset{\approx}{\sigma}} \text{ is a second-order tensor with } ij \text{ components } \frac{\partial f}{\partial \sigma_{ij}}. \qquad (2.14)$$

$$\frac{\partial f}{\partial \kappa} \text{ is a scalar.} \qquad (2.15)$$

Other derivatives are defined similarly. For example, the derivative of a second-order tensor $\underset{\approx}{A}$ with respect to another second-order tensor $\underset{\approx}{B}$ is a fourth-order tensor with $ijkl$ components $\partial A_{ij}/\partial B_{kl}$. The most important fourth-order tensors in Kayenta theory is the plastic tangent stiffness tensor, formally equal to the derivative of the stress rate with respect to the strain rate. In numerical implementations, manipulation and construction of fourth-order tensors is often avoided by exploiting applicable (or presumed) material symmetries.

3. The Stress Tensor

This section defines the stress tensor, its principal values, its invariants, and its sign convention. This chapter describes four canonical stress paths used to parameterize Kayenta: hydrostatic (HYD), triaxial compression (TXC), triaxial extension (TXE), and shear (SHR). For transient dynamics, Kayenta additionally requires Hugoniot and/or Kolsky (split Hopkinson) bar data to parameterize the viscoplasticity*. This chapter defines the distinction between the spatial Cauchy stress and the unrotated "reference" stress. In preparation for a detailed discussion of Kayenta theory, this chapter closes with a detailed description of "stress space" and Lode coordinates.

The **stress tensor** $\underset{\approx}{\sigma}$, is defined such that the **traction** vector $\underset{\sim}{t}$ (i.e., force per unit area), acting on any given plane with unit normal $\underset{\sim}{n}$, is given by

$$\underset{\sim}{t} = \underset{\approx}{\sigma} \bullet \underset{\sim}{n}. \tag{3.1}$$

Of course, the traction and normal vectors may be described in terms of their Cartesian components, $\{t_1, t_2, t_3\}$ and $\{n_1, n_2, n_3\}$ with respect to an orthonormal basis. The stress tensor has a 3×3 Cartesian component matrix such that the above equation may be written in matrix form as

$$\begin{bmatrix} t_1 \\ t_2 \\ t_3 \end{bmatrix} = \begin{bmatrix} \sigma_{11} & \sigma_{12} & \sigma_{13} \\ \sigma_{21} & \sigma_{22} & \sigma_{23} \\ \sigma_{31} & \sigma_{32} & \sigma_{33} \end{bmatrix} \begin{bmatrix} n_1 \\ n_2 \\ n_3 \end{bmatrix}, \tag{3.2}$$

or in indicial form as

$$t_i = \sigma_{ij} n_j, \tag{3.3}$$

where (recalling the implied summation convention) the repeated index "j" is understood to be summed from 1 to 3 and the non-repeated "free" index "i" appearing in each term takes values from 1 to 3 so that the above equation is actually a compact representation of three separate equations (one for each value of the free index).

The stress is symmetric, which means that $\sigma_{ij} = \sigma_{ji}$. In continuum mechanics, and in this report, stress is taken *positive* in tension. This sign convention can be the source of considerable confusion, especially when discussing stress invariants. For example, the trace of the stress, I_1, is positive in tension. However, brittle materials have very low strength in tension. Consequently, most of the functions defined in this report are nontrivial over only a small range of the tensile states where I_1 is positive. On the other hand,

---

* Until rate dependence is discussed separately in Chapter 6, all incremental or rate equations in this report are understood to apply only under quasistatic loading and may therefore be regarded as "inviscid" equations. Incorporating viscoplastic rate dependence requires, as a pre-requisite, solution of these quasistatic inviscid equations.

most of Kayenta functions are non-trivial over a relatively large range of compressive states where I_1 is negative. To help manage the sign convention problem, we will introduce a new notation that an over-bar on a variable denotes the *negative*. Specifically, for any variable x,

$$\bar{x} \equiv -x$$

DEFINITION OF THE "OVER-BAR." (3.4)

In our plots of any variable that varies as a function of I_1, we will usually employ an abscissa of $\bar{I}_1$, which (being the negative of I_1) is positive in compression. Any variable typeset with an overbar will be positive more often than negative in most applications.

The **principal stresses** are the eigenvalues $(\sigma_1, \sigma_2, \sigma_3)$ of the stress matrix, positive in tension. Their negatives $(\bar{\sigma}_1, \bar{\sigma}_2, \bar{\sigma}_3)$ are positive in compression.* When cast in terms of the principal basis (i.e., the orthonormal eigenvectors of the stress matrix), the diagonal components of the stress matrix will equal the principal stresses, and the off-diagonals will be zero.

The **stress deviator** $\underset{\approx}{S}$ is the deviatoric part of the stress (see Eq. 2.10):

$$\underset{\approx}{S} = \underset{\approx}{\sigma} - \tfrac{1}{3}(\mathrm{tr}\underset{\approx}{\sigma})\underset{\approx}{I}.$$ (3.5)

Loosely speaking, the stress deviator is a *tensor* measure of shear stress. An overall scalar measure of shear will be defined later. The quantity $\tfrac{1}{3}(\mathrm{tr}\underset{\approx}{\sigma})$ is called the **mean stress**, and we will denote it by p. The negative of the mean stress, $\bar{p} = -p$, is called the **pressure**, and is positive in compression. Noting that the mean stress (or pressure) is simply a multiple of I_1, its value is an invariant, meaning that the sum of diagonal stress components will have the same value regardless of the orthonormal coordinate system used to describe the stress components. The principal directions of the stress deviator are the same as those for the stress itself, and the principal values for the stress deviator are related to the principal stresses by

$$s_1 = \sigma_1 - \tfrac{1}{3}(\sigma_1 + \sigma_2 + \sigma_3)$$ (3.6)

$$s_2 = \sigma_2 - \tfrac{1}{3}(\sigma_1 + \sigma_2 + \sigma_3)$$ (3.7)

$$s_3 = \sigma_3 - \tfrac{1}{3}(\sigma_1 + \sigma_2 + \sigma_3).$$ (3.8)

The trace of $\underset{\approx}{S}$ is zero, which implies that the numerically largest principal value of any nonzero stress *deviator* will always be positive and the smallest will always be negative. In model parameterization tests, a sufficiently high confining pressure $\bar{p}$ is typically superimposed on the stress deviator to make all principal *stress* components compressive even though the principal deviatoric stresses always have mixed signs.

---

* Of course, if principal stresses are ordered such that $\sigma_1 \leq \sigma_2 \leq \sigma_3$, then the barred principal stresses will be ordered $\bar{\sigma}_1 \geq \bar{\sigma}_2 \geq \bar{\sigma}_3$.

Stress invariants

The trace operator is an invariant, which means its value will be the same regardless of which orthonormal basis is used for the stress components. Being symmetric, the stress tensor has a total of *three* independent invariants:

$$I_1 = \text{tr}\underset{\approx}{\sigma} \qquad\qquad = \sigma_1 + \sigma_2 + \sigma_3 \qquad\qquad (3.9)$$

$$J_2 = \tfrac{1}{2}\text{tr}(\underset{\approx}{S}^2) \qquad\qquad = \tfrac{1}{2}(s_1^2 + s_2^2 + s_3^2) \qquad\qquad (3.10)$$

$$J_3 = \tfrac{1}{3}\text{tr}(\underset{\approx}{S}^3) \qquad\qquad = \tfrac{1}{3}(s_1^3 + s_2^3 + s_3^3). \qquad\qquad (3.11)$$

The fact that these invariants are computed from the *stress* tensor $\underset{\approx}{\sigma}$ is sometimes emphasized by typesetting them as I_1^σ, J_2^σ, and J_3^σ. Similarly defined invariants for some *other* tensor $\underset{\approx}{\xi}$ would be typeset as $\{I_1^\xi, J_2^\xi, J_3^\xi\}$. Invariants for a tensor $\underset{\approx}{\alpha}$ would be written $\{I_1^\alpha, J_2^\alpha, J_3^\alpha\}$, and so forth. Any invariant written without a clarifying superscript should be understood to be a *stress* invariant.

The mean stress p is defined to be the average of the principal stresses, whereas pressure $\bar{p}$ is just the negative of mean stress:

$$\text{mean stress: } p = \frac{I_1}{3} \qquad\qquad \text{pressure: } \bar{p} = \frac{\bar{I}_1}{3}, \text{ where } \bar{I}_1 \equiv -I_1. \qquad (3.12)$$

Superimposing an extra pressure $\bar{P}$ on *any* stress state causes the pressure to increase from $\bar{p}$ to $\bar{p} + \bar{P}$, while having no effect on the stress deviator and therefore no effect on the second and third invariants. Because the stress *deviator* $\underset{\approx}{S}$ has a zero trace, it can be shown that J_3 also equals the determinant of the stress deviator so that $J_3 = s_1 s_2 s_3$, and the second invariant can be written alternatively as $J_2 = -(s_1 s_2 + s_2 s_3 + s_3 s_1)$.

Equation (3.10) shows that the invariant J_2 is never negative, which permits us to define a supplemental stress invariant, the **signed equivalent shear stress** τ as

$$\tau = \text{sign}[\sqrt{J_2}, J_3]. \qquad\qquad (3.13)$$

The "transfer of sign" operator* is defined

$$\text{sign}[x, y] = \begin{cases} |x| & \text{if} \quad y \geq 0 \\ -|x| & \text{if} \quad y < 0 \end{cases}. \qquad\qquad (3.14)$$

As defined, the equivalent shear stress will have a numerical sign that is positive in triaxial extension states (defined below), negative in triaxial compression, and it will be identically equal to the applied shear stress if the stress tensor happens to be in a state of pure shear (also defined below).

---

* which is an intrinsic function in most computing languages

For clarity, the values of the invariants have been shown here in terms of the principal values of the stress and its deviator. However, because the trace operation gives the same result regardless of which basis is used, the invariants are computed in practice directly from fully-populated 3×3 component matrices, thereby avoiding the need for an expensive eigenvalue analysis.

Derivatives of the stress invariants

For *isotropic* material modeling, each scalar-values function of stress, $\phi(\underset{\approx}{\sigma})$, is presumed to depend only on the principal stress values, not on the principal stress directions. Equivalently, the function $\phi(\underset{\approx}{\sigma})$ is isotropic if and only if it may be expressed alternatively as a function of the three stress invariants I_1, J_2, J_3. In situations where the derivative of ϕ with respect to stress is required, the chain rule can be applied as follows:

$$\frac{\partial \phi}{\partial \sigma_{ij}} = \frac{\partial \phi}{\partial I_1}\frac{\partial I_1}{\partial \sigma_{ij}} + \frac{\partial \phi}{\partial J_2}\frac{\partial J_2}{\partial \sigma_{ij}} + \frac{\partial \phi}{\partial J_3}\frac{\partial J_3}{\partial \sigma_{ij}}. \tag{3.15}$$

In symbolic tensor notation, this expansion is written as

$$\frac{\partial \phi}{\partial \underset{\approx}{\sigma}} = \frac{\partial \phi}{\partial I_1}\frac{dI_1}{d\underset{\approx}{\sigma}} + \frac{\partial \phi}{\partial J_2}\frac{dJ_2}{d\underset{\approx}{\sigma}} + \frac{\partial \phi}{\partial J_3}\frac{dJ_3}{d\underset{\approx}{\sigma}}. \tag{3.16}$$

Because the three invariants are each proper functions of the stress tensor, their derivatives may be computed in advance:

$$\frac{dI_1}{d\underset{\approx}{\sigma}} = \underset{\approx}{I} \qquad = \text{the identity tensor} \tag{3.17}$$

$$\frac{dJ_2}{d\underset{\approx}{\sigma}} = \underset{\approx}{S} \qquad = \text{dev}(\underset{\approx}{\sigma}) \quad = \text{the stress deviator} \tag{3.18}$$

$$\frac{dJ_3}{d\underset{\approx}{\sigma}} = \underset{\approx}{T} \qquad = \text{dev}(\underset{\approx}{S}^2) \quad = \text{the "Hill" tensor} \tag{3.19}$$

Thus, Eq. (3.16) may be written

$$\boxed{\frac{\partial \phi}{\partial \underset{\approx}{\sigma}} = \left(\frac{\partial \phi}{\partial I_1}\right)\underset{\approx}{I} + \left(\frac{\partial \phi}{\partial J_2}\right)\underset{\approx}{S} + \left(\frac{\partial \phi}{\partial J_3}\right)\underset{\approx}{T}} \;. \tag{3.20}$$

Of particular interest is the trace of the above expression, $\text{tr}(\partial \phi / \partial \underset{\approx}{\sigma})$. Since both $\underset{\approx}{S}$ and $\underset{\approx}{T}$ are deviatoric, the result is

$$\text{tr}\left(\frac{\partial \phi}{\partial \underset{\approx}{\sigma}}\right) = 3\left(\frac{\partial \phi}{\partial I_1}\right). \tag{3.21}$$

The factor of 3 appears simply because $\text{tr}\underset{\approx}{I} = 3$. This, by the way, is a good example of the fallibility of indicial notation. Specifically,

14

$$\text{tr}\left(\frac{\partial \phi}{\partial \underset{\approx}{\sigma}}\right) = \sum_{k=1}^{3} \frac{\partial \phi}{\partial \sigma_{kk}} \qquad \neq \qquad \frac{\partial \phi}{\partial \sum_{k=1}^{3} \sigma_{kk}} \, . \tag{3.22}$$

Special stress states

This section defines the four main stress states that are used to parameterize Kayenta. These are hydrostatic loading (HYD), triaxial compression (TXC), triaxial extension (TXE), and shear (SHR). The purpose of Kayenta is to interpolate realistically between known material response at these canonical states to describe material behavior under *general* stress states.

HYDROSTATIC (HYD). Loading is "**hydrostatic**" when components of the stress tensor are of the form

$$[\underset{\approx}{\sigma}] = \begin{bmatrix} -\bar{p} & 0 & 0 \\ 0 & -\bar{p} & 0 \\ 0 & 0 & -\bar{p} \end{bmatrix} \qquad \text{for hydrostatic stress states.} \tag{3.23}$$

In practice, the pressure $\bar{p}$ is usually compressive (and therefore positive). Hydrostatic testing is very important to parameterization of Kayenta because it indirectly characterizes the influence of material porosity. When hydrostatically loaded to a high pressure and then unloaded, a *non*-porous material will trace through the same stress states on both the loading and unloading curves. A *porous* material, on the other hand, will unload along a *different* path. If possible, hydrostatic testing for Kayenta should be conducted to sufficiently high pressures to compress out all pores, as indicated in Fig. 3.1.[*]
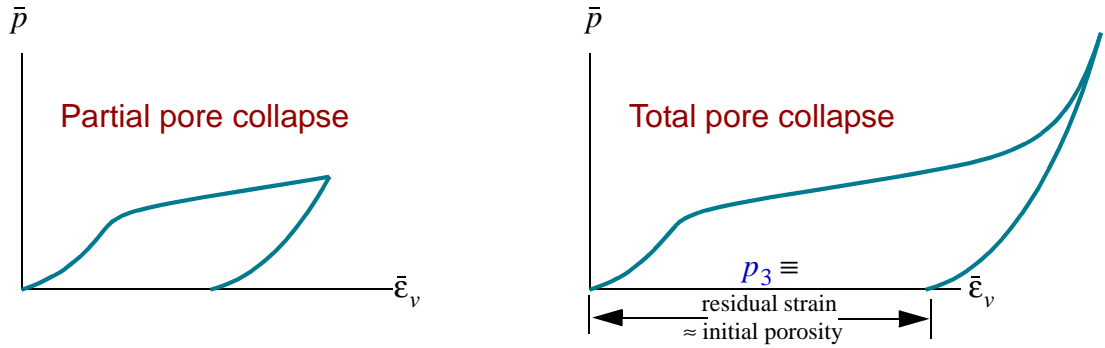
Figure 3.1. *Typical hydrostatic (pressure vs. volumetric strain) compression data.* Total pore collapse is achieved when the unloading curve (here shown as nonlinearly elastic) is tangent to the loading curve. In this case, the residual volumetric strain approximately equals the initial porosity.

---

[*] Kayenta parameter p_3 is the logarithmic (Hencky) residual volumetric strain after full void collapse. It is related to initial porosity ϕ_0 by $p_3 = \ln[1/(1 - \phi_0)]$, or $p_3 \approx \phi_0$ if ϕ_0 is small. Assuming the matrix material is plastically incompressible, the time-varying porosity during pore collapse can be inferred from Kayenta output variable ε_v^p (plot keyword EQPV). Specifically,
$$\phi = 1 - (1 - \phi_0)e^{\varepsilon_v^p} = 1 - \exp[-(\varepsilon_v^p + p_3)] \, .$$

When a material is loaded under hydrostatic *tension* instead of compression, inelastic response is again possible, but the mechanism of failure is catastrophic growth and coalescence of microcracks, resulting in material softening and, ultimately, complete loss of load carrying ability.

TRIAXIAL (TXC and TXE): Loading is "**triaxial**" whenever two principal stresses (denoted σ_L and called the "lateral" stresses) are equal to each other, but distinct from the third "axial" principal stress (denoted σ_A). Thus, with respect to the principal basis,

$$[\underset{\approx}{\sigma}] = \begin{bmatrix} \sigma_A & 0 & 0 \\ 0 & \sigma_L & 0 \\ 0 & 0 & \sigma_L \end{bmatrix} \qquad \text{for triaxial stress states,} \qquad (3.24)$$

and

$$[\underset{\approx}{S}] = \frac{\sigma_A - \sigma_L}{3}\begin{bmatrix} 2 & 0 & 0 \\ 0 & -1 & 0 \\ 0 & 0 & -1 \end{bmatrix} \qquad \text{for triaxial stress states.} \qquad (3.25)$$

Also,

$$I_1 = \sigma_A + 2\sigma_L \qquad \text{for triaxial stress states} \qquad (3.26a)$$

$$J_2 = \tfrac{1}{3}(\sigma_A - \sigma_L)^2 \qquad \text{for triaxial stress states} \qquad (3.26b)$$

$$J_3 = \tfrac{2}{27}(\sigma_A - \sigma_L)^3 \qquad \text{for triaxial stress states.} \qquad (3.26c)$$

The *signed* equivalent shear stress for triaxial loading is

$$\tau = \frac{\sigma_A - \sigma_L}{\sqrt{3}} \qquad (3.27)$$

The invariants defined here may be written alternatively in terms of *compressive* stress measures as

$$\boxed{\bar{I}_1 = \sqrt{3}\bar{\tau} + 3\bar{\sigma}_L} \qquad \boxed{J_2 = \bar{\tau}^2} \qquad \boxed{\bar{J}_3 = \tfrac{2\sqrt{3}}{9}\bar{\tau}^3}$$

$$(3.28)$$

where

$$\bar{\tau} = \frac{\bar{\sigma}_A - \bar{\sigma}_L}{\sqrt{3}}. \qquad (3.29)$$
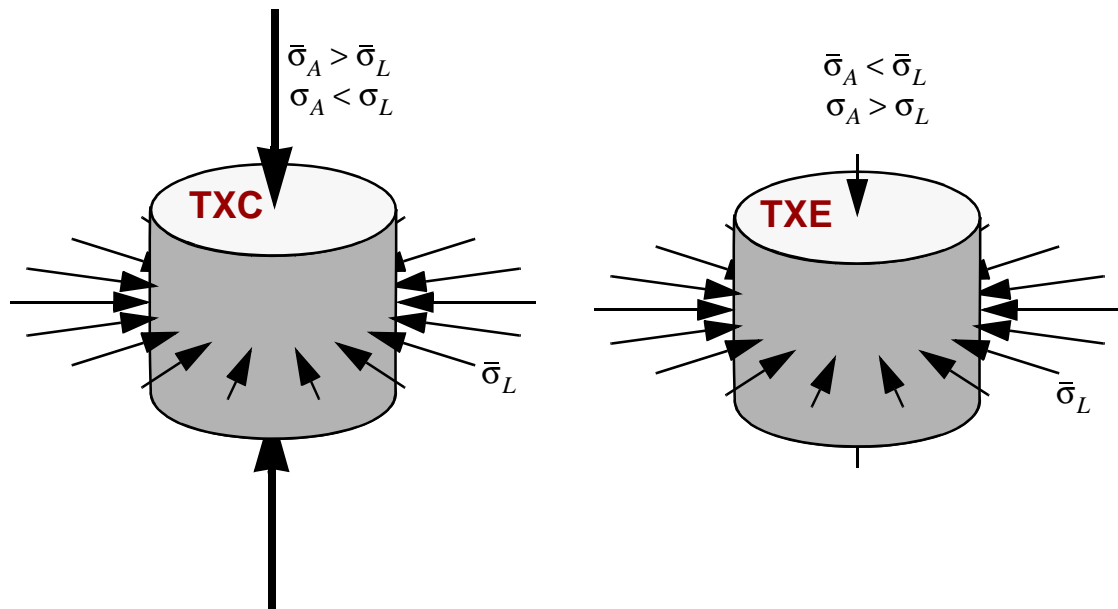
Figure 3.2.   *Triaxial compression (TXC) and triaxial extension (TXE)*   Two principal stresses (the lateral stress) are equal. For TXC, the axial stress is more compressive than the lateral stress. For TXE, the axial stress is less compressive than the lateral stress. In the labels, $\bar{\sigma} = -\sigma$; stress σ is positive in tension while stress $\bar{\sigma}$ is positive in compression.

The term "triaxial" is a bit of a misnomer because there are not really three independent loads applied — the lateral stresses are equal. These experiments are normally performed on cylindrical test specimens with the lateral load supplied by a pressure bath. For **triaxial compression** (**TXC**) the axial stress is more compressive than the lateral stress. For **triaxial extension** (**TXE**) the axial stress is not necessarily *tensile* — it is merely *less compressive* than the lateral stress. For TXC, the specimen changes shape such that its length-to-diameter ratio decreases. For TXE, the length-to-diameter ratio *increases* even though the length and diameter might *individually* both decrease. Uniaxial stress *compression* (also called **unconfined compression**) is a special form of TXC in which the axial stress is compressive and *the lateral stress is zero*. Uniaxial stress *extension* is a special form of TXE in which the axial stress is tensile and the lateral stress is zero. **Uniaxial *strain* compression**, which is typical in flyer-plate impact experiments is a special case of TXC in which the axial stress is compressive, while the lateral *strain* is zero (making the lateral stress also compressive, but less compressive than the axial stress). **Biaxial tension** is a special case of TXC in which the lateral stress is tensile and the *axial* stress is zero. **Biaxial compression** is a special case of TXE in which the lateral stress is com-

17

pressive and the axial stress is zero. According to Eq. (3.27), the signed shear stress satisfies $\bar{\tau} > 0$ for TXC, whereas $\bar{\tau} < 0$ for TXE. Consequently, Eq. (3.28) shows that $\bar{J}_3 > 0$ (and hence $J_3 < 0$) for TXC, while $\bar{J}_3 < 0$ (and hence $J_3 > 0$) for TXE. Of course, $J_2 > 0$ for *both* TXC and TXE because it is the *square* of $\bar{\tau}$.

In typical triaxial experiments, the lateral stress is held fixed (via a pressure bath) while only the axial stress is varied. In this case, Eq. (3.28) implies that

$$\frac{d\bar{\tau}}{d\bar{I}_1} = \frac{1}{\sqrt{3}} \quad \text{for triaxial stress loading with fixed lateral stress.} \tag{3.30}$$
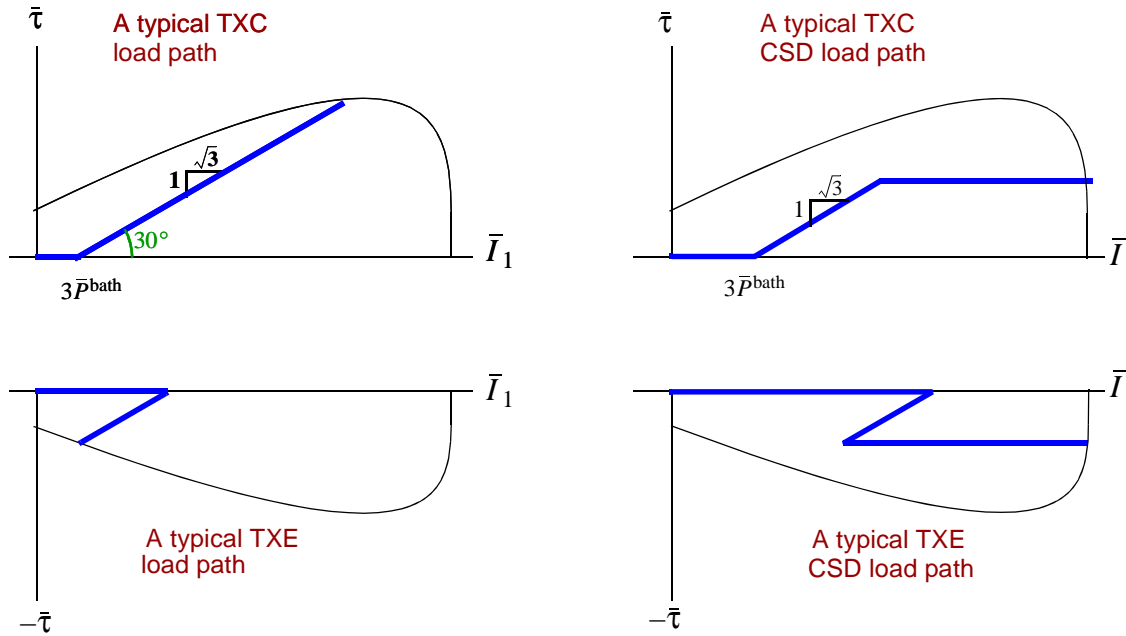
Figure 3.3. *Triaxial and CSD load paths.* The material is first compressed hydrostatically to a pre-selected bath pressure $\bar{P}^{\text{bath}}$; at this point, the value of the first stress invariant is $I_1 = -3\bar{P}^{\text{bath}}$ and therefore $\bar{I}_1 = 3\bar{P}^{\text{bath}}$. When the triaxial leg begins, the lateral stress is held constant ($\bar{\sigma}_L = \bar{P}^{\text{bath}}$) while the axial stress is varied. This causes both the first and second invariants to change such that the path in this stress plot is a straight line with slope $1/\sqrt{3}$. For simple triaxial loading, the stress difference is increased until material failure occurs. For CSD loading, the stress difference is increased to a pre-selected value, and then held fixed while all stress components are thereafter varied equally until failure occurs.

Being easily achieved in the laboratory, TXC and TXE data are essential to parameterize Kayenta. In a typical triaxial test, the material is first loaded hydrostatically in a pressure bath until all three principal stresses reach a compressive pressure $\bar{P}^{\text{bath}}$. Thereafter, the lateral stresses are held fixed at this value ($\bar{\sigma}_L = \bar{P}^{\text{bath}}$) while the axial stress is then

increased beyond $\bar{P}^{\text{bath}}$. For some experiments, the axial stress might be increased only until the stress difference reaches a given value, after which all stresses are again increased by equal amounts. These are called **constant stress difference (CSD)** experiments. Typically, these experiments are run to the point of material failure. Periodic partial unloading during a test reveals yielding if the unloading stress-strain curve has a noticeably different slope than the loading curve (without unloading, it would be impossible to definitively distinguish plasticity from non-linear elasticity).

As illustrated in Fig. 3.3, a series of TXC experiments at various bath pressures and/or stress differences results in a family of ($\bar{I}_1$, $\bar{\tau}$) stress-at-yield points that map out the TXC meridional profile of Kayenta yield surface. Similar experiments under TXE map out the TXC meridional profile. Usually, the TXE failure envelope will be shaped similarly to the TXC envelope, but lower in magnitude because, at a given value of I_1, the value of $\sqrt{J_2}$ at failure is generally lower for TXE than for TXC. A plot of the failure envelope in $\bar{\tau}$ vs. I_1 space is essentially equivalent to the meridional "side" view of the yield surface (Fig. 1.0b), except with the axes scaled differently. The TXE experiments are mapping out the cross-section of the yield surface along which pressure varies while staying on the "base" of the triangular octahedral profile in Fig. 1.0c (page 1), whereas TXC experiments reveal how the apex of the triangle varies with pressure. For metals, there is little difference between the stress intensity required to initiate failure in TXC compared to TXE. However, for brittle materials, the difference is quite noticeable and (according to idealized microphysical theories) can be attributed to internal frictional resistance to shear crack growth. Because friction increases with pressure, the material strengths in TXC and TXE tend to increase with pressure but in approximately the same proportions so that the ratio of TXC strength to TXE strength is approximately pressure independent. Consequently, the TXE profiles shown in Fig. 3.3 are shaped identically to the TXC profiles except smaller in magnitude.

Another form of triaxial loading, commonly used for dynamic material testing, is **uniaxial strain**, in which the lateral *strain* ε_L is held constant. If the lateral strain ε_L is held constant while continuing to compress axially, the lateral compressive *stress* $\bar{\sigma}_L$ will increase to prevent lateral motion. For uniaxial strain, $\dot{\varepsilon}_L = 0$, and therefore Hooke's law[*] in rate form reduces to

$$\text{Uniaxial strain:} \quad \dot{\sigma}_A = \left(K + \frac{4}{3}G\right)\dot{\varepsilon}_A \quad \text{and} \quad \dot{\sigma}_L = \frac{\nu}{1-\nu}\dot{\sigma}_A = \left(K - \frac{2}{3}G\right)\dot{\varepsilon}_A, \tag{3.31}$$

where K and G are, respectively, the tangent elastic bulk and shear moduli.

---

[*] The general form of Hooke's law, applicable to any form of triaxial loading, is given in Eq. (4.11). Eq. (3.31) is a special case of Eq. (4.11) in which $\dot{\varepsilon}_L = 0$, with Eq. (4.13) used to express Young's modulus E and Poisson's ratio ν in terms of K and G.

For uniaxial strain, the rate of the signed equivalent shear stress and the rate of the first stress invariant are

$$\text{Uniaxial strain:}\quad \dot{\bar{\tau}} = \frac{2G\dot{\bar{\varepsilon}}_A}{\sqrt{3}} \qquad \text{and} \qquad \dot{\bar{I}}_1 = 3K\dot{\bar{\varepsilon}}_A, \tag{3.32}$$

and therefore the path through stress space is a straight line with slope

$$\frac{d\bar{\tau}}{d\bar{I}_1} = \frac{1}{\sqrt{3}}\frac{2G}{3K} = \frac{1}{\sqrt{3}}\left(\frac{1-2\nu}{1+\nu}\right) \quad \text{for triaxial stress with fixed lateral strain,} \tag{3.33}$$

where ν is Poisson's ratio. Since Poisson's ratio typically varies between 0 and $1/2$,* this result shows that the trajectory in the meridional profile will generally have a shallower slope under uniaxial strain loading than under uniaxial stress loading. This result should make some intuitive sense. Uniaxial strain experiments are conducted by applying increasing levels of compression in the axial direction while holding the lateral strain fixed. As the axial strain is compressed, the material "wants" to expand laterally, but is not permitted to — a lateral compressive force prevents this outward motion. This constraining lateral compression makes $\bar{I}_1$ larger than it would be when lateral expansion is unconstrained. The larger $\bar{I}_1$ results in a shallower slope in the stress trajectory.

SIMPLE/PURE SHEAR and PRESSURE-SHEAR LOADING (SHR).

A material is in a state of **simple shear** with respect to a given coordinate system if the stress matrix in that system is of the form

$$[\underset{\approx}{\sigma}] = [\underset{\approx}{S}] = \begin{bmatrix} 0 & s & 0 \\ s & 0 & 0 \\ 0 & 0 & 0 \end{bmatrix} \quad \text{for simple shear,} \tag{3.34}$$

where s is the shear stress. The eigenvalues of this matrix are $\{s, -s, 0\}$. In general, any stress state that is deviatoric with one eigenvalue being zero is said to be a **pure shear** [36, p. 16]. (Thus, simple shear is a special type of pure shear). For an isotropic material model like Kayenta, yield depends only on the principal stresses, so there is no practical difference between simple and pure shear (except when the model is anisotropic because of kinematic hardening).

For conducting material characterization experiments, **pure shear** of the form

$$[\underset{\approx}{\sigma}] = [\underset{\approx}{S}] = \begin{bmatrix} s & 0 & 0 \\ 0 & -s & 0 \\ 0 & 0 & 0 \end{bmatrix} \quad \text{for pure shear} \tag{3.35}$$

---

* Strictly speaking, positive definiteness of the elastic stiffness tensor merely requires $-1 < \nu < 1/2$. Whereas negative Poisson's ratio has been observed in man-made materials with re-entrant microstructures, it has not (to our knowledge) been reported for naturally occurring materials. Performance of Kayenta has not been verified for materials with negative Poisson's ratio.

is most convenient. For brittle materials, pure shear is difficult to attain because one of the eigenvalues is always tensile. Frequently, pure shear is superimposed with enough confining hydrostatic pressure to make all principal stresses negative (compressive). Specifically, superimposing the hydrostatic loading of Eq. (3.23) onto the shear stress of Eq. (3.35), gives a state of **combined pressure-shear (SHR)** loading:

$$[\underset{\approx}{\sigma}] = \begin{bmatrix} s - \bar{p} & 0 & 0 \\ 0 & -s - \bar{p} & 0 \\ 0 & 0 & -\bar{p} \end{bmatrix} \qquad \text{for combined pressure-shear loading.} \qquad (3.36)$$

The invariants for combined pressure-shear loading are

$$I_1 = -3\bar{p} \qquad\qquad \text{for combined pressure-shear loading} \qquad (3.37a)$$

$$J_2 = s^2 \qquad\qquad \text{for combined pressure-shear loading} \qquad (3.37b)$$

$$J_3 = 0 \qquad\qquad \text{for combined pressure-shear loading} \qquad (3.37c)$$

$$\tau = |s|. \qquad\qquad (3.38)$$

Spatial and Reference stress (frame indifference)

The spatial Cauchy stress tensor defined in Eq. (3.1) is the "familiar" stress tensor used in everyday engineering applications. Let us now denote that stress by $\underset{\approx}{\sigma}^{\text{spatial}}$. The elasticity component of solids models requires knowledge of both the *initial* and *current* configurations. Moreover, the principle of material frame indifference demands that if a *second* problem were considered that had the same initial configuration, but a current configuration that is identical to the current configuration of the first problem, except also rigidly rotated, then the predicted spatial stresses for the second problem should be identical to those of the first problem, except rigidly rotated by the same amount. This concept is quite different from a mere basis change because the *initial configuration* is identical for both problems.

Satisfying material frame indifference in a *spatial* context can be computationally expensive and error-prone because anisotropic internal state variables (such as directions of material fibers or orientation of the backstress) must be rotated *into* the spatial frame, and special "objective" rates must be integrated in constitutive models. A mathematically equivalent (and numerically more accurate and efficient) strategy instead applies the constitutive model within an *unrotated* reference configuration. With this approach, rotation of internal variables is not required, and all rates that appear in the constitutive model are more easily integrated *true* rates instead of co-rotational rates.

If $\underset{\approx}{\boldsymbol{R}}$ is the proper orthogonal tensor (found from a polar decomposition of the deformation) that characterizes the material rotation, then the unrotated stress is simply

$$\underset{\approx}{\sigma}^{\text{unrotated}} = \underset{\approx}{\boldsymbol{R}}^T \bullet \underset{\approx}{\sigma}^{\text{spatial}} \bullet \underset{\approx}{\boldsymbol{R}} \qquad (3.39)$$

By working in the unrotated reference configuration, Kayenta predicts the stresses for the non-rotating problem. Upon receiving Kayenta's update of the unrotated stress, the host code then rotates the predicted stress back into the spatial frame. Roughly speaking, this approach will give results identical to a spatial constitutive model that is cast in terms of polar objective rates.

For problems involving massive material rotation (e.g., turbine blades, vortices, tumbling rock fragments, etc.), the "unrotation" strategy can give considerably more accurate answers because the host code may, optionally, use the rotation tensor $\underset{\approx}{\pmb{R}}^n$ at the beginning of the time step when computing the starting value of $\underset{\approx}{\sigma}^{\text{unrotated}}$, but then the host code may use $\underset{\approx}{\pmb{R}}^{n+1}$ at the *end* of the step when recasting the updated value of $\underset{\approx}{\sigma}^{\text{unrotated}}$ (output of Kayenta) to the spatial frame. Hence, this approach supports so-called "strong objectivity" [47] in a very natural way.

Throughout the remainder of this report, the "stress" $\underset{\approx}{\sigma}$ must be understood to be the *unrotated* stress $\underset{\approx}{\sigma}^{\text{unrotated}}$. Likewise all other vector or tensor variables (such as the strain rate) mentioned in this report are understood to be cast in the unrotated configuration (material frame). Any host code that uses Kayenta must **(1)** perform these unrotation operations, **(2)** call Kayenta, and then **(3)** re-rotate the result back to the spatial frame upon return. For more information, see page 89.

Lode coordinates

Any isotropic yield function may be expressed in terms of the principal stresses $(\sigma_1, \sigma_2, \sigma_3)$. Therefore, the yield surface may be visualized in a 3D space for which the Cartesian coordinates are these principal stresses. The value of the yield function $f(\sigma_1, \sigma_2, \sigma_3)$ must be independent of the ordering of the eigenvalues. Therefore, as seen in Fig. 1.0 (page 1), the yield surface must have $120°$ rotational symmetry about the [111] (hydrostat) direction and reflective symmetry about the TXE and TXC axes in the octahedral plane (i.e., the view looking down the [111] axis).

The **principal Cartesian coordinates** $(\sigma_1, \sigma_2, \sigma_3)$ comprise an adequate choice for characterizing stress space, but the yield function is often cast in terms of different independent variables to exploit the yield surface's natural symmetries optimally. The natural symmetries suggest instead using cylindrical $(r, \bar{\theta}, z)$ coordinates — called **Lode cylindrical coordinates** — for which the z-axis is parallel with the [111] symmetry axis. We have placed a bar on the symbol $\bar{\theta}$ for the angular coordinate because we intend to define it so that it will be positive in TXC and negative in TXE. A constant $\bar{\theta}$ plane is a **meridional plane**, and a plot of r vs. z. at a given value of $\bar{\theta}$ is called a **meridional profile**. Because most of the yield surface resides in the compressive domain where $z < 0$, we will usually display meridional profiles as r vs. $\bar{z}$ (where $\bar{z} = -z$). Any constant-z plane is an **octahedral plane**, and any cross-section looking down the [111] axis (i.e., on a plane of constant z) is in an **octahedral profile**. Meridional and octahedral profiles are illustrated in Fig. 1.0 (page 1).

In this report, the Lode angle $\bar{\theta}$ is defined so that it equals zero in SHR. It varies from $-30°$ in TXE to $+30°$ in TXC. Superimposing pressure on a stress state changes only the axial z-coordinate, leaving the octahedral $(r, \bar{\theta})$ coordinates unchanged, which makes Lode coordinates a natural choice when decomposing tensors in to their isotropic and deviatoric parts. The radial r coordinate equals the magnitude of the stress deviator. The z coordinate is proportional to the mean stress. The angular coordinate is a measure of the relative proportions of the principal values of the stress deviator. Thus, as the Lode angle varies from $-30°$ to $+30°$, the stress transitions through TXE, SHR, and TXC states. Cylindrical Lode coordinates are especially useful because they may be expressed in terms of stress invariants, thereby eliminating the need for an eigenvalue decomposition.

The axial z-coordinate is positive on the tensile part of the hydrostat, so $\bar{z}$ is positive on the compressive hydrostat. We define the Lode angle $\bar{\theta}$ to be positive in TXC and negative in TXE. The change in variables from principal coordinates to Lode coordinates permits the yield function $f(\sigma_1, \sigma_2, \sigma_3)$ to be alternatively expressed in the form $f(r, \bar{\theta}, \bar{z})$. When phrased in terms of Lode coordinates, the yield function needs to be defined only over a $60°$ sextant on any octahedral plane. The symmetry properties of the yield surface may be used to reconstruct the octahedral profile over the full range from $0°$ to $360°$.

Performing these necessary but tedious coordinate transformations from principal stresses to cylindrical Lode coordinates, it can be shown [40] that the cylindrical Lode coordinates may be determined directly from the I_1, J_2, and J_3 scalar stress invariants, eliminating the need for an eigenvalue analysis. Specifically,

$$r = \sqrt{2J_2} \tag{3.40a}$$

$$\sin 3\bar{\theta} = -\frac{J_3}{2}\left(\frac{3}{J_2}\right)^{3/2} \tag{3.40b}$$

$$\bar{z} = \frac{\bar{I}_1}{\sqrt{3}} \tag{3.40c}$$

The square root coefficients are merely by-products of the coordinate transformations. For example, since the z-coordinate is the projection of the stress onto the [111] axis, the $\sqrt{3}$ appears because the magnitude of the [111] vector is $\sqrt{3}$. The Lode radius r is zero if $J_2=0$. Also, the Lode angle $\bar{\theta}$ is undefined when $J_2=0$, which should not be too disturbing since the angular coordinate for any cylindrical system is undefined when the point in question lies on the symmetry axis (which, in this case, is the [111] hydrostat).

Later, when we give the mathematical formulation for Kayenta yield function, it will be phrased as $f(r, \bar{\theta}, \bar{z})$. Using the above formulas, the yield function is ultimately implemented in the form $f(I_1, J_2, J_3)$. The invariant J_3 influences only the Lode angle. When simpler yield models (Drucker-Prager) are independent of the third stress invariant, they

are therefore independent of the Lode angle, which makes their octahedral yield profile a circle. Kayenta must include a *non-circular* yield profile to reproduce TXE/TXC strength differences clearly evident in the data for geological materials. Thus, Kayenta must necessarily use all three Lode coordinates (equivalently, all three stress invariants).

Octahedral yield profile visualization. Given a yield function $f(r, \bar{\theta}, \bar{z})$, yield profiles may be generated by solving $f = 0$ to obtain r expressed as a function of $(\bar{\theta}, \bar{z})$. A meridional profile is generated by plotting r vs. $\bar{z}$ at a fixed value of $\bar{\theta}$. An octahedral profile, which corresponds to a yield surface cross-section at a given value of $\bar{z}$, describes how the Lode radius at yield varies with the Lode angle. Rather than plotting r vs. $\bar{\theta}$, octahedral profiles are obtained by parametrically plotting Cartesian coordinates

$$x_1 = r\cos\overline{\Theta} \text{ and } x_2 = r\sin\overline{\Theta} \tag{3.41}$$

Here, Θ is an angle that varies over the full range from 0 to $360°$. The Lode angle $\bar{\theta}$, which is permitted to vary only over the range from $-30°$ to $30°$, is generated from the full-range angle Θ by the sawtooth function

$$\bar{\theta} = \frac{1}{3}\text{ArcSin}[\sin(3\overline{\Theta})] \tag{3.42}$$

With $\bar{\theta}$ known, the value of corresponding Lode radius r can be found from the yield condition, and finally, the family of (x_1, x_2) points on the octahedral yield profile may be generated parametrically as Θ varies from 0 to $360°$, as illustrated in Fig. 3.4.
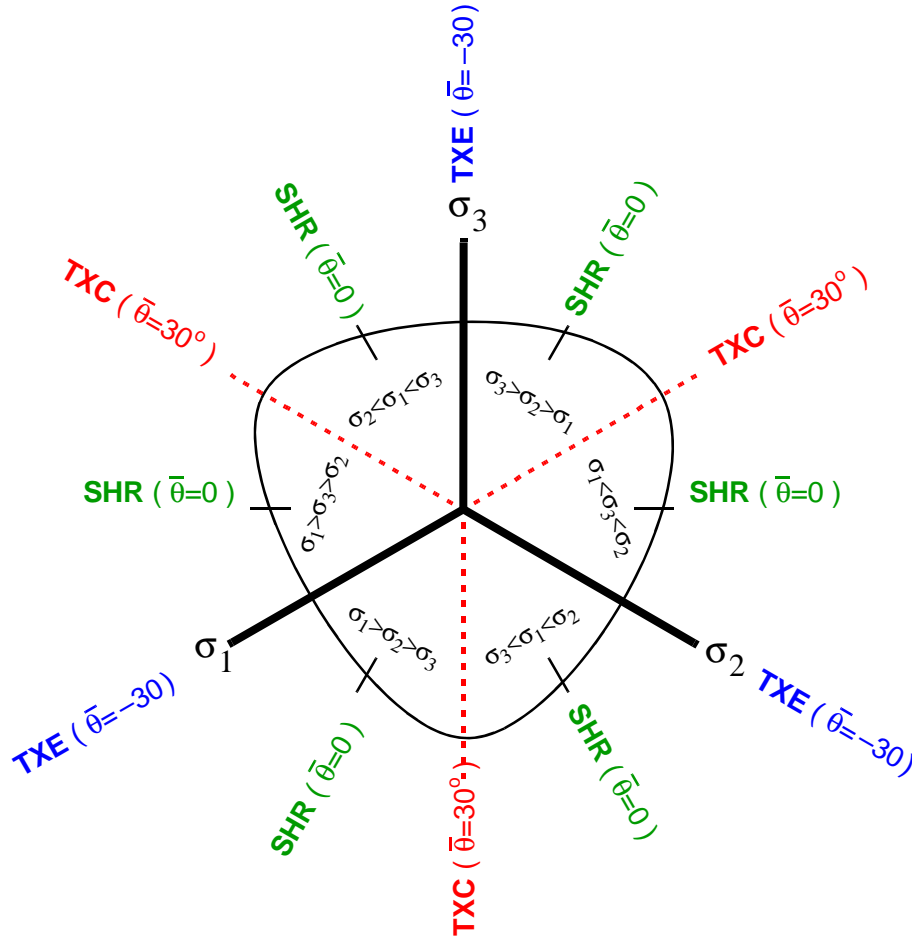
Figure 3.4.   An octahedral yield profile. Geological materials tend to be stronger in TXC than in TXE, which is why the TXC axes are always on an apex of the rounded triangle (i.e., farther from the origin, corresponding to higher strength). The Lode angle $\bar{\theta}$ alternates cyclically from $-30°$ in TXE to $30°$ in TXC because the yield threshold must be independent of the eigenvalue ordering.

Meridional yield profile visualization. To draw a *geometrically accurate* meridional cross-section of the yield surface, the profile should be plotted as r vs. $\bar{z}$ for a given value of $\bar{\theta}$. Typically, we will plot the TXC ($\bar{\theta} = 30°$) profile. Using the r and $\bar{z}$ Lode coordinates as the axes in a meridional plot ensures that lengths and angles in the meridional profile will equal corresponding lengths and angles in stress space. Many times, however, we will depict a geometrically *distorted* view of the meridional profile by instead plotting $\bar{\tau}$ vs. $\bar{I}_1$, where the signed equivalent shear stress $\bar{\tau}$ equals $\pm\sqrt{J_2}$, depending on whether the loading is closer to TXE or TXC. Recalling from Eqs. (3.40a) and (3.40c) that $\sqrt{J_2} = r/\sqrt{2}$ and $\bar{I}_1 = \sqrt{3}\bar{z}$, a plot of $\bar{\tau}$ vs. $\bar{I}_1$ is equivalent to changing the aspect ratio of an r vs. $\bar{z}$ plot by a factor of $\sqrt{6} = 2.45$, as illustrated in Fig. 3.5. Thus, whenever we plot the meridional profile as $\bar{\tau}$ vs. $\bar{I}_1$, keep in mind that the actual meridional cross-section in stress space is smaller in width by a factor of 2.45. Meridional profile distortion is an issue only when ascertaining the direction of the yield surface normal. Figure 3.5 shows that the normal to the yield profile in a distorted plot does *not* correspond to the normal in stress space.
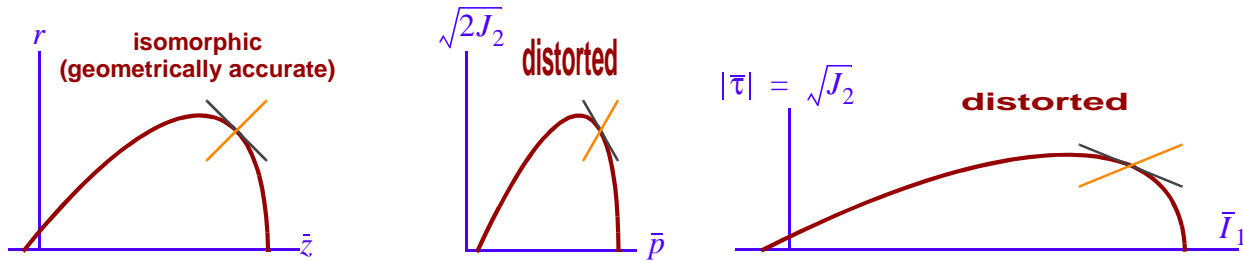
Figure 3.5. *Distortion of the meridional profile when using non-isomorphic stress measures.* Only a plot of r vs. z will result in a geometrically accurate depiction of a meridional cross-section of stress space for which angles and lengths are preserved. The middle plot shows the magnitude of the stress deviator plotted against the pressure, resulting in a plot eccentricity of $1/\sqrt{3} = 0.577$. The last plot shows the equivalent shear stress plotted against the first stress invariant, for a plot eccentricity of $\sqrt{6} = 2.45$.

Closed-form solution for ordered eigenvalues. Recalling that Lode cylindrical coordinates merely represent a coordinate change from the principal coordinates $(\sigma_1, \sigma_2, \sigma_3)$ to a new set of coordinates $(r, \bar{\theta}, z)$, it follows that inverse transformation formulas should exist for obtaining the principal stresses from Lode coordinates. Each distinct sextant in Fig. 3.4 merely corresponds to a different eigenvalue ordering. Regardless of the sextant in which the stress resides, $\bar{\theta} = 30°$ falls on the pi-plane axis corresponding to the smallest eigenvalue, whereas $\bar{\theta} = -30°$ falls on the axis of the largest eigenvalue. Therefore, transformation formulas that convert cylindrical coordinates back to Cartesian coordinates only need to be defined over the range from $-30°$ through $+30°$ to determine the *ordered* eigenvalues.

Letting the compressive eigenvalues be ordered $\bar{\sigma}_3 \leq \bar{\sigma}_2 \leq \bar{\sigma}_1$, the *tensile* eigenvalues must be ordered $\sigma_3 \geq \sigma_2 \geq \sigma_1$, and the inverse transformation formulas are

low:
$$\sigma_1 = \frac{z}{\sqrt{3}} - \frac{r}{\sqrt{2}}\left[\cos\bar{\theta} + \frac{\sin\bar{\theta}}{\sqrt{3}}\right] = \frac{I_1}{3} - \sqrt{J_2}\left[\cos\bar{\theta} + \frac{\sin\bar{\theta}}{\sqrt{3}}\right] \qquad (3.43a)$$

middle:
$$\sigma_2 = \frac{z}{\sqrt{3}} + \sqrt{\frac{2}{3}}\, r\sin\bar{\theta} = \frac{I_1}{3} + \frac{2}{\sqrt{3}}\sqrt{J_2}\sin\bar{\theta} \qquad (3.43b)$$

high:
$$\sigma_3 = \frac{z}{\sqrt{3}} + \frac{r}{\sqrt{2}}\left[\cos\bar{\theta} - \frac{\sin\bar{\theta}}{\sqrt{3}}\right] = \frac{I_1}{3} + \sqrt{J_2}\left[\cos\bar{\theta} - \frac{\sin\bar{\theta}}{\sqrt{3}}\right]. \qquad (3.43c)$$

These formulas constitute a closed-form solution for the ordered eigenvalues of *any* real symmetric 3×3 matrix, not just a stress.[*] Using these formulas, any yield function that is stated in terms of principal stresses, $f(\sigma_1, \sigma_2, \sigma_3)$, can be immediately re-cast into a form expressed in terms of stress invariants, $f(I_1, J_2, J_3)$, which is more convenient for plasticity modeling because it can be differentiated without an eigenvector analysis (see Eq. 3.16). For example, any material model that seeks to initiate failure when the largest tensile principal stress σ_3 reaches a critical value, σ_3^{crit}, can do so by simply substituting Eq. (3.43c) into the failure criterion, $\sigma_3 = \sigma_3^{\text{crit}}$. The above closed-form solution for ordered eigenvalues is applied in Appendix B (page B-25) to convert the Mohr-Coulomb theory of failure into a formulation expressed in terms of stress invariants, as required in Kayenta.

---

[*] The solution quoted here is equivalent to the closed form solution derived by Malvern [41] via a trigonometric substitution. Malvern's angle α is a Lode angle, but defined to be zero in TXE and $60°$ in TXC.

4. Kayenta theory

Being a generalized plasticity theory, Kayenta is founded upon an additive decomposition of the strain rate $\dot{\underset{\approx}{\varepsilon}}$ into separate contributors: $\dot{\underset{\approx}{\varepsilon}}^e$ from elastic straining and $\dot{\underset{\approx}{\varepsilon}}^p$ from inelastic straining:

$$\dot{\underset{\approx}{\varepsilon}} = \dot{\underset{\approx}{\varepsilon}}^e + \dot{\underset{\approx}{\varepsilon}}^p. \tag{4.1}$$

Kayenta permits the host code to employ any definition of the strain so long as its rate is conjugate to the stress $\underset{\approx}{\sigma}$ in the sense that the work rate per unit volume is given by

$$\underset{\approx}{\sigma}:\dot{\underset{\approx}{\varepsilon}}. \tag{4.2}$$

To satisfy the principle of material frame indifference, the host code must cast the stresses and strain rates in an unrotated configuration. At present, all implementations of Kayenta have approximated the strain rate by the unrotated symmetric part of the velocity gradient:

$$\dot{\varepsilon}_{ij} \approx \frac{1}{2}\left(\frac{\partial v_m}{\partial x_n} + \frac{\partial v_n}{\partial x_m}\right) R_{mi} R_{nj}, \tag{4.3}$$

where $\underset{\sim}{v}$ is the velocity vector, $\underset{\sim}{x}$ is the current spatial position vector, and the tensor $\underset{\approx}{R}$ is the rotation from the polar decomposition of the deformation gradient. The conjugate stress is the unrotated Cauchy stress defined in Eq. 3.39. Henceforth, all references to the stress σ_{ij} and the strain rate $\dot{\varepsilon}_{ij}$ must be understood to be the *unrotated* stress and strain rate.

All Kayenta material parameterizations to date have been based on the above approximation for the strain rate. Using a different choice for the conjugate stress and strain rate measures would, of course, entail adjusting material parameters appropriately. The strain rate in Eq. (4.3) is an approximation because, for general deformations, it is not precisely equal to the rate of any proper function of the deformation[*]. The approximate strain rate in Eq. (4.3) exactly equals the unrotated logarithmic (Hencky) strain rate for any deformation having stationary principal stretch directions. It is an excellent approximation to the Hencky strain rate even when principal stretch directions change orientation as long as the shear strains remain small (volumetric strains may be arbitrarily large). For geological applications, material rupture generally occurs well before shear strains become large, so Eq. (4.3) is a prudent choice for the strain rate measure. If, however, the model is to be subjected to significant cyclical loading (e.g. fatigue), then a proper strain rate should be used instead of Eq. (4.3) even if the distortional strains are always small.

---

[*] Paths can be devised for which the starting and ending configurations are identical, but the time integral of $\dot{\varepsilon}_{ij}$ does not evaluate to zero [13].

Elasticity

Kayenta supports both linear and nonlinear hypoelasticity*. Kayenta presumes the material is elastically isotropic and that the elastic stiffness tensor C_{ijkl} is itself isotropic (i.e., deformation-induced elastic anisotropy is not included). Consequently, the stress is governed by a rate form of Hooke's law:

$$\overset{\circ}{\sigma}_{ij} = C_{ijkl}\dot{\varepsilon}^e_{kl}. \tag{4.4}$$

Because the elastic tangent stiffness tensor, C_{ijkl}, is presumed to be isotropic, Eq. (4.4) can be written as two separate and much simpler equations, one for the volumetric response and the other for the deviatoric response:

$$\dot{\bar{p}} = K\dot{\bar{\varepsilon}}^e_v \tag{4.5}$$

and

$$\dot{S}_{ij} = 2G\dot{\gamma}^e_{ij}. \tag{4.6}$$

Here, G and K are the *tangent* shear and bulk elastic moduli; $\bar{p}$ is the pressure (negative of the mean stress); $\dot{\bar{\varepsilon}}^e_v$ is the volumetric elastic strain rate computed by the trace operation,

$$\dot{\bar{\varepsilon}}^e_v = \dot{\bar{\varepsilon}}^e_{kk}, \tag{4.7}$$

S_{ij} is the stress deviator; and $\dot{\gamma}^e_{ij}$ is the deviatoric part of the elastic strain rate, defined

$$\dot{\gamma}^e_{ij} \equiv \dot{\varepsilon}^e_{ij} - \tfrac{1}{3}\dot{\varepsilon}^e_v \delta_{ij}. \tag{4.8}$$

We have used the overbar (which, recall, simply denotes the negative of a variable) in our equation for the pressure-volume response because the mean stress is typically compressive (negative) in most applications of Kayenta and therefore $\bar{p}$ and ε^e_v are typically positive. Of course, Eq. (4.5) remains valid for volumetric expansion ($\varepsilon^e_v < 0$) and tensile mean stresses ($\bar{p} < 0$) as well. No overbar is used in Eq. (4.8) because deviatoric tensors always have eigenvalues of mixed signs.

For *linear* elasticity, the user merely specifies constant values for the bulk modulus K and the shear modulus G. For nonlinear elasticity, the moduli are stress-dependent *tangent* moduli (i.e., slopes of the tangents to the stress-strain curves). Three parameters are available for fitting the nonlinear tangent bulk modulus K to laboratory data obtained from unloading curves in hydrostatic compression. Similarly, three parameters are available for fitting the nonlinear tangent shear modulus G indirectly from triaxial test data. Additional elastic parameters are available for materials whose elastic properties are affected by inelastic deformation (see Eqs. 4.33 and 4.34). Step-by-step instructions for determining elastic properties from measured data are provided in Appendix A.

---

* "Hypoelastic" means the stress can be written as a function of the strain, but is *not* derivable from an energy potential. When a potential exists, then the formulation is "hyperelastic."

Nonlinear elasticity. At the user's option, Kayenta supports nonlinear elasticity by permitting the elastic tangent moduli to vary with the stress according to

$$K = b_o + b_1 \exp\left(-\frac{b_2}{|I_1|}\right) \tag{4.9}$$

$$G = g_o \left[\frac{1 - g_1 \exp(-g_2 J_2^{1/2})}{1 - g_1}\right]. \tag{4.10}$$

In these equations, the b_k and g_k parameters are material constants determined via nonlinear regression fitting to the unloading portions of hydrostatic compression and triaxial compression experiments, as described in Appendix A.* Further descriptions of the physical meanings of the parameters in these equations are given Appendix B. Kayenta's functional forms for the nonlinear elastic tangent moduli are phenomenological to permit tight empirical fits to experimental data for a wide variety of materials. Suitability of these functions for fitting material data is demonstrated in Chapters 9 and 10, starting on page 113.

Incidentally, it can be shown that an elasticity model of the form in Eq. (4.4) is hyperelastic (i.e., derivable from an isotropic elastic potential) if and only if the shear modulus is constant and the bulk modulus depends at most only on I_1. Because Eq. (4.34) permits the shear modulus to vary, Kayenta is *hypoelastic* if $g_1 \neq 0$.

Assigning values to the elastic constants. The bulk modulus K is determined from the local tangent of the elastic part of a pressure vs. volumetric strain plot obtained from hydrostatic testing. Rather than determining the shear modulus directly from a shear loading experiment (where geomaterials tend to be weak), the shear modulus is typically found indirectly from triaxial loading data. For triaxial loading, the stress rates are related to the strain rates by†

$$\dot{\varepsilon}_A = \frac{\dot{\bar{\sigma}}_A - 2\nu\dot{\bar{\sigma}}_L}{E} \qquad \text{and} \qquad \dot{\varepsilon}_L = \frac{-\nu\dot{\bar{\sigma}}_A + (1 - \nu)\dot{\bar{\sigma}}_L}{E}, \tag{4.11}$$

where E and ν are, respectively, Young's modulus and Poisson's ratio. If E and ν are known, then the bulk modulus K, the Lame modulus λ, and the shear modulus G may be determined from the well-known elasticity equations [26],

$$K = \frac{E}{3(1 - 2\nu)} \qquad\qquad \lambda = \frac{E\nu}{(1 + \nu)(1 - 2\nu)} \qquad\qquad G = \frac{E}{2(1 + \nu)}. \tag{4.12}$$

---

* The generalized nonlinear elasticity formulas on page 40 may be used when elastic properties appear to be affected by inelastic deformation.

† Here, we are writing Hooke's Law in rate form to allow for the possibility that the elastic moduli might be nonlinear. Thus, the elastic properties used here are the *tangent* moduli (i.e. based on the local slope of an elastic stress vs. strain curve).

Because Kayenta casts its elasticity model in terms of the bulk modulus K and the shear modulus G, the following formulas are convenient for converting various combinations of elastic constants into expressions involving only K and G (see, for example, Ref. [26], page 139):

$$\lambda = K - \frac{2}{3}G \qquad\qquad \nu = \frac{3K - 2G}{2(3K + G)} \qquad\qquad E = \frac{9KG}{3K + G} \qquad (4.13)$$

$$\frac{E}{\nu} = \frac{18KG}{3K - 2G} \qquad\qquad \frac{\lambda}{\nu} = \frac{2}{3}(3K + G) \qquad\qquad \frac{\nu}{1 - \nu} = \frac{3K - 2G}{3K + 4G} \qquad (4.14)$$

$$\frac{E}{1 - \nu} = \frac{18KG}{3K + 4G} \qquad\qquad 2G + \lambda = K + \frac{4}{3}G \qquad\qquad G = \frac{3KE}{9K - E} \qquad (4.15)$$

$$K + \frac{4}{3}G = \frac{E(1 - \nu)}{(1 + \nu)(1 - 2\nu)} \qquad \text{(uniaxial } strain \text{ modulus — see Eq. 3.31).} \qquad (4.16)$$

Eq. (4.11) implies that triaxial experiments conducted under constant lateral stress $(\dot{\bar{\sigma}}_L = 0)$ satisfy

$$\dot{\bar{\sigma}}_A = E\dot{\bar{\varepsilon}}_A. \qquad\qquad \text{(this applies if lateral stress is constant)} \qquad (4.17)$$

A fixed lateral stress implies that $\dot{\bar{\sigma}}_A = \dot{\bar{\sigma}}_A - \dot{\bar{\sigma}}_L$. Thus, when a stress-strain curve is obtained by plotting the stress difference $\bar{\sigma}_A - \bar{\sigma}_L$ against the axial strain $\bar{\varepsilon}_A$ for a triaxial loading experiment in which the lateral stress is fixed, the local tangent of the curve equals Young's modulus E. With the bulk modulus K having been obtained separately from hydrostatic test data, Eq. (4.15c) may then be used to determine the tangent shear modulus G.

The elastic limit (yield surface)

Like most plasticity models, Kayenta begins each solution phase (i.e., each time step) by tentatively presuming that the loading is elastic. This produces a trial elastic stress, which is then checked to see if it is inside or on the yield surface. If so, the tentative assumption of elasticity is validated and the actual updated stress is set equal to the trial elastic stress. If, on the other hand, the trial elastic stress falls outside the yield surface, then the tentative assumption of elastic response was wrong, and the solution phase is then solved anew using the equations governing inelastic deformation. Before discussing these inelastic governing equations, we must first characterize the yield surface itself. We will begin by discussing yield surfaces in some generality and then progressively work towards the precise functional form for Kayenta's yield surface.

Mathematically, Kayenta is a generalized plasticity model. The term "plasticity" is broadened to include not only the usual flow of material via dislocations (a phenomenon that has actually been observed in brittle materials when they are loaded under extraordinarily high confining pressure), but also any other mechanisms that lead to a marked departure from elasticity. Examples include crack growth, void collapse, or perhaps even phase transition. Rather than explicitly tracking each of these microscale failure mechanisms explicitly, the "yield" surface itself characterizes *them all* in an ensemble phenomenological manner. If the stress state $(\sigma_1, \sigma_2, \sigma_3)$ is "not too severe," then material response will be elastic and therefore reversible (non-dissipative). Once the stress

becomes critically severe, however, the material will undergo irreversible structural changes that manifest as inelastic strains (nonrecoverable upon removal of the load). The material response is elastic whenever the stress is on the *inside* of the yield surface. If continuing to apply elasticity theory would move the stress into regions outside the yield surface, then plasticity equations are applied.

Kayenta's yield criterion and yield function are

KAYENTA YIELD CRITERION:

$$\sqrt{J_2^{\xi}} = \frac{[F_f(I_1) - N]\sqrt{F_c(I_1, \kappa)}}{\Gamma(\bar{\theta}^{\xi})}.$$
(4.18)

KAYENTA YIELD FUNCTION:

$$f(\underset{\sim}{\sigma}, \underset{\sim}{\alpha}, \kappa) = J_2^{\xi}\Gamma^2(\bar{\theta}^{\xi}) - [F_f(I_1) - N]^2 F_c(I_1, \kappa).$$
(4.19)

The remainder of this chapter is devoted to motivating the functional forms of these equations and defining the numerous variables that appear in them. Briefly, the yield *function f* is defined such that elastic states satisfy $f < 0$. The yield *criterion* corresponds to $f = 0$. The "building block" functions F_f and Γ are used to describe the elastic limit caused by the presence of microcracks, whereas the function F_c accounts for strength reduction by porosity. The function F_f represents the ultimate limit on the amount of shear the material can support in the absence of pores (i.e., F_f represents the softening initiation *limit* threshold, sketched in Fig. 1.1, resulting exclusively from microcracks). The material parameter N characterizes the maximum allowed translation of the yield surface when kinematic hardening is enabled, in which case J_2^{ξ} is the second invariant of the *shifted* stress tensor $\underset{\sim}{\xi} = \underset{\sim}{S} - \underset{\sim}{\alpha}$, where $\underset{\sim}{\alpha}$ is the backstress. When kinematic hardening is disabled (i.e., when N is specified to be zero), the backstress will be zero and therefore J_2^{ξ} would be simply the invariant of the stress deviator. The function F_f describes the *limit* strength, whereas $F_f - N$ defines the *yield* threshold associated with cracks, which can evolve toward the limit surface via kinematic hardening as explained later in the context of Fig. 4.7. The function $\Gamma(\bar{\theta}^{\xi})$, where $\bar{\theta}^{\xi}$ is the Lode angle of the shifted stress, is used to account for differences in material strength in triaxial extension and triaxial compression. By appearing as a multiple of $[F_f - N]^2$, the function F_c accommodates material weakening caused by porosity. The function F_c depends on an internal state variable κ whose value controls the hydrostatic elastic limit, as explained later in the context of Figs. 4.4, 4.5, and 4.16.

The principal goal of this section is to describe the physical motivations of Kayenta's yield criterion cited in Eq. (4.18). This criterion describes the geometrical shape of the yield surface in stress space. For rocks and rock-like materials, the yield surface will have a shape similar to the one illustrated in Fig. 1.0 (page 1).* Figure 1.0*(b)* shows a "side" **meridional profile** of the yield surface in **bold**, along with a family of other profiles from which the yield surface might have evolved over time (via continuously varying values of the κ internal state variable); Fig. 4.7 shows a similar plot when kinematic hardening is allowed. Very little of the yield surface in Fig. 1.0*(b)* exists in the tensile domain (left side of the meridional plot), implying that materials of this type are very weak in tension.

Figure 1.0*(c)* shows the yield surface profile from a perspective looking down onto a plane — called an **octahedral plane** — that is perpendicular to the [111] symmetry axis and therefore represents a cross-section of the yield surface at a given pressure. Since the onset of yield must not depend on the ordering of the principal stresses, the yield surface for *any* isotropic yield model possesses 120° rotational symmetry about the hydrostat (i.e., the [111] axis), as well as reflective symmetry about any of the triaxial compression or triaxial extension axes labeled TXC and TXE in Fig. 1.0*(c)*. As seen in Fig. 1.0*(c),* the octahedral profile is somewhat triangular in shape. This periodic asymmetry corresponds to differences in the failure limit under triaxial compression (TXC) and triaxial extension (TXE). Because the yield surface is farther from the origin on a TXC axis than on a TXE axis, this material has higher strength in TXC than in TXE. The $\Gamma(\bar{\theta})$ function characterizes the *shape* of the octahedral profile because r is proportional to $1/\Gamma(\bar{\theta})$. The *size* of the octahedral profile at various pressures is governed by the functions F_f and F_c.

Elastic stress states are "inside" the yield surface ($f < 0$). Stress states for which $f = 0$ are said to be "on the yield surface." Like classical plasticity models, the yield surface in Kayenta characterizes the point of departure from elastic to inelastic behavior. If applying elasticity theory would result in an updated stress that falls outside the yield surface ($f > 0$), then plasticity equations must be applied. Stress states outside the yield surface are unachievable except through a hardening evolution of the internal state variables (κ and/or $\underset{\approx}{\alpha}$) corresponding to a fundamental change of the underlying microstructure of the material. Stresses outside the *limit* surface are unachievable by *any* quasistatic means.

The internal state variable κ controls the location of the yield cap (wire frame in Fig. 1.0a on page 1). When κ increases in response to pore collapse, octahedral profiles that pass through the cap will expand isotropically (i.e., the octahedral profile changes size, but not shape, and it does so without translating in stress space). The amount of isotropic expansion or contraction varies with pressure in such a manner that the family of yield surfaces corresponding to various values of κ is bounded by the shear limit surface, $\sqrt{J_2} = F_f(I_1)/\Gamma(\bar{\theta})$.

---

* At the user's option, Kayenta parameters can be set to alternatively duplicate classical idealized Von Mises or Mohr-Coulomb theory. Doing this would be inappropriate when modeling real materials, but it can be useful in benchmark testing.

Though not needed in many applications, Kayenta supports kinematic hardening for which the symmetry axis of the yield surface is permitted to shift in stress space so that the invariants in the yield function are based on the **shifted stress** tensor, defined

$$\xi_{ij} \equiv S_{ij} - \alpha_{ij}. \tag{4.20}$$

As illustrated in Fig. 4.1, the **backstress** α_{ij} is a deviatoric tensor-valued internal state variable that defines the origin about which the yield surface is centered. When the backstress tensor changes, the yield surface translates in stress space, thereby supporting deformation-induced anisotropy (Bauschinger effect) in a limited capacity. The backstress is initially zero,

Figure 4.1.   *Backstress and shifted stress.*

but then evolves according to an evolution equation described in detail on page 64. Kayenta is otherwise fully isotropic, both elastically and plastically. Consequently, the yield function is isotropic with respect to the *shifted* stress deviator ξ_{ij}, implying that it depends on the invariants of the shifted stress deviator, as well as I_1 and an internal state variable κ that characterizes *isotropic* hardening caused by void collapse or softening caused by porosity increases. Specifically, Kayenta's yield function is of the form

$$f = f(I_1, J_2^\xi, J_3^\xi \ ; \kappa), \tag{4.21}$$

where

$$J_2^\xi = \frac{1}{2}\mathrm{tr}\,\underset{\approx}{\xi}^2 \qquad \text{and} \qquad J_3^\xi = \frac{1}{3}\mathrm{tr}\,\underset{\approx}{\xi}^3. \tag{4.22}$$

In this section, we seek to describe the size and shape of the yield surface at an instant frozen in time. Thus, we will focus on how the yield function depends mathematically on the stress invariants (I_1, J_2^ξ, J_3^ξ), with the internal state variables (κ and $\underset{\approx}{\alpha}$) regarded as constants. The means by which the yield surface evolves in response to time variation of κ and/or $\underset{\approx}{\alpha}$ is discussed separately.

Before discussing the physical foundations of Kayenta's yield function in Eq. (4.19), we will first discuss qualitative features of any yield function of the more general form in Eq. (4.21). Given that an isotropic yield function possesses alternating 30° symmetry about the [111] direction in stress space, the yield function in Eq. (4.21) is most naturally cast in terms of the cylindrical Lode coordinates as

$$f = f(r, \bar{\theta}, \bar{z} \ ; \kappa), \tag{4.23}$$

where these Lode coordinates are defined with respect to the kinematically *shifted* origin in stress space. For any given values of $\bar{\theta}$, $\bar{z}$, and κ, there must exist only one radius r that is a solution to $f(r, \bar{\theta}, \bar{z}; \kappa) = 0$ (otherwise, the yield surface would not be convex). Thus, without loss in generality, elastic stress states for *any* isotropic yield function always can be characterized in the general functional form

$$r < g(\bar{\theta}, \bar{z}; \kappa), \tag{4.24}$$

where $g(\bar{\theta}, \bar{z}; \kappa)$ is regarded as a material function determined from experimental data and is introduced here only to discuss the structure of isotropic yield functions in generality (i.e., Kayenta has an *implied* "*g*" function, but does not construct one explicitly). The yield function corresponding to Eq. (4.24) may be written

$$f = r^2 - [g(\bar{\theta}, \bar{z}; \kappa)]^2 \quad \text{(Any isotropic yield function can be written in this form.)} \tag{4.25}$$

At present, Kayenta assumes that the *shape* of the octahedral yield profile is the same at all pressures — only its *size* varies with pressure.* Moreover, Kayenta presumes that the shape of the octahedral yield profile is constant in time (i.e., it does not evolve to any different *shape* in response to plastic deformation even though it can permissibly vary in size and translate in stress space). Consequently, Kayenta's yield function is structured such that $g(\bar{\theta}, \bar{z}; \kappa)$ is *separable* into the product of two distinct functions, one depending only on $\bar{\theta}$ and the other depending only on $\bar{z}$ and κ, permitting Eq. (4.24) to be structured in the general form:

$$r < h_1(\bar{\theta})h_2(\bar{z}\;; \kappa) \quad \text{(This form results from a \textit{separability} assumption.)} \tag{4.26}$$

As was the case with the g function, h_1 and h_2 have been introduced here only to illustrate the basic structure of Kayenta's yield function. Kayenta's specific formulations will be discussed soon. A degree of ambiguity exists in the definitions of h_1 and h_2 because they may be replaced respectively by ηh_1 and h_2/η for any scalar η without loss in generality. To remove this ambiguity, the function h_1 is scaled such that it merely describes the *shape* of the octahedral profile (i.e., the view of the yield surface looking down the [111] direction). The function h_2 defines the meridional profile of the yield function, and therefore this function also defines the *size* of the octahedral profile.

Kayenta aims to model rocks and rock-like brittle materials. The mechanical behavior of such materials is typically driven by two underlying mechanisms: porosity and microcracks. To date, microphysical research has focused on the effects of only one of these mechanisms at a time. Figure 4.2*(a)* shows the qualitative shape of the meridional profile typically that is predicted when only porosity is considered. In this case, the meridional yield profile is a "cap" function that is essentially flat like a Von Mises profile for a large range of pressures ($\bar{z}$ is proportional to pressure), and then the profile drops to zero when pressure becomes large enough to collapse voids. Figure 4.2*(b)* shows the general shape of

---

* Some evidence suggests that the octahedral yield profile should in fact vary in shape from strongly triangular at low pressures to nearly circular at extraordinarily high pressures [31]. Consequently, Kayenta's current assumption of a constant octahedral profile shape might change in future releases.

a meridian profile that is typically predicted for theories that consider only the influence of microcracks *without* considering porosity. Microcracks lead to low strength in tension, but strength increases as pressure is increased because pressure generates additional friction at crack faces, thereby reducing the shear load suffered by the matrix material. Kayenta unifies these separate microscale theories to obtain a combined porosity and microcrack model, as sketched qualitatively in Fig. 4.2*(c)*. Loosely speaking, Kayenta obtains the combined meridional yield function by multiplying the individual porosity and microcrack profiles (and scaling the ordinate appropriately to match data).
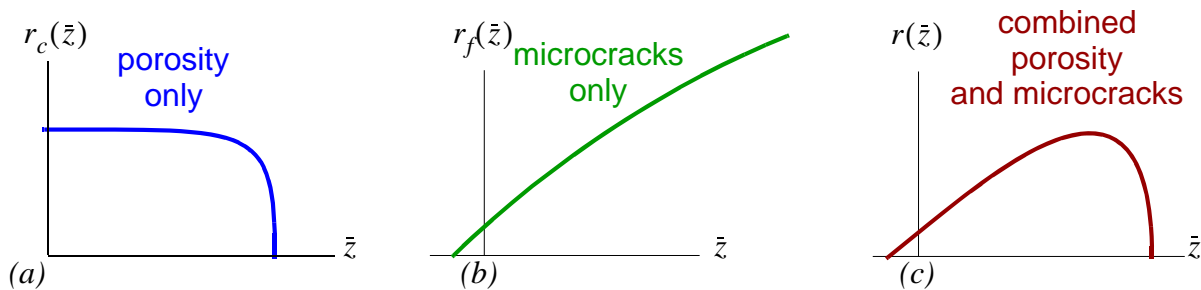
Figure 4.2.   *Qualitatively meridional profile shapes resulting from (a) porosity alone, (b) microcracks alone, and (c) porosity and microcracks in combination.*

To date, the *combined* effect of voids and microcracks remains a poorly developed branch of materials constitutive modeling. Some early models simply asserted that a material is elastic (safe from yield) if and only if it is safe from both crack growth and void collapse, with each criterion tested *separately*. However, as illustrated in Fig. 4.3(a), this approach results in a discontinuous slope in the meridional yield profile and fails to account for interactions between voids and cracks. Kayenta [Fig. 4.3(b)], phenomenologically permits cracks and voids to interact in a way that results in a continuously differentiable meridional profile, making Kayenta better suited for reproducing observed data.
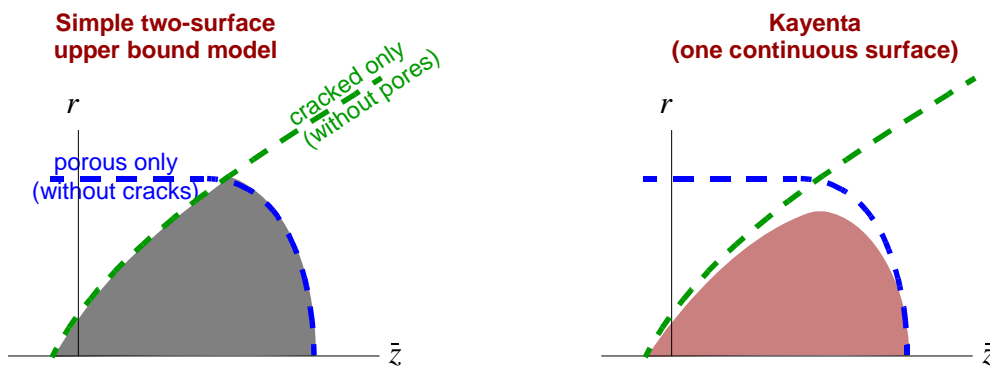
Figure 4.3.   *Distinction between two-surface upper-bound models and Kayenta.*

Kayenta achieves a *combined* porous+cracked yield surface by multiplying the fracture function $r_f(\bar{z})$ in Fig. 4.2*(b)* times the cap function $r_c(\bar{z})$ in Fig. 4.2*(a)* so that

$$r(\bar{z}) \quad \text{is proportional to } r_f(\bar{z})r_c(\bar{z}). \tag{4.27}$$

The proportionality factor depends on the Lode angle $\bar{\theta}$ so that the equivalent shear stress at yield (which, recall, is simply a constant multiple of r) can be made lower in TXE than in TXC. Cap functions depend on the porosity level (which controls where the cap curve intersects the z-axis). The curvature of a cap function controls the degree to which porosity affects the shear response. Although Kayenta does not explicitly track porosity, it does include an internal state variable κ that equivalently accounts for the *presence* of porosity. As explained later (page 54), the value of κ and one additional material constant, R, determine both the cap curvature and the location where the cap intersects the hydrostat (the $\bar{z}$ axis). Thus, the cap function $r_c(\bar{z})$ implicitly depends on κ and R.

Recalling that the Lode cylindrical radius r equals $\sqrt{2J_2^{\xi}}$ and the Lode axial coordinate z is proportional to I_1, Kayenta implements the notion of multiplying fracture and cap functions by using Eq. (3.40) to express Eq. (4.27) in terms of stress invariants instead of Lode coordinates, so Kayenta's yield function is of the form

$$\sqrt{J_2^{\xi}} = \frac{f_f(\bar{I}_1)f_c(\bar{I}_1)}{\Gamma(\bar{\theta})}. \qquad \text{[Γ also varies with $\bar{I}_1$ if user parameter RK=-1]} \tag{4.28}$$

Comparing with Eq. (4.18), the f and F functions are related by

$$f_f = F_f - N \qquad \text{and} \qquad f_c = \sqrt{F_c}. \tag{4.29}$$

The invariant J_2^{ξ} is computed using the *shifted* stress tensor $\underset{\sim}{\xi} \equiv \underset{\sim}{S} - \underset{\sim}{\alpha}$, where $\underset{\sim}{\alpha}$ is the deviatoric tensor-valued backstress that is nonzero only when kinematic hardening is enabled. Thus, in addition to depending explicitly on the stress tensor, the yield criterion depends implicitly on material constants and on two internal state variables, κ (mentioned earlier) and $\underset{\sim}{\alpha}$.

The fracture function f_f characterizes the cracking-related portion of the meridional yield profile. Kayenta's cap function f_c is normalized to have a peak value of 1. The function $\Gamma(\bar{\theta})$ characterizes the Lode angle dependence of the meridional profile and is normalized to equal 1 in triaxial compression ($\bar{\theta} = 30°$). At different Lode angles, Γ usually has values *greater* than 1, which (because it is a *divisor* in Eq. 4.28) reduces equivalent shear strength. Rather than regarding Γ as a strength reducer, it can be alternatively interpreted as a *stress intensifier*. Qualitatively, these functions are typically shaped as shown in Fig. 4.4.

$$f_c(\bar{I}_1) = \sqrt{F_c}$$

$$f_f(\bar{I}_1) = F_f - N$$
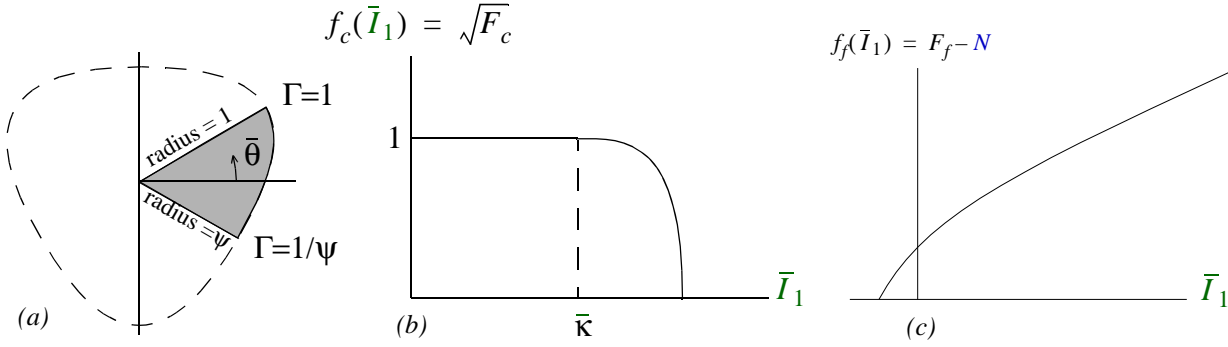
Figure 4.4. *Basic shapes of the three key functions that characterize the composite shape of the yield surface.* (a) Lode angle dependence, (b) porosity cap curve, (c) limit failure curve. The Lode angle function $\Gamma(\bar{\theta})$ is the *reciprocal* of the radius in the octahedral plane, making it best regarded as a stress intensifier; $\Gamma(\bar{\theta})$ is normalized to equal 1 in triaxial compression, which implies that it must equal $1/\psi$ in triaxial extension (where ψ is the TXE/TXC strength ratio). Shear influence on void collapse begins at the point where the cap function branches into an ellipse. Since the cap function is multiplied by the fracture curve, this transition point also marks where the composite Kayenta failure surface branches away from f_f, beyond which macroscale response is influenced simultaneously by *both* cracks and voids. For *pure* (shear-free) hydrostatic compression, void collapse begins at the point where the ellipse intersects the horizontal. Only the function f_f has dimensions of stress (the others are dimensionless).

As explained on page 47, the precise expression for the Γ function is determined by user-specification of two parameters: the TXE/TXC strength ratio ψ and an integer-valued option (**J3TYPE**), which controls the manner in which the octahedral profile radius varies from the value $1/\psi$ at TXE to 1 at TXC. As explained below, the porosity (cap) function f_c is defined by two parameters: the initial intersection p_0 on the horizontal axis and the eccentricity or "shape factor" R for the ellipse (i.e., the width to height ratio of the ellipse). As explained on page 61, Kayenta internally computes evolution of the cap function resulting from void collapse. As explained on page 45, the very important f_f function, which reflects influence of microcracks, is determined by fitting triaxial compression data to an exponential spline [up to five parameters (a_1, a_2, a_3, a_4, N)]. Standard experiments (needed to assign values to these parameters) are discussed in Appendix A. The remainder of this chapter is dedicated to providing further details about the three key functions f_c, f_f, and Γ used in Kayenta.

The cap function, f_c. Under compression, the pores in a material can irreversibly collapse, thereby resulting in permanent (plastic) volume changes when the load is removed. Plastic volume changes can occur for porous media even if the matrix material is plastically incompressible. Permanent volume changes can also occur if a material undergoes an irreversible phase transformation. Kayenta supports plastic volume changes, but it does so without explicitly modeling the underlying microphysical mechanisms. Nonetheless, Kayenta does reflect the influence of micromechanical theory by phenomenologically incorporating plastic volume changes observed in hydrostatic loading. To motivate Kayenta's cap theory, we will explain the equations and their qualitative features in the context of porosity, but keep in mind that any other microphysical compactive mechanisms are equally well accommodated by the phenomenological cap model.

The cap function f_c accounts for the presence of pores in a material by controlling where the yield function will intersect the $\bar{I}_1$ axis in compression. This intersection point corresponds to $J_2 = 0$ and, because we are considering compressive states, we will denote the value of $\bar{I}_1$ at the intersection point by $\bar{I}_1 = \bar{X}$, where $\bar{X}/3$ is the pressure (positive in compression) at which inelastic deformation commences in *purely hydrostatic* loading for a given level of porosity. As voids compress out, the value of $\bar{X}$ will change, as explained later when we discuss the evolution equations for Kayenta's internal state variable κ. Porosity also degrades material *shear* strength because, recalling Eq. (4.28), the cap function effectively reduces the nonporous yield strength, defined previously by the fracture function f_f.
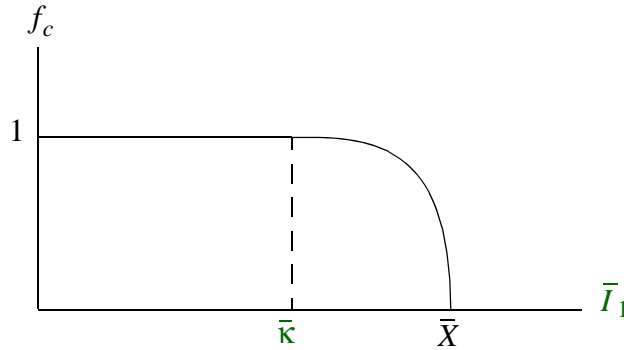
Figure 4.5.   Kayenta cap function

Kayenta employs a cap function* defined

$$f_c^2(\bar{I}_1, \kappa) = \begin{cases} 1 & \text{if} \quad \bar{I}_1 < \bar{\kappa} \\ 1 - \left(\dfrac{\bar{I}_1 - \bar{\kappa}}{\bar{X} - \bar{\kappa}}\right)^2 & \text{otherwise.} \end{cases} \tag{4.30}$$

---

* evaluated in the code by a Pelessone [43] function, $f_c^2(\bar{I}_1, \bar{\kappa}) = 1 - \dfrac{(\bar{I}_1 - \bar{\kappa})(|\bar{I}_1 - \bar{\kappa}| + (\bar{I}_1 - \bar{\kappa}))}{2(\bar{X} - \bar{\kappa})^2}$.

Neither $\bar{\kappa}$ nor $\bar{X}$ are user-supplied material parameters. Instead, these variables are computed internally within Kayenta code by enforcing consistency with more intuitive user-supplied parameters obtained from hydrostatic testing (see page 59).

The equation of the elliptical portion of the cap curve is

$$f_c^2 + \left(\frac{\bar{I}_1 - \bar{\kappa}}{\bar{X} - \bar{\kappa}}\right)^2 = 1. \tag{4.31}$$

The intersection point $\bar{X}$ will be later related to the value of $\bar{\kappa}$ so that knowledge of the internal state variable $\bar{\kappa}$ will be sufficient to compute a value for $\bar{X}$. For now, while describing the geometry of the yield surface, both $\bar{\kappa}$ and $\bar{X}$ should be regarded as internal state variables whose values are computed internally in Kayenta using evolution equations discussed later. Rather than using f_c directly, recall that Kayenta uses the function F_c that is simply the square of f_c given in Eq. (4.30):

$$F_c = f_c^2. \tag{4.32}$$

Elastic-plastic coupling. The cap model is used when the material being studied contains enough porosity (or highly compliant second phase inclusions) so that inelastic volume reduction becomes possible through irreversible reduction of void space. Intuitively, one might expect the elastic moduli to stiffen as voids collapse, but the material might actually become more elastically compliant as shown in Fig. 9.4 (a phenomenon that might be explained, for example, by rubblization of a ligament network). Regardless of its microphysical origins, the elastic moduli are permitted to vary with plastic strain by generalizing the nonlinear elastic moduli expressions in Eqs. (4.9) and (4.10) to

$$K = f_K \left\{ \left[b_o + b_1 \exp\left(-\frac{b_2}{|I_1|}\right) \right] - b_3 \text{Exp}\left(-\frac{b_4}{|\bar{\varepsilon}_v^p|}\right) \right\} \tag{4.33}$$

$$G = f_G \left\{ g_o \left[\frac{1 - g_1 \exp(-g_2 J_2^{1/2})}{1 - g_1} \right] - g_3 \text{Exp}\left(-\frac{g_4}{\gamma_{\text{eqiv}}^p}\right) \right\}. \tag{4.34}$$

In the absence of joints, the scale factors f_G and f_K equal 1.0; otherwise, they are computed internally within Kayenta as described in a separate sequel report. In the above equations, γ_{eqiv}^p is the equivalent plastic shear strain (which, for proportional loading, is conjugate to the equivalent shear stress, $\sqrt{J_2}$), and $\bar{\varepsilon}_v^p$ is the plastic compaction volume change. Mathematically,

$$\gamma_{\text{eqiv}}^p = \int \sqrt{2} \left\| \dot{\underset{\approx}{\gamma}}^p \right\| dt \tag{4.35}$$

$$\bar{\varepsilon}_v^p = \int \text{tr}\, \dot{\underset{\approx}{\varepsilon}}^p dt. \tag{4.36}$$

Though defined mathematically as stated, Kayenta computes the plastic volume change, $\bar{\varepsilon}_v^p$ indirectly, as explained later in the context of Eq. (4.68).

Meridional shear limiter function, F_f. In a loose sense, the previous sub-section described Kayenta's cap function f_c by considering a material that contained pores, but no cracks. In this sub-section, we describe Kayenta's fracture function f_f by considering a material that contains microcracks *but no porosity*. Numerous microphysical analyses (as well as a preponderance of data) suggest that, for microcracked media, the onset of "yield" depends on all three stress invariants, which implies that the yield function for microcracked media must depend on all three cylindrical Lode coordinates. Kayenta supports this singularly common prediction of microscale damage theory. Though they differ in specific details, microphysical damage theories and laboratory observations for brittle materials also tend to share the following qualitative features:

- At a given mean stress, yield in triaxial extension (TXE) occurs at a lower stress than in triaxial compression (TXC), which implies that octahedral yield profiles are generally triangular (or distorted hexagon) in shape, with the triangle apex being located on TXC axes, as sketched in Fig. 1.0*(c)* on page 1.

- Brittle materials are very weak in tension. This implies that the meridional yield profile will include few if any tensile stress states. Brittle materials are also vulnerable to shear cracking at low pressures, but they become able to support increasingly large shear stresses as pressure is increased because friction at crack faces helps reduce the shear load that must be suffered by the matrix material itself. Thus, in the absence of porosity, the meridional profile is expected to monotonically increase with pressure.

- When microscale theories regard brittle crack fracture to be the *only* failure mechanism, they predict that the material strength (i.e., the Lode radius at failure) will increase monotonically with increasing pressure, so that the meridional profile expands in an ever-expanding cone-like shape like the limit surface in Fig. 1.1. Microphysical idealizations such as Mohr-Coulomb theory predict the meridional profile is a straight line whose slope is directly related to the friction coefficient. When microscale theories allow for both crack growth and ductility of the matrix material, they predict that the increase in strength from friction will continue only until ductile yield (at extraordinarily high pressures) becomes more likely; such theories correspond to a meridional yield profile that is cone-like at low to moderate pressures but asymptotes to a zero slope (like a Von Mises cylinder) at high pressures.

Given the wide variety of microscale predictions for the meridional profile, Kayenta is equipped with a four-parameter exponential spline that is capable of replicating any of these microphysical idealized theories, as well as actual observed material yield and rupture response at low and moderate pressures (i.e., at pressures well below the cap elastic limit) so that observed data primarily reflect microcrack damage rather than combined cracking with pore collapse (covered elsewhere in this report).

In the meridional plane (i.e., at a given value of the Lode angle), the **yield surface** characterizes the transition boundary for inelastic flow. Stress states that were, at one time, outside the yield surface might become realizable through hardening evolution of the yield surface. However, the allowable amount of hardening is not unbounded. At some point, the material will fail catastrophically (i.e., rupture). Often, the stress at rupture is *smaller* than the peak stress. Stress-strain curves might or might not exhibit post-peak softening, depending on whether or not the experiment is stress-controlled or strain-controlled.

The *peak* stress (not the stress at rupture) defines the stress-carrying limit of the material. As first mentioned on page 6, the **limit surface** is the boundary of all stress states that the material is *capable* of supporting. Many of these achievable stress states can be reached only through inelastic processes. Appendix A (step 4 on page A-5) describes in detail how to determine the limit surface from experimental data. Mathematically, the limit surface is characterized by a limit function that is similar in form to the yield function. Specifically, the limit surface is defined by $F(\underset{\approx}{\sigma}) = 0$, where

$$F(\underset{\approx}{\sigma}) = J_2(\underset{\approx}{\sigma}) - \frac{F_f^2[I_1(\underset{\approx}{\sigma})]}{\Gamma^2[\bar{\theta}(\underset{\approx}{\sigma})]} \,. \tag{4.37}$$

The limit function $F(\underset{\approx}{\sigma})$ depends *only* on $\underset{\approx}{\sigma}$, not on any internal state variables. A yield function $f(\underset{\approx}{\sigma}, \underset{\approx}{\alpha}, \kappa)$, on the other hand, depends on the backstress tensor $\underset{\approx}{\alpha}$ and on the scalar internal state variable κ. Unlike a yield surface, which can evolve over time because it depends on time-varying internal state variables, the limit surface is *fixed* in stress space. The yield function is presumed to share some qualitative features with the shear limit surface, but depends additionally on internal state variables as follows:

$$f(\underset{\approx}{\sigma}, \underset{\approx}{\alpha}, \kappa) = J_2(\underset{\approx}{\xi}) - \frac{\{F_f[I_1(\underset{\approx}{\sigma})] - N\}^2 F_c(I_1(\underset{\approx}{\sigma}), \kappa)}{\Gamma^2[\bar{\theta}(\underset{\approx}{\xi})]}$$

$$, \quad \text{where} \quad \underset{\approx}{\xi} \equiv \underset{\approx}{S} - \underset{\approx}{\alpha} \,. \tag{4.38}$$

When examining experimental data, it is generally easier to determine the maximum limit point than the point at which plasticity first begins. Consequently, Kayenta provides an empirical fitting function F_f for the limit surface in the meridional plane, and the initial meridional yield surface is simply $F_f - N$, reduced perhaps by a cap function F_c if the material initially contains voids. Comparing Eq. (4.38) with (4.37) reveals that the yield surface inherits its octahedral profile *shape* (i.e., its Lode angle dependence) from the limit surface. The *size* of the yield octahedral profile is generally smaller than the limit surface profile because of the multiplier (cap) function F_c, which represents the effect of porosity. The yield surface origin is also offset from the limit surface origin by an amount governed by the kinematic hardening backstress tensor $\underset{\approx}{\alpha}$. The limit surface always has a [111] symmetry axis *passing through the actual (not kinematically shifted) origin* in stress space. When kinematic hardening is enabled, the yield surface has a symmetry axis parallel to [111] that is off-set so that it does *not* pass through the origin.

When advancing the solution, the initial meridional profile can harden kinematically and/or isotropically. The equations governing yield surface evolution are designed to permit only a limited amount of hardening. As sketched in Fig. 4.6, the initial yield surface is permitted to translate upward in the meridional plane by no more than a user-specified limit N.

When the yield surface has reached the limit surface *and when the stress itself lies on the limit surface*, the material will begin to soften. At that point, a *constitutive-level* description of material response no longer remains possible; the host code must intervene by

Figure 4.6. *Kinematic hardening.* The user defines parameters (a_1, a_2, a_3, a_4) for the <u>ultimate</u> shear limit surface. The initial yield surface is identical except shifted down by a user specified amount N. Kinematic hardening allows the initial yield surface to translate until reaching the ultimate failure surface (at which point, the host code must initiate "element death" or perhaps some other strategy for supporting macroscale softening.

inserting void or by invoking special elements capable of supporting displacement discontinuities or by accounting for statistical variability and scale effects as described on page 72. The limit surface marks the point at which a continuum material model is inadequate to characterize macroscale material response because softening localization becomes possible. Before reaching the limit surface, material response is handled entirely by Kayenta with no need for host code intervention.

The shifted shear limiter function $F_f(I_1) - N$ defines how the shear stress at yield varies with pressure for a *nonporous*, but microcracked, material in its initial (virgin) state. When this microcrack yield function is combined with the cap function $F_c(I_1, \kappa)$ the actual shear stress at yield is further reduced because porosity makes inelasticity possible even for purely hydrostatic compression (i.e., loading along the $\bar{I}_1$ axis). Kayenta evolves this combined porous yield function in such a way that the yield surface grows up to the limit surface.
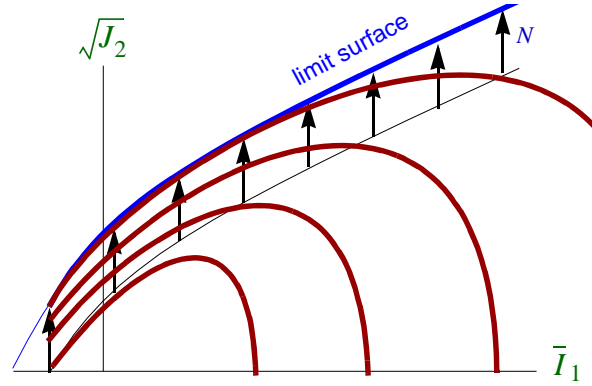
Figure 4.7.   *Yield surface evolution with both microcracking and porosity.* For real materials, that contain both cracks and voids, it is difficult to identify a single envelope for the combined porous/cracked fracture yield function f_f. However, ultimate failure data can be more readily mapped out.

Kayenta's behavior *after* reaching the limit surface depends on the value of the user control parameter "JOBFAIL". Properly, the host code should allow scale-dependent softening and localization as discussed on page 72. If JOBFAIL=0.0, then Kayenta will treat the limit surface as if it were a nonhardening yield surface (making its post-peak predictions robust and mesh insensitive but probably not realistic). This option is used in many of the Kayenta verification tests where softening is not desired (and nonhardening analytical solutions are available). If JOBFAIL>0.0, then Kayenta will allow the material to soften as described in Section 5 on page 69.
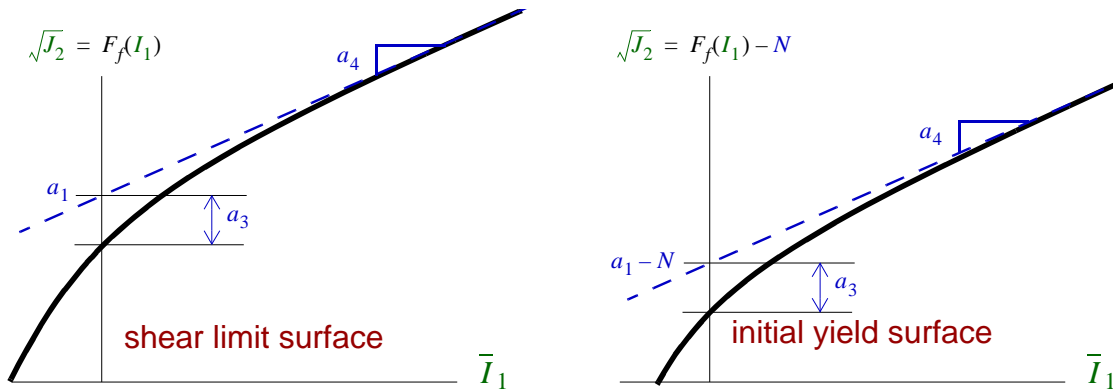
Figure 4.8.   *Shear limiter function (unshifted and shifted).* The shifted function should be regarded as a nominal shape of the yield surface in the meridional plane, although porosity further lowers and distorts the meridional yield profile by multiplying the shifted shear limit function by F_c.

Kayenta supports modeling microcracked material by providing flexible fitting functions that can reproduce octahedral and meridional yield profiles observed for real materials. In particular, the shear limit function used in Kayenta is of the form

$$\boxed{F_f(I_1) \;=\; a_1 - a_3 e^{-a_2 \bar{I}_1} + a_4 \bar{I}_1} \; \text{, where } \; \bar{I}_1 = -I_1 \qquad \text{shear limit surface in TXC. (4.39)}$$

where the a_k are user-specified material parameters determined from experimental data as explained in Appendix A. The initial (nonporous) meridional yield profile is

$$f_f(I_1) \;=\; F_f(I_1) - N \qquad \qquad \text{initial yield surface (non-porous).} \qquad (4.40)$$

where N is the user-specified shift parameter. Therefore, $a_1 - N$ is the zero pressure intercept of the nonporous meridional yield surface on the $\sqrt{J_2^\xi}$ axis. Frequently, N is taken to be zero. The shear limiter function, Eq. (4.39), asymptotes to a linear envelope, as indicated in Fig. 4.8. To force the material to obey a Von-Mises type yield response at extremely high pressures, the slope coefficient a_4 is merely set to zero.

Let us now explain why the shear limiter function has the general shape depicted in Fig. 4.8. Then we will list constraints on the model parameters necessary to achieve this shape. Brittle materials fail at very low shear stresses when the pressure is low, but they are able to sustain higher levels of shear stress without failing if loaded under higher confining pressures. Consequently, the shear limiter function is expected to increase monotonically with pressure. Or, since $\bar{I}_1$ is proportional to the pressure, F_f is expected to increase monotonically with $\bar{I}_1$. Furthermore, a fundamental tenant from plasticity theory is that the yield function must be semi-convex, which implies that the second partial derivative of $F_f(I_1)$ must be negative or zero. When we speak of the "shear" stress at failure, we are effectively speaking of the value of the Lode radius at failure corresponding to the Lode angle for the stress state. For any cylindrical coordinate system — including the Lode system — the radius must always be non-negative and therefore F_f is defined only over the domain for which it yields positive values. Finally, in its virgin state, any material should be unfailed at zero stress, which means that the origin must fall below the meridional yield profile. All of these physical considerations lead to the following constraints on allowable values for the parameters:

$$a_1 - a_3 - N \ge 0 \qquad \qquad \text{unloaded virgin material must be below yield} \qquad (4.41)$$

$$a_2 a_3 + a_4 \ge 0 \qquad \qquad \text{non-negative slope at low pressures} \qquad (4.42)$$

$$a_2 > 0 \qquad \qquad \text{positive Lode radius} \qquad (4.43)$$

$$a_3 \ge 0 \qquad \qquad \text{convexity condition} \qquad (4.44)$$

$$a_4 \ge 0 \,. \qquad \qquad \text{non-negative slope at high pressures} \qquad (4.45)$$

The upper bound in Eq. (4.42) corresponds to a maximum principal stress criterion. Specific values for these model parameters are determined from triaxial test data, as explained in Fig. 3.3 on page 18 (and in Figs A.4 and A.5 of Appendix A). Sample fits of Kayenta's shear limit function to data can be found in Fig. 9.1 on page 113 and Fig. 9.5 on page 116. Incidentally, $a_2 a_3 + a_4 < 1/\sqrt{3}$ for most materials ($1/\sqrt{3}$ is typical for sand).

The complete Kayenta yield function.

Equation (4.28) is the yield *criterion*. The yield *function f* must be negative for all elastic states (inside the yield surface), zero for all stress states satisfying the yield criterion (on the yield surface), and positive for all stress states (outside the yield surface) that cannot be reached except through an inelastic process — if at all. For computational reasons, Kayenta's yield function is based on the square of Eq. (4.28):

$$f = \Gamma^2(\bar{\theta}^\xi)J_2^\xi - f_f^2(I_1)f_c^2(I_1, \kappa). \tag{4.46}$$

When kinematic hardening is used, the stress invariants, $\bar{\theta}^\xi$ and J_2^ξ, are those for the kinematically shifted stress tensor, $\underset{\sim}{\xi} \equiv \underset{\sim}{S} - \underset{\sim}{\alpha}$. Otherwise, when kinematic hardening is disabled, these are simply the stress invariants. Of course, I_1 is the first invariant I_1^σ of the stress tensor $\underset{\sim}{\sigma}$. (Since backstress $\underset{\sim}{\alpha}$ is deviatoric, $I_1^\xi = 0$).

The building block functions f_f and f_c are implemented in Kayenta in a slightly altered form by being expressed in terms of the shear limit function F_f and an alternative (computationally more efficient) cap function F_c:

$$f_f(I_1) = F_f(I_1) - N \tag{4.47}$$

$$f_c(I_1, \kappa) = \sqrt{F_c(I_1, \kappa)}. \tag{4.48}$$

The first of these equations allows the user to specify a maximum amount, N, that the yield function is permitted to translate under kinematic hardening. Thus, the function F_f can be regarded as a "limit" or "softening" envelope, beyond which stresses can *never* be reached quasistatically (not even via hardening). The second equation recasts the f_c function as the square root of a different function F_c for computational reasons. The second equation also shows explicitly the presence of the internal state variable κ related to the isotropic hardening part of Kayenta associated with void collapse. The internal state variable κ marks the branch point where combined porous/cracked yield surface deviates from the nonporous yield surface. As explained on page 61, this branch point is determined internally within Kayenta in a manner that ensures consistency with measured hydrostatic data.

In terms of the new building block functions, the critical Lode radius in triaxial compression (TXC), where $\Gamma(\bar{\theta}) = 1$, may be expressed as a function of the Lode axial coordinate z as

$$r^{\text{TXC}} = \sqrt{2}[(F_f(\sqrt{3}\ z) - N)\sqrt{F_c(\sqrt{3}\ z, \kappa)}]. \tag{4.49}$$

Plotting r^{TXC} vs. z (at a given value of κ) will produce a *geometrically accurate* visualization of the meridional yield profile. Often we instead plot $\sqrt{J_2}$ vs. $\bar{I}_1$ to label the axes with more broadly recognized stress measures, but in doing so we are actually showing a geometrically distorted view of the yield profile, as explained on page 26.

Substituting Eqs. (4.47) and (4.48) into (4.46) gives the yield criterion cited at the beginning of this section [Eq. 4.18].

The "J3TYPE" Lode-angle function, Γ. This section describes available functional forms for the Lode angle dependence function $\Gamma(\bar{\theta})$. This function controls the shape of the octahedral yield profile. Since this function controls only the *shape*, not size, of the octahedral profile, its magnitude is inconsequential. The Γ function is normalized to equal unity in TXC ($\bar{\theta} = +30°$).* At other Lode angles, $\Gamma(\bar{\theta}) > 1$. Thus, since $\Gamma(\bar{\theta})$ appears in the yield function as a *multiplier* of J_2^{ξ}, it acts as a pseudo stress *raiser*, causing yield to occur at smaller values of J_2^{ξ} at Lode angles differing from the fiducial (TXC) angle where $\Gamma(\bar{\theta}) = 1$. To ensure convexity of the octahedral yield profile, the Lode angle function must satisfy

$$\Gamma''(\bar{\theta}) + \Gamma(\bar{\theta}) \geq 0. \qquad (4.50)$$

A hallmark trait of rocks and rock-like materials (concrete, ceramics, etc.) is a higher strength in triaxial compression than in triaxial tension at any given mean pressure. Loosely speaking, this characteristic results from friction at crack faces being able to carry a larger portion of the load under compression, therefore sparing the surrounding matrix material from having to carry the entire resolved shear stress at crack tips. Classical Mohr-Coulomb theory, which is supported by Kayenta primarily for comparisons with idealized analytical solutions, has an octahedral profile in the shape of a distorted hexagon, causing considerable computational difficulties when dealing with the vertices. The computational attractiveness of removing yield surface corners has motivated numerous proposals of smoothed three-invariant models for frictional materials [38,37,3,59,9], and Lade [39] was among the first efforts to additionally include curvature in the meridional plane. According to Borja, et. al. [8], there is evidence that smoothed yield surfaces capture mechanical response more accurately than vertex models, but these authors point to no data to back up this claim. Kayenta presently supports three yield-type options (specified by a value of 1, 2, or 3 for the user parameter, **J3TYPE**):

1. Gudehus (an efficient smoothed profile, with restrictions on convexity)
2. Willam-Warnke (a relatively inefficient smooth profile with no convexity constraints)
3. Mohr-Coulomb (distorted hexagon polygon)

The Gudehus and Willam-Warnke options both correspond to fully differentiable yield functions (no vertices). The Mohr-Coulomb option (which is available principally for comparisons with analytical solutions) is differentiable everywhere except at triaxial states where yield surface vertices require special numerical handling.[†]

---

* With this normalization, the f_f meridional function then quantifies the pressure-varying *size* of octahedral profiles

† Kayenta averages directions on either side of the vertex if the strain rate points within the limiting (Koiter) fan of unit normals. If the strain rate points within a sextant of the octahedral plane, then the normal in that sextant is used.

Recognizing logistical constraints of most laboratories, Kayenta presumes that experimental data are available *at most* only for a limited number of canonical loading paths: perhaps triaxial extension ($\bar{\theta}=-\pi/6$), perhaps simple shear ($\bar{\theta}=0$), and almost certainly triaxial compression ($\bar{\theta}=\pi/6$). Regardless of which yield-type (Gudehus, Willam-Warnke, or Mohr-Coulomb) is selected, the shape of the octahedral yield profile is described, in part, by user specification of a parameter ψ, equal to the **triaxial extension/compression (TXE/TXC) strength ratio** at a given pressure. Kayenta presumes that only the *size* of the octahedral yield profile — not its shape — varies with pressure. Consequently, the strength ratio ψ equals its user-specified value at *all* pressures and throughout the entirety of the simulation (i.e., ψ is a *constant*, not a time varying internal state variable). Appendix A gives instructions for inferring a value of ψ from experimental data.

Precise functional forms of available Lode angle functions are given below:

1. Gudehus: $\Gamma(\bar{\theta}) \;=\; \dfrac{1}{2}\left[1 + \sin 3\bar{\theta} + \dfrac{1}{\psi}(1 - \sin 3\bar{\theta})\right].$

   To satisfy the convexity requirement of Eq. (4.50), the strength ratio must satisfy $\dfrac{7}{9} < \psi < \dfrac{9}{7}$.

2. Willam-Warnke: $\Gamma(\bar{\theta}) \;=\; \dfrac{4(1 - \psi^2)\cos^2\alpha^* + (2\psi - 1)^2}{2(1 - \psi^2)\cos\alpha^* + (2\psi - 1)\sqrt{4(1 - \psi^2)\cos^2\alpha^* + 5\psi^2 - 4\psi}}\,,$

   where $\alpha^* \;=\; \dfrac{\pi}{6} + \bar{\theta}$.   The Willam-Warnke option is convex for $\dfrac{1}{2} \le \psi \le 2$.

3. Mohr-Coulomb: $\Gamma(\bar{\theta}) \;=\; \dfrac{2\sqrt{3}}{3 - \sin\phi}\left(\cos\bar{\theta} - \dfrac{\sin\phi\sin\bar{\theta}}{\sqrt{3}}\right)$. Here, the internal **friction angle** ϕ is the angle of the failure envelope in the Mohr-diagram ($\tan\phi \;=\; \mu$, where μ is the coefficient of friction). Within Kayenta, ϕ is determined from the user-supplied strength ratio by $\sin\phi \;=\; 3\dfrac{(1 - \psi)}{1 + \psi}$.   The Mohr-Coulomb option is convex for $\dfrac{1}{2} \le \psi \le 2$.

These three options are distinguished by how the octahedral yield profile varies in stress space in the transition from TXE to simple shear to TXC at a fixed pressure. Graphs of the octahedral yield profile corresponding to any of the above options may be constructed by parametrically plotting

$$x \;=\; r\cos\bar{\Theta} \qquad y \;=\; r\sin\bar{\Theta} \tag{4.51}$$

Here, $\qquad r \;=\; \dfrac{\sqrt{2}}{\Gamma(\bar{\theta})}\,, \qquad$ where $\qquad \bar{\theta} \;=\; \dfrac{1}{3}\mathrm{ArcSin}(\sin 3\bar{\Theta})\,.$ $\tag{4.52}$

The angle $\bar{\Theta}$ varies from 0 to $360°$, and therefore $\bar{\theta}$ varies between $-30°$ and $+30°$.

48
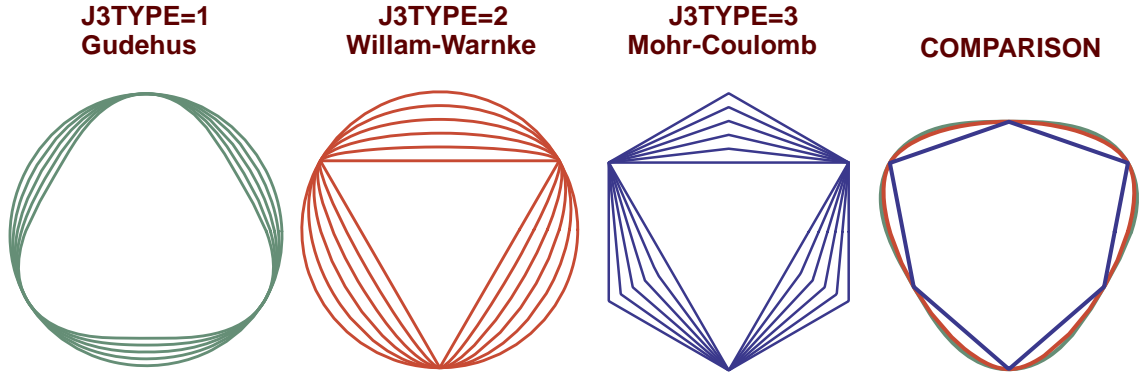
Figure 4.9.   Octahedral yield profiles, plotted at allowable values of the strength ratio.   The comparison plot corresponds to a strength ratio of ψ=0.8. The $\Gamma(\theta)$ function is defined so that all models return a value of 1 in triaxial compression.

As illustrated in Fig. 4.9, the Mohr-Coulomb model (**J3TYPE=3**) interpolates linearly *in octahedral stress space*, resulting in a distorted hexagon if $1/2 < \psi < 1$, a perfect hexagon (Tresca) if $\psi=1$, and a triangle if $\psi = 1/2$. For a detailed explanation of the Mohr-Coulomb formulation, see Appendix B (page B-25). The Mohr-Coulomb model has yield surface vertices at $\bar{\theta} = \pm\pi/6$, which results in extra computational effort to determine plastic strain rates in triaxial states. The Gudehus and Willam-Warnke options, on the other hand, involve no yield surface vertices, which speeds up computations. The Gudehus option is the default because of its computational simplicity, but it supports only a limited range of TXE/TXC strength ratios, the Willam-Warnke option should be used if a rounded but strongly triangular octahedral yield profile is desired. Appendix A (STEP 6) provides guidance for selecting the Lode angle option most appropriate for matching experimental data.

Kayenta subsumes many simpler (classical) models as special cases. For example, if failure is hypothesized to occur when the largest principal stress (or strain) reaches a critical value, then the octahedral yield profile will be a triangle. If, on the other hand, failure is presumed when the equivalent shear stress reaches a critical value, independent of the Lode angle (like a Von Mises or Drucker-Prager criterion), then the octahedral yield profile is a circle, which can be modeled with the Gudehus option. As a rule, any classical failure criterion that is expressed directly in terms of the principal stresses will imply an appropriate J3TYPE option (and an appropriate value for the TXE/TXC ratio), but such criteria will *also* imply functional constraints on the meridional failure function f_f as well, which requires appropriate Kayenta inputs to mimic. Simplified Kayenta input sets, corresponding to these classical special-case idealized theories may be found at the end of Appendix B.

Octahedral profile plots like the ones shown in Fig. 4.9 are most illuminating from a qualitative perspective. However, for parameterizing Kayenta to quantitative laboratory data, simple plots of Γ vs. $\bar{\theta}$ are more useful. Fig. 4.10 shows the $\Gamma(\bar{\theta})$ functions for each of the `J3TYPE` options. In all cases, the lower bound on Γ is 1.0 at TXC.
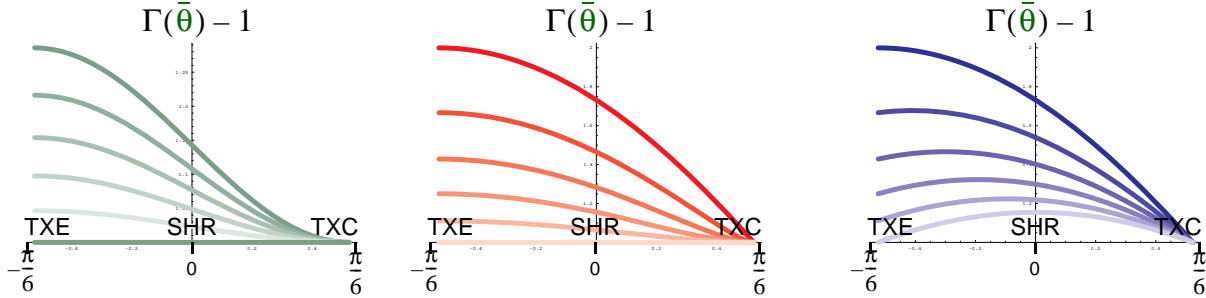
Figure 4.10.   Lode angle function (for various ψ strength ratios) plotted vs. the Lode angle varying from –30 degrees (TXE) to +30 degrees (TXC).   The larger the value of Γ, the smaller the radial distance to the octahedral yield profile and therefore the smaller the shear failure strength. The Gudehus and Willam-Warnke options both predict lowest strength (largest value of Γ) at TXE, whereas Mohr-Coulomb theory predicts lowest strength at an intermediate Lode angle somewhere between TXE and TXC. For example, when $\psi = 1$, Mohr-Coulomb theory reduces to Tresca theory and the lowest strength (highest Γ) occurs at the zero Lode angle (pure shear).

Advancing the solution (groundwork discussion)

So far, we have discussed how some microphysically based, but generally oversimplified theories can be used to predict *theoretical* shapes of yield or failure surfaces. Kayenta implicitly captures microscale phenomena by using *macroscale* measurable variables in phenomenological manner. Direct use of idealized theories would require initializing and evolving microscale quantities (such as porosity) that are impractical to measure in the laboratory. Therefore, the algebraic *structure* of functions used in Kayenta is guided by idealized microscale theories, but recast in terms of directly measurable macroscopic variables. Simplified failure criteria help guide choices for interpolation functions to be fitted to real *observed* data that likely reflect the specific phenomena considered in microscale idealizations and possibly some other "unknown" sources of inelastic flow.

Microphysical theories are also used to guide how Kayenta treats the partitioning of inelastic flow, once it begins. For example, most theories of inelastic flow (including Kayenta) presume that the total strain rate $\dot{\underset{\approx}{\varepsilon}}$ can be partitioned additively as

$$\dot{\underset{\approx}{\varepsilon}} = \dot{\underset{\approx}{\varepsilon}}^{e} + \dot{\underset{\approx}{\varepsilon}}^{p}, \qquad (4.53)$$

where $\dot{\underset{\approx}{\varepsilon}}^e$ represents the elastic (or recoverable) part of the strain rate and $\dot{\underset{\approx}{\varepsilon}}^p$ denotes the "plastic" part of the strain rate. More correctly, $\dot{\underset{\approx}{\varepsilon}}^p$ represents the *inelastic* strain rate, which reflects contributions from any and all sources of inelastic material response. Many classical theories presume that the *direction* of the plastic strain rate is parallel to the normal to the yield surface. In this case, since the normal to the yield surface can be obtained by the gradient of the yield function $f(\underset{\approx}{\sigma}, \underset{\approx}{\alpha}, \kappa)$, the plastic part of the strain rate is presumed to be of the form

$$\dot{\varepsilon}_{ij}^p = \dot{\lambda}\left(\frac{\partial f}{\partial \sigma_{ij}}\right)_{\underset{\approx}{\alpha}, \kappa}, \tag{4.54}$$

where $\dot{\lambda}$ is a multiplier (called the **consistency parameter**) determined by demanding that the stress must remain on the yield surface during inelastic loading. The subscripts on the partial derivative merely indicate that the internal state variables are held constant. When the plastic strain rate direction is determined from the stress gradient of the yield function, as shown here, the model is said to be "associative" (to indicate that the plastic strain rate is associated with the yield function*).

While Kayenta does support associativity at user request, many researchers report that normality tends to over-predict the amount of volumetric plastic strain [53]. Therefore, *non*-normality is supported in Kayenta as well. For non-normality the user specifies a **flow function** $\phi(\underset{\approx}{\sigma}, \underset{\approx}{\alpha}, \kappa)$ such that†

$$\dot{\varepsilon}_{ij}^p = \dot{\lambda}\left(\frac{\partial \phi}{\partial \sigma_{ij}}\right)_{\underset{\approx}{\alpha}, \kappa}. \tag{4.55}$$

The plastic strain rate $\dot{\varepsilon}_{ij}^p$ includes both deviatoric and isotropic parts. If the flow potential depends on the first invariant I_1, then applying Eq. (3.21), the *volumetric* plastic strain rate is

$$\dot{\varepsilon}_v^p = \mathrm{tr}\dot{\underset{\approx}{\varepsilon}}^p = 3\dot{\lambda}\frac{\partial \phi}{\partial I_1}. \tag{4.56}$$

---

* For materials that exhibit elastic-plastic coupling, the terms "associativity" and "normality" can have distinct meanings, depending on whether the portion of the total strain rate attributable to rates of elastic moduli is absorbed into the elastic strain rate or the inelastic strain rate. When the coupling terms (from *rates* of elastic moduli) are incorporated into the inelastic strain rate, normality and associativity are *not* interchangeable terms. If the coupling terms are incorporated into the elastic strain rate, then associativity and normality are interchangeable, but at the cost that the elastic strain rate ceases to be an exact differential with respect to deformation.

† While considerable data does exist to *suggest* that the inelastic strain rate is *not* directed normal to the yield surface for some materials, such behavior is not well understood. The mathematical validity of assuming existence of a non-associated flow potential function has been called into question by Sandler and Pucik [49,46], who have demonstrated that such a model is inherently unstable, inadmissibly generating unbounded energy from quiescent states. The instability arises from the fact that any classically non-associative model admits plastic waves that travel faster than elastic waves [11].

The plastic strain rate points normal to the isosurface $\phi = 0$.[*] If the flow function is associative, then the plastic potential function is identical to the yield function and the plastic strain rate will therefore point normal to the yield surface. Flow surface vertices reside at points where the flow potential is non-differentiable, in which case the plastic strain rate points within a "cone of limiting normals" (Koiter fan) at the vertex and is determined through additionally considering the trial elastic stress rate associated with the total strain rate.

In Kayenta, the functional form of ϕ is the same as that of f, but with different values for material constants. Specifically, the flow potential ϕ can be made to differ from the yield function by assigning values to a_2^{PF}, a_4^{PF}, R^{PF}, and ψ^{PF} that differ from their counterpart parameters (a_2, a_4, R, ψ) used to define the yield surface. For associativity, the potential function parameters should be given values identical to their counterparts in the yield function.

If continuing to apply elasticity theory would result in a predicted stress lying outside the yield surface, the governing equations are no longer elastic. At this point, the strain rate is decomposed into two parts, elastic plus plastic, as mentioned in Eq. (4.53). The stress rate is determined by applying elasticity. That is,

$$\dot{\sigma}_{ij} = C_{ijkl}\dot{\varepsilon}_{ij}^e = C_{ijkl}(\dot{\varepsilon}_{ij} - \dot{\varepsilon}_{ij}^p), \tag{4.57}$$

where C_{ijkl} denotes the isotropic tangent elastic stiffness tensor. In Eq. (4.57), our goal is to compute the stress *rate*. The current state is known, and therefore the instantaneous stress state and elastic moduli are known. In numerical implementations of constitutive models, the strain rate is known (it is provided by the host code after solution of the momentum equation). Thus, the only unknown in this equation is the plastic strain rate. Equation (4.55) allows us to compute the *direction* of the plastic strain rate from the known instantaneous stress state. Thus, after substitution of Eq. (4.55) into (4.57), the stress rate can be written

$$\dot{\sigma}_{ij} = C_{ijkl}\dot{\varepsilon}_{ij}^e = C_{ijkl}\left[\dot{\varepsilon}_{ij} - \lambda\left(\frac{\partial\phi}{\partial\sigma_{ij}}\right)_{\underset{\sim}{\alpha,\,\kappa}}\right]. \tag{4.58}$$

Everything on the right-hand-side of this equation is known except the value of the consistency parameter, λ.

A recent and fundamental change in Kayenta revises Eq. (4.58) to be instead

$$\dot{\sigma}_{ij} - \dot{\alpha}_{ij} = C_{ijkl}\dot{\varepsilon}_{ij}^e = C_{ijkl}\left[\dot{\varepsilon}_{ij} - \lambda\left(\frac{\partial\phi}{\partial\sigma_{ij}}\right)_{\underset{\sim}{\alpha,\,\kappa}}\right]. \tag{4.59}$$

---

[*] Because the current stress might not reside on the isosurface $\phi = 0$, Kayenta projects the stress to the nearest point on this isosurface. The need for such revisions is rarely recognized in plasticity programs (and casts doubt on the very notion flow potentials).

where α_{ij} are components of the backstress tensor. With this revision, the backstress becomes the center for elasticity as well as the center for the yield surface. This revision allows the yield surface to translate under kinematic hardening in such a way that zero stress might eventually become a point outside the yield surface, as observed in some laboratory experiments [17]. The documentation in this section continues to be based on the formulation in Eq. (4.58). The model revisions using Eq. (4.59) are still in the testing phase and therefore will be documented in later updates of this manual.

The consistency parameter is obtained by demanding that, not only must the stress be on the yield surface during plastic loading $(f = 0)$, it must also *remain on the yield surface throughout a plastic loading interval*. Thus, $\dot{f} = 0$ during plastic loading. The yield function f depends on the stress, but it also depends on the isotropic hardening internal state variable, κ and (if applicable) on the kinematic hardening backstress state variable tensor α_{ij}. Thus, the assertion that $\dot{f} = 0$ can be written via the chain rule as

$$\dot{f} = \frac{\partial f}{\partial \sigma_{ij}} \dot{\sigma}_{ij} + \frac{\partial f}{\partial \kappa} \dot{\kappa} + \frac{\partial f}{\partial \alpha_{ij}} \dot{\alpha}_{ij} = 0. \tag{4.60}$$

The first term may be simplified through application of Eq. (3.20). The last two terms reflect the fact that the yield surface can evolve in shape and translate in stress space during inelastic loading. In what follows, we will present "evolution equations" that govern how the state variables change in response to plastic flow. It will be argued that the evolution of each internal state variable should be proportional to the plastic strain rate. Equivalently, these rates must be proportional to our unknown plastic consistency parameter $\dot{\lambda}$. By substituting Eq. (4.58) and these soon-to-be-derived evolution equations for the internal state variables into Eq. (4.60) we will be able to solve Eq. (4.60) for the consistency parameter $\dot{\lambda}$. Once the consistency parameter is known, it can be substituted into Eq. (4.58) to obtain the stress rate, which may then be integrated numerically to update the stress. With the consistency parameter $\dot{\lambda}$ known, then *rates* of internal state variables (ISVs) become known through their evolution equations, allowing the ISVs themselves to be updated to the end of the timestep. Thus, the key to advancing the solution is to now derive in detail the internal state variable evolution equations.

Evolution equations

Equation (4.60) may be used to determine the plastic consistency parameter $\dot{\lambda}$ if hardening evolution laws can be found for which the rate of each internal state variable (κ and α_{ij}) is proportional to $\dot{\lambda}$. Once the plastic consistency parameter is known, the evolution laws may be integrated through time to model the time varying hardening evolution of the yield surface.
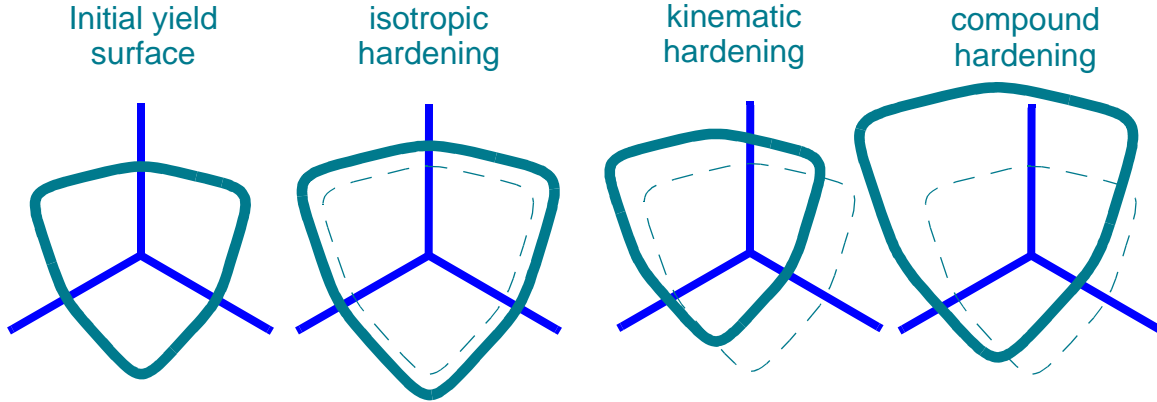
Figure 4.11. *Hardening mechanisms.* At a given pressure, isotropic hardening entails an increase in size, kinematic hardening translates the yield surface, and compound hardening includes both mechanisms. Softening corresponds to a yield surface *contraction*.

As indicated in Fig. 4.11, isotropic hardening (governed by κ and related to void collapse) causes a change in *size* of octahedral yield profiles, while kinematic hardening (governed by the backstress tensor $\underset{\approx}{\alpha}$) produces a *translation* of all octahedral yield profiles. In general, both types of hardening can occur simultaneously.

In this section, we will derive explicit expressions for an isotropic hardening modulus h_κ and a kinematic hardening tensor, $\underset{\approx}{H}_\alpha$, such that the evolution of the internal state variables may be written in the forms

$$\dot{\kappa} = h_\kappa \dot{\lambda} \tag{4.61}$$

and

$$\dot{\underset{\approx}{\alpha}} = \underset{\approx}{H}_\alpha \dot{\lambda}. \tag{4.62}$$

Later, substituting these expressions into Eq. (4.60) will lead to an expression for the plastic consistency parameter $\dot{\lambda}$. Once the consistency parameter is known, the above equations can be themselves integrated through time to update κ and $\underset{\approx}{\alpha}$.

Evolution equation for the porosity-related internal state variable, κ.

We begin this section with some background discussion about the meaning of the internal state variable κ, connecting it to some classical microphysical theories for purely porous (non-cracked) materials. Kayenta's re-interpretation of κ for both porous and cracked materials will lead ultimately to an evolution law of the desired form, $\dot{\kappa} = h_\kappa \dot{\lambda}$ where h_κ is called the **isotropic hardening modulus**.

In Kayenta, void collapse commences at different pressures depending on the amount of shear stress present. The effect of shear stress on void collapse is characterized by the cap function illustrate in Fig. 4.5. Even though void collapse depends on shear stress, *characterizing* this effect requires only specification of two numbers $\bar{\kappa}$ and $\bar{X}$ on the hydrostat [see Fig. 4.5]. In Kayenta, $\bar{\kappa}$ and $\bar{X}$ are presumed to be interrelated so that knowledge of $\bar{X}$ is sufficient to compute the value of $\bar{\kappa}$. We will discuss this relationship later. For now, we will focus on how the hydrostat intercept $\bar{X}$ should vary as porosity is reduced.

If a material is capable of permanent volume change (i.e., if hydrostatic testing exhibits nonzero residual plastic volumetric strain ε_v^p upon releasing the pressure), then the material likely contains voids. The hydrostat intercept $\bar{X}$ is proportional to the critical "elastic limit" pressure required to initiate irreversible void collapse. Therefore, the larger the porosity, the smaller $\bar{X}$ will be. As porosity is crushed out, the hydrostat intercept will move to the right so that increasing pressure will be required to continue crushing out the pores. Recognizing that ε_v^p is an indirect measure of porosity changes, our first goal is to describe how the relationship between ε_v^p and $\bar{X}$ can be inferred from hydrostatic test data. Then we will discuss the relationship between $\bar{\kappa}$ and $\bar{X}$. With these two relationships in hand, we will ultimately assert that

$$\dot{\kappa} = \left(\frac{d\kappa}{d\bar{X}}\right)\left(\frac{d\bar{X}}{d\bar{\varepsilon}_v^p}\right)\dot{\bar{\varepsilon}}_v^p, \tag{4.63}$$

from which substitution of Eq. (4.56), during hydrostatic compression or compaction dominated processes, will give the evolution equation in the desired form,

$$\dot{\kappa} = h_\kappa \lambda, \quad \text{where} \quad h_k = 3\left(\frac{d\kappa}{d\bar{X}}\right)\left(\frac{d\bar{X}}{d\bar{\varepsilon}_v^p}\right)\frac{\partial \phi}{\partial \bar{I}_1}. \tag{4.64}$$

During dilatation-dominated processes, a different form is used for h_k (see Eq. 4.75).

Relationship between $\bar{X}$ and ε_v^p (the hydrostatic crush curve)

If the *matrix* material for a porous medium is plastically incompressible, then it can be shown [42] that the unloaded porosity Π (i.e., the innate porosity at the rest state, not the slightly different porosity that reflects reversible *elastic* porosity reduction under loading) evolves under plastic loading according to

$$\dot{\Pi} = (1 - \Pi)\dot{\varepsilon}_v^p , \tag{4.65}$$

where Π is the void volume in a sample divided by the total volume of the sample (both volumes are those in the unloaded state), and $\dot{\varepsilon}_v^p$ is the trace of the logarithmic plastic strain rate. To second order accuracy, Eq. (4.65) implies that the *change* in porosity is approximately equal to the plastic volumetric strain:

$$\Pi - \Pi_o \approx \varepsilon_v^p . \tag{4.66}$$

Considering *only* hydrostatic loading, early research on pore collapse focused on deriving and/or experimentally measuring so-called "crush curves" in which porosity in a material is plotted as a function of the applied pressure, as in Fig. 4.12. Kayenta uses a similar curve, but inferred directly from hydrostatic stress-strain data so that porosity measurements are *not* necessary. By using the cap function, Kayenta incorporates the results from this specialized *hydro-static* experiment into the general theory in such a manner that pore collapse will commence at lower pressures in the presence of *shear*. Recall that the cap function, loosely speaking, represents material response in the absence of microcracks. Porous-only

Figure 4.12. A conventional porosity crush curve (dashed) and state path (solid). Porosity is constant until a critical elastic limit pressure $\bar{P}_E$ is reached. Thereafter, porosity is reduced as pressure is increased.

theories typically predict meridional cap profiles similar to Kayenta's cap function. For example, Gurson [28] reported the following upper-bound yield criterion (expressed in terms of Lode cylindrical coordinates):

$$r = k\sqrt{f_v^2 + 1 - 2f_v\cosh\left(\frac{z}{\sqrt{2}k}\right)} , \tag{4.67}$$

where k is a constant (the yield stress of the matrix material) and f_v is the porosity. Being independent of the Lode angle, the Gurson yield function is a circle in the octahedral plane; Gurson's *meridional* profile is compared with Kayenta's cap function in Fig. 4.13 for various porosities. As porosity goes to zero, the meridional profile approaches the pressure insensitive Von-Mises profile for the matrix material (in other words, in the absence of microcracks, the yield surface becomes a cylinder in stress space as the porosity goes to zero). This property holds only in the absence of microcracks. When microcracks are later included, the common envelope of yield surfaces will be the shear *fracture* curve F_f.

Figure 4.13.   The Gurson theory for porous yield surfaces compared with Kayenta cap function at various values of the internal state variable κ. Qualitatively, the theories are similar.   When microcrack effects are included, Kayenta forms a pressure-dependent envelope, as in Fig. 1.0(b) on page 1, instead of the horizontal Von-Mises-like envelope shown here.

Under Gurson theory, the key material properties are *microphysical* (the yield stress k for the matrix material and the porosity f_v), which are difficult to measure directly. To obtain analytical results, these theories must resort to over simplistic assumptions about the matrix material and pore morphology (e.g., Gurson theory presumes perfectly spherical voids arranged in a perfectly periodic array). Finally, microphysical theories are typically *upper bounds*, which are of limited use in applications since the tightness of the bound is unknown.

Rather than *directly* using models like Gurson theory, Kayenta is *guided* by the general trends they predict. Except at extremely high porosity, the Gurson model predicts that the cap surface will be essentially *flat* for a large range of pressures (*z*-coordinates). The loss in shear strength caused by pores is pronounced over only a small range of pressures near the hydrostatic limit pressure. This region (beyond which the yield surface noticeably branches down to zero) is called the **cap** region. As seen in Figure 4.13, Gurson theory predicts the yield surface will evolve with porosity in such a manner that the cap essentially translates along the pressure (*z*) axis — the curvature of the cap region does not change significantly. Kayenta supports these general trends by using a computationally simpler Rubin-Sandler cap function which is simply constant until a critical branch pressure is reached, after which the cap function drops to zero along an ellipse. The cap curve evolves by simple translation along the hydrostat without changes in cap curvature.

In the Gurson model, the current location of the translated cap is a function of the matrix yield stress and the porosity. Rather than using essentially unknowable matrix properties like these as internal state variables, Kayenta recognizes that the appropriate location for the cap can be determined directly from hydrostatic compression test data and

the branch point at which shear begins to affect pore collapse is presumed in Kayenta to translate with the hydrostatic limit point. Thus, characterizing how the entire cap function evolves in response to plastic loading boils down to characterizing how the hydrostat intercept point (i.e., where the cap intersects the *z*-axis) evolves.

Kayenta presumes that it is experimentally tractable to obtain pressure vs. volumetric strain data. If possible, the experiment should be run to the point of total pore collapse (as in Fig. 3.1 on page 15). The elastic response of the material must be first determined by fitting the unloading curve to the nonlinear elasticity fitting function in Eq. (4.9). "Copies" of the elastic unloading function may be superimposed anywhere on the hydrostatic pressure vs. total strain data. As indicated in Fig. 4.14, the elastic unloading curves can be used to determine a shift distance that must be applied at any given pressure to remove the elastic part of the strain. After applying these shifts, the pressure vs. *total* strain plot is converted to a pressure vs. *plastic* strain plot, called an X-function. The X-function in Fig. 4.14 asymptotes to infinity when the plastic volume strain (i.e., the change in porosity) has reached its maximum value corresponding to all of the pores having been crushed out. Rotating the X-curve and shifting the origin produces a classical crush curve in which porosity is plotted as a function of pressure. Kayenta never *explicitly* refers to porosity. Instead, the plastic volumetric strain is employed as an indirect measure of porosity changes.
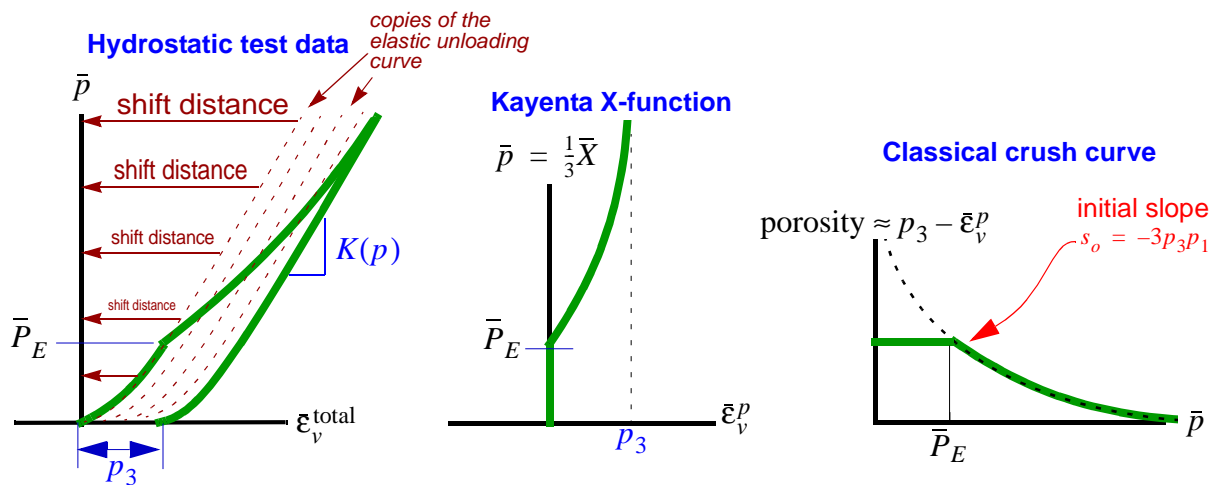
Figure 4.14.   Relationship between (a) hydrostatic pressure vs. volumetric strain data, (b) Kayenta X-function, and (c) a traditional porosity vs. pressure crush curve.   Test data are pressure vs. total volumetric strain. Once the elastic unloading curves have been parameterized to Kayenta fitting functions, the elastic strain at each pressure value may be subtracted from the total strain to generate the X-function. This function asymptotes to a limit value for the plastic strain when all voids have crushed out (and plastic volume changes therefore become negligible). The limit strain is approximately the initial porosity in the material. Rotating the X-plot 90° and moving the origin as shown will produce a traditional porosity vs. pressure crush curve.

Parameterizing Kayenta so that it will adequately model the changes in the yield surface resulting from pore collapse requires converting hydrostatic pressure vs. volumetric strain data as illustrated in Fig. 4.14 to obtain a classical porosity vs. pressure crush curve in which the porosity is plotted as a function of the pressure $\bar{p}$. Specialized parameteriza-

tion software is available from the model developers to perform this conversion task and to fit the resulting crush curve to an exponential spline (see Appendix A). The plastic volume strain of a virgin (pre-deformation) material is zero. Therefore the user-specified parameter p_3 is approximately equal to the initial porosity in the material. As pressure is increased from zero, the crush curve [Fig. 4.14(c)] shows that the porosity remains unchanged for a while until an elastic limit pressure $\bar{P}_E$ is reached. Continuing to apply increasing pressure beyond this elastic limit results in irreversible pore collapse and therefore reduction in porosity. Kayenta allows fitting the post yielding part of the crush curve according to the **crush curve spline** formula,

$$\boxed{p_3 - \bar{\varepsilon}_v^p = p_3 e^{-(p_1 + p_2\bar{\xi})\bar{\xi}}}, \quad \text{where} \quad \bar{\xi} = \bar{X} - \bar{p}_0 = 3(p - P_E). \tag{4.68}$$

Here, p_0, p_1, p_2, and p_3 are fitting constants. Referring to the porosity vs. pressure crush curve, these parameters are interpreted physically as follows:

- p_0 equals $-3\bar{P}_E$, where $\bar{P}_E$ is the elastic limit pressure at the initial onset of pore collapse.

- p_1 equals $|s_o|/(3p_3)$, where s_o is the initial slope of the porosity vs. pressure crush curve (see Fig. 4.14).

- p_2 is an optional fitting parameter that may be used if a measured crush curve has an inflection point (i.e., initially concave down, transitioning to concave up at high pressures).

- p_3 is the maximum achievable plastic volume strain, which corresponds approximately to the initial porosity in the material. Complete crushing out of all pores in the material is recognized in the hydrostatic pressure vs. total strain curve if the elastic release curve is tangent to the loading curve.

Equation (4.68) coincides with hydrostatic test data only during pore collapse. During the initial elastic loading, Eq. 4.68 describes the dashed line in Fig. 4.14, which is *not* required to coincide with the data. At pressures above the elastic limit ($\bar{\xi} > 0$), Eq. 4.68 may be used to compute the plastic volumetric strain according to

$$\bar{\varepsilon}_v^p = p_3[1 - e^{-(p_1 + p_2\bar{\xi})\bar{\xi}}], \quad \text{where} \quad \bar{\xi} = \bar{X} - \bar{p}_0 = 3(\bar{p} - \bar{P}_E) \tag{4.69}$$

This relationship may be differentiated to obtain the derivative $d\bar{X}/d\bar{\varepsilon}_v^p$ needed in Eq. (4.64). Now all we need to compute the isotropic hardening modulus h_κ is the relationship between κ and X so that we can substitute the derivative $d\kappa/dX$ into Eq. (4.64).

Incidentally, to mimic the crush curve implied in Gurson's porosity model [28], Fossum's parameters should be set as follows:

$$p_1 = \frac{-q_2}{6Y}, \quad p_2 = 0, \quad p_3 = \ln\left(\frac{1}{1 - q_1\phi_0}\right) \tag{4.70}$$

where ϕ_0 is the initial porosity (void volume fraction) and Y is the uniaxial yield strength of the matrix material. The parameters q_1 and q_2 are Tvergaard's adjustments to Gurson's model (both equal to 1 in Gurson's original model).

The p2 parameter and its implication on pore <u>growth</u>. Laboratory data for hydrostatic loading is often like that sketched in Fig. 4.15, where the onset of pore collapse corresponds to a smooth change in slope of the stress-strain diagram rather than the abrupt slope discontinuity illustrated in Fig. 4.14. The corresponding crush curve (porosity vs. pressure) is therefore initially concave down before transitioning to concave up. For monotonic compression, this behavior is reproduced in Kayenta by having a nonzero p2 parameter. The dashed lines, in Figs. 4.14 and 4.15 are the crush curves defining the relationship between plastic volume strain (which is related to porosity) and pressure for pressures exceeding the elastic limit $\bar{P}_E$.
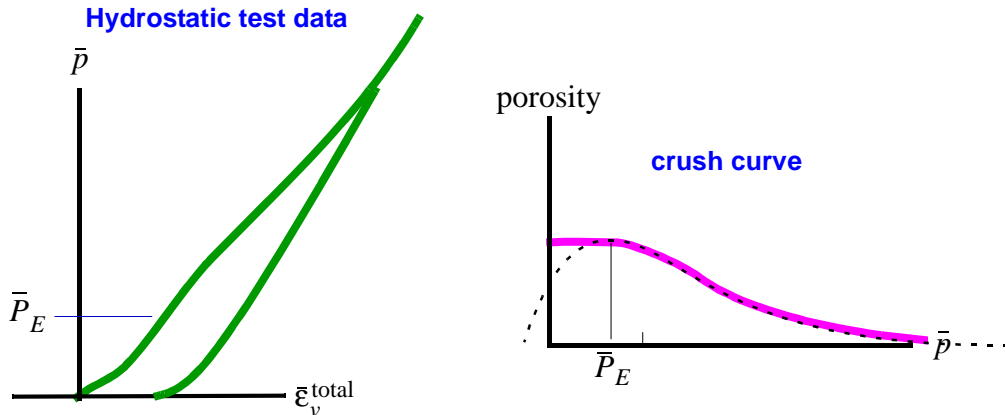
Figure 4.15.   A soft "knee" in the onset of pore collapse requires a nonzero value of the p2 parameter, but the resulting crush curve (dashed line) is reasonable only for $\bar{P} > \bar{P}_E$.

Kayenta faithfully reproduces the crush curve in compression. In practice, however, a load path might involve compression followed by tension, in which case the porosity would need to initially decrease and then subsequently increase. In a traditional porosity model, this is usually modeled by assuming that the tensile crush curve is a copy of the compressive crush curve, (perhaps with a scalar reduction factor applied to pressure, as

indicated in the inset figure). In the tensile domain, the porosity would move *upward* along the dashed crush curve. However, when p2 is nonzero to model the soft bend at the onset of failure, the crush curve has an unrealistic upper bound on porosity — pores cannot grow beyond the initial porosity! The problem lies in the attempt to model the softly bending "knee" in experimental data at the onset of pore collapse. This knee corresponds to heterogeneous material response *at the microscale* in the transition where only a portion of the solid matrix material is deforming plastically [4]. However, Kayenta presumes that deformation is either elastic or plastic, with no transition region. To correctly model the "knee" and tensile pore growth, Kayenta would need to be enhanced to include two yield surfaces: one marking the onset of plasticity at the microscale and another corresponding to fully developed plasticity throughout the solid matrix.
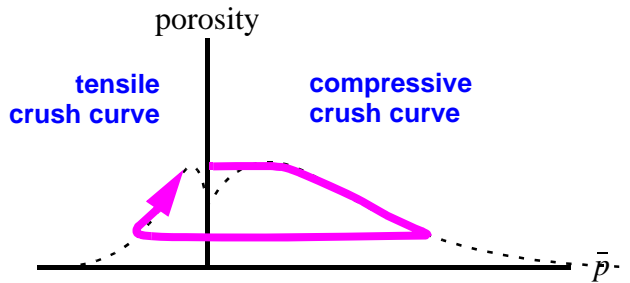
Relationship between $\bar{\kappa}$ and $\bar{X}$ (cap curvature model)

For a *purely porous* material, Fig. 4.13 suggests that $\bar{\kappa}$ is simply smaller than $\bar{X}$ by a fixed amount. Therefore, knowing $\bar{X}$ is sufficient to determine $\bar{\kappa}$. For a material that contains both pores and microcracks, the relationship between the branch point $\bar{\kappa}$ and $\bar{X}$ is similar, but influenced by the pressure sensitivity of the fracture function. Recall that the continuously differentiable meridional yield function f is constructed by multiplying a function f_f times a cap porosity function f_c. Qualitatively, the fracture function f_f marks the onset of shear crack growth, with significant pressure strengthening being the result of friction at crack faces. This yield envelope function f_f might be lower than the ultimate shear limit envelope F_f if kinematic hardening is allowed. The cap porosity function f_c intersects the hydrostat ($\bar{I}_1$-axis) at $\bar{X}$, marking the point at which pressure *under hydrostatic loading* would be sufficient to induce pore collapse. Variation of the cap function with shear stress (along the ellipse) merely reflects an expectation that pore collapse will commence at a lower pressure than the hydrostatic limit when shear assisted.

Isotropic hardening in Kayenta is cast in terms of the branch point located at $I_1 = \kappa$ (or, equivalently, $\bar{I}_1 = \bar{\kappa}$) where the yield function f begins to deviate from the envelope function f_f. The height of the branch point b in Fig. 4.16 is considerably lower than the peak height B.

Between the branch and the peak, material response begins to be influenced by porosity, but is still shear crack (dilatation) dominated, and therefore plastic volume *increases* because of crack bulking. Between the peak and the hydrostatic limit point $\bar{X}$, porosity dominates the material response,
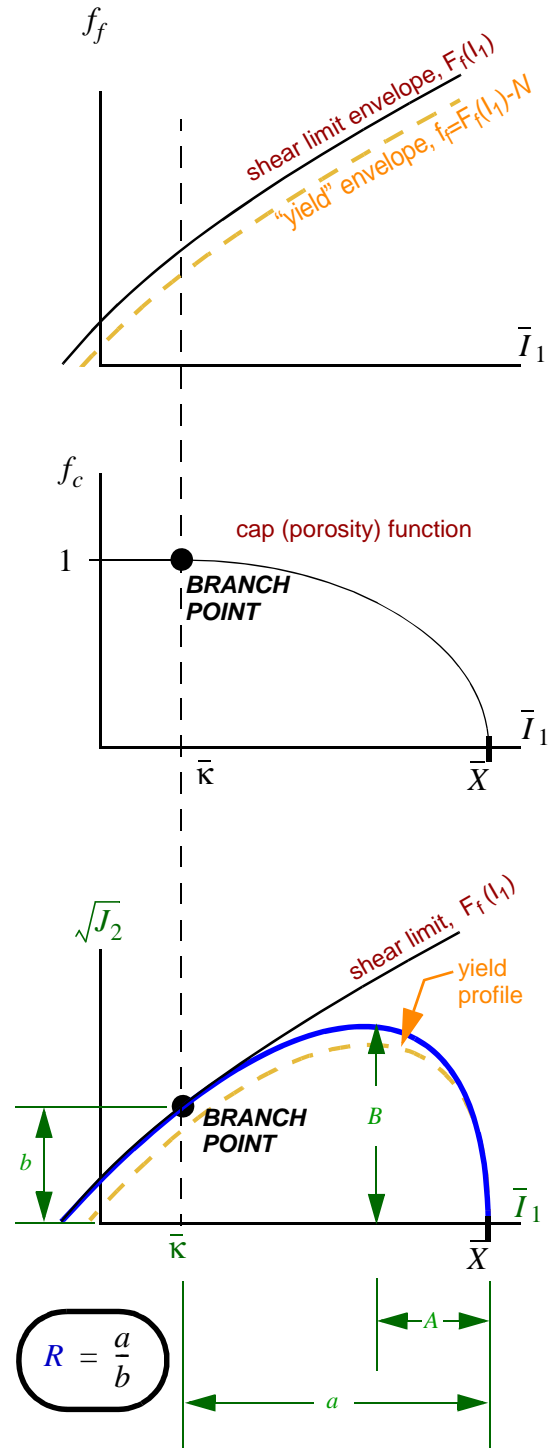
Figure 4.16. Continuously differentiable Kayenta yield function and some characteristic dimensions. The ratio a/b is usually larger than 1, whereas A/B is usually smaller than 1. The bold blue curve is $F_f f_c$. The dashed yield curve is $f_f f_c$.

resulting in plastic volume *compaction* (from pore collapse). At the critical zero-slope point on the yield surface, material response is influenced equally by both cracks and pores so that no net volume change is apparent at the macroscale.

Two-surface models [e.g., Ref. 50] typically construct and evolve the yield function by making direct reference to the ratio A/B, which (referring to Fig. 4.16) is typically smaller than unity. Kayenta, however, constructs and evolves its yield function based on the ratio $R \equiv a/b$, which is typically *larger* than unity. This distinction between the two ratios is important to emphasize in publications and presentations to avoid confusion between Kayenta and conventional two-surface models.

Guided both by trends in observed data and by microphysical theories (e.g., Fig. 4.13), Kayenta presumes that hardening proceeds such that the ratio between the distances a and b labeled in Fig. 4.16 remains always equal to a user-specified constant R. The axis labels in Fig. 4.16 indicate that $a = \bar{X} - \bar{\kappa}$ and $b = F_f(\kappa)$. Therefore the **cap eccentricity** (also called the cap **shape parameter**) $R = a/b$ is given by $R = (\bar{X} - \bar{\kappa})/F_f(\kappa)$ or, solving for $\bar{X}$,

$$\bar{X} = \bar{\kappa} + RF_f(\kappa). \tag{4.71}$$

When written without the overbar denoting the negative, this equation becomes

$$\boxed{X = \kappa - RF_f(\kappa)}. \tag{4.72}$$

This expression is evaluated internally within Kayenta coding to determine X as a function of the internal state variable κ. Differentiating both sides of this equation with respect to κ gives

$$\frac{dX}{d\kappa} = 1 - RF_f'(\kappa). \tag{4.73}$$

The κ evolution law

Substituting Eq. (4.73) into (4.64) gives

$$\boxed{\dot{\kappa} = h_\kappa \hat{\lambda}}, \tag{4.74}$$

where the "**isotropic hardening parameter**" h_κ is

compaction-dominated hardening modulus   dilatation-dominated hardening modulus

$$\boxed{h_\kappa = \min\left[3\frac{\partial\phi}{\partial I_1}\left(\frac{dX/d\varepsilon_v^p}{1 - RF_f'(\kappa)}\right) , \left(\frac{I_1 - \kappa}{R}\right)\left(\frac{dX/d\varepsilon_v^p}{1 - RF_f'(\kappa)}\right) \right]} \tag{4.75}$$

subject to the constraint, $0 > h_\kappa > -\infty$.* For numerical convenience, this constraint is replaced by $0 > h_\kappa > -0.01 b_0^2$, where b_0 is the initial bulk modulus. The derivative $dX/d\varepsilon_v^p$ is found from crush-curve data fitted to Eq. (4.69).

The first term in the minimum function of Eq. (4.75) dominates when the stress state falls on the "compaction dominated" part of the yield surface, labeled in Fig. 4.17, while the second term dominates in the dilatation regime. The second term in the minimum function is guided by trends in observed data.

Figure 4.17. *Meridional plane in which the magnitude of the stress deviator "r" is plotted against –z (which is proportional to the pressure "p") The yield surface (solid) demarks the onset of inelastic flow. Under continued inelastic loading, the yield surface hardens (expands and/or translates) toward the shear limit surface (dashed).*

Even under monotonic loading, the relative position of the stress state on the yield surface can move from compaction to dilatation regimes. Figure 9.6*(a)* (page 117) shows a triaxial compression load path (angled red arrow) that falls initially on the porosity (compaction) dominated portion of the yield surface, which therefore results in plastic volume reduction and an isotropic expansion of the yield surface. Compaction from void collapse and dilatation from crack bulking are relatively balanced in the vicinity of the critical point. After the stress passes through the critical point, the hardening modulus h_κ in Eq. (4.75) transitions from its compaction-dominated value to the dilatation-dominated value.

Evolution equation for the kinematic hardening backstress tensor. Kayenta supports kinematic hardening, but is otherwise isotropic. Kinematic hardening entails using a shifted stress tensor $\underset{\approx}{\xi} = \underset{\approx}{S} - \underset{\approx}{\alpha}$ in the yield function instead of the actual stress. The deviatoric tensor internal state variable $\underset{\approx}{\alpha}$ is called the **backstress**, and it is computed using evolution equations described here.

Recall that the yield criterion with kinematic hardening is given by

$$J_2^\xi = [F_f(I_1) - N]^2 F_c(I_1), \tag{4.76}$$

where J_2^ξ is the second invariant of the shifted stress,

$$\underset{\approx}{\xi} = \underset{\approx}{S} - \underset{\approx}{\alpha}. \tag{4.77}$$

---

* When using the overbar to denote the negative, Eq. (4.74) may be written $\dot{\bar{\kappa}} = \bar{h}_k \dot{\gamma}$ subject to $0 < \bar{h}_k < \infty$. Thus, since $\dot{\gamma}$ is never negative, this constraint ensures that $\bar{\kappa}$ will never decrease. Physically, this is equivalent to demanding that porosity must always decrease. Increases in porosity (i.e., softening) cannot be accommodated at the material constitutive level — to avoid mesh dependencies of the solution, softening must be handled at the field scale by the host code. See page 69.

The backstress tensor $\underset{\sim}{\alpha}$ is initialized to zero. Upon onset of yielding, the backstress evolves in proportion to the deviatoric part of the plastic strain rate:

$$\dot{\underset{\sim}{\alpha}} = HG^\alpha(\underset{\sim}{\alpha})\underset{\sim}{\gamma}^p, \tag{4.78}$$

where $\underset{\sim}{\gamma}^p = \mathrm{dev}\,\dot{\underset{\sim}{\varepsilon}}^p = \mathrm{dev}\left(\dot{\lambda}\frac{\partial\phi}{\partial\underset{\sim}{\xi}}\right).$ \hfill (4.79)

Hence, comparing with Eq. (4.62), the kinematic hardening modulus tensor is given by

$$\underset{\sim}{H}_\alpha = HG^\alpha(\underset{\sim}{\alpha})\mathrm{dev}\left(\frac{\partial\phi}{\partial\underset{\sim}{\xi}}\right), \tag{4.80}$$

where H is a material constant and $G^\alpha(\underset{\sim}{\alpha})$ is a scalar-valued decay function designed to limit the kinematic hardening such that $G^\alpha \to 0$ as $\underset{\sim}{\alpha}$ approaches the shear limit surface, $F_f(I_1)$. Since the yield function itself is defined in terms of $F_f(I_1) - N$, the maximum kinematic translation that can occur before reaching the limit surface equals the model off-set parameter N. Kayenta uses the G^α function to "slow down" the rate of hardening as the limit surface is approached so that $\underset{\sim}{H}_\alpha$ will equal zero upon reaching the limit surface. Specifically, Kayenta uses the following decay function:

$$G^\alpha(\underset{\sim}{\alpha}) = 1 - \frac{\sqrt{J_2^\alpha}}{N}, \qquad \text{where} \qquad J_2^\alpha = \frac{1}{2}\mathrm{tr}\,\underset{\sim}{\alpha}^2. \tag{4.81}$$

Kinematic hardening causes the octahedral profile to translate so that it no longer remains centered at the origin (See Fig. 4.11). Consequently, the yield surface will appear to have translated upward in the meridional plane that contains the backstress (see Fig. 4.18). The translation distance equals $\sqrt{J_2^\alpha}$ and Eq. (4.81) prevents this distance from ever exceeding the user-specified offset limit N. Of course, on the meridional plane *perpendicular* to the backstress, the meridional profile will *not* appear to have translated.
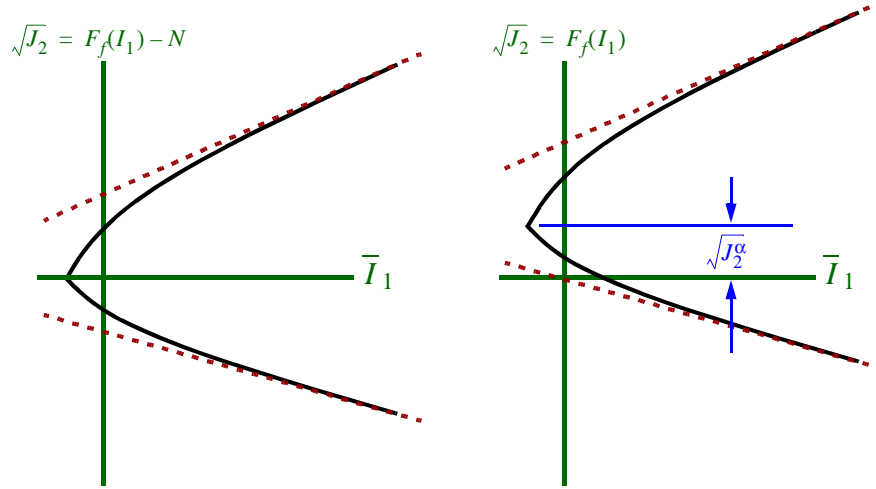
Figure 4.18. *The effect of kinematic hardening on the meridional plane that contains the backstress.* According to the hardening rule, this meridional profile is permitted to translate in deviatoric stress space by as much as a shift parameter N. The meridional plane *perpendicular* to the back stress shows no translation at all.

Advancing the solution (final step, consistency parameter)

Recall from Eq. (4.60) that the consistency parameter $\dot{\lambda}$ is determined from the consistency condition, $\dot{f} = 0$, applied during plastic loading intervals. Specifically,

$$\dot{f} = \frac{\partial f}{\partial \sigma_{ij}}\dot{\sigma}_{ij} + \frac{\partial f}{\partial \alpha_{ij}}\dot{\alpha}_{ij} + \frac{\partial f}{\partial \kappa}\dot{\kappa} = 0. \tag{4.82}$$

Recall the key equations governing the rates of the field and internal state variables:

$$\dot{\sigma}_{ij} = C_{ijkl}\dot{\varepsilon}_{kl}^e = C_{ijkl}\dot{\varepsilon}_{kl} - C_{ijkl}\dot{\varepsilon}_{kl}^p \tag{4.83a}$$

$$\dot{\alpha}_{ij} = H_{ij}^\alpha\dot{\lambda} \tag{4.83b}$$

$$\dot{\kappa} = h_\kappa\dot{\lambda} \tag{4.83c}$$

$$\dot{\varepsilon}_{ij}^p = \dot{\lambda}\frac{\partial \phi}{\partial \sigma_{ij}}. \tag{4.83d}$$

With these, the consistency condition in Eq. (4.82) becomes

$$\frac{\partial f}{\partial \sigma_{ij}}C_{ijkl}\left(\dot{\varepsilon}_{kl} - \dot{\lambda}\frac{\partial \phi}{\partial \sigma_{kl}}\right) + \frac{\partial f}{\partial \alpha_{ij}}H_{ij}^\alpha\dot{\lambda} + \frac{\partial f}{\partial \kappa}h_\kappa\dot{\lambda} = 0. \tag{4.84}$$

From which it follows that

$$\dot{\lambda} = \frac{1}{\chi} \frac{\partial f}{\partial \sigma_{ij}} C_{ijkl} \dot{\varepsilon}_{kl} , \qquad (4.85)$$

where

$$\chi = \frac{\partial f}{\partial \sigma_{ij}} C_{ijkl} \frac{\partial \phi}{\partial \sigma_{kl}} - \frac{\partial f}{\partial \alpha_{ij}} H^{\alpha}_{ij} - \frac{\partial f}{\partial \kappa} h_{\kappa} . \qquad (4.86)$$

Formal equivalence with oblique return algorithms. With the plastic parameter determined from Eq. (4.85), the stress rate may be written

$$\dot{\sigma}_{ij} = \dot{\sigma}^{E}_{ij} - \frac{A_{ij} B_{kl} \dot{\sigma}^{E}_{kl}}{\chi} , \qquad (4.87)$$

where

$$\dot{\sigma}^{E}_{ij} = C_{ijkl} \dot{\varepsilon}_{kl} \qquad \text{(trial elastic stress rate)} \qquad (4.88)$$

$$A_{ij} = C_{ijrs} \frac{\partial \phi}{\partial \sigma_{rs}} \text{ and } B_{kl} = \frac{\partial f}{\partial \sigma_{mn}} . \qquad (4.89)$$

In Kayenta, the stress state is updated through *direct* integration of Kayenta plasticity equations. However, for our upcoming discussion of rate dependence, it is important to understand that the update formula in Eq. (4.87) implies that the stress may be alternatively integrated through time by first computing a trial elastic stress σ^{E}_{ij} at the end of the timestep which may be projected back to the yield surface (which itself has been updated to the end of the step) to determine the final stress. If the trial elastic stress falls outside the yield surface, plastic flow must have occurred during at least part of the solution interval. Therefore, after evolving the internal state variables appropriately to update the yield surface to the end of the step, it can be shown that Eq. (4.87) implies that the stress at the end of the step may be found by obliquely projecting the trial elastic stress back onto the updated yield surface. Because $\underset{\sim}{A}$ is not generally proportional to $\underset{\sim}{B}$, the projection is oblique to the yield surface even if plastic normality is used. As explained in Chapter 6, the trial stress is projected only *partly* back to the yield surface whenever rate sensitivity is applied.

Quasistatic inelastic tangent stiffness tensor. For any constitutive model, the inelastic tangent stiffness T_{ijkl} is a fourth-order tensor formally equal to the derivative of the stress rate with respect to the total strain rate. That is,

$$\dot{\sigma}_{ij} = T_{ijkl} \dot{\varepsilon}_{kl} . \qquad (4.90)$$

Therefore, comparing this equation with Eqs. (4.87) and (4.89), Kayenta's tangent stiffness is given by

$$T_{ijkl} = C_{ijkl} - \frac{1}{\chi} P_{ij} Q_{kl}$$ quasistatic tangent modulus

where $P_{ij} = C_{ijrs} \frac{\partial \phi}{\partial \sigma_{rs}}$, $Q_{kl} = \frac{\partial f}{\partial \sigma_{mn}} C_{mnkl}$, and $\chi = \frac{\partial f}{\partial \sigma_{ij}} C_{ijkl} \frac{\partial \phi}{\partial \sigma_{ij}} - \frac{\partial f}{\partial \alpha_{ij}} H G^{\alpha} \frac{\partial \phi}{\partial \sigma_{ij}} - \frac{\partial f}{\partial \kappa} h_{\kappa}$. (4.91)

The tangent stiffness is major symmetric ($T_{ijkl} = T_{klij}$) only for associative models ($f = \phi$).*

Stability issues. The last term in Eq. (4.91) is *subtracted* from the positive-definite elastic stiffness C_{ijkl}, so inelastic flow can potentially make the inelastic tangent stiffness tensor T_{ijkl} non-invertible. In other words, the tangent stiffness tensor might eventually have a zero eigenvalue, marking the onset of softening (yield surface contraction). Whether or not the occurrence of a zero tangent stiffness results in stress-strain softening (i.e., a change from a positive to negative slope in a stress-strain plot) depends on the loading direction. For example, if the strain rate is orthogonal to the null space of a non-invertible tangent stiffness tensor, then no stress-strain softening will be observed and no change in type of the momentum equation will occur even if the yield surface is contracting.

A standing wave (i.e., a non-moving discontinuity in displacement or velocity) is another form of material instability that has been extensively studied in the literature. The acoustic wave speeds (i.e., the speed at which inelastic perturbations can propagate through a material in the direction of a given unit vector $\underline{n}$) are given by $c = \sqrt{x/\rho}$, where x denotes the eigenvalues of the second-order acoustic tensor,

$$a_{jk} = n_i T_{ijkl} n_l \tag{4.92}$$

Thus, for Kayenta, substituting Eq. (4.91) into (4.92),

$$a_{jk} = a_{jk}^e - \frac{1}{\chi} p_j q_k, \tag{4.93}$$

where

$$a_{jk}^e = n_i C_{ijkl} n_l = \text{the } \textit{elastic} \text{ acoustic tensor} \tag{4.94}$$

and

$$p_j = n_i C_{ijrs} \frac{\partial \phi}{\partial \sigma_{rs}} \quad \text{and} \quad q_k = \frac{\partial f}{\partial \sigma_{mn}} C_{mnkl} n_l. \tag{4.95}$$

If the plastic tangent stiffness T_{ijkl} is not major symmetric, then the acoustic tensor will not be symmetric. In this case, not only are standing waves ($x = 0$) possible, but so are imaginary wave speeds (flutter instability). A complete spectral analysis of acoustic tensors of the form in Eq. (4.93) is provided in Ref. [11], where every possible ordering of the inelastic wave speeds relative to elastic wave speeds is derived and where every possible

---

* Actually, equivalence of associativity and normality holds only in the absence of elastic-plastic coupling. When elastic moduli can change in response to plastic loading, an associative ($f = \phi$) model will *not* exhibit normality and will *not* have a major-symmetric tangent stiffness [23].

acoustic eigenvector is presented. Physically, the eigenvector characterizes the velocity jump direction. If the eigenvector is parallel to the wave propagation direction $\underset{\sim}{n}$, then the wave is a compression wave. If the eigenvector is perpendicular to $\underset{\sim}{n}$, the wave is a shear wave. For elastic materials, these are the only two possible kinds of waves, but for inelastic tangent tensors of the form (4.91), other modes are possible.

For rate dependent materials, the question of material stability must be examined anew because, as explained in the next section, the *dynamic* tangent stiffness tensor is generally *stiffer* than the quasistatic tangent stiffness.

5. Softening

In Kayenta, softening refers to a progressive loss of strength and stiffness. Support for softening is a relatively new addition to Kayenta that is still under development. The governing equations are under refinement as new data, associated improved theories, and enhanced computational solvers become available. Therefore, since the research is in flux, this section will describe only the qualitative features of the softening model along with information (such as keywords) needed by users to activate and interpret the beta softening model.
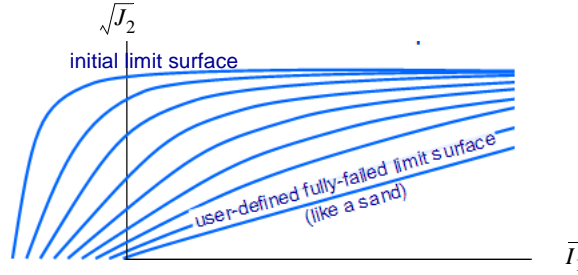
Figure 5.1.   Damage regarded as progressive limit surface collapse.

The limit surface in Fig. 1.1 on page 6 is treated as stationary prior to the onset of softning. As is commonly done in other engineering damage models [16], Kayenta supports softening by allowing the limit surface to collapse as sketched in Fig. 5.1. To initiate softening, the stress state must reach the limit surface. Thereafter, because the limit surface collapses, the stress state cannot reach the same peak state ever again.* Once a state on the limit surface has been reached, the material undergoes irreversible damage, thus degrading its load carrying capacity. The fully failed material loses essentially all resistance to loading in tension, but it retains as much strength in compression as is specified by the user. If the user specifies no fully failed limit strength parameters, Kayenta defaults to a limit surface that is typical of sand.

Strength and stiffness degradation in softening

The initial and fully failed limit surfaces are described through user specification of the four parameters labeled in Fig. 5.2.[†] Those slope and intercept parameters are specified via input keywords ending in "I" for the initial limit surface and ending in "F" for the final surface. The dynamically collapsing limit surface is an interpolation between the initial and final surfaces such that

$$\text{FSLOPE} = (1\text{-}D)*(\text{FSLOPEI}) + D*(\text{FSLOPEF}) \tag{5.1}$$
$$\text{PEAKI1} = (1\text{-}D)*(\text{PEAKI1I}) + D*(\text{PEAKI1F}) \tag{5.2}$$
$$\text{STREN} = (1\text{-}D)*(\text{STRENI}) + D*(\text{STRENF}) \tag{5.3}$$
$$\text{YSLOPE} = (1\text{-}D)*(\text{YSLOPEI}) + D*(\text{YSLOPEF}) \tag{5.4}$$

---

* The framework can be modified if, in the future, material healing (i.e., recovery of strength following damage) is desired. However, the current implementation does not support healing.

† which are internally converted to the four "a" parameters in Eq. (4.39).

Here, "*D*" is an interpolation parameter called "damage." Initially, $D=0$, and D goes to 1 as softening progresses. Rather than having any physical significance *per se*, the damage *D* is merely an interpolation parameter. Ties to microphysical processes lie in the evolution equations for *D*, which are under development. Internally, the code uses a "coherence" parameter called **COHER**, which is merely 1-*D*.
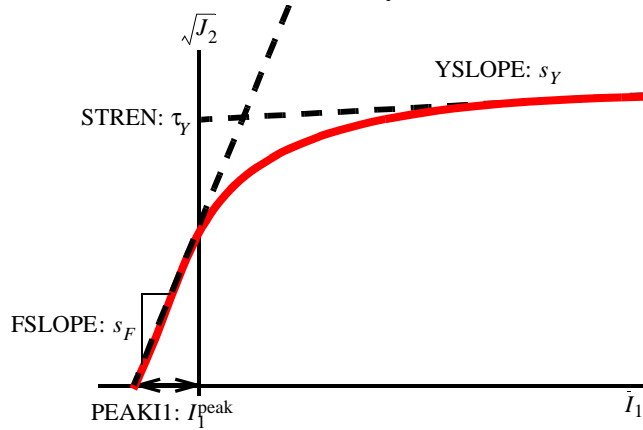
Figure 5.2.   Alternative parameterization of the limit curve.

Ideally, the evolution of *D* should be determined from sound physical arguments and direct fitting to observed softening data. In practice, however, the evolution of damage is ad hoc in most damage models, including Kayenta. Since physically derived damage progression equations appear to be an open research question, Kayenta currently supports a time-based damage evolution function that is inspired by the observation that crack growth speed appears to be relatively insensitive to loading rate. If crack growth speed is regarded as constant, a finite amount of time must pass before a crack finishes propagating across a finite element domain. This time delay, t^{fail}, is treated within Kayenta as a material parameter, which means that the host code must apply appropriate scaling of this parameter based on the mesh size. Once the stress state has reached the initial limit surface, an internal variable called **TGROW** is incremented such that it equals the amount of time that the stress state has been at the limit surface.
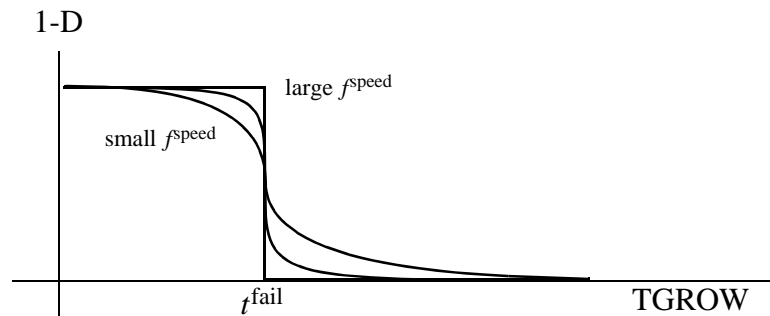
Figure 5.3.   Ad hoc time-based damage evolution.

Once the initial limit surface has been reached, the limit surface then begins to collapse. As illustrated in Fig. 5.3, the rate of collapse is controlled by the user through parameters f^{speed} and t^{fail}. Loosely speaking, the parameter t^{fail} specifies the amount of time that must pass with the stress state at the limit surface before the limit surface collapses. This parameter plays a role similar to the "plastic strain to failure" used by other models such as the Johnson-Holmquist models, JH1 and JH2 [33]. By using a "time to failure" parameter t^{fail}, the Kayenta damage model has the property that apparent strain to failure will increase with strain rate. The "failure speed" parameter f^{speed} is provided merely to allow softening to proceed quickly when f^{speed} is large (>30) or more gradually when f^{speed} is small (<5). This parameter therefore allows Kayenta's softening to emulate either the JH1 or JH2 models and other similar models. As illustrated in Fig. 5.4, the time delay t^{fail} is analogous to the plastic-strain-to-failure used in other dynamic damage models such as the Johnson-Holmquist model [33]. However, by using a fixed time delay, both plastic-strain-to-failure and energy of failure automatically increase with increased loading rate.
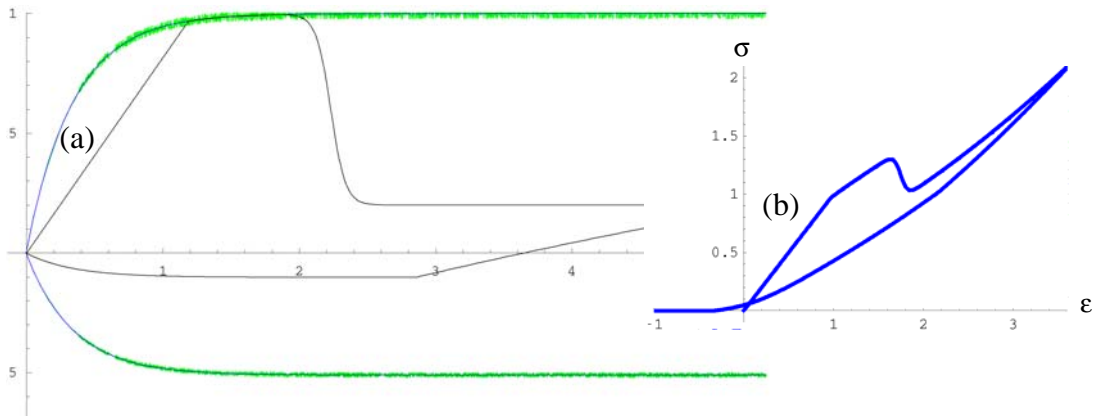
Figure 5.4.   Demonstration that a time-to-failure criterion leads to apparent plastic-strain-to-failure.   For this test case, the failed limit surface was specified to mimic the failed surface in the Johnson-Holmquist ceramic model [33]. *Shown are (a) path through stress space and (b) stress-strain response for uniaxial strain loading, each illustrating an apparent plastic strain to failure with this time-to-failure model.*

In addition to losing limit strength, a softening material also loses elastic stiffness. At present, the Kayenta model presumes that the stiffness remains isotropic as damage proceeds. Future plans include support for orthotropic degradation of the elastic moduli. In the current isotropic elastic damage framework, the elastic moduli are degraded using the *isotropic* part of the damaged compliance proposed by Dienes *et al.* [19]. Dienes's damaged compliance is expressed in terms of an overall measure of crack size. As mentioned earlier in the context of limit surface collapse, we contend that the rate of limit surface collapse is also tied to crack growth speed. Therefore, Dienes compliance reduction formulas are accordingly converted to functions of the damage parameter *D*. Details of the damage evolution equations will not be further discussed here because more careful analysis, extension, and validation are clearly needed.

Implementation requirements for softening

It is well known that softening induces a change in type of the governing equations. An initially quasistatic problem becomes hyperbolic, perhaps marking the onset of localized failure and unstable structural collapse. An initially dynamic problem loses hyperbolicity, marking the onset of localized failure and also resulting in damage waves that propagate slower than shock waves. Without intervention from the host code, the change in type of the governing equations in a local constitutive model will result in non-physical dependency of the solution on the mesh resolution. One means of reducing this problem is to introduce spatial perturbations and scale effects in the strength of the material that are consistent with the following laboratory observations:

- large variability in strength in low-pressure experiments
- a tendency for small specimens to have higher ultimate strength than large specimens
- reduced variability and scale effects at high pressure

These qualitative observations suggest that the deterministic limit surface should be perturbed as illustrated in Fig. 5.5, where all uncertainty and scale effects have been imposed in the I_1^{peak} limit surface parameter.
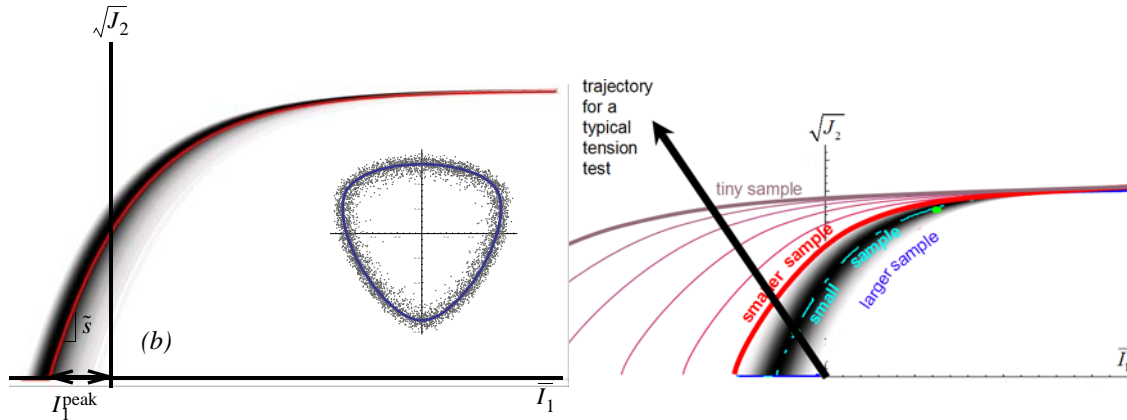
Figure 5.5.   Incorporation of uncertainty and scale effects in damage.   This figure depicts the character of uncertainty and scale effects expected for a quasibrittle material such as rock. (a) Significantly variability is imposed at low pressure by statistically varying the I_1^{peak} parameter. (b) corresponding scale effects ensure that small specimens are stronger, on average, than large specimens.

At time zero, before calculations begin, a random number R is generated at each finite element in the simulation. This random number is converted into a scale-dependent Weibull-perturbed realization for I_1^{peak} at each element by

$$I_1^{\text{peak}} = \overline{I_1^{\text{peak}}} \left[\frac{\overline{V} \ln R}{V \ln (1/2)} \right]^{1/m} \tag{5.5}$$

72

where $\overline{I_1^{\text{peak}}}$ is the median value of the tensile spherical strength measured (or presumed to be measured) at a known specimen volume $\overline{V}$, and m is the "Weibull modulus" that quantifies the extent of variability. The volume V is the finite element volume to account for scale effects. Note: since this variability is imposed on the *spherical* tensile I_1^{peak}, it produces a non-Weibull scale dependence in *axial* tensile strength as illustrated in Fig. 5.5(b) and Fig. 5.6(b). This non-Weibull character of scale dependence of strength is well known [5].
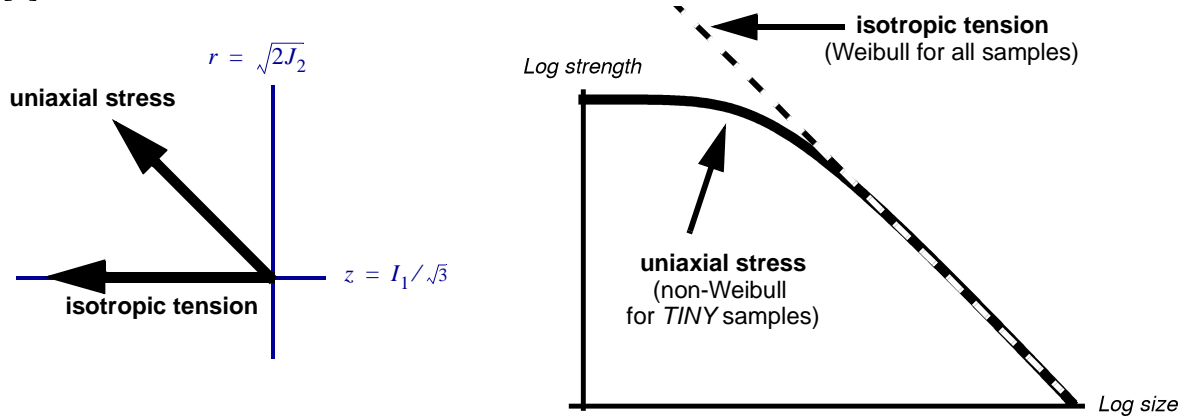
Figure 5.6.   The strength size effect in "directed-Weibull" theory varies with stress space trajectory. Whereas strength can increase with bound for small samples in isotropic tension, it saturates to a classical plasticity limit for non-hydrostatic loading of tiny samples (relative to aggregate size).

Some applications of the damage model with statistical uncertainty and scale effects are illustrated in Figs. 5.7 and 5.8. Although incorporation of uncertainty and scale effects does reduce mesh sensitivity in some cases, one must be warned that it does not eliminate mesh sensitivity altogether. The Brazilian simulations, in particular continue to suffer from an unacceptable level of mesh sensitivity. Even though their predictions of trends in the statistics of failure are very similar to laboratory observations, the quantitative median strength continues to be mesh dependent and therefore non-predictive.
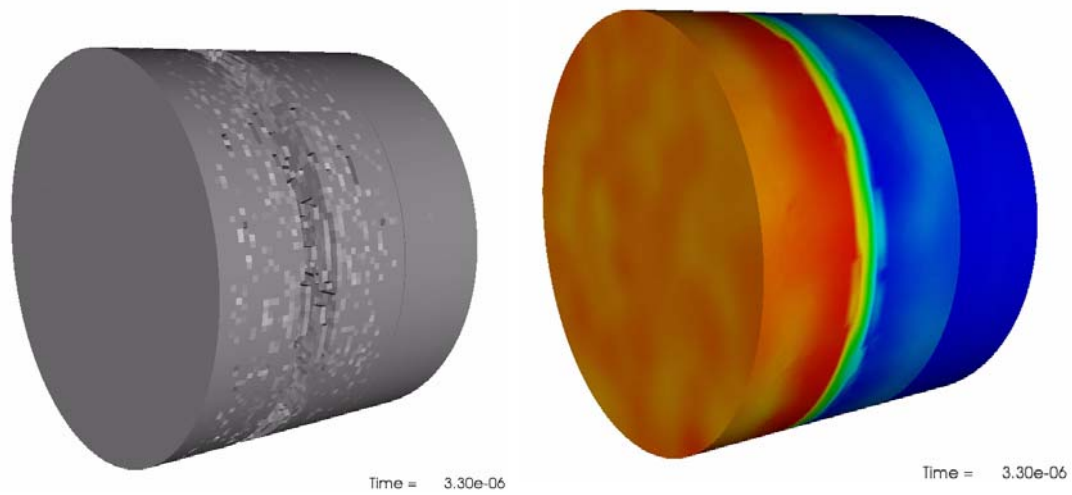
Figure 5.7.   Spall with strength variability and scale effects. The left plot shows intact material. The right plot shows material velocity with clear variability.
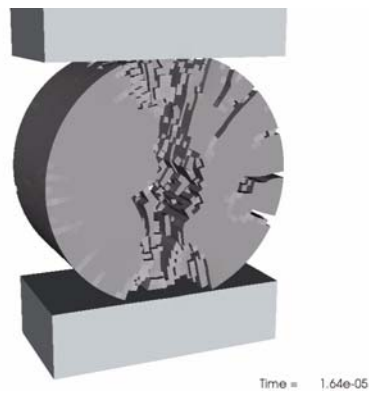
Figure 5.8.   Brazilian simulation with variability and scale effects.

Further verification and validation of this approach to softening may be found on page 111.

6. Rate Dependence

The governing equations discussed so far are rate independent, so they only apply for quasistatic loading. Under high strain rates, the elastic response of a material occurs almost instantaneously, but the physical mechanisms that give rise to observable inelasticity can *not* proceed instantaneously. Materials have inherent "viscosity" or "internal resistance" that retards the rate at which damage can accumulate. For example, cracks grow at a finite speed — they cannot change instantaneously from one size to another. If a stress level is high enough to induce crack growth, then the quasistatic solution for material damage will not be realized unless sufficient time elapses to permit the cracks to change length. Likewise, void collapse takes finite time. Simple inertia also contributes to rate dependence. During the time that cracks are growing towards the quasistatic solution, the stress will drop down toward the quasistatic solution. Until sufficient time has elapsed for the material to equilibrate, the stress state will lie *outside* the yield surface. If the applied strain is released any time during this damage accumulation period, then the total damage will be ultimately lower than it would have been under quasistatic loading through the same strain path.

Viscoplasticity model overview

The evolution of the yield function, and the very character of the inelastic deformation itself, can be dramatically altered by the rate at which loads are applied. In the limit of extraordinarily high load rates (as near the source of an explosion), material response is essentially elastic because insufficient time exists for plasticity to fully develop. At high strain rates, the equation of state (i.e., the pressure-volume part of the elasticity) plays the predominant role in material response. To allow for rate dependence, an overstress model is used. The user specifies a "relaxation" parameter governing the characteristic speed at which the material can respond inelastically. If the loads are applied over a time interval that is significantly smaller than the characteristic response time, then essentially no inelasticity will occur during that interval. If, on the other hand, the loads are applied slowly (as in quasistatic testing), then inelasticity will be evident.

Kayenta uses a generalized Duvaut-Lions [20] rate-sensitive formulation, illustrated qualitatively in Fig. 6.1. Consider a loading increment Δt during which the strain increment is prescribed to be $\Delta \underset{\sim}{\varepsilon}$. Two limiting solutions for the updated stress can be readily computed: (1) the low-rate (quasistatic) solution $\underset{\sim}{\sigma}^L$ which is found by solving the rate-independent Kayenta equations described previously, and (2) the high-rate solution $\underset{\sim}{\sigma}^H$ corresponding to insufficient time for any plastic damage to develop so that it is simply the trial elastic stress. As explained below and illustrated in Fig. 6.1, the Duvaut-Lions rate formulation is based on a viscoplastic differential equation, the solution of which

shows that the updated stress will be (approximately) a linear interpolation between the low-rate quasistatic plasticity solution $\underset{\sim}{\sigma}^L$ and the high-rate purely elastic solution $\underset{\sim}{\sigma}^H$. In other words, there exists a scalar η between 0 and 1 that depends on the strain rate such that

$$\underset{\sim}{\sigma} \approx \underset{\sim}{\sigma}^L + \eta(\underset{\sim}{\sigma}^H - \underset{\sim}{\sigma}^L). \tag{6.1}$$
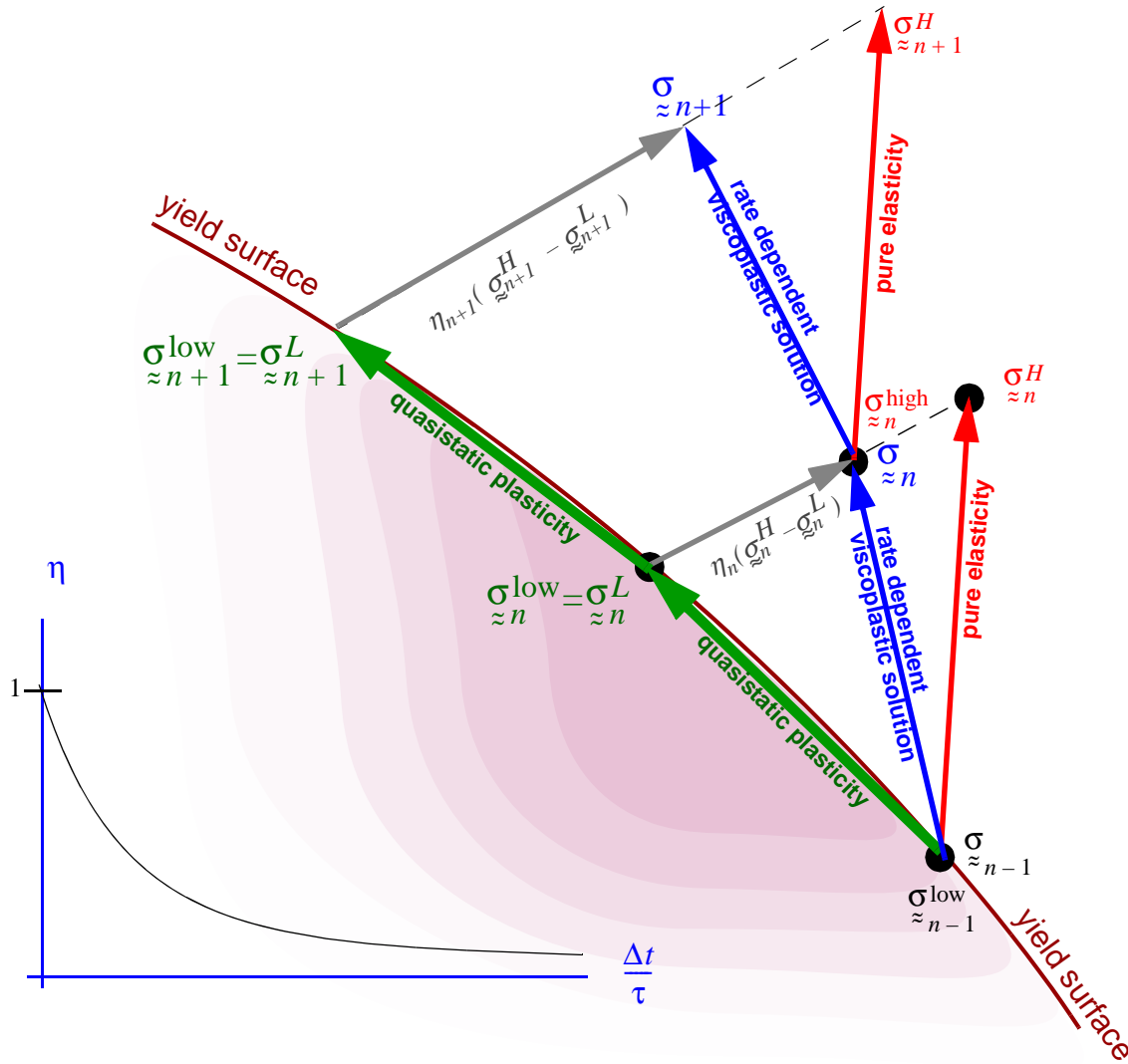
Figure 6.1.   *Rate dependence.*   For a given strain increment, two limiting solutions can be readily found. The "low rate" solution $\underset{\sim}{\sigma}^L$, which lies on the yield surface, is the solution to the rate independent Kayenta governing equations. The high rate solution $\underset{\sim}{\sigma}^H$ is simply the trial elastic stress. The actual updated rate-dependent viscoplastic stress $\underset{\sim}{\sigma}$ falls between these two limiting case solutions so that $\underset{\sim}{\sigma} = \underset{\sim}{\sigma}^L + \eta(\underset{\sim}{\sigma}^H - \underset{\sim}{\sigma}^L)$. The inset graph shows how the scale factor η varies with the loading interval. If the loading interval is long relative to the material's characteristic response time τ, then sufficient time exists to fully develop plastic response and the updated solution therefore coincides with the quasistatic solution $\underset{\sim}{\sigma}^L$. If the loading interval is considerably shorter than the material's characteristic response time, then the solution will be the high-rate elastic solution.

The update for internal state variables is structured similarly, but uses a somewhat different weighting factor, as explained below. For both the stress and internal state variable updates, the interpolation factor η varies from 1 at high strain rates (when Δt is small) to 0 at low strain rates (when Δt is large), as illustrated in the graph inset of Fig. 6.1, where the abscissa is normalized by a factor τ called the material's "characteristic" response time. At the end of this chapter, we will describe how Kayenta assigns a value for the characteristic material response time τ. Incidentally, for simplicity, Fig. 6.1 shows a stationary yield surface. In general, the yield surface will evolve in size or translate according to the hardening rules described earlier.

A time interval Δt is deemed to be "long" if $\Delta t \gg \tau$. A time interval is "short" if $\Delta t \ll \tau$. Soon we solve the viscoplastic equations to prove that, if the initial stress is on the yield surface, then the high-rate scale factor internal state variable (ISV) is

$$\eta = \frac{1 - e^{-\Delta t/\tau}}{\Delta t/\tau}. \tag{6.2}$$

This is also the rate factor for the stress *at the onset of yielding* when $\underset{\sim}{\sigma}$ and $\underset{\sim}{\sigma}^{low}$ coincide. At the end of a viscoplastic step, the final stress state will *not* lie on the yield surface. We will prove that, in this case, the scale factor is smaller than the value cited in Eq. (6.2). Consequently, the "attraction" that the dynamic stress has for the quasistatic solution increases somewhat as the stress moves farther from the yield surface.

Referring to Fig. 6.2, the η weighting factor is large when the time step is significantly smaller than the characteristic time required for the material's plasticity solution to develop. Effects of plasticity are apparent in Kayenta only when the time interval is long or when the characteristic material response time is short so that η will be small. In this case, according to Eq. (6.1), the solution will be near the quasistatic (low-rate) solution $\underset{\sim}{\sigma}^{L}$.

Figure 6.1 illustrates that the viscoplastic solution will follow a trajectory that is similar to the quasistatic solution except displaced from the yield surface. Consequently, experimental data for high-rate loading scenarios have the *appearance* of inducing a higher yield stress in the material. Unlike some plasticity models, Kayenta does *not* alter the material yield stress as a function of strain rate. Instead, the overstress model accomplishes the same effect in a much more physically justifiable manner.

Viscoplasticity model derivation

In the context of viscoplasticity, an inviscid (rate-independent) solution $\underset{\approx}{\sigma}^L$ for the stress is presumed to exist. Likewise inviscid (rate-independent) solutions q^L are presumed available for the internal state variables, here denoted collectively by "q". These limiting case solutions are merely the solutions of the rate-independent Kayenta equations described in earlier chapters. Viscous effects are incorporated by presuming that the strain rate is decomposed as the sum of an elastic part $\underset{\approx}{\dot{\varepsilon}}^e$ plus a *viscoplastic* part $\underset{\approx}{\dot{\varepsilon}}^{vp}$:

$$\underset{\approx}{\dot{\varepsilon}} = \underset{\approx}{\dot{\varepsilon}}^e + \underset{\approx}{\dot{\varepsilon}}^{vp}. \tag{6.3}$$

The viscoplastic part of the strain rate includes both the usual plastic strain rate from the quasistatic (low-rate) solution as well as additional (retarding) contributions resulting from viscosity. The viscoplastic strain rate is governed by

$$\dot{\varepsilon}_{ij}^{vp} = \frac{1}{\tau}C_{ijkl}^{-1}[\sigma_{kl} - \sigma_{kl}^{\text{low}}]. \tag{6.4}$$

The fourth-order tensor C_{ijkl}^{-1} is the elastic compliance (inverse of the stiffness), τ is a material parameter called the relaxation time, and $\underset{\approx}{\sigma}^{\text{low}}$ is the rate-independent stress solution whose value at the beginning of a time increment Δt is tracked as an extra state variable (called **QSSIGXX**, **QSSIGYY**, etc. in Appendix B).[*] At the end of the time interval, $\underset{\approx}{\sigma}^{\text{low}}$ ultimately has the value $\underset{\approx}{\sigma}^L$, which is found by integrating the rate-independent Kayenta equations from the earlier chapters. During viscoplastic loading, each internal state variable q is presumed to vary according to

$$\dot{q} = \frac{-1}{\tau}[q - q^{\text{low}}]. \tag{6.5}$$

Here q^{low} is the value of the internal state variable (κ or $\underset{\approx}{\alpha}$) throughout the time interval, initially being equal to q_0 at the beginning of the step, and (through application of Kayenta's rate-independent equations in earlier chapters) ultimately equalling the low rate solution q_L at the end of the step. Like the inviscid quasistatic stress, the inviscid quasistatic ISVs (**QSEL**, **QSBSXX**, etc.) must be tracked as distinct extra state variables.

The stress rate is, as usual, given by the elastic stiffness acting on the elastic part of the strain rate: $\dot{\sigma}_{ij} = C_{ijkl}\dot{\varepsilon}_{kl}^e$. Thus, using Eq. (6.3), the stress rate may be written

$$\dot{\sigma}_{ij} = \dot{\sigma}_{ij}^{\text{high}} - \frac{1}{\tau}(\sigma_{ij} - \sigma_{ij}^{\text{low}}), \qquad \text{where} \quad \dot{\sigma}_{ij}^{\text{high}} \equiv C_{ijkl}\dot{\varepsilon}_{kl}. \tag{6.6}$$

Here, $\dot{\sigma}_{ij}^{\text{high}}$ is the elastic trial stress rate, and therefore $\sigma_{ij}^{\text{high}}$ is the time varying elastic trial stress that ultimately equals the high-rate solution σ_{ij}^H at the end of the step.

---

[*] The "low" or "inviscid" stresses must be tracked independently. They cannot be inferred by projecting the actual stress onto the yield surface. Attempting to do so causes undesirable results in rate-dependent load-unload cycles.

Eq. (6.6) is a set of linear first-order differential equations which may be integrated exactly over a time step with the use of integrating factors [27] *provided that σ_{ij}^{low} is known as a function of time throughout the time step.* In principle, we would need to solve the rate independent equations *analytically* over the entire time step to integrate Eq. (6.6) exactly, but this is not tractable in practice. In what follows, we will describe how the time history of σ_{ij}^{low} can instead be well approximated over the step. First, let's introduce a change of variables by defining

$$u_{ij} \equiv \sigma_{ij} - \sigma_{ij}^{\text{high}}, \tag{6.7}$$

so that the governing equation for the stress rate may be written

$$\dot{u}_{ij} = -\frac{1}{\tau}(u_{ij} + \sigma_{ij}^{\text{high}} - \sigma_{ij}^{\text{low}}). \tag{6.8}$$

This equation can be solved exactly if the time variation of $\underset{\sim}{\sigma}^{\text{high}} - \underset{\sim}{\sigma}^{\text{low}}$ is known throughout the time step. Time variation of $\underset{\sim}{\sigma}^{\text{low}}$ is governed by known quasistatic rate equations. Consequently, the dynamic accuracy can be maximized by presuming that the *rate* of $\underset{\sim}{\sigma}^{\text{low}}$ is constant over the step so that $\underset{\sim}{\sigma}^{\text{low}}$ itself is approximated to vary linearly over the step.

Recall that the final solution $\underset{\sim}{\sigma}^{H} - \underset{\sim}{\sigma}^{L}$ can be presumed known at the end of the step because $\underset{\sim}{\sigma}^{H}$ is found by integrating the elasticity equations and $\underset{\sim}{\sigma}^{L}$ is found separately by integrating the inviscid quasistatic plasticity equations. Similarly, the difference $\underset{\sim}{\sigma}_{0}^{\text{high}} - \underset{\sim}{\sigma}_{0}^{\text{low}}$ is known at the beginning of the step because $\underset{\sim}{\sigma}_{0}^{\text{high}}$ is $\underset{\sim}{\sigma}$ at the beginning of the step and $\underset{\sim}{\sigma}_{0}^{\text{low}}$ is retrieved from the saved quasistatic stress extra state variable array. The high-rate stress $\underset{\sim}{\sigma}^{\text{high}}$ is simply the elastic trial stress. Thus, it varies linearly through time from its initial to final value (with small higher-order nonlinearities if the strain rate and/or elastic moduli are not constant). The quasistatic stress rate $\dot{\underset{\sim}{\sigma}}^{\text{low}}$ is an oblique projection of the trial stress rate onto the yield surface, so $\underset{\sim}{\sigma}^{\text{low}}$ also varies approximately linearly through time (with nonlinear effects from flow potential surface curvature being higher order). Thus, we may call on the mean value theorem to assert that

$$(\underset{\sim}{\sigma}^{\text{high}} - \underset{\sim}{\sigma}^{\text{low}}) \approx (\underset{\sim}{\sigma}^{H} - \underset{\sim}{\sigma}^{L})\left(\frac{t - t_0}{\Delta t}\right) + (\underset{\sim}{\sigma}_0^{\text{high}} - \underset{\sim}{\sigma}_0^{\text{low}})\left(1 - \frac{t - t_0}{\Delta t}\right). \tag{6.9}$$

With this approximation, the ODE in Eq. (6.8) may be solved exactly. Since $\underset{\sim}{\sigma}_0^{\text{high}}$ equals $\underset{\sim}{\sigma}_0$ at the beginning of the step, the initial condition is that $u_{ij} = 0$ when $t = t_0$. Integrating the ODE, evaluating the result at the end of the step, and applying the definition of u_{ij} to obtain the updated solution for σ_{ij} eventually gives

$$\boxed{\underset{\sim}{\sigma}^{\text{FINAL}} = \underset{\sim}{\sigma}^{L} + R_H(\underset{\sim}{\sigma}^{H} - \underset{\sim}{\sigma}^{L}) + r_h(\underset{\sim}{\sigma}_0^{\text{high}} - \underset{\sim}{\sigma}_0^{\text{low}})}, \tag{6.10}$$

where

$$R_H = \frac{1 - e^{-\Delta t/\tau}}{\Delta t/\tau} \qquad \text{and} \qquad r_h = e^{-\Delta t/\tau} - R_H. \tag{6.11}$$

79

With the presence of the last term, the solution in Eq. (6.10) is not *precisely* of the form shown in Eq. (6.1) unless $\sigma_{\approx 0}^{high} = \sigma_{\approx 0}^{low}$. As seen in timestep "n-1" in Fig. 6.1, the initial values for the "high" and "low" rate paths coincide only at the *onset* of plasticity. Eq. (6.10) can be put into the form of Eq. (6.1) if we approximate that $\sigma_{\approx 0}^{high} - \sigma_{\approx 0}^{low}$ is *parallel* to $\sigma_{\approx}^{H} - \sigma_{\approx}^{L}$. With this assumption, Eq. (6.1) becomes

$$\sigma_{\approx}^{FINAL} = \sigma_{\approx}^{L} + \eta(\sigma_{\approx}^{H} - \sigma_{\approx}^{L}), \qquad (6.12)$$

where

$$\eta = R_H + r_h \Upsilon \qquad (6.13)$$

and

$$\Upsilon \equiv \frac{\left\| \sigma_{\approx 0}^{high} - \sigma_{\approx 0}^{low} \right\|}{\left\| \sigma_{\approx}^{H} - \sigma_{\approx}^{L} \right\|}. \qquad (6.14)$$

Figure 6.2. *High-rate weighting factor at various initial states.* The largest weight factor (upper red curve) applies when the initial stress is on the yield surface. The factor is lower if the initial state is already off the yield surface at the beginning of the step.

Fig. 6.2 shows how the weighting factor η varies with the stress difference ratio Υ appearing in the last term of Eq. (6.13). For plastic loading, Υ equals 0 only when the initial state is on the yield surface. Otherwise, beyond this onset of yielding moment, Υ increases, eventually asymptoting to 1 under steady strain rates. The lowering of the rate factor η caused by nonzero Υ makes the dynamic stress more strongly attracted to the quasistatic solution as the distance between them increases.

For the rate dependent update of internal state variables, Eq. (6.5) can be integrated analytically if the time variation of q over the step is approximated by $q^{low} = q^H + (q^L - q^H)(t - t_o)/\Delta t$. The resulting solution for q is

$$\boxed{q^{FINAL} = q^L + R_H(q^H - q^L)}, \qquad (6.15)$$

where the high-rate weight factor R_H is the same as in Eq. (6.11). The weight factor R_H for the internal state variables differs from the weight factor η for the stress because the two problems have different initial conditions. Recall that the material responds elastically at extremely high rates. Hence, because the internal state variables can evolve only when plasticity occurs, the high rate solution q^H for any internal state variables is simply its value at the beginning of the time increment.

Limiting case. If a strain rate is held constant for a long enough period then the difference between the dynamic stress σ_{ij} and the inviscid stress σ_{ij}^L will sometimes reach a steady-state value in the laboratory. In this case, the equations outlined in this chapter imply that this steady state stress difference is given by

$$\sigma_{ij} - \sigma_{ij}^L = \frac{\tau}{\chi} P_{ij} Q_{mn} \dot{\varepsilon}_{mn} \qquad (6.16)$$

where χ, P_{ij}, and Q_{ij} are defined in Eq. (4.91).

In the very simplified context of non-hardening Von-Mises plasticity, this equation becomes

$$\sigma_{ij} - \sigma_{ij}^L = (2G\tau)\hat{S}_{ij}\hat{S}_{mn}\dot{\varepsilon}_{mn} \qquad (6.17)$$

where G is the shear modulus and $\hat{S}_{ij}$ is a unit tensor in the direction of the stress deviator. For example,

$$[\hat{S}] = \frac{1}{\sqrt{2}}\begin{bmatrix} 0 & 1 & 0 \\ 1 & 0 & 0 \\ 0 & 0 & 0 \end{bmatrix} \quad \text{for simple shear} \qquad (6.18)$$

$$[\hat{S}] = \frac{1}{\sqrt{6}}\begin{bmatrix} 2 & 0 & 0 \\ 0 & -1 & 0 \\ 0 & 0 & -1 \end{bmatrix} \quad \text{for uniaxial (axisymmetric) loading} \qquad (6.19)$$

Therefore, in the case of simple shear for non-hardening Von Mises plasticity, Eq. (6.17) implies that

$$\sigma_{12} - \sigma_{12}^L = 2G\tau\dot{\varepsilon}_{12} \qquad \text{for simple shear} \qquad (6.20)$$

$$\sigma_{11} - \sigma_{11}^L = \frac{4G}{3}\tau\dot{\varepsilon}_{11} \qquad \text{for uniaxial (axisymmetric) loading} \qquad (6.21)$$

These simple analytical results can be used to trend-test the numerical implementation of rate sensitivity, as described in Fig. 6.3.
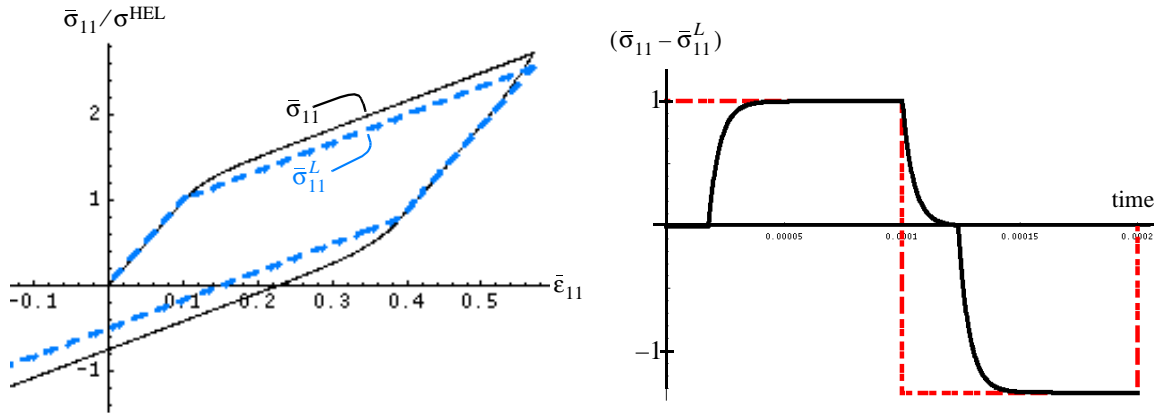
Figure 6.3. *Rate dependence in uniaxial strain loading of a nonhardening pressure-insensitive material.* In the stress-strain plot, the normalizer σ^{HEL} is the quasistatic uniaxial yield stress. The dynamic (black) stress-strain plot exhibits an apparent increase in strength relative to the quasistatic (dashed blue) solution. This rate-induced stress difference is plotted in the second figure (normalized by the peak value), where the dashed red line shows the analytical asymptote envelope from Eq. (6.21). This calculation included a lower strength in tension (interestingly, the *difference* between dynamic and quasistatic strengths is higher in tension).

Assigning a value to the characteristic material time

Kayenta permits the user to control the value of the characteristic time through the use of up to seven parameters, T_1 through T_7. In the pre-2009 builds of Kayenta (called the "GeoModel" at that time), the T-parameters were used to assign a value of the characteristic time according to the following formulas:

$$\tau = \begin{cases} f(\dot{\varepsilon}^{\text{equiv}}) & \text{if} \quad \bar{\varepsilon}_v^p \leq 0 \\ T_6 f(\dot{\varepsilon}^{\text{equiv}})(1 + (<T_7(\bar{I}_1 + T_5)>)^2) & \text{if} \quad \bar{\varepsilon}_v^p > 0 \quad \text{and} \quad \bar{I}_1 \geq -T_5 \end{cases}, \tag{6.22}$$

where

$$f(\dot{\varepsilon}^{\text{equiv}}) = T_1\left(\frac{1}{\tau^{\text{ref}}\dot{\varepsilon}^{\text{equiv}}}\right)^{T_2}, \quad \text{and} \quad \dot{\varepsilon}^{\text{equiv}} = \left\| \dot{\underset{\approx}{\varepsilon}} \right\|, \tag{6.23}$$

$$\text{and} \quad <x> = \begin{cases} 0 & \text{if} \quad x \leq 0 \\ x & \text{if} \quad x > 0 \end{cases} \quad \text{(McCauley brackets)}. \tag{6.24}$$

Here, τ^{ref} is a constant equal to 1.0 s^{-1}. If a *constant* characteristic time τ is desired, then set $T_1 = \tau$, and all other T's to zero. Fig. 6.3 used a constant τ, as did the simple-shear rate-dependent simulation shown in Fig. 8.9*(b)* on page 107. Suitability of this model of rate-dependence for predicting laboratory data is illustrated in Fig. 9.9 on page 120.

Kayenta is currently undergoing revisions of its rate dependence model to permit user-specification of laboratory data for the apparent steady-state strength as a function strain rate, which is what is typically available in the literature [*cf.* 57]. These revisions will lead to new interpretations of the T-parameters. Therefore, users of 2009 and later builds of Kayenta should consult with the model developers for assigning rate dependence parameter values.

Thermodynamics considerations

In pre-2009 builds, Kayenta's equation of state was incorporated within the purely mechanical model — it contained no thermal terms (i.e., terms involving material properties such as the specific heat and Grüneisen parameter). Nonetheless, Kayenta's nonlinear elasticity model had been moderately well fitted to Hugoniot shock data. In thermodynamics, pressure is typically expressed as a function of two variables: the density ρ and a thermal variable (usually temperature or entropy). For example,

$$p = f(\rho, T).\tag{6.25}$$

In thermodynamics, you can always use a purely mechanical equation of state if you restrict the class of allowable problems so that one or two of the thermal variables are inter-related in some known way. If, for example, you restrict attention to isothermal loading, then the pressure will be expressible in the form $p = F(\rho)$, where the "material constants" in the equation (such as the bulk modulus) must be set to their isothermal values. Likewise, if you can consider only adiabatic loading, then the pressure is again expressible as a mechanical function if the parameters such as the bulk modulus are set to their adiabatic values.

Through the above rather hand-waving reasoning, the pre-2009 builds of Kayenta (called the Sandia GeoModel) were able to perform adequately under high rate shock loading. Recent work, to be summarized in subsequent updates to this manual, has included incorporation of any user-specified equation of state. This work has included verification that Kayenta can (with appropriately matched parameters) reproduce the high-rate thermoelastic-plastic material response predicted using the Johnson-Cook plasticity model in conjunction with a Mie-Grüneisen equation of state.

7. Kayenta Numerical Solution scheme

Aside from kinematic hardening and limited elastic anisotropy from joints, Kayenta is isotropic and therefore the yield function depends only on principal stresses. An eigenvalue analysis is avoided by casting the yield function in terms of stress invariants. The principal stress directions (eigenvectors) are not needed to evaluate the yield function. For any isotropic elasticity model, however, evolution of plastic response must allow for rotation of principal stress directions caused by the elastic portion of the loading. Thus, the governing equations must be cast in incremental tensorial form, requiring all six independent components of symmetric tensors to be passed to the model. Careful numerical integration schemes [8] are required to ensure accuracy and convergence.

This chapter begins with a description of how Kayenta is to be used within a host (finite-element) code, followed by a discussion of the influence of material softening on *field-scale* stability (i.e., stability of the spatial finite-element solution, not stability of Kayenta's internal time integration algorithm). Next, Kayenta installation instructions are provided that describe the public[*] subroutines and memory requirements. Following a summary of plotable Kayenta output, Kayenta's time integration algorithm is briefly summarized.

Role of Kayenta within a finite-element program

Kayenta is designed for use in host codes (typically finite-element programs) that solve the momentum balance PDE,

$$\frac{\partial \sigma_{ik}}{\partial x_k} + f_i = \rho a_i, \tag{7.1}$$

where σ_{ik} is the *spatial* Cauchy stress tensor (denoted $\underset{\approx}{\sigma}^{\text{spatial}}$ in Eq. 3.39), x_k is the spatial position vector, f_i is the body force per unit volume, ρ is the mass density, and a_i is the material acceleration that is related to the spatial velocity field v_i by material time derivative

$$a_i = \frac{\partial v_i}{\partial t} + \frac{\partial v_i}{\partial x_k} v_k = \frac{Dv_i}{Dt} = \left(\frac{\partial v_i}{\partial t} \right)_{\underset{\sim}{X}} \tag{7.2}$$

---

[*] i.e., called directly from the host code.

Here, $\underset{\sim}{X}$ is the time-zero reference position vector, which serves to identify Lagrangean material points. The spatial position vector $\underset{\sim}{x}$ is related to the reference position $\underset{\sim}{X}$ through the deformation mapping function, such that the deformation gradient tensor is

$$F_{ij} = \left(\frac{\partial x_i}{\partial X_j}\right)_t \tag{7.3}$$

The stress and velocity fields (as well as displacement or velocity boundary conditions) are known at the beginning of each time step, so that application of Eq. (7.1) permits evaluation of the acceleration field. In most host codes, the updated position of a material particle is computed to second-order accuracy with respect to the time step Δt through application of

$$\underset{\sim}{x}^{n+1} = \underset{\sim}{x}^n + \left(\frac{\partial \underset{\sim}{x}}{\partial t}\right)^n_{\underset{\sim}{X}} \Delta t + \frac{1}{2}\left(\frac{\partial^2 \underset{\sim}{x}}{\partial t^2}\right)^n_{\underset{\sim}{X}} (\Delta t)^2 \tag{7.4}$$

or

$$\underset{\sim}{x}^{n+1} = \underset{\sim}{x}^n + \underset{\sim}{v}^n \Delta t + \frac{1}{2}\underset{\sim}{a}^n (\Delta t)^2 . \tag{7.5}$$

Equivalently,

$$\underset{\sim}{x}^{n+1} = \underset{\sim}{x}^n + \underset{\sim}{v}^{n+1/2} \Delta t , \tag{7.6}$$

where $\quad \underset{\sim}{v}^{n+1/2} \equiv \underset{\sim}{v}^n + \frac{1}{2}\underset{\sim}{a}^n \Delta t . \tag{7.7}$

To date, all installations of Kayenta have approximated the *unrotated* strain rate by the *unrotated* symmetric part of the velocity gradient defined in Eq. (4.3), evaluated at the half-step by using the velocity field in Eq. (7.7). Kayenta integrates the unrotated strain rate to predict the *unrotated* stress at the end of the step, which must then be rotated into the spatial configuration by the host code. As mentioned on page 22 (and clarified later in this chapter), optimizing the accuracy of the *spatial* solution for problems involving massive material rotation requires the host code to apply its un/rotation operations using polar rotation tensors that are consistent with the part of the time step (beginning, half, or end) at which un/rotation operations are required.

Of course, once Kayenta and any other constitutive models in the problem have been applied to determine stresses at the end of a time step, Eq. (7.1) may be integrated again to update the acceleration field, thus launching a new timestep cycle.

Spatial stability (mesh dependence/loss of strong ellipticity)

As rock deforms inelastically, the initial yield surface (lower curve in Fig. 4.17) evolves toward — and is not permitted to evolve *beyond* — the limit surface (upper curve in Fig. 4.17). If the stress reaches the limit surface, the rock has, in a loose sense, failed catastrophically. More correctly, Kayenta has reached the limit of its applicability because large scale cracking and subsequent loss in strength *cannot be modeled locally at the constitutive level*. Material softening generally produces a change in type of the momentum equation, requiring intervention from the host code to change its solution scheme appropriately (for further details, see page 67). In the GeoModel predecessor to Kayenta, the state variable "**CRACK**" was a flag equaling 1.00 whenever a principal stress (or I_1) cutoff has been applied or 2.00 when the stress has reached the limit surface and can harden no further; otherwise "**CRACK**" equals 0.0. In either case, a positive value of "**CRACK**" marks the onset of softening. In the current version of Kayenta, the meaning of the "**CRACK**" flag is in flux and should be regarded as a developer's flag not of interest to users.

Because Kayenta comes equipped with its own criteria for failure, this model should *not* be used with other fracture models such as a maximum principal stress criterion. Instead, the "**CRACK**" flag should be queried by the host code to determine when it is appropriate to add void (when pressure is tensile) or to apply discontinuous shear displacement element shape functions (when pressure is compressive) or to apply any other appropriate response[*] to material softening that will ensure localization response that converges as the spatial mesh size is reduced. However, since Kayenta's treatment of material softening, along with its update and usage of the "**CRACK**" flag, are under current development, host code owners should consult with the model developers for guidance on proper implementation of material softening. Also see page 72.

---

[*] We are investigating a field-scale softening strategy that introduces a length scale based on Weibull perturbations of the material strength field, which is especially appealing because (unlike "element death" and cohesive zone models) it can be easily justified physically. Specifically, softening results from sub-grid-scale flaw clustering, which can be shown to have a Weibull (or nearly Weibull) distribution and can be parameterized via standard laboratory-scale experiments. Preliminary investigations [6] have shown that Weibull-like softening strategies lead to *very* realistic fragment patterns and are mesh-independent.

If the host code fails to activate any special response when the "**CRACK**" flag becomes nonzero, Kayenta will continue to run, but its predictions are suspect. Without a meaningful host-code response to failure, Kayenta will handle the inelastic response at the limit state in a manner similar to non-hardening plasticity (i.e., rather than properly softening down away from the limit state, Kayenta will force the stress to dwell at the limit state). To summarize, Kayenta is intended to model *only* the portion of material response that is appropriate to compute at the local constitutive level. Kayenta sends flags back to the host code at the *onset* of softening (a non-local phenomenon). The *host code* is responsible for responding appropriately to these flags by initiating material softening.

Kayenta files, subroutines, memory requirements, and model installation requirements.

This section is a software requirements specification that must be followed by anyone who installs Kayenta into a host code.* Kayenta is designed to be implemented into multiple host codes without *any* revision of the source code. As described below, the model has *three* public† subroutines (**GEOCHK**, **GEORXV**, and **ISOTROPIC_GEOMATERIAL_CALC**). To support portability, Kayenta conforms to Sandia's Model Interface Guidelines (MIG) [12]. Therefore, the model presumes that calculations entail three distinct phases, the first two of which are performed at start-up while the last one is applied for every element at every timestep:

1. **User input.**   Kayenta requires the host code to acquire user input values and save them into a single array using the keywords and ordering listed in Appendix B. This property array must be passed to the subroutine **GEOCHK** for "domain certification" (i.e., verifying that input values fall within allowable ranges, as explained on page 95). Additionally, the routine **GEOCHK** sets defaults for unspecified user inputs.

2. **Storage.**   To be portable, Kayenta does not actually *allocate* storage for internal state variables (ISVs) — this is the responsibility of the host because data lay-out varies from code to code. Kayenta provides a *list* of storage requirements by requiring the host code to call subroutine **GEORXV**. This routine returns physical dimensions, initial values, plot keywords, and advection requirements for each internal state variable. To use this routine, the host code loops over the *lists* returned by **GEORXV** to then allocate the storage, define plot options, and initialize the ISV fields.

3. **Execution.**   Every cycle, **ISOTROPIC_GEOMATERIAL_CALC** must be called to update the stress to the end of the step. Detailed descriptions of the input-output arguments are provided below.

---

* Any deviation from these model installation instructions (as well as any modification of Kayenta source code itself) may result in loss of technical support. Model installers who believe that a deviation from these instructions is warranted are encouraged to contact Kayenta developers.

† i.e., routines that are called directly from the host code. All other routines in Kayenta are "private" and should not be called by the host. To serve codes that re-mesh, one additional public routine, **isotropic_geomaterial_state**, is available that will repair advection errors.

Kayenta must, upon occasion, relay messages to the user or terminate the calculation. Log message protocols and bombing procedures vary among host codes. For portability, Kayenta follows MIG guidelines by calling subroutines **LOGMES**, **FATERR**, or **BOMBED** whenever it needs to relay messages to the user, log fatal errors, or terminate calculations, respectively. These routines are *not* part of Kayenta source code. Because these actions require host-code responses that vary from code to code, these routines must be written and maintained by the host-code architects. Likewise, a routine called **TOKENS** (used only in the extra variable request routine) is expected to pre-exist in the host code. Any host code that *already* supports MIG models will already have these MIG-utilities in their repository. Host code architects of non-MIG-compliant codes may request sample MIG-utilities that they may customize to suit their own code's protocols for information passing and code termination.

Kayenta source code is available in both FORTRAN 77 and 90. To date, large-scale production codes have used the F77 version to best ensure portability, so those routines will be described here. The F90 routines, which are not significantly different, are generated from the F77 master files to ensure consistency.

Arguments passed to and from Kayenta's driver routine

The following list describes variables passed between the host code and Kayenta's driver routine (**isotropic_geomaterial_calc**):

INPUT:
- **NBLK**: The number of cells or finite elements to be processed. Parallel codes send only one cell at a time (**NBLK=1**).
- **NINSV**: The number of internal state variables for Kayenta.
- **DT**: The time step
- **PROP**: the user-input array, filled with real numbers, as summarized at the top of the nomenclature table in Appendix B and also summarized within the source code prolog itself.
- **SIG**: The unrotated Cauchy stress tensor at time *n*. The six independent components of the stress must be passed in the ordering $\{\sigma_{11}, \sigma_{22}, \sigma_{33}, \sigma_{12}, \sigma_{23}, \sigma_{31}\}$. Within the FORTRAN, this array is dimensioned "**SIG(6, NBLK)**" so that the stress components for any given finite element are in six contiguous memory locations.
- **D**: The unrotated strain rate tensor, preferably evaluated at time *n+1/2* because Kayenta treats the strain rate tensor as constant over the entire interval. Most codes approximate the strain rate tensor as the unrotated symmetric part of the velocity gradient (see Eq. 4.3). Component ordering and contiguous storage are the same as for stress.
- **SV**: the internal state variable array containing reals, as described in the nomenclature table in Appendix B.

OUTPUT:
- **SIG**: The unrotated stress tensor at time *n+1*. The component ordering is the same as described above.
- **SV**: The internal state variable array (updated to time *n+1*)

- **USM**: Uniaxial strain (constrained) elastic modulus equal to $H = K + \frac{4}{3}G$. The host code may use the USM output to compute an upper bound on the wave speed ($\sqrt{H/\rho}$, where ρ is mass density) when setting the timestep.

These arguments require unrotation of spatial stress at time *n*, unrotation of the strain rate at time *n+1/2*, and rotation of the updated stress back to the spatial frame at time *n+1*. For problems involving significant material rotation, this requires using *three* different polar rotation tensors [21]. For moderate rotation problems, it might be acceptable to use the rotation tensor evaluated at time *n+1/2* for all three operations, but the accuracy consequences of this simplified approach have not been carefully examined in the computational mechanics literature.

PLOTABLE OUTPUT

In addition to the stress, any variable in the **SV** state variable array is available for plotting. The plot keywords (and ordering of variables in the **SV** array) are listed in Nomenclature Appendix B.

As mentioned earlier, the "**CRACK**" flag may be plotted to visualize softening regions. The "**INDEX**" flag may be plotted to locate regions that are deformed inelastically (the meaning of this output varies to support code debugging; currently it is a flag that indicates what part of the yield surface is active). To visualize regions that are *currently* deforming inelastically, the "**SHEAR**" variable should be plotted.

The "**SHEAR**" variable is an informational output, equal to zero during elastic cycles and equaling a measure of normality of the trial elastic stress rate during plastic intervals. Specifically, as illustrated in Fig. 7.1, "**SHEAR**" ranges from zero when the trial stress rate is tangent to the yield surface to unity when it is normal to the yield surface; an intermediate value of "**SHEAR**" indicates oblique plastic loading relative to the yield surface. While "**SHEAR**" quantifies the plastic loading direction relative to the yield surface, the internal state variable "**DCSP**", which is the plastic consistency parameter $\dot{\lambda}$, may be plotted as a measure of the *magnitude* or intensity of plastic loading.
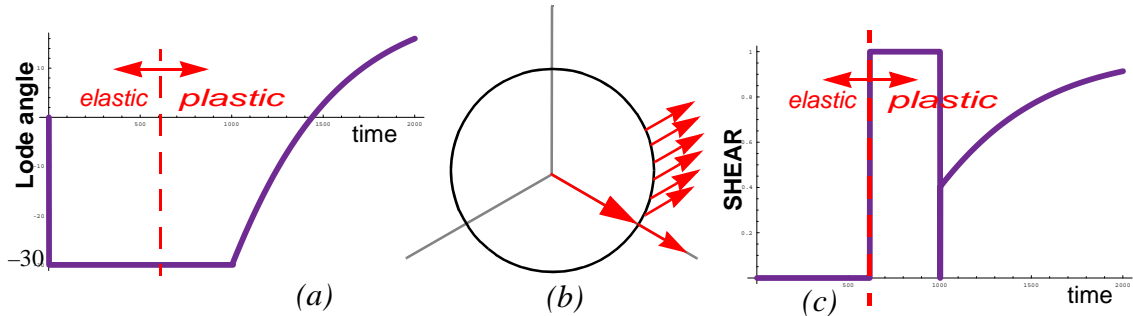
Figure 7.1.   *Meaning of the "SHEAR" output variable.*   This calculation uses a Von Mises yield surface. The strain rate remains in triaxial extension for half of the calculation, which is why the Lode angle *(a)* is initially constant at $-30°$. During this interval, the stress reaches the yield surface and continues to push directly against it, which is why **SHEAR** *(c)* jumps to and holds at 1.0. Halfway through the problem, the strain rate direction is changed in stress space [as indicated by arrows in *(b)*] to move the stress toward triaxial compression. At the beginning of this transition, **SHEAR** first jumps to 0.5 where the normal and tangential components are equal, and moves back toward 1.0 as the tangential component decays.

The "**EQDOT**" variable may be plotted to gain an overall sense of intensity of the current strain rate. Small values of "**EQDOT**" correspond to relatively quiescent regions. Plotting "**EQPS**" will show equivalent plastic shear strain, while "**EQPV**" gives plastic volume strain (and is roughly equal to the porosity change from inelastic void collapse).

The stress invariant "**I1**" is three times the negative of pressure. "**ROOTJ2**" may be regarded as a scalar measure of effective shear stress and is proportional to the radial coordinate of the stress in the octahedral plane. The Lode angle, "**LODE**", quantifies the angular location of the stress in the octahedral plane, and it varies from 30 for triaxial compression to –30 for triaxial extension (0 for simple or pure shear). If kinematic hardening is enabled, "**BACKRN**" quantifies the distance that the origin of the octahedral profile has shifted in stress space.

The complete list of other (less useful) plotable output is in Appendix B.

Kayenta algorithm

Kayenta presumes that the strain rate is constant throughout the entire step, and the stress is integrated as follows:

Rate independent (inviscid) part of the viscoplasticity equations.

STEP 1. To guard against unpredictable host-code advection errors (or similar corruption of the updated state from the last time step), apply a return algorithm to ensure the initial stress is on or inside the yield surface.

STEP 2. Compute the nonlinear elastic tangent moduli appropriate to the stress at time *n*.

STEP 3. Apply Hooke's law in rate form to obtain the elastic stress rate at time *n*.

STEP 4. Integrate the elastic stress rate using first-order differencing to obtain an estimate for the trial elastic stress at the end of the step.

STEP 5. Evaluate the yield function at the trial elastic stress. If the yield function evaluates to a negative number, the trial elastic stress is accepted as the final updated stress, and the inviscid algorithm returns (i.e., go to STEP 16). Otherwise, continue.

STEP 6. To reach this step, the trial elastic stress state was found to lie outside the yield surface. At this point, the time step is divided into an internally determined number of subcycles. All subsequent steps described below this point apply to the smaller time steps associated with subcycles.

STEP 7. Evaluate the gradients of the yield function for eventual use in Eq. (4.85).

STEP 8. Evaluate the flow potential gradients for eventual use in Eqs. (4.89) and (4.87)

STEP 9. Evaluate the isotropic hardening coefficient h_κ in Eq. (4.74).

STEP 10. Evaluate the G^α function in Eq. (4.78).

STEP 11. Apply Eq. (4.85) to obtain the consistency parameter.

STEP 12. Use forward differencing (within the subcycle) to integrate Eqs. (4.74) and (4.78), thereby updating the internal state variables, κ and α_{ij}. Similarly integrate Eq. (4.87) to advance the stress to the end of the subcycle.

STEP 13. The above steps will have directly integrated the governing equations through the end of the subcycle, so the updated stress will be *in principle* already on the yield surface.

However, guard against slight round-off and integration errors by applying an iterative return correction to place the stress *exactly* on the yield surface.

STEP 14.   Increment the subcycle counter, and save the partially updated inviscid internal state variables.

STEP 15.   If subcycles remain to be evaluated, go to STEP 7. Otherwise, continue to STEP 16.

Viscous part of the viscoplasticity equations.

STEP 16.   The previous set of steps govern computation of the equilibrium state. Now apply Eq. (6.22) to compute the characteristic material response time.

STEP 17.   Using the trial elastic stress corresponding to an update to the end of the time step, apply Eq. (6.10) to compute the dynamic stress. Apply Eq. (6.15) to similarly compute the dynamic values of internal state variables to account for rate sensitivity.

STEP 18.   Save the values of the internal state variables into the state variable array.

STEP 19.   STOP.

8. Software "confidence building" activities

This chapter describes progress towards Software Quality Assurance (SQA), which encompasses a broad range of activities including code maintenance, documentation, and (most importantly) code verification. "Code verification" is defined by the IEEE [30] as "formal proof of program correctness" in the sense that the governing equations are numerically solved correctly within a tolerable degree of accuracy. Model *validation** will not be discussed until Chapter 10.

We make no claims at this point that Kayenta software has been exhaustively verified. In other words, we cannot state with *absolute* certainty that the governing equations presented in this report are in fact solved correctly. One might challenge the Verification and Validation (V&V) community to prove that "formal proof of program correctness" is even possible. Realistically, the confidence one can place in the veracity of any model prediction can be based only on the extent to which documented evidence *suggests* that the equations are solved correctly. It seems acceptable, therefore, to speak of varying *degrees of progress* towards verification†, or, more generally, varying degrees of SQA. In this sense, Kayenta has undergone a higher level of SQA than is normally applied to modern material constitutive models of comparable complexity.‡ Even though we claim that Kayenta's verification and SQA status is above average, we do *not* assert that such activities have progressed to the point where we consider the job "finished." Here in this chapter, we aim only to build confidence in Kayenta by summarizing some of the SQA activities that have been applied to Kayenta to date (a comprehensive *detailed* discourse would fall well outside the scope of this report).

Once a constitutive model is installed within a host code, it becomes only a single component of a much *larger* and *different* model (the finite-element code). Constitutive SQA should include ensuring that the model can be installed and run in a variety of host codes, but verification of the installation is primarily a *host code* (not constitutive) responsibility. Constitutive SQA in the context of larger-scale model integration is limited to pro-

---

* Whereas "Verification" seeks to confirm that the equations are solved correctly without questioning their appropriateness, "validation" compares model predictions against experimental data to determine whether or not the equations themselves are indeed suitable for the application.

† Suppose, for example, that one constitutive model has been verified for both uniaxial strain and simple shear, whereas another one has been tested only in uniaxial strain. If these are the only tests, *neither* model is "well verified," but the first one is certainly *better* verified.

‡ From a practical (rather than philosophical) standpoint, the complexity of a model must be considered when speaking about how well a model has been validated. With a given level of financial and computational resources, solids models cannot be tested to the same level of certainty as fluids models. Conclusively demonstrating only *first-order* accuracy of an anisotropic solid constitutive model would require more than *twenty* times the effort needed to verify first-order accuracy of a simple fluids model (this follows because a general anisotropic stiffness tensor has 21 independent components, and therefore 21 independent strain paths would be required to conclusively verify accuracy; moreover comprehensive testing for solids models requires coordinate invariance tests that are not needed for scalar fluids models).

viding adequate model installation instructions (including operational constraints), delivering correct solutions to the constitutive governing equations, and ensuring that the model will, wherever feasible, "trap" invalid calling arguments (much as a compiler "traps" IEEE errors such as division by zero).

Numerical schemes for solving field PDEs (such as Navier-Stokes equation or Maxwell's electromagnetism equations) have received considerable attention in the V&V literature, while verification of *constitutive models* has been relatively ignored. Constitutive models are *sub-components* within field-scale calculations. As such, a *partitioning* of responsibility for SQA is needed. (As an analogy, note that the quality assurance responsibilities for a turn-signal manufacturer must be different from those of an automobile manufacturer.) *Constitutive* verification aims to build confidence that the model will return correct solutions to the governing equations, *presuming* that the host code sends inputs falling within the admissible domain for the model. SQA may additionally include some checking of the inputs themselves, as long as doing so does not compromise efficiency. When a host code sends inadmissible inputs (such as corrupted strain rates caused by mesh entanglement, advection, or artificial viscosity errors), then correcting such errors is *not* the responsibility of a constitutive modeler unless it can be proved *by the host code developers* that such errors originated from constitutive model output errors.

Similarly, because Kayenta is a *local* constitutive model (i.e., because it does not solve space-time PDEs), demonstrating convergence with respect to the *spatial* mesh is not a Kayenta verification responsibility. It is well known that mesh dependence can occur when local constitutive models permit material softening. Therefore, we regard *suppression* of softening as an implicit software requirement specification unless our customers (finite-element code teams) have implemented the code infrastructure that is needed to properly handle the change in type of their governing PDEs that occurs upon softening. Unless such enhancements are made *at the host code (not constitutive) level*, Kayenta's applicability domain is limited to predicting only the *onset* of catastrophic failure, not its subsequent evolution into macroscale fragments and fractures. If host code enhancements are implemented as described on page 72, then Kayenta's applicability domain is marginally expanded into the softening realm, but it must be understood that nonphysical mesh sensitivities might still be present in certain calculations. In short, models for softening continue to be an active research area.

In the lexicon of Ref. [34], "static" SQA testing is a prerequisite to the verification process that encompasses tests that are performed without running the code. To date, Kayenta has undergone the following static SQA:

- **Independent[*] line-by-line review of the source code.** The source code was aggressively inspected to locate and remove possibilities for IEEE errors (e.g. trying to take the ArcSin of a number larger than unity†, dividing by zero, etc.). Another goal was to confirm that the equations being solved in the code were indeed the equations documented in this report.

- **Model domain certification (preventing "Garbage In $\Rightarrow$ Garbage Out").** No function or set of equations is well posed without a domain of applicability. The domain for Kayenta includes constraints on run-time subroutine arguments (e.g., the backstress must be deviatoric) as well as constraints on the input parameters (e.g., the bulk modulus must be positive). Except where computational efficiency would be degraded, SQA includes appraising quality of both user input and run-time arguments sent from the host code. A new routine (`geochk`) was recently added to Kayenta that terminates calculations if the user-input falls outside allowable ranges. Run-time testing of this routine is discussed in the next section. Direct run-time testing of *time varying* subroutine arguments is computationally inefficient, so Kayenta's domain certification for variable calling arguments relies primarily on our model installation instructions (page 87), which serve as software requirement specifications that must be obeyed by the host code developers.

- **Portability and version control.** Kayenta has been designed such that it can be implemented in multiple host codes *without altering the source code*, thus allowing Kayenta developers to maintain a single master version. A host code owner who faithfully obeys the model installation instructions on page 87 may update Kayenta by simply replacing three FORTRAN files (posted on WebFileShare under keyword "Kayenta") with the latest Kayenta release and then recompiling. Each Kayenta release is identified by a six digit code‡ that prints to the screen at run time. Kayenta has been compiled on multiple platforms (Sun, Dell, and HP workstations or clusters running Linux and/or Windows) in multiple host codes (Alegra, Presto, Pronto, JAS3D, and two independent drivers) using multiple commercial compilers (gnu, pgf77, pgf90, and Compaq visual FORTRAN). The source code compiles without warnings when using stringent SQA options (such as -Wall -O3 in the gnu compiler).

- **Model documentation.** *This report* is the first publication that describes the numerical algorithm, provides input definitions, and gives model installation instructions that describe how SQA responsibilities are partitioned between the model and the host code.

- **Technical support.** Two stand-alone single-cell codes that exercise Kayenta under prescribed strain and stress paths are available to help host (finite-element) code owners verify their Kayenta installations. Kayenta includes a "problem-resolution" feature that generates a debugging file (geo.barf) and terminates calculations whenever unacceptable solution quality is detected. The debugging file may be emailed to Kayenta team, who can import it into their driver to resolve the problem quickly.

---

* Here, "independent" (which is not synonymous with "unbiased") means that the source code has been inspected by an individual who has not written the code. Kayenta code inspection was first performed by Brannon (the second author of this report) upon joining this modeling effort at the beginning of fiscal year 2003-04. Subsequent new code revisions and enhancements have been reviewed by the member of the Fossum-Brannon team who did *not* write the new code.

† This can happen because of slight round-off errors, as in `ASIN(1.0000001)`.

‡ The code's build identification number is simply the release date in the form "yymmdd". For example, "Kayenta version 1.0 build 090217" was released in 2009 on Feb. 17.

So-called "dynamic" SQA refers to tests performed by actually running Kayenta. Some of the dynamic SQA activities to date are summarized here. A detailed documentation of all Kayenta SQA would require a second report itself, so the following list should be regarded as simply an overview. A small number specific examples will be given later.

- **Model domain certification:** The "geochk" feature for checking quality of user inputs was tested by confirming that Kayenta would abort when *intentionally* sent invalid inputs. As explained below, the "geobarf" problem-resolution feature can often *indirectly* trap invalid forcing functions (caused, for example, by mesh entanglement). However, the *responsibility* for sending valid forcing functions to Kayenta remains the onus of the host code, not Kayenta.

- **Run-time monitoring of the solution quality:** The problem-resolution (geo.barf) feature has been verified to **(1)** detect "Garbage Out" predictions such as negative plastic work, **(2)** terminate calculations, and **(3)** write a debugging file that can be emailed to model developers to determine whether the problem was caused by bad user input, bad arguments passed from the host code, or a bug in the internal coding.

- **Driver regression testing:** Two stand-alone drivers are available for exercising Kayenta in a homogenous deformation field.* Considerable dynamic testing was performed using our research (non-production) model driver that allows visualizing (and algebraically processing) the output within Mathematica [60]. The other driver [45], which runs either from a command line or from an Excel front-end (see Fig.8.1), is now also deployed in the WISDM materials information database [29], allowing the predictions of Kayenta to be compared directly against experimental calibration data. These drivers have been used to assemble a suite of regression tests (hydrostatic loading, two types of shear loading, uniaxial strain, uniaxial stress, biaxial plane stress, and numerous mixed load-unload problems using a variety of input parameters), several of which are simple enough to admit analytical solutions for verification purposes. The driver regression problems (15 problems to date) are all re-run and inspected for undesirable changes whenever *any* change is made to Kayenta.

- **Trend testing:** Engineering judgement was used to ensure that solutions vary as expected when parameters change. For example, Fig. 7.1 depicted a simple trend test in which analytical (exact) arguments could be used to prove that the "**SHEAR**" should equal 1.0 at the onset of yielding and should dwell at 1.0 until the loading direction changes, after which it should drop instantaneously to 0.5 and then asymptote to 1.0. Similarly, Figs. 6.3 and Figure 8.9b confirmed that increasing Kayenta's characteristic response time (see Eq. 6.22) would indeed produce the analytically predicted increase in the apparent strength of the material. These tests were quite valuable because they allowed correction of a serious bug in an earlier version of Kayenta where the response trend upon *load reversal* was clearly flawed. Trend and robustness testing also demands that Kayenta must predict *qualitatively* reasonable trends when subjected to deformations that exceed what is expected in applications (e.g., massively large elongations or pressures). For example, one problem in our driver regression suite verifies that load/unload curves do indeed asymptote toward each other under hydrostatic compression as sketched in Fig. 3.1 and verified in Fig. 8.1. Many other trend tests such as these have been conducted, but (for lack of space) will not be described in detail in this report.

---

* Stand-alone testing obviates many constraints and sources of *non-constitutive* errors in production finite-element simulations (artificial viscosity, hour-glassing, time-step control, boundary-condition errors, code compilation and run-time overhead, etc.).

Problem description:

Fossum Geomodel

Salem Limestone

Hydrostatic Compression (Stress-Driven)

****

Path to Fortran MMD executable:

C:\home\data\mdrive\rb\mmd0402c\Debug\mmd0402c.exe

****

Material model:

Index	Name (optional)
11	Fossum Geomodel

****

Material model input parameters:

B0	B1	B2	B3	B4	G0	G1	G2	G3	G4
(Pa)	(Pa)	(Pa)	(Pa)	(ndim)	(Pa)	(ndim)	(1/Pa)	(Pa)	(ndim)
1.30E+10	4.25E+10	4.11E+08	1.20E+10	0.021	9.86E+09	0	0	0	0

RJS	RKS	RKN	A1	A2	A3	A4	P0	P1	P2
(m)	(Pa/m)	(Pa/m)	(Pa)	(1/Pa)	(Pa)	(rad)	(Pa)	(1/Pa)	(1/Pa^2)
0.00E+00	2.00E+13	1.00E+12	8.43E+08	2.73E-10	8.22E+08	1.00E-10	-3.14E+08	1.22E-10	1.28E-18

P3	CR	RK	RN	HC	CUTI1	CUTPS	T1	T2	T3
(1)	(ndim)	(ndim)	(Pa)	(Pa)	(Pa)	(Pa)	(s)	(1/s)	(ndim)
8.40E-02	6	0.72	5.00E+06	9.00E+10	1.00E+11	3.00E+06	0.00E+00	0	0

T4	T5	T6	T7	J3TYPE	A2PF	A4PF	CRPF	RKPF	SUBX
(1/s)	(Pa)	(s)	(Pa)	(ndim)	(1/Pa)	(rad)	(ndim)	(ndim)	(ndim)
0.00E+00	0.00E+00	0.00E+00	0.00E+00	3	2.73E-10	1.00E-10	6	0.72	0

****

Load path specifications:

leg	time	npts	nprt	ltype*	c11	c22	c33	c12	c13	c23
(ndim)	(s)	(ndim)	(ndim)	(ndim)						
0	0	0	0	111111	0	0	0	0	0	0
1	1	100	2	444222	-1.00E+09	-1.00E+09	-1.00E+09	0	0	0
2	2	100	2	444222	0.00E+00	0.00E+00	0.00E+00	0	0	0

*Load type parameter for each component, cij:

1 = strain rate   (1/s)
2 = strain   (1)
3 = stress rate   (Pa/s)
4 = stress   (Pa)

Figure 8.1.   *Screen shot of the MS Excel interface for Kayenta's material-model driver (MMD).*   This tool serves as a reliable platform for exercising Kayenta under homogeneous deformations in a simplified host code architecture that is free from solution corruption caused by *unneeded* finite-element code features such as artificial viscosity, wave motion, contact algorithms, etc.

- **Symmetry testing:** Consistent predictions were verified for identical loading applied in different directions (e.g. uniaxial strain in the 1-direction compared with the 2-direction). Consistency has also been tested for stress paths that intersect the yield surface at symmetrically equivalent points and for trial stress rates normal to the yield surface (to verify that the stress rate had no tangential component).

- **Extensive comparison testing:*** To date, Kayenta has been implemented in five finite-element codes: (ALEGRA [10,61], PRESTO [35], JAS3D [7], EPIC [32], legacy PRONTO3D [55]). A disturbing number of discrepancies (e.g., wave arrival times differing by as much as 10% or peak stresses differing by almost an order of magnitude) have been identified by comparing predictions for the *same problem* simulated by different finite-element codes. In all but a few cases, these discrepancies have been traced to *host-code-level (not constitutive-level)* errors (e.g., hour-glassing, handling of boundary conditions, artificial viscosity, time-step control, etc.). Resolving such discrepancies is the model verification responsibility of the host code owners, not Kayenta developers.† The ability of Kayenta to reduce to simpler models (e.g., nonhardening elastoplasticity) has often proved invaluable in determining if a simulation problem originates from Kayenta or elsewhere in the host code. When, for example, an undesired feature in a calculation persists even when Kayenta is run using simplified parameters, a comparison test can be performed using the existing (presumably better verified) independent version of that model within the finite-element code. We have, for example, often compared a host code's standard elasticity model with Kayenta run in an elastic mode. In one instance where a discrepancy was traced to Kayenta, it was attributed to failure of the code owner to follow Kayenta installation instructions (page 87). In a few cases, comparison testing did indeed reveal Kayenta bugs that have since been corrected.

- **Comparison with exact analytical solutions:** Analytical solutions are not available to verify all of Kayenta's features acting *simultaneously*. However, each Kayenta feature has been individually verified to ensure that the promised *quantitative* material response is delivered (e.g., accurate tracking of a specified porosity crush curve, exact apparent strengthening in high rate loading, etc.). Depending on how the model parameters are set, Kayenta can be idealized to a form for which some problems admit exact solutions. One example is that of a linear Mohr-Coulomb material with an associative or a non-associative flow rule in homogeneous loading. This class of problems was recently studied in a verification and benchmarking activity sponsored by the Defense Threat Reduction Agency (DTRA) through its Advanced Concepts Technology Demonstration (ACTD) Project. These exercises were part of a larger Verification and Validation (V&V) effort to increase confidence in prediction of low-yield nuclear damage of underground (tunnel) facilities in jointed (in situ) rock mass. The problems are designed to increase in complexity, by invoking additional physics in the material models, until a level is reached that is deemed sufficient to model precision field tests. This work will be described in further detail later in this chapter.

---

* Testing a numerical model in multiple host codes has been vital to our SQA process. If two codes agree, then no conclusion may be drawn. If, however, two codes predict different answers, then at least one of them is not solving the equations properly (or is not solving the same equations). Resolving such discrepancies has *time and again* expedited bug identification and resolution.

† Incidentally, the disquieting frequency of bugs originating within the host code (not the constitutive model) reiterates the importance of specialized constitutive model drivers in constitutive model verification. Constitutive models should *not* use finite-element codes as their primary verification platform.

- **Method of manufactured solutions (MMS):** The MMS method of SQA entails *first* solving an inverse problem in which simple (e.g., quadratically varying) analytical time histories for the *response* functions are substituted into the governing differential operators to obtain (probably with the assistance of a symbolic mathematics program such as *Mathematica*) an expression for the *input* functions that would produce the pre-specified response function [34, 48, 52]. The numerical model is then sent this *analytically determined* input function to verify that the original (pre-selected) response function is recovered. For Kayenta, using MMS would require pre-selecting an analytically simple stress history to determine a strain history to use as input in the numerical simulation. To date, this technique has not been used extensively in the Kayenta verification process. Solving the inverse problem is usually prohibitively difficult because Kayenta's differential operators are "branched" (one set is used during elastic deformation, while another is used during plastic loading, and the internal state variable evolution equations themselves are coupled to the location of the stress on the current yield surface). However, the inverse problem tractable for extremely simplified model parameters. In particular, one such exercise (developed as part of an ACTD verification activity [54]) involved plane stress deformation of a non-associative Mohr-Coulomb material. Strictly speaking, this verification problem was an instance of MMS because plane stress entails specification of one of Kayenta's outputs (the out-of-plane stress). An analytical solution was found for the strains required to produce plane stress results. These strains were then used to drive Kayenta in a single element strain-controlled driver, where it was confirmed that the predicted out-of-plane stress was zero (on the order of 10^{-5} relative error, which was comparable error in the prescribed strain table). Moreover, as illustrated in Fig. 8.2, the in-plane stresses agreed with the analytical result (with similar relative error). Details of the strain path and the analytical solution, which are available upon request, are likely to be documented in a future journal article.
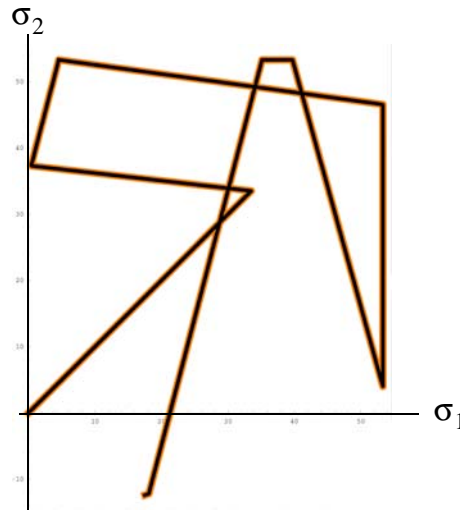
Figure 8.2.   MMS verification of Mohr-Coulomb idealization.   This plot shows the motion of the principal in-plane stresses in response to a prescribed strain path. The simulation (thin black line) overlays the analytical solution (thick orange line), with computed relative error in the predicted stresses on the order of known error in boundary conditions.

- **order-of-convergence:**[*]   Time steps for complicated plasticity models often must be much smaller than the time step used by the host (finite-element) code. Kayenta's governing equations change upon reaching yield, and this transition typically occurs somewhere in the middle of the host code's time step, which implies that the constitutive

99

model must break the step into elastic and plastic parts. Moreover, further subcycling within the constitutive model is required to avoid "drift" of internal state variables into non-physical or inconsistent domains.* Subcycling complicates the meaning of a convergence study performed at the host code level. Preliminary tests (see page 101) indicate that *each subcycle* within Kayenta is first-order convergent, but (recall the last footnote on page 93) we have not yet performed sufficient tests to consider this claim fully verified for a broad variety of load paths. Subcycling in Kayenta has been massively improved over earlier versions. Problems that formerly took 2000 code steps to converge to an acceptable accuracy† can now be run to the same pointwise accuracy in only 10 apparent *host-code* steps (internally, Kayenta still runs ~2000 subcycle steps, but this improvement in allowable *host-code* step size is essential in field-scale finite-element simulations). An independent research effort [24] is nearing completion in which an implicit integration scheme has been developed for a *simplified* version of Kayenta, but verification of its order-of-convergence is not yet completed.

---

* The term "order-of-convergence" is preferred over "order-of-accuracy" because a converged solution is never necessarily a *correct* solution. For example, if the return direction is incorrect in a classical predictor-corrector plasticity scheme, then the algorithm will converge, *but to the wrong result*. Kayenta, by the way, does not use a return method — it explicitly integrates the equations, using subcycling to assist with the change of governing equations upon yielding.

* Of course, higher-order integration is also an option, but the total computational overhead sometimes exceed that of a well-written subcycling algorithm. Moreover, higher-order integration algorithms are notoriously difficult to maintain when the governing equations themselves are being revised during parallel development of the physical theory.

† At this stage in our ongoing verification process, we are using so-called "viewgraph" assessment of accuracy in which solutions are compared visually by plotting them together. This easy assessment method simply *bounds* the discrepancy between two seemingly overlaying plots to be less than differences perceptible to the human eye relative to the size of the graph.

Preliminary convergence testing. Let $F(x)$ denote a fine-resolution solution curve (e.g. stress as a function of strain) corresponding to N evenly spaced time steps. Let $f(x)$ denote a coarser solution corresponding to $n < N$ time steps. In both cases, the *continuous* curves $F(x)$ and $f(x)$ are here regarded as piecewise linear interpolations between discrete function values at the timesteps. Both curves are normalized by the peak value of $F(x)$.

The "integrated discrepancy" is defined

$$\left(\sum_{K=1}^{N} [F(x_K) - f(x_K)]^2 \right)^{1/2} \tag{8.1}$$

The "pointwise discrepancy" is defined similarly except that the sum ranges to n instead of N:

$$\left(\sum_{k=1}^{n} [F(x_k) - f(x_k)]^2 \right)^{1/2} \tag{8.2}$$

Figure 8.4 shows that the basic algorithm *without subcycling* is first-order accurate. Figures 8.4 and 8.3 show that subcycling makes the solution nearly pointwise converged ($\text{discrepancy} \approx 2^{-6}$) even for inordinately coarse calculations of 1 to 3 time steps. This highly desirable behavior can be of paramount importance when the model is run in finite-element codes that take large steps.

Figure 8.3. *Subcycling test for hydrostatic loading.* The ordinate is the first stress invariant $\bar{I}_1$ and the abscissa is volumetric strain $\bar{\varepsilon}_v$. Red is without subcycling. Green is with subcycling. Black, $F(x)$, corresponds to 2^{15} time steps.

Figure 8.4. *Rate of convergence.* The dashed blue line (shown for reference) has a slope exactly equal to -1.

Verification: single-element problems (regression suite)

A single-element problem is one for which the stress and strain fields do not vary in space. As summarized below, this section presents four different single-element load paths, each separately solved using two different Kayenta parameter sets (associative and non-associative linear Mohr-Coulomb — see Appendix B, page B-25). To determine corresponding sets of material parameters for Kayenta, the linear Mohr-Coulomb parameters were used to create simulated data pairs for the limit state and plastic potential functions. Following the instructions in Appendix A, Kayenta was then fitted to these data pairs to determine the limit-state parameters ψ, a_1, a_2, a_3, a_4 and non-associative material parameters $\{\psi^{PF}, a_2^{PF}, a_1^{PF}\}$. The compaction parameters $\{R, R^{PF}, p_0, p_1, p_2, p_3\}$ were selected such that no compaction occurred over the stress range specified for the load paths. Likewise, hardening and rate dependence were disabled. Results are summarized in Figs. 8.5

TXC0

Point	sigx=sigy	epsz
1	0	0.000000
2	0	0.005000
3	0	0.003274

TXC20

Point	sigx=sigy	epsz
1	0	0.000000
2	20	0.000310
3	20	0.005000
4	20	0.002060

RTX100

Point	sigx=sigy	epsz
1	0	0.000000
2	100	0.001548
3	100	-0.005000
4	100	-0.002295

PSTRN

Point	epsz
1	0.000000
2	0.010000
3	0.008391

- Simple load paths clearly demonstrate basic model response

- Run for both full and partial associativity

- Triaxial Compression
  — Activates compression meridian
  — Same load path as a real lab test

- Reduced Triaxial Extension
  — Activates extension meridian
  — Same load path as a real lab test

- Plane Strain
  — Activates meridians at Lode angle(s) (triaxiality) between compression and extension

Table 8.1: Mohr-Coulomb Parameters for single-element verification testing

Parameter (Material Properties)	Symbol	Associative	Non-associative
Young's Modulus	E	31.0 GPa	31.0 GPa
Poisson's Ratio	ν	0.26	0.26
Friction angle	ϕ	29°	26°
Dilation angle	ω	29°	14°
Cohesion	S_o	15.7 MPa	15.7 MPa
Dry bulk density	ρ	2.34 MPa/m^3	2.34 MPa/m^3

through 8.8.

SINGLE ELEMENT VERIFICATION RESULTS
UNCONFINED COMPRESSION
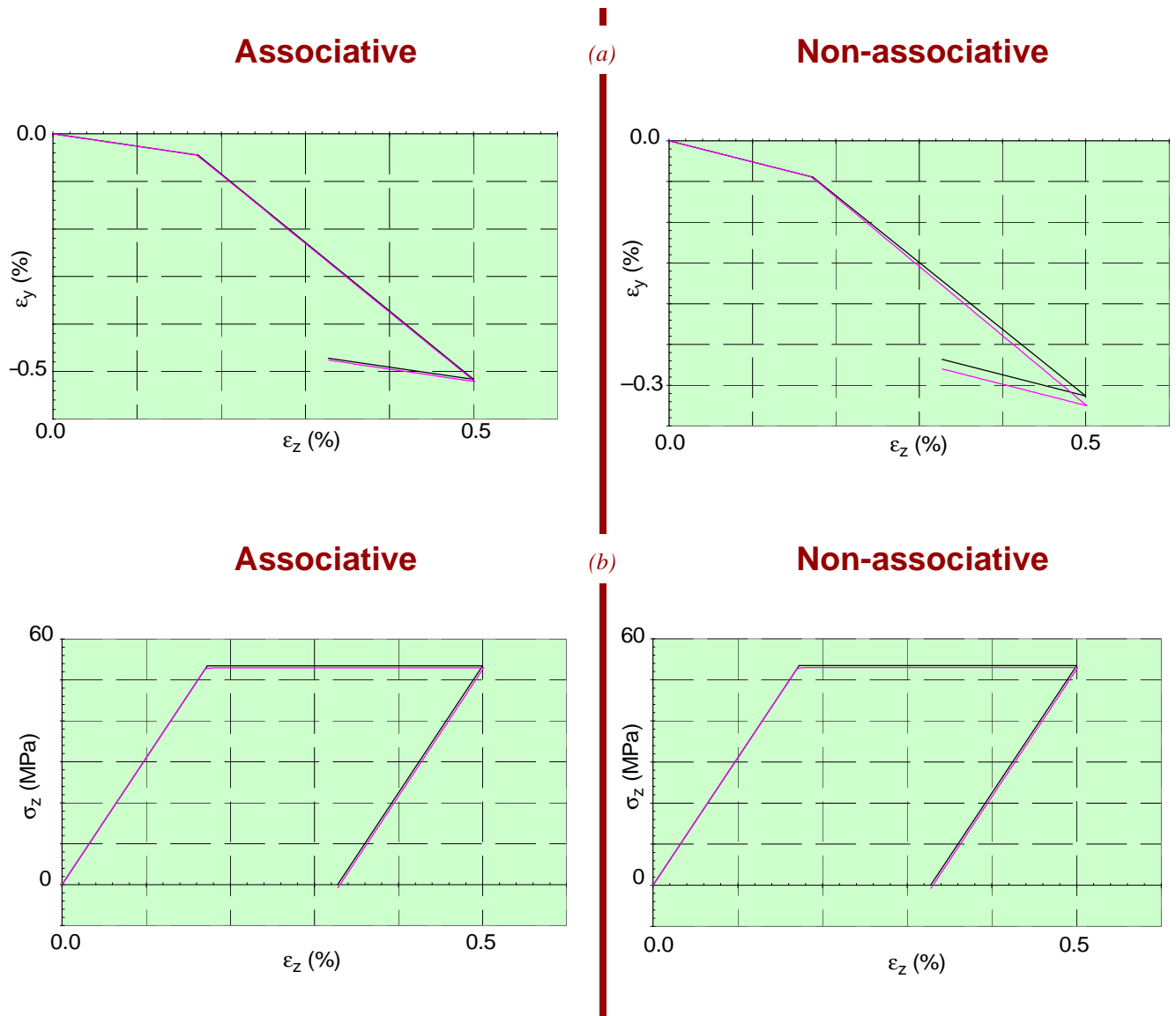
Figure 8.5.   *Unconfined compression.*   Exact (black) solutions compared with ALEGRA Kayenta simulation (pink). *(a)* lateral strain vs. axial strain   *(b)* Stress vs. strain.

SINGLE ELEMENT VERIFICATION RESULTS
20 MPa TRIAXIAL COMPRESSION
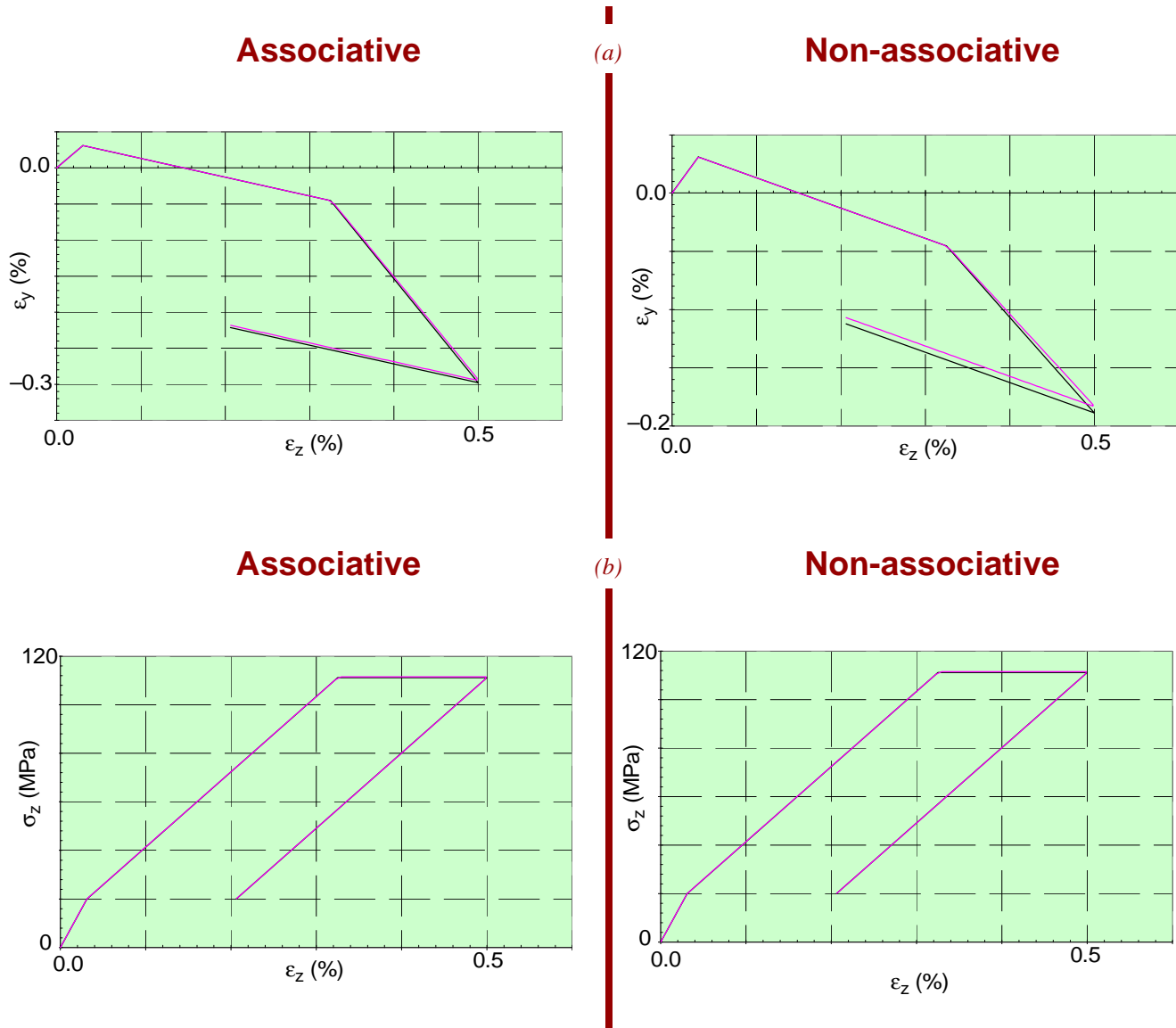
Figure 8.6. *20 MPa triaxial compression.* Exact (black) solutions compared with ALEGRA Kayenta simulation (pink). *(a)* lateral strain vs. axial strain *(b)* Stress vs. strain.

SINGLE ELEMENT VERIFICATION RESULTS
REDUCED TRIAXIAL EXTENSION

Associative *(a)* **Non-associative**
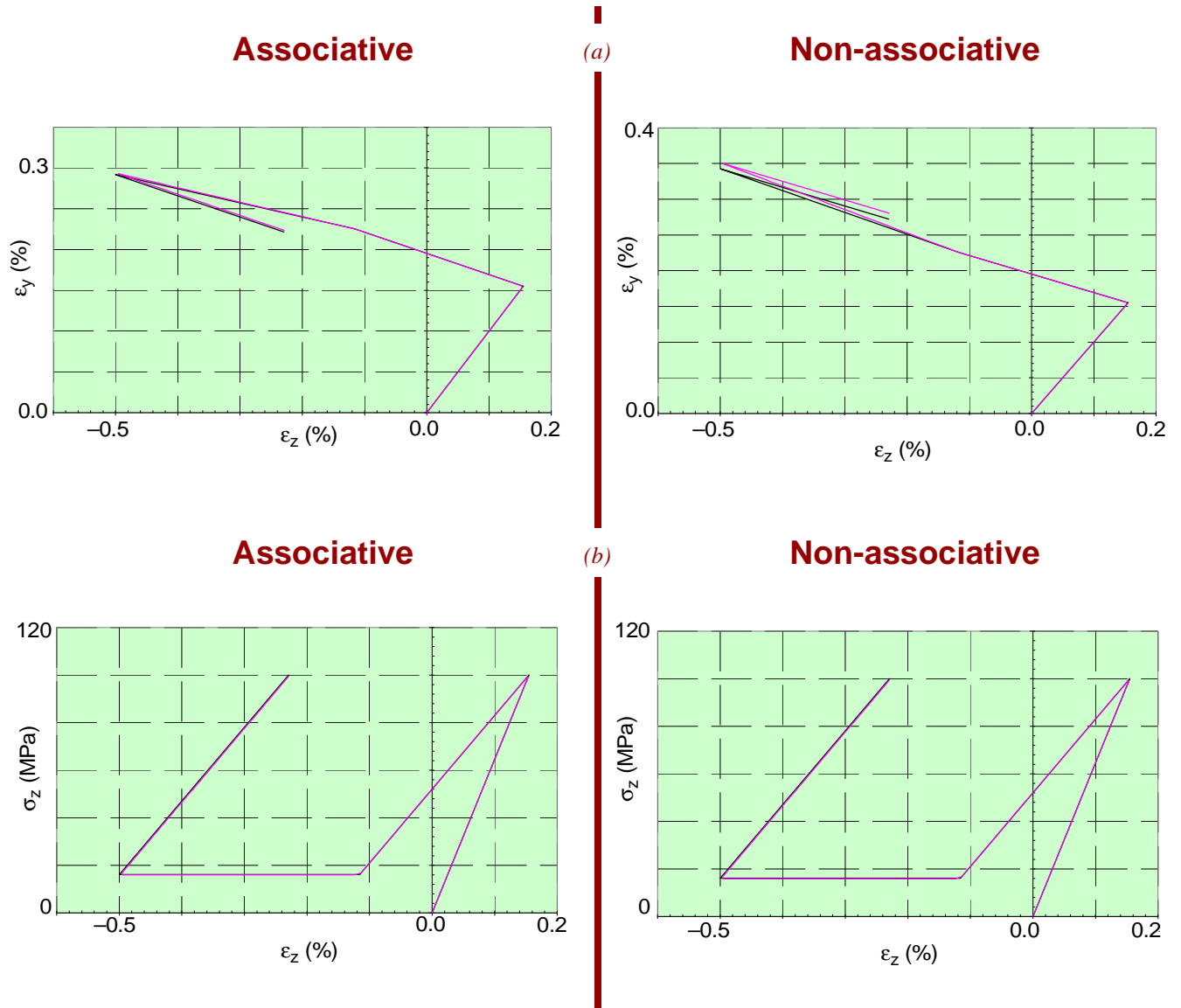
Figure 8.7. *Reduced triaxial extension.* Exact (black) solutions compared with ALEGRA Kayenta simulation (pink). *(a)* lateral strain vs. axial strain *(b)* Stress vs. strain.

SINGLE ELEMENT VERIFICATION RESULTS
PLANE STRAIN
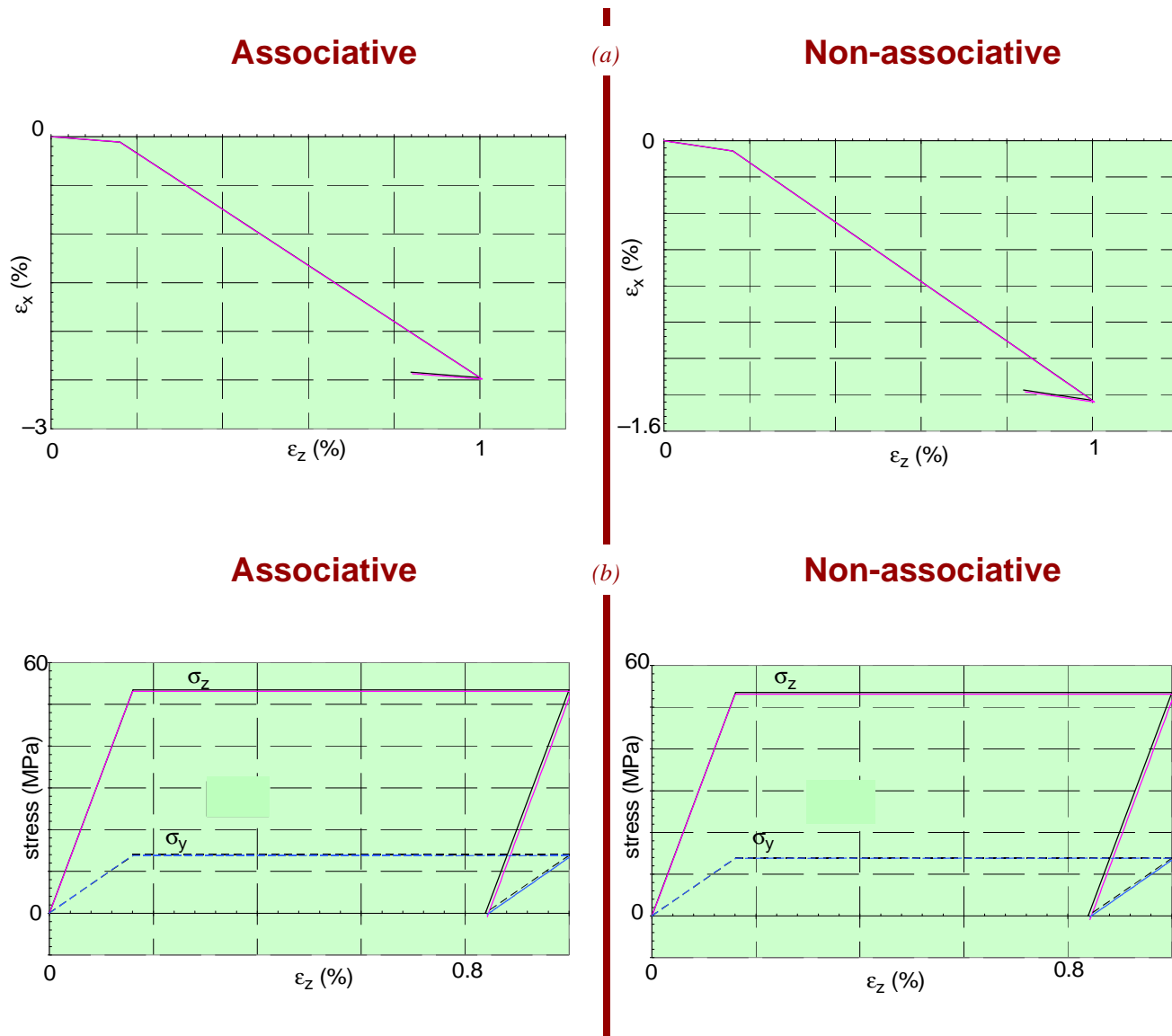
Figure 8.8. *Plane Strain.* Exact (black) solutions compared with ALEGRA Kayenta simulation (pink). *(a)* lateral strain vs. axial strain *(b)* Stress vs. strain.

Discussion.

In Fig. 8.8, predictions of Kayenta overlay the analytical results.[*] Though not yet proved conclusively, we contend that the slight discrepancy apparent in Figs 8.5 and 8.6 arises *not from constitutive model errors*, but instead from host code errors in the handling of stress boundary conditions. The fully strain-controlled problem (Fig. 8.8) exhibits no significant solution discrepancy. However, moderate error is apparent in Figs 8.5 and 8.6, which involve *two* stress boundary conditions (the lateral stresses). Like most constitutive models, Kayenta takes strain rate as input and returns updated stress as output. If the host finite-element code handles stress boundary conditions improperly, then it will have slight errors in the strain rate that it sends to Kayenta, thereby causing predictions to deviate slightly from analytical solutions. Such errors are not uncommon when dynamic finite-element codes are used to attempt to simulate homogeneous deformations.[†] To reiterate, we believe boundary condition errors in the host code (not Kayenta) are responsible for the solution errors, and we anticipate re-running these simulations in a true constitutive model driver to verify this claim.

Other single-element tests. Whenever the source code is changed, we perform approximately 20 single-feature single-element verification checks for each of our regression tests performed under loading that is simple enough to admit analytical solutions.
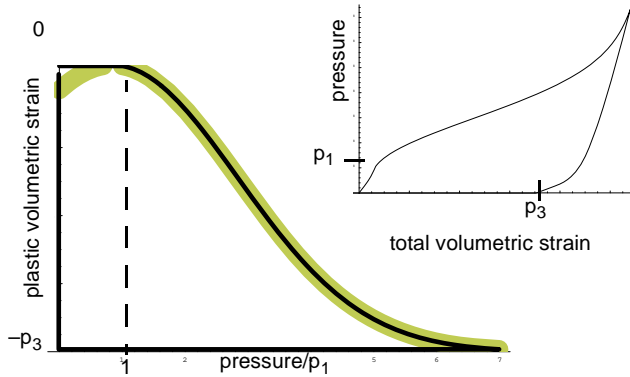
Figure 8.9a.   Crush curve and hydrostatic loading verification.
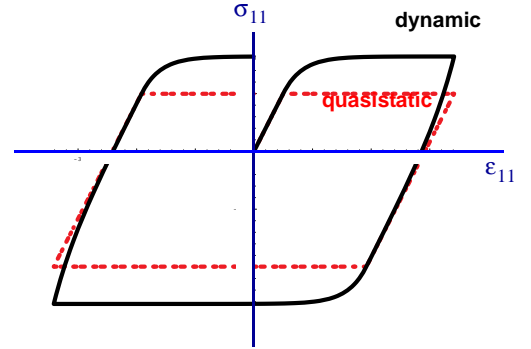
Figure 8.9b.   Rate dependence TXE/TXC ratio verification for triaxial load/unload.

Fig. 8.9a depicts results from a hydrostatic loading simulation in which plastic volumetric strain (**EQPV**) is plotted against pressure ($-$**I1**/3). The thick yellow curve in Fig. 8.9a is the crush curve (Eq. 4.68) determined independently by user specified values of Kayenta parameters p_1, p_2, p_3. The *predicted* volumetric strain ε_v^p (black line in Fig 8.9a) is verified to remain zero until the pressure reaches the crush curve, after which it

---

[*] Precisely *quantifying* verification error lags far behind other more important constitutive SQA priorities, so we will be satisfied here and throughout this chapter with assessing agreement between computed and analytical results via a so-called "viewgraph metric," where the error is nebulously bounded by what can be perceived visually, given the plot size.

[†] The only way to ensure a precisely homogeneous deformation in a dynamics finite-element code is to bypass solution of the momentum equation. More correctly, homogeneous loading requires a body force $\underset{\sim}{b}$ identically equal to particle acceleration $\underset{\sim}{a}$, making the momentum equation trivial.

drops along the crush curve as it should. The stress-strain curve (inset in 8.9a) unloads correctly to the user-specified peak strain parameter p_3. For *non-hydrostatic* loading, we have verified (trend-test) that shear-enhanced pore collapse causes inelasticity to commence *prior* to the pressure reaching the crush curve.

Fig. 8.9b simultaneously verifies Kayenta's ability to predict an apparent increase in strength under dynamic loading and its ability to predict different strengths in triaxial extension vs. compression. In that problem, pressure dependence of yield was suppressed and the TXE/TXC strength ratio was set to 1/2, resulting in a tensile strength half as large as the compressive strength.*

Verification: Hendren & Ayier pressurized cylinder

The problem depicted below, solved for subcases of associative and non-associative flow, involves a circular tunnel in a Mohr-Coulomb material loaded in a plane strain configuration. A DTRA contractor provided the analytical solutions. The material parameters are the same as those used in the previous verification problems.
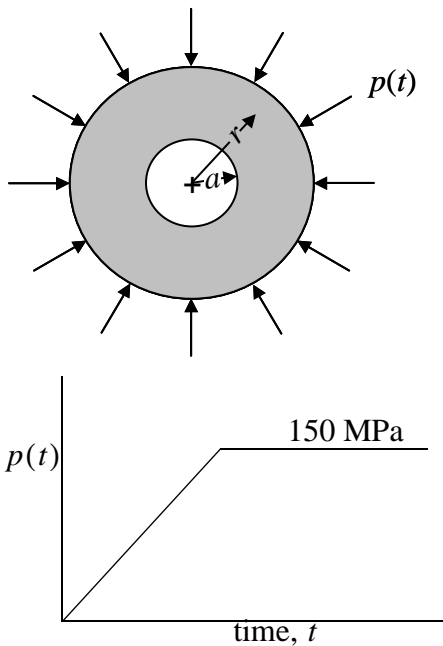
Geometry

Tunnel radius	a	1 m	1 m
Far field radius	b	10 m	10 m

Loading

Internal pressure	p_a	0	0
Far field pressure	p_b	0-150 MPa	0-150 MPa

The results in Fig. 8.10 show that Kayenta solutions agree with analytical results. Though not confirmed conclusively, the very slight discrepancies are hypothesized to result from different strain definitions used in Kayenta and the analytical solution (or possibly host code traction boundary condition issues similar to those discussed earlier).

---

* The TXE/TXC strength ratio applies to TXE and TXC states at the same pressure. When pressure dependence of yield is allowed, the TXE peak in a verification test like this will not *and should not* be 1/2 the magnitude of the TXC peak.

HENDRON & AYIER VERIFICATION RESULTS
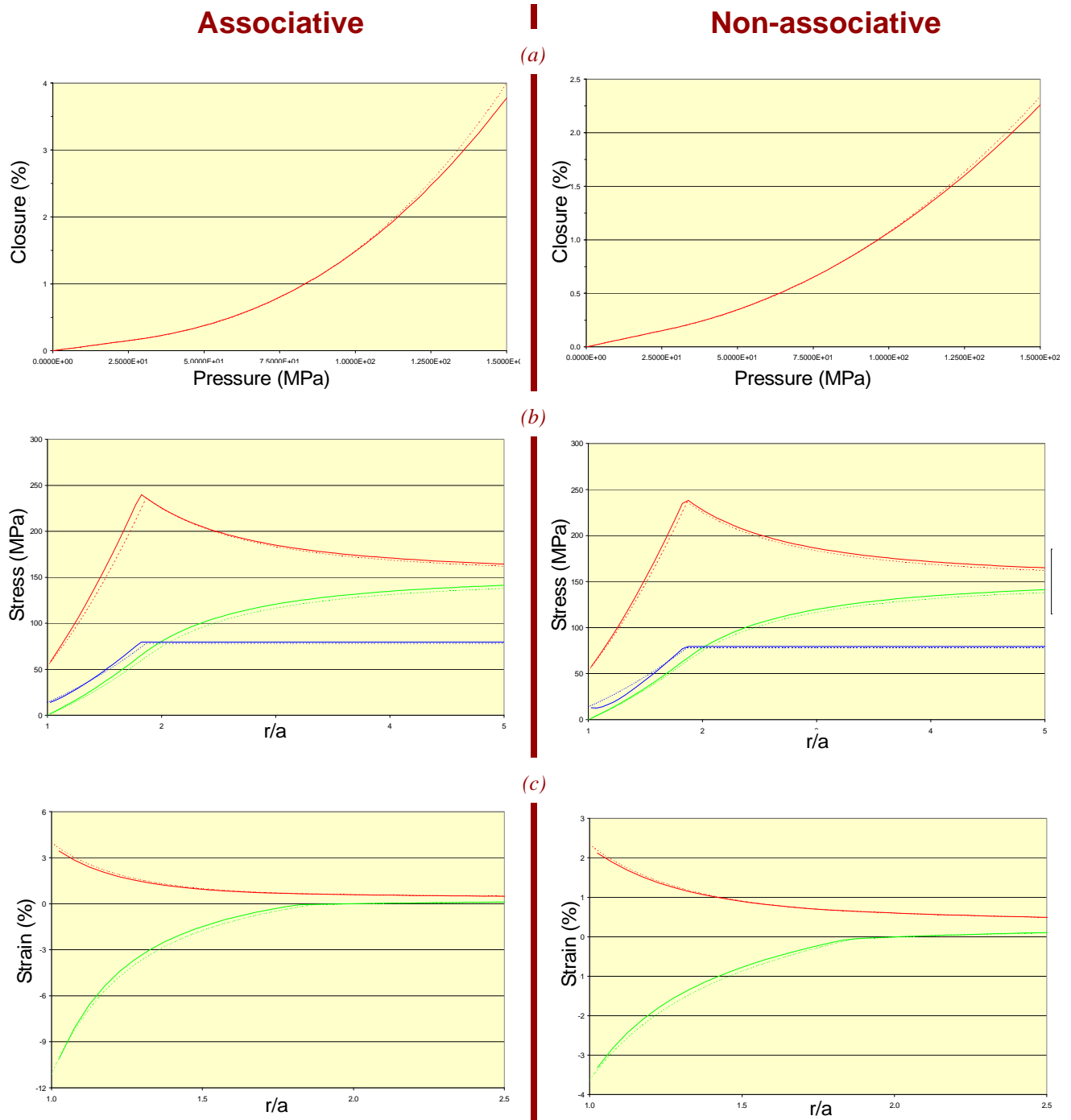
Figure 8.10.   Hendron & Ayier verification problem. Exact (dash) solutions compared with ALEGRA Kayenta simulation (solid). *(a)* Tunnel closure vs. far-field pressure *(b)* Stress components vs. normalized range, *(c)* strain components vs. normalized range.

Elastic free-field wave form (finite-element verification)

This section describes a field-scale test for verifying installation of Kayenta in host finite-element codes. As emphasized earlier, verifying a constitutive model is distinct from verifying its implementation within a finite-element code. After a constitutive model becomes one *of many* components within a much larger finite-element model, the potential sources of solution error expand to now include boundary conditions, artificial viscosity, and other aspects of the host code's method of solving the partial differential equation that governs momentum balance.

As indicated in Fig. 8.11, a time varying velocity (identical to the one later discussed on page 124) was applied at the boundary of a spherical cavity (radius 204m). Kayenta's yield features were disabled to allow predictions for the velocity at the outer radius (470m) to be compared with an analytical *elasticity* solution.* Implementations of Kayenta in two finite-element codes were tested. One code was unable to reproduce the correct response because of bugs in roller boundary conditions. Fig. 8.12 demonstrates that the second code (JAS3D) was capable of repro-
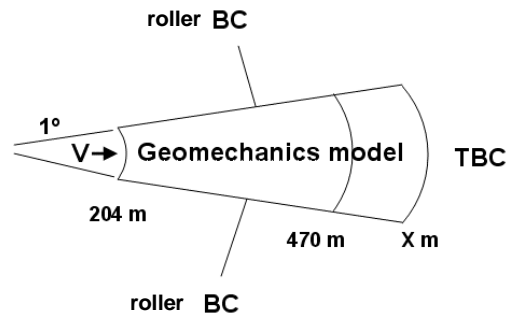
Figure 8.11.   Spherical cavity geometry.

ducing the analytical solution well enough to suggest that *Kayenta* is performing correctly. While the moderate solution error might be attributable to the analytical solution's presumption of small strains, further study (by the code owners, not Kayenta developers) is warranted to determine if the solution errors result from under-integration, or some other aspect of the finite-element model such as artificial viscosity (both codes' solutions were strongly affected by artificial viscosity — default settings for artificial viscosity were insufficient to reproduce the analytical results). This elasticity verification problem is revisited and generalized in the *plasticity* validation test on page 124, where code predictions are compared with data.
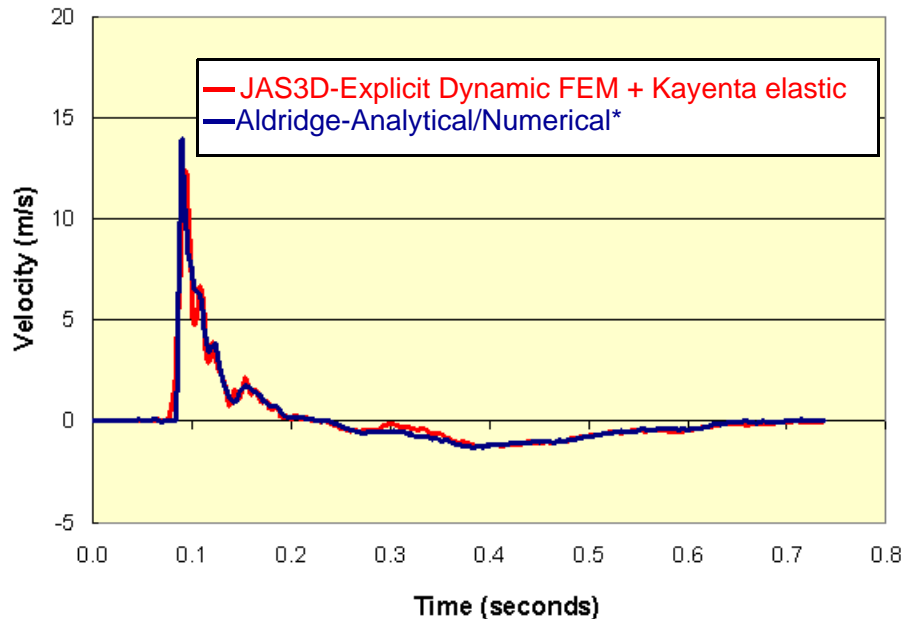
Figure 8.12.   Finite-element vs. analytical/numerical elastic wave velocity at 470 meters from a velocity spherical cavity source at 204 meters.

---

* Aldridge's analytical solution [1] is expressed in terms of integrals that are evaluated numerically in the frequency domain using independent software provided by Aldridge.

Softening verification and validation

Softening and failure is a relatively new capability within Kayenta. As such, the softening and failure implementation is still under development, and its verification and validation is incomplete. This section summarizes only some basic trend testing.

The softening capabilities of Kayenta should be used only in conjunction with additional measures taken within the host code to mitigate mesh sensitivity associated with the change in type of the governing equations that occurs upon the onset of softening. As discussed on page 72 and illustrated in Fig. 8.13, one means of mitigating mesh dependence allows development of localized failure by introducing statistical variability and scale effects in strength.

EXPERIMENT

Conventional damage model without variability
Same model with spatial variability

(major radial cracks are shown in black for clarity)
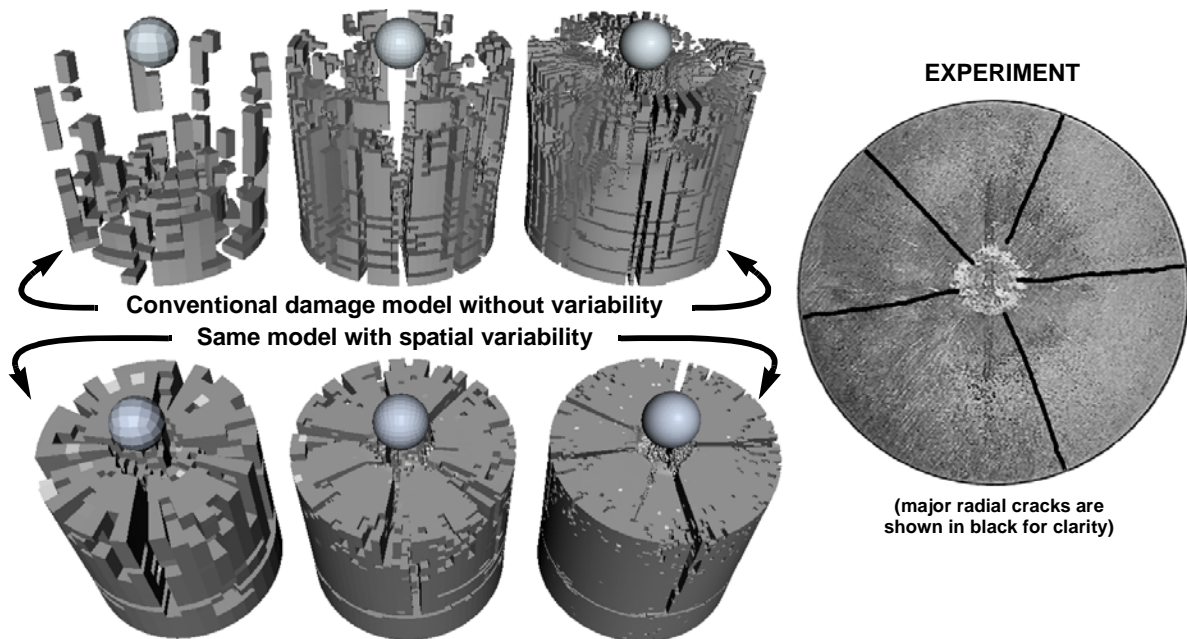
Figure 8.13. Reduced mesh dependence and improved accuracy in dynamic indentation (tungsten carbide sphere impacting SiC-N ceramic at 500 m/s). All simulations show intact material at the same moment in time, but at three mesh resolutions. All use the Kayenta damage model with the same median properties. Simulations in the bottom row merely allow the material properties to deviate from the median based on experimental evidence for aleatory uncertainty and size effects.

When statistical uncertainty is incorporated in a simulation, verification and validation testing becomes considerably more difficult since one must run a statistically significant number of simulations to check for convergence of results toward an analytical distribution function. One such study, summarized in Fig. 8.14, used the "**FAILSTAT**" user control parameter (see page B-8) to verify that the onset of failure under nominally homogeneous loading in spherical tension was indeed consistent with the user specified failure line in Weibull space. The ordinate in a Weibull plot is the indicated transformation of the complementary cumulative probability P_s which may be interpreted as the probability the sample is safe at the specified stress level. The abscissa is the log of the stress

111

normalized by the median failure stress. Fig. 8.14 also shows a very light level of valida-
tion by illustrating that observed deviations of measured strength data from a Weibull line
are finite sampling effects consistent with similar deviations in finite sampling of *exactly*
Weibull distributed data.
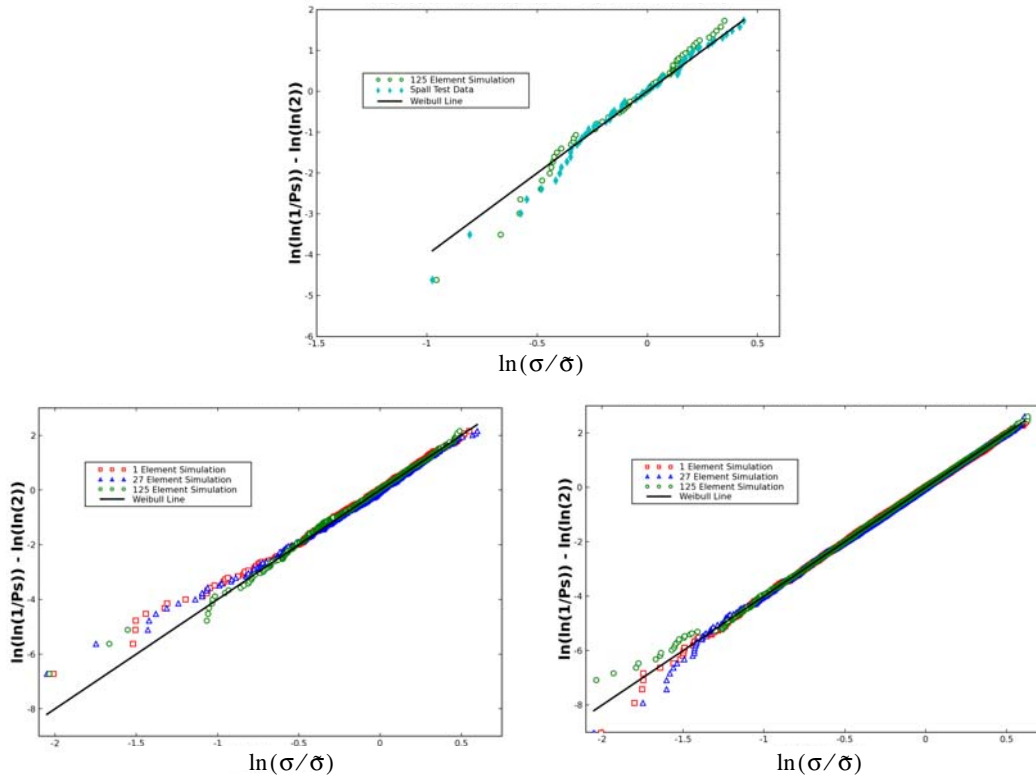
Figure 8.14.   Reduction in sampling error with number of data points.   The top figure com-
pares experimental data against numerically generated failure strengths that are *exactly* Weibull
distributed with the same Weibull modulus. The lower two figures show simulated data for the
onset of failure (using the "FAILSTAT" control parameter) for three mesh resolutions to demon-
strate that the failure statistics are mesh insensitive and approach the Weibull distribution as the
number of realizations is increased.

Users should always assess believability of their simulations by performing mesh sensitiv-
ity analysis. This verification and validation practice is even more essential in any soften-
ing or failure simulation. Accounting for statistical variability and scale effects appears to
be *necessary* for obtaining realistic predictions of material failure. However, in the interest
of full disclosure, it should be noted that variability and scale effects are not *sufficient* to
ensure mesh insensitive results. Our simulations of Brazilian failure (see Fig. 5.8) pro-
duced failure statistics having trends consistent with laboratory data, but the quantitative
median strength was found to be mesh dependent.

9. Parameterization (calibration)

Appendix A describes how to characterize a material for Kayenta. Using these procedures, several materials have already been fit, as summarized in Fig. 9.1 (compare these with Figs. 1.1 and 3.3). Kayenta parameters for these materials are in Appendix B.
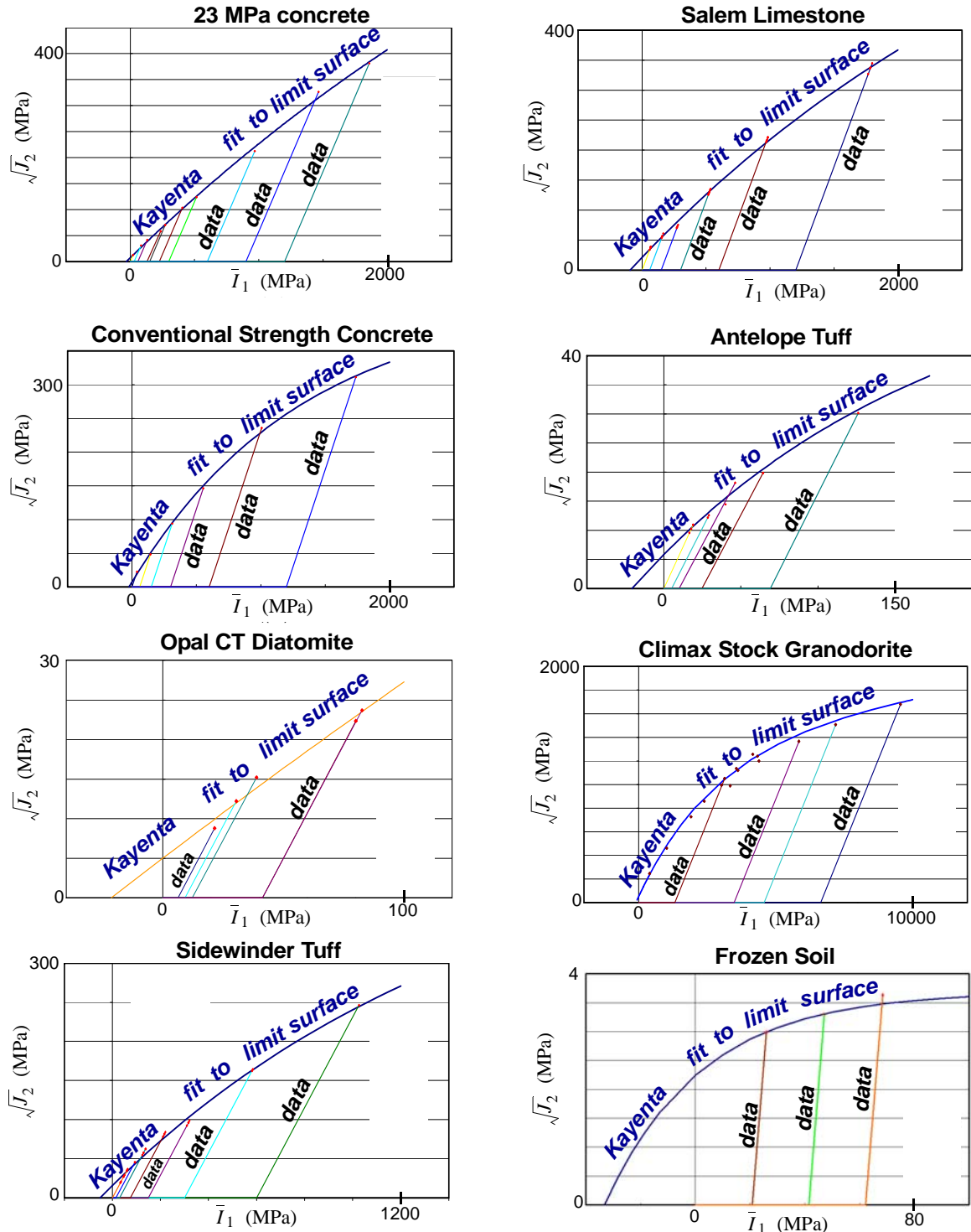
Figure 9.1.   Meridional limit curves for some materials already parameterized to Kayenta.

Nonlinear elasticity

Figures 9.2 and 9.3 demonstrate the ability of Kayenta's nonlinear elasticity fitting functions (Eqs. 4.10 and 4.9) to reproduce nonlinear elasticity data. Parameters were assigned using the least-squares model calibration tools described in Appendix A.
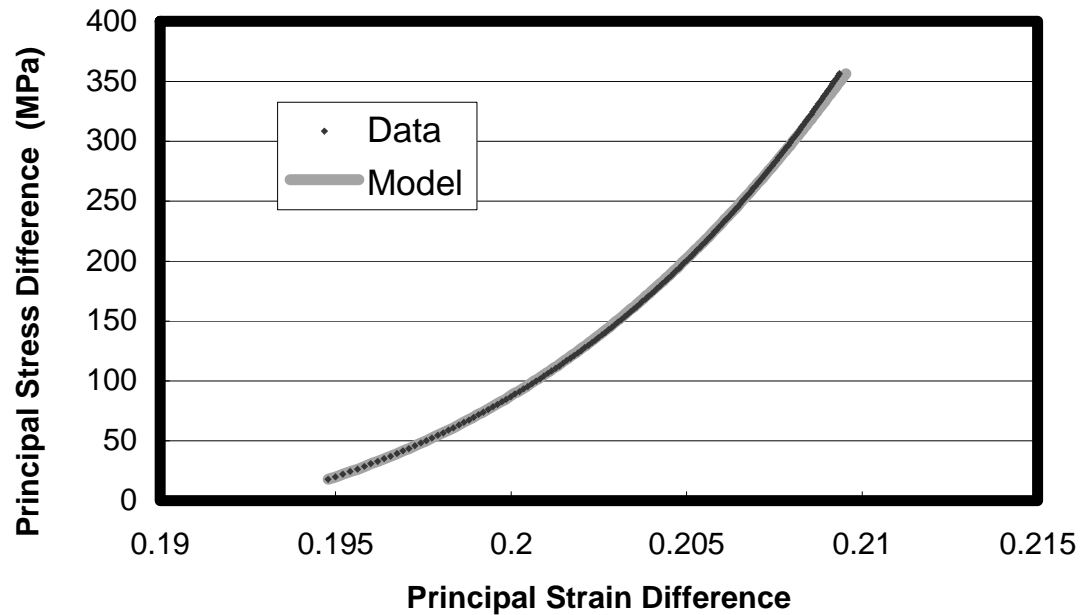
Figure 9.2. *Nonlinear elasticity in shear.* This figure shows Kayenta's fit to concrete data [58] from the unload portion of a triaxial compression test conducted at a confining pressure of 200 MPa. Here, the principal stress difference is plotted against the principal strain difference, thereby making the slope equal to twice the shear modulus.
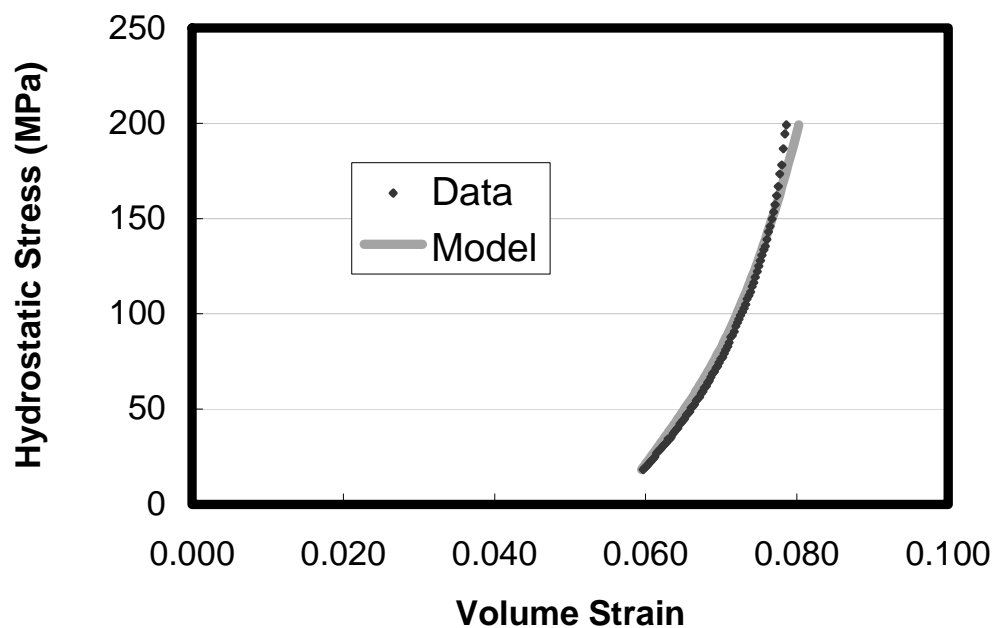
Figure 9.3. *Nonlinear elasticity in hydrostatic loading.* This figure shows Kayenta's fit to concrete data [58] from the unload portion of a hydrostatic compression test from 200 MPa. Here, the slope equals the bulk modulus.

114

Elastic-plastic coupling

For many materials, elastic moduli are unaffected by inelastic deformation. However, Fig. 9.4 shows data for a material whose elastic properties *are* affected by inelasticity. Modeling this effect requires using the enhanced moduli fitting functions, Eqs. (4.33) and (4.34), which permit the shear and bulk moduli to vary with equivalent plastic strain (determined from data by the residual strain upon unloading to a zero stress, as explained in Appendix A). For Kayenta to be considered a good fit to data, the simulated unloading curves merely need to be parallel to experimental unloading curves (not necessarily overlapping unless the data and simulation unload from the same strain).

(a)

HYDROSTATIC LOADING

(b)

TRIAXIAL LOAD DATA CONVERTED TO SHEAR DATA
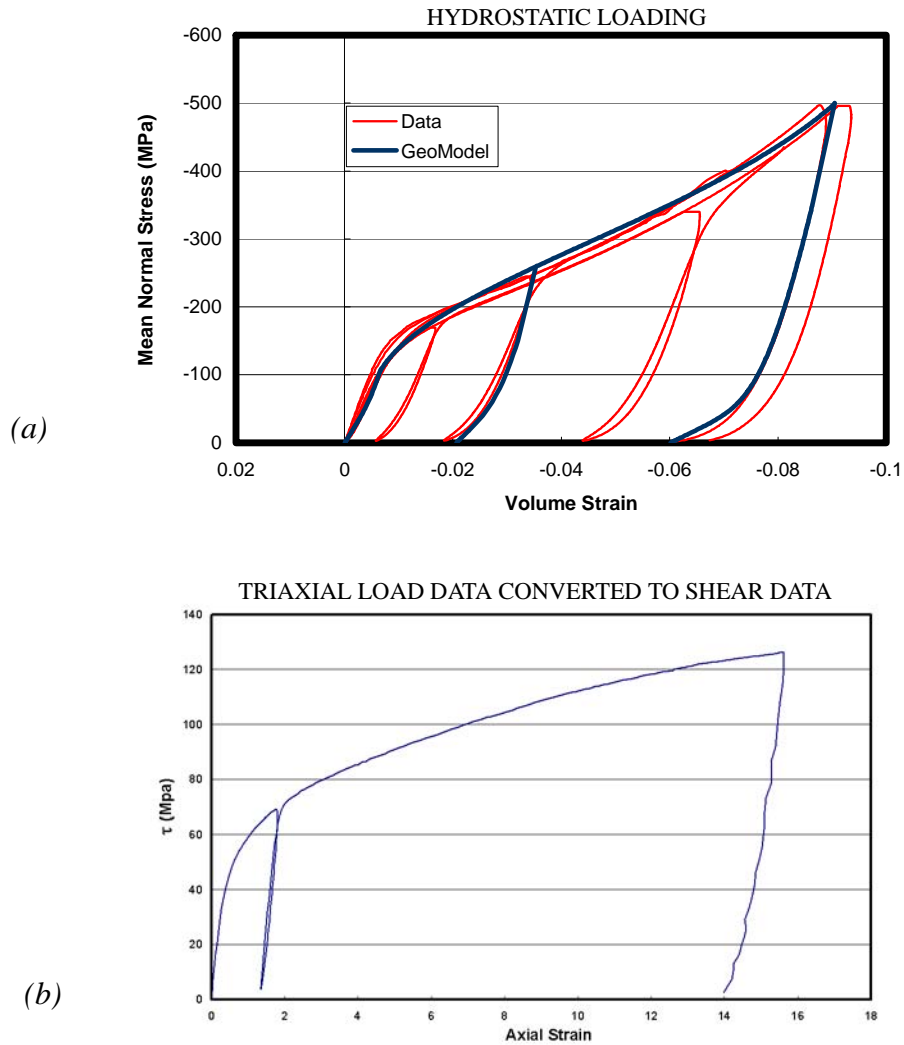
Figure 9.4.   Elastic-plastic coupling: deformation-induced changes in elastic moduli (Salem Limestone).   (a) the tangent bulk modulus can change in response to changes in porosity (i.e., volumetric plastic strain). (b) Likewise, the tangent shear modulus, especially at low shear stresses, can change in response to plastic deformation.

Triaxial Compression

Triaxial compression (TXC) and triaxial extension (TXE) testing is integral to parameterization of Kayenta. By performing a series of tests, as described in Fig. 3.3, the limit state (onset of softening) can be mapped out. For example, Fig. A.5(a) on page A-6 shows raw data from a a suite of TXC tests, indicating how the peak values in each test provide one data point on Kayenta's limit surface Fig. A.5(b). Data from a similar set of experiments for concrete, along with Kayenta's least-squares fit of Eq. (4.8) are shown in Fig. 9.5. Figure 9.1 shows similar plots for other materials. Appendix A describes the least-squares fitting procedures in more detail.

$\sqrt{J_2}$ *MPa*

A = 1255.68 MPa
B = 1.93E-04 1/MPa
C = 1248.20 MPa
θ = 0.0 Rad

Data

Model

$-I_1$ *MPa*
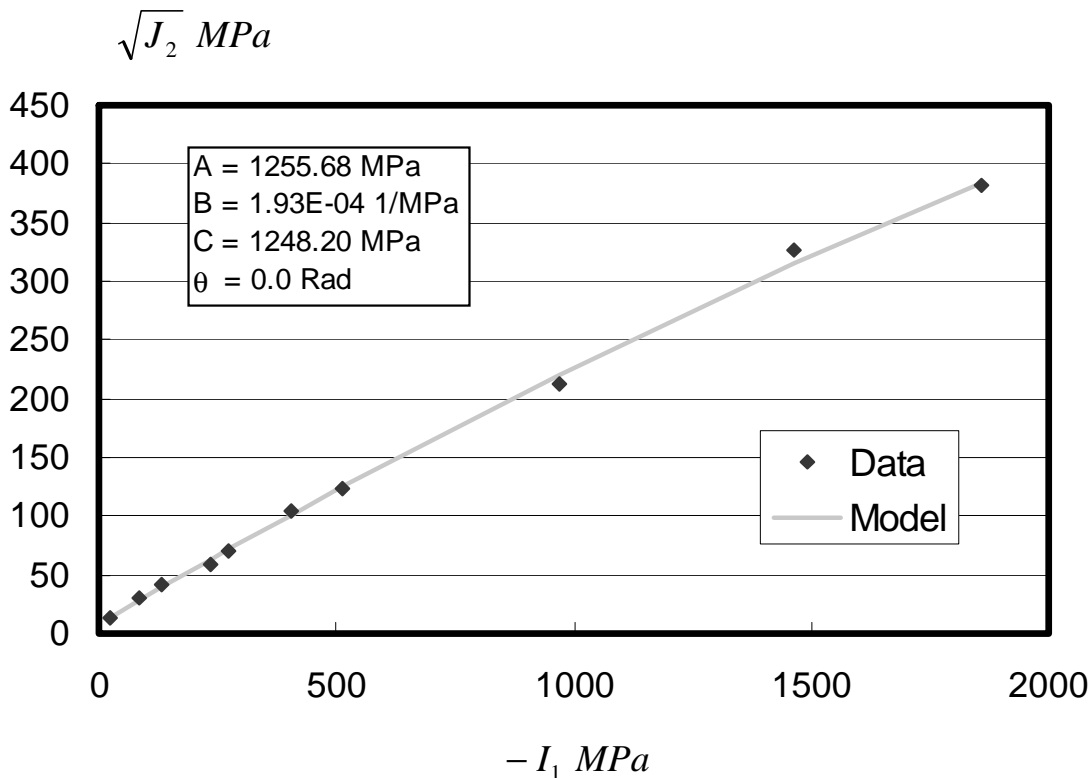
Figure 9.5.   Shear failure limit curve compared with concrete data.   Ref. [58].

Recall that triaxial testing normally begins with a hydrostatic "load-up" phase, indicated by the horizontal red arrow Fig. 9.6a (where $\sqrt{J_2} = 0$). During the hydrostatic leg, deformation is initially nonlinearly elastic until the virgin yield surface is reached, at which time microscale stress concentrations caused by the presence of pores become too large to resist elastically. Continuing to push the hydrostatic stress to higher levels results in inelastic pore collapse with associated hardening (expansion) of the yield surface. In Fig. 9.6, the target hydrostatic stress state for a given experiment (which marks the transition from the hydrostatic leg to the triaxial leg) was $P = 400$ MPa, giving an I_1 value of -1200 MPa. Pressure-volume data taken during the hydrostatic leg may be used to deter-

mine Kayenta parameters $\{p_0, p_1, p_2, p_3\}$ by following instructions in Appendix A. Because multiple triaxial experiments must be performed to fully characterize a geological material, variations observed during hydrostatic loading from different tests can be used to quantify the material property variability.

(a)

(b)
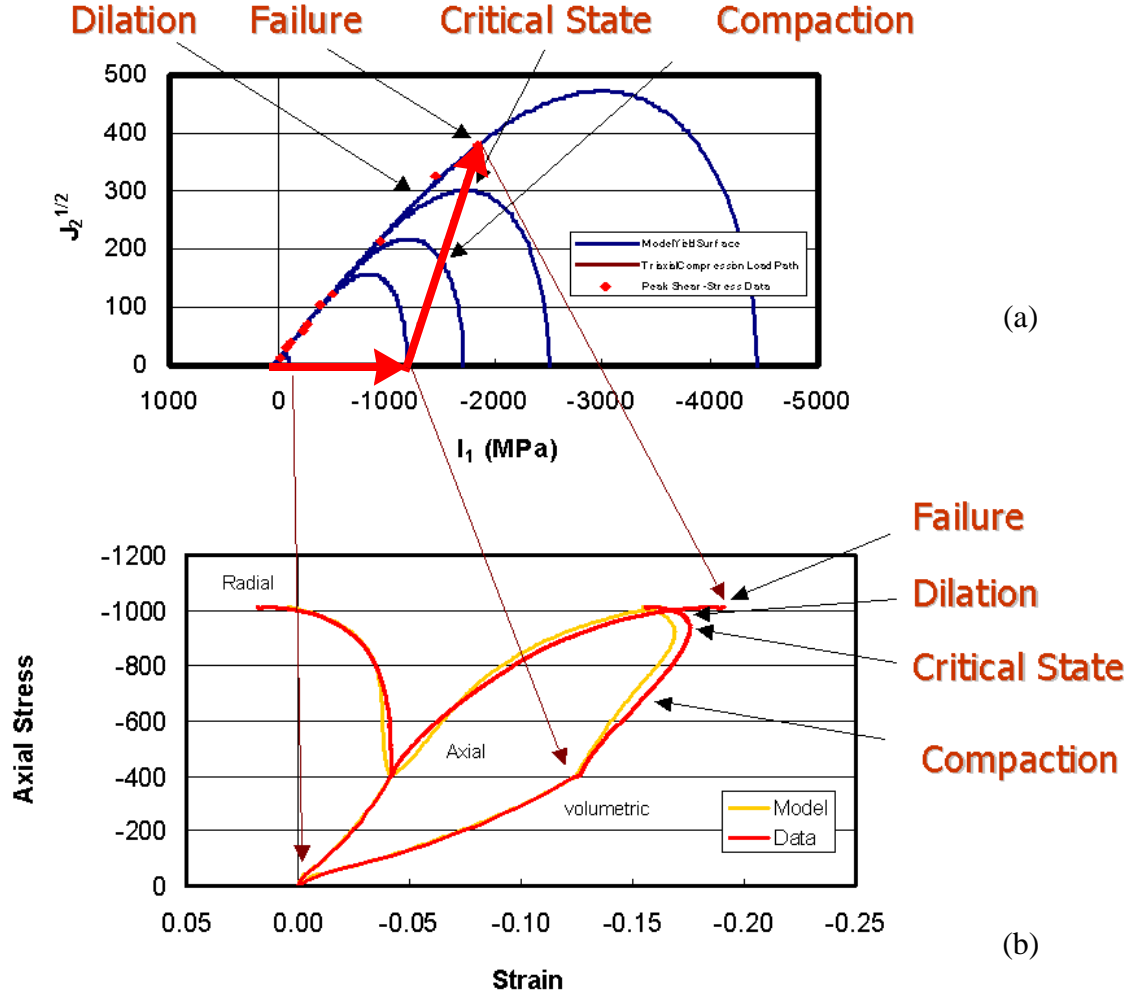
Figure 9.6.   Progression of the hardening yield surface (family of blue lines) under a triaxial compression test (red path), illustrated with correspondence of the meridional plane to the stress-strain diagram.
    The straight red line segments shown show this two-stage stress trajectory (hydrostatic loading followed by triaxial loading) in the meridional plot of $\sqrt{J_2}$ (which is proportional to the effective shear) versus $\bar{I}_1$. Shear-enhanced dilatation corresponds to reaching a zero local yield slope.

After the hydrostatic leg, the triaxial leg (angled red arrow in Fig. 9.6a) commences by increasing the axial load on the specimen while holding the lateral stress constant. As explained on page 18, the stress path follows a straight trajectory in the meridional plane with a slope given by

$$\frac{d(\sqrt{J_2})}{d(\bar{I}_1)} = \frac{1}{\sqrt{3}}$$

(9.1)

The transition from hydrostatic to triaxial loading is reflected by a pronounced change in slope in the stress-strain plot of Fig. 9.6. As the axial stress is increased during the triaxial leg, the yield surfaces continues to harden outward even more, now further assisted by the presence of a nonzero stress deviator. In Fig. 9.6 the slope of the yield surface is initially negative at the stress state (i.e., where the straight red load path and curved blue yield surface lines intersect). Consequently, the outward *normal* to the yield surface during this early part of the triaxial phase has both a deviatoric component *and a compressive isotropic component*. When the normal to the yield surface is compressive, the inelastic volumetric strain will be compressive as well. However, the isotropic component of the yield surface normal *changes direction* towards the end of the triaxial leg (i.e., the local slope of the yield surface changes sign), which means that the inelastic volumetric strain is *dilatational* (expanding) even though all stress components are compressive. The "critical state" at which the yield surface has a zero local slope on the load path marks the onset of shear-enhanced dilatation. Thus, as illustrated qualitatively in Fig. 9.7 and explained in detail in Appendix A, triaxial loading is used to determine parameters in Kayenta that govern yield surface evolution and cap curvature.
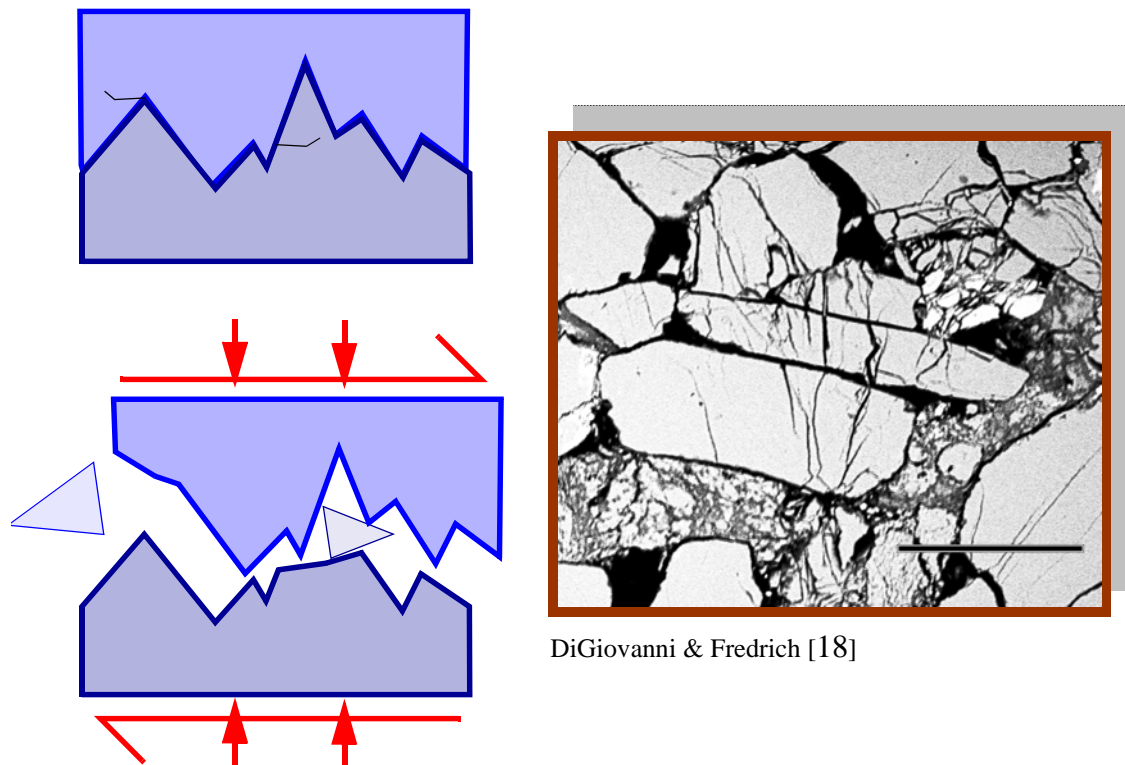
DiGiovanni & Fredrich [18]

Figure 9.7. Shear-enhanced dilatation under compression. The exaggerated schematic shows that crack faces must overcome surface incompatibilities — they cannot slip over each other without opening even if they are in compression. Moreover, fragments of broken material can become lodged in the crack face and cause crack opening by their rotation. Crack kinking (in the direction of Mode I loading) further contributes to the dilatation associated with crack opening. The dark regions in the micrograph [18] are pores (which collapse under sufficient pressure). The cracks in inclusions produce "micro-rubble" that ultimately generates, through rotation, inelastic volume increase under shear loading even if all principal stresses are compressive.

Physically, an increase in inelastic volume during compression (which is quite commonly observed for brittle materials) is typically attributed to the growth of microcracks under shear. As the surfaces of these cracks move relative to one another, the crack must open up (dilatate) both to overcome geometric incompatibilities in their surface roughness and to permit crack kinking. This interpretation of shear-enhanced dilatation is illustrated schematically and through SEM imaging in Fig. 9.7.

Parameterization: Rate dependence

Kayenta's relaxation parameters $(T_1, \ldots, T_7)$ may be determined through a series of lab-scale laterally-confined Kolsky bar tests [Fig. 9.8] in which a sample is subjected to uniaxial compression at various strain rates.
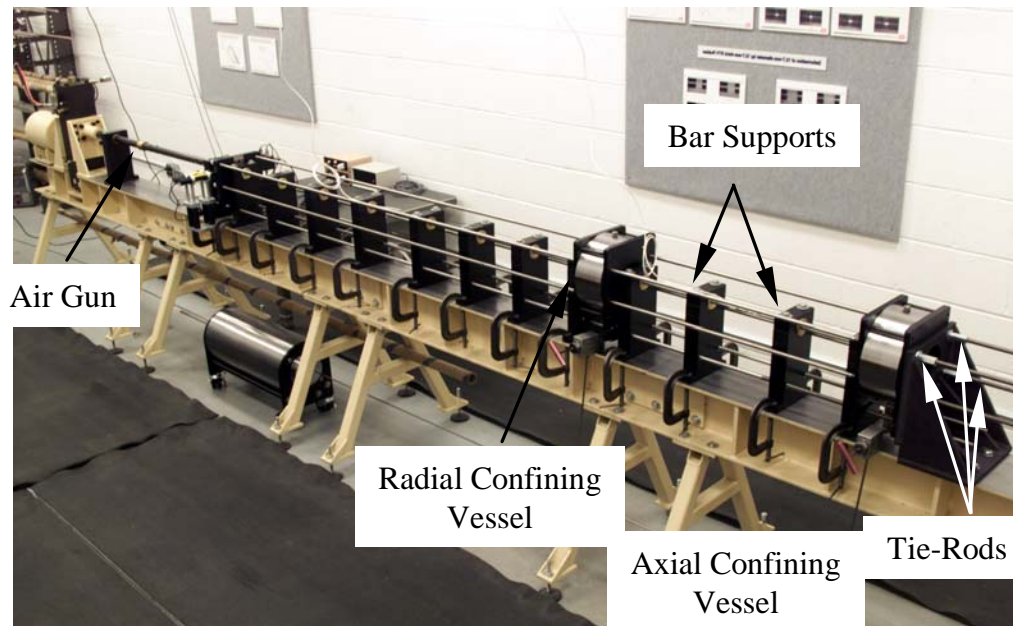
Figure 9.8.   Kolsky (split Hopkinson) bar apparatus used to obtain data in Fig. 9.9

Figure 9.9 shows results for a series of Kolsky (split Hopkinson) bar strain rate tests conducted on unconfined compression specimens of Salem Limestone [25]. The peak stress in these experiments is used to assign values of Kayenta relaxation parameters to properly correlate apparent strength with strain rate. As seen, the unconfined compressive strength increases with strain rate and is well accommodated by Kayenta theory.

For a discussion of how the data in Fig. 9.9b are used to assign values to $\{T_1, \ldots, T_7\}$, see Appendix A.

119
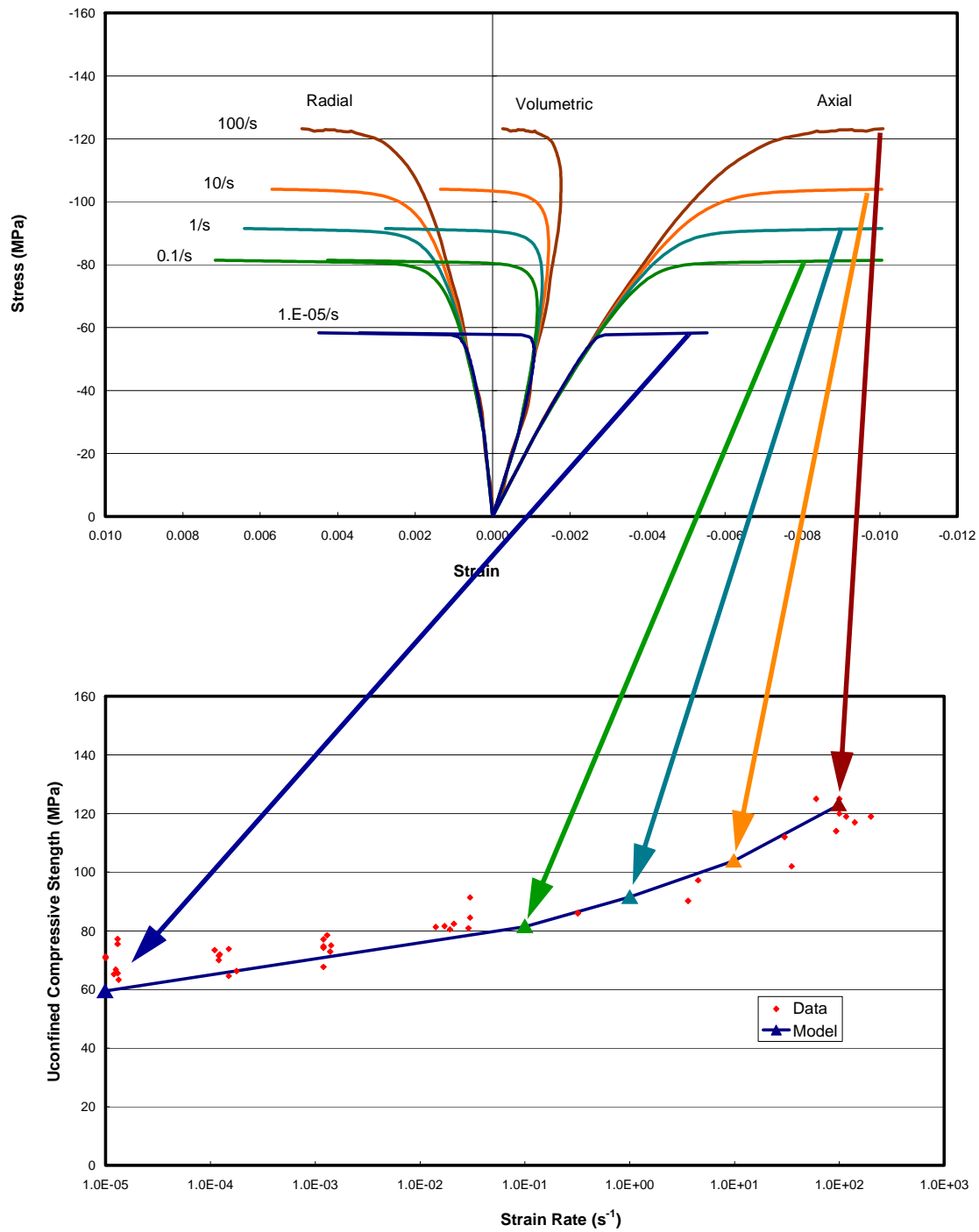
Figure 9.9. *Suitability of Kayenta's overstress rate-dependence model to match observed data.*
(a) Model predictions of stress-strain behavior at various strain rates. (b) Corresponding Kolsky (Hopkinson) bar unconfined compressive strength as a function of strain rate

120

10. Building confidence in the physical theory

In a weak sense, demonstrating (as we did in the previous chapter) that Kayenta is capable of being parameterized from controlled laboratory data lends some credibility to the physical foundations of the model. However, truly *validating* a model after its parameters have been determined from standard laboratory data requires showing that the model can, *without any change in pre-calibrated parameters*, predict material response under different (non-calibration) loading scenarios. Ideally, to validate *a constitutive model* (not its implementation into a host finite-element code), one would prefer to compare the model predictions against test data from homogeneous loading experiments that were different from the homogeneous loading tests conducted for calibration.

Thorough testing of any material constitutive model *along with its implementation in a host code* must, of course, include simulation of applications for which model predictions can be compared with structural response measurements. The goal is to assess the degree to which the integrated model (i.e., its installation into a host code) is capable of predicting material system response to non-trivial loading scenarios.

Parameterization entails fitting to a subset of discrete points in parameterization data tables (e.g., as described on page 116, the limit function is parameterized by using only the *peak* stress values, not all values measured in the test). Model validation therefore includes assessing the fitted model's ability to interpolate well between *other* points in these stress-strain response curves (i.e., points that were *not* used in calibration). Similarly, Kayenta's rate dependence parameters are determined by using only the *peak* stress values in Kolsky bar experiments. Therefore, the model's ability to match the *other* data points in those experiments is a validation test.

In addition to merely ensuring that all data in parameterization tests are well modeled, a better validation test should exercise the model in application domains in which multiple physical mechanisms are acting simultaneously. The goal is to assess whether or not Kayenta parameterization instructions in Appendix A can lead to a high-quality set of material model properties that are *predictive* in general loading scenarios. This chapter describes some validation problems that have been studied to date. In all cases, these problems were run *using only the single Kayenta parameter set obtained from calibrating to <u>other</u> data for the material — no parameter adjustments were made to improve model agreement for these tests*.

Post-calibration Triaxial loading

The nonlinear elasticity Eqs. (4.9) and (4.10) are parameterized from shear and hydrostatic unloading data. The shear limit function Eq. (4.39) parameterized through *peak states* in triaxial testing. The crush curve Eq. (4.68) parameterized through purely hydrostatic testing. Once parameterized in this way, Kayenta may be applied to predict the irreversible plastically-hardening stress-strain response at a *variety* of other stress paths. For example, Fig. 10.1 compares Kayenta predictions with simple triaxial data at various confining pressures (these simulations all use *a single set* of Kayenta parameter values).
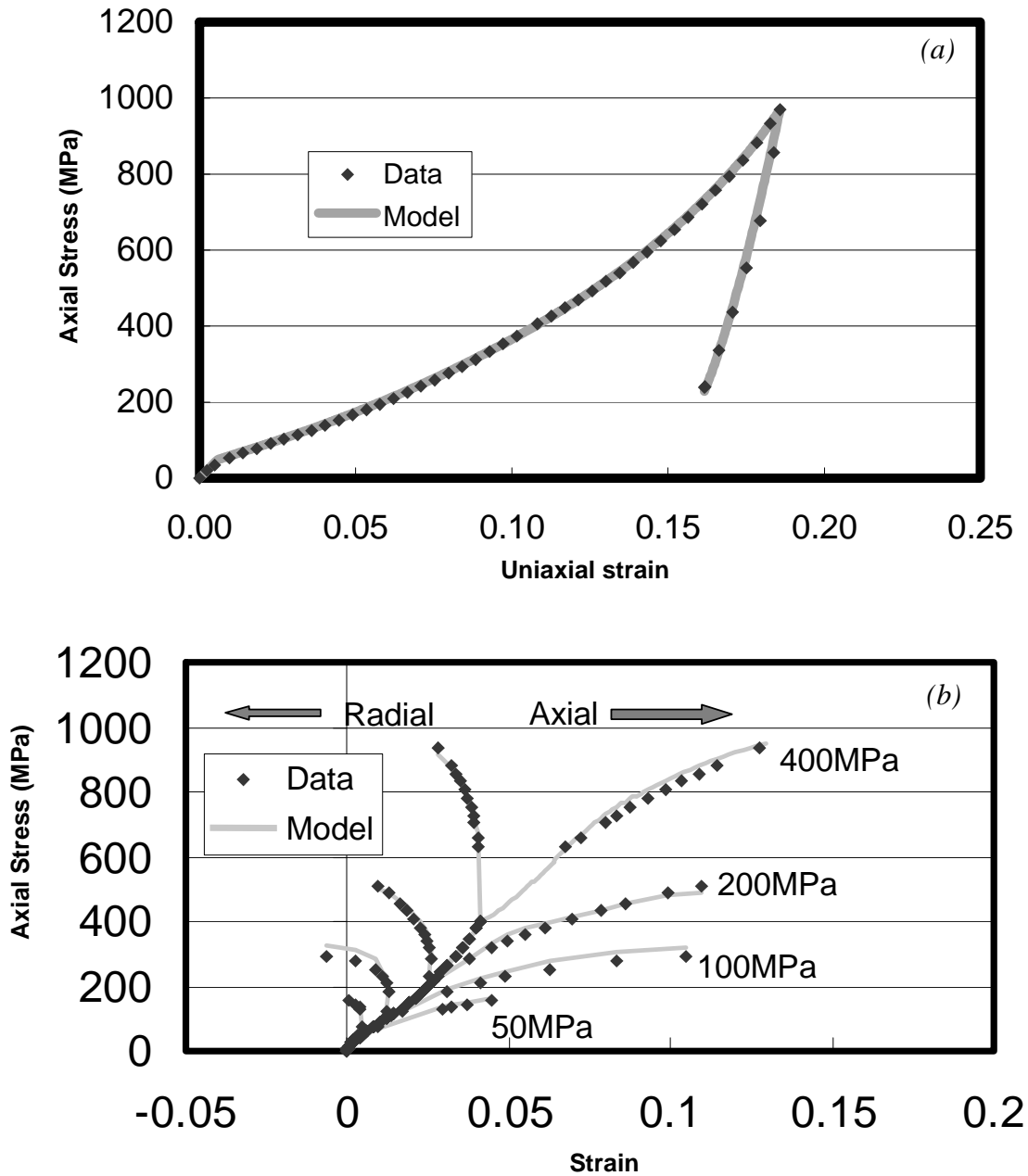
Figure 10.1.   (a) Kayenta prediction of uniaxial strain loading. (b) Kayenta predictions of triaxial stress-strain response at various confining pressures.   From Ref. [58]. The ability of a single parameter set to agree so remarkably well with this suite of data is a validation.

Field-scale penetration

Figure 10.2 shows results from a *pre-test* prediction of depth of penetration and displacement histories. In tests like these, material constitutive models are often considered "above average" if they are predictive within 20%. As seen, Kayenta performed exceptionally well by this metric.
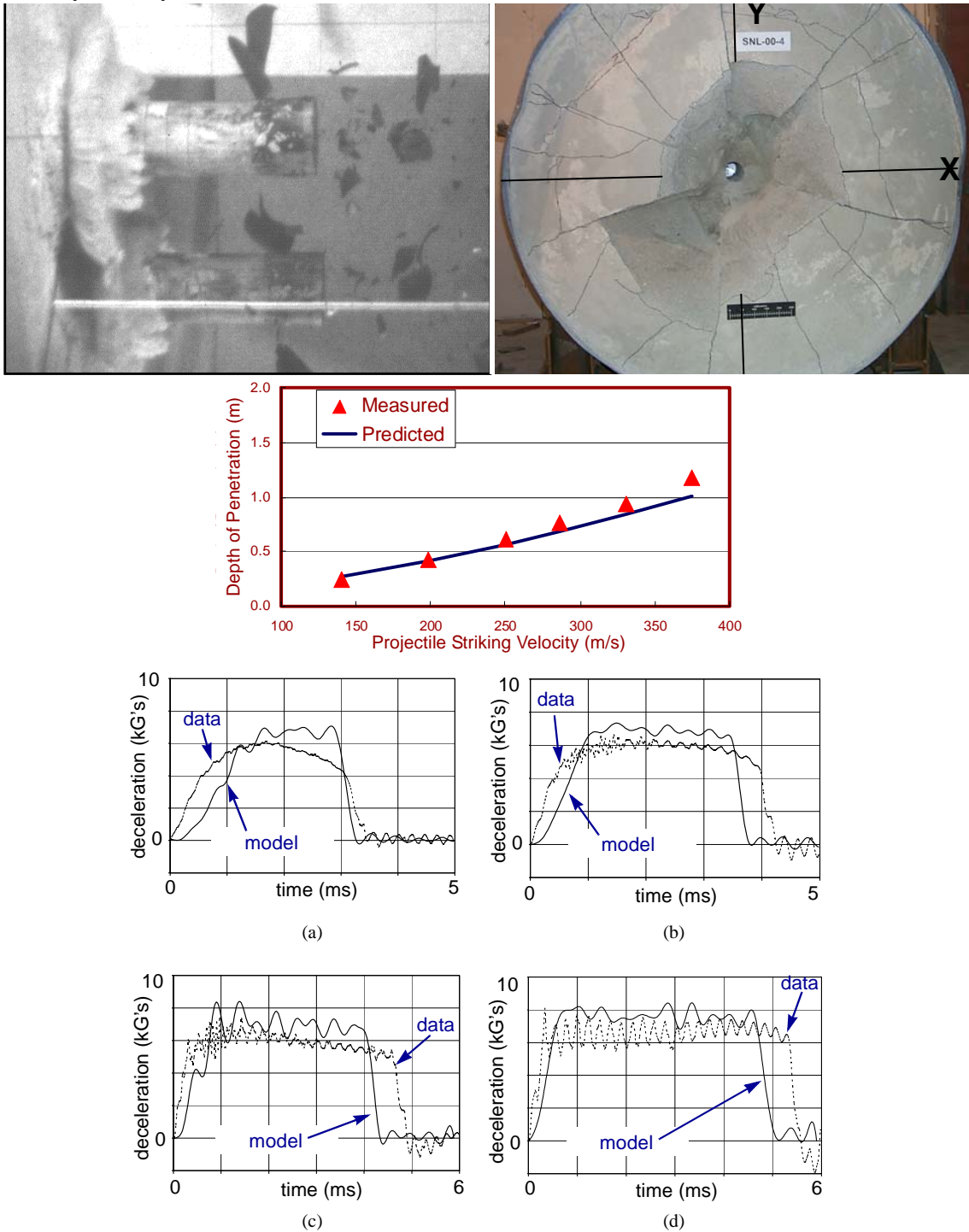
Figure 10.2.   After Kayenta was fitted to laboratory-scale material property tests, it was used to predict projectile penetration depth using spherical cavity expansion analysis.

Free field wave form for spherical shock loading

Figure 10.4 shows displacement and velocity histories for an underground test in which a wave propagates from an explosive point source. A measured velocity history at a point 204 meters from the source was used as the velocity boundary condition of the simulation. The goal was to predict a second measured velocity history at a point 470 meters from the source (see Fig. 10.3). Unlike the similar *elasticity* verification test described on page 110, this validation test used elastic-*plastic* field-scale parameters that were determined by applying Kayenta's calibration procedures described in Appendix A *(back-fitting alteration of these independently determined calibration parameters was disallowed, as should be the case for any validation test).*
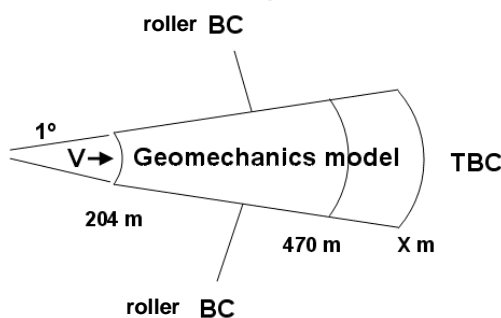
Figure 10.3.   Spherical cavity geometry.
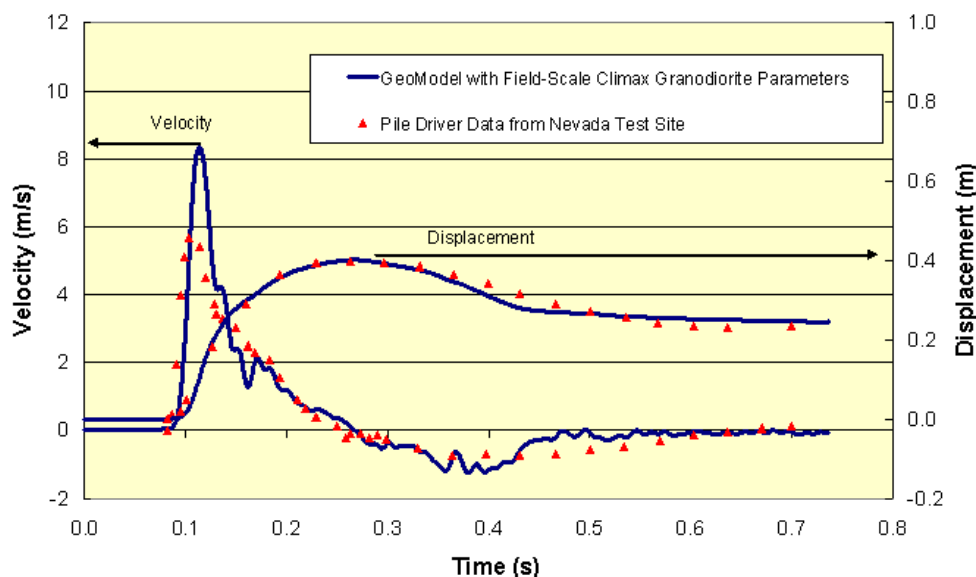
Figure 10.4.   Kayenta + JAS3D finite-element prediction (blue) vs. measured (red) velocity and displacement at 470 m. from a spherical cavity velocity source at 204 meters.

Kayenta (along with its implementation within the host finite-element code, JAS3D) comes far closer to matching data than simpler models such as non-hardening Von Mises plasticity, indicating that Kayenta's advanced physical features (especially pressure sensitivity) are important. Because Kayenta falls short of a *compelling* agreement with data, further study is warranted. Unlike the verification study presented on page 110, this validation simulation is over-predicting peak velocity. As was the case in the verification study, code predictions were strongly affected by artificial viscosity, suggesting that disagreement with data *might* be rooted in host code problems as much as shortcomings of Kayenta. Of course, natural spatial variability of in-situ rock (which is neglected in the simulation) may play a role, as might the response time of gauges used to acquire the data, or myriad other possible error sources.

This concludes our overview of preliminary validation testing. More extensive model validation activities (now underway) require publication of this theory and user's guide to provide a resource document that allows analysts to apply Kayenta properly.

124

11. Closing Remarks

The preceding chapters have attempted to elucidate the physical foundations and domain of applicability of Sandia's Kayenta. This model was developed in response to the need for a predictive model that could be used for a wide range of applications while maintaining numerical tractability in the context of Sandia's solid mechanics finite-element software. Three key applications for this work are in projectile penetration research, analysis of hard and deeply buried targets, and reservoir-scale modeling of formation compaction caused by pore pressure drawdown during oil or gas production. With the emergence of the capability to simulate the large-scale mechanical behavior of complex geosystems by virtue of recent advances in software and hardware, Sandia recognized the need to enhance the material modeling capabilities for geomaterials. A large-scale, long-term effort was begun that brings together activities in laboratory testing, basic research, software development, verification, validation, documentation, and quality assurance. The goal is to provide a rock mechanics predictive capability that fully accounts for the complex nature of in situ rock masses. While this is an on-going program, Kayenta has reached a stage of maturity that warrants documentation of the effort to date. Kayenta is a genuine unification and generalization of simpler models, and as such it is capable of satisfying the needs of almost any structural application involving geomaterials. While "first-principles" microscale theories have influenced the general model framework, physically motivated phenomenological judgements about relations between stress and strain have been given ultimate priority to more accurately match observed laboratory behavior.

In the laboratory, most rocks exhibit nonlinear elastic deformation upon unloading and re-loading, hysteresis loops, different behavior in extension than in compression, strain-rate sensitivity, pressure dependence, and post-peak softening. Moreover, high porosity rocks under compressive mean stresses and non-zero deviatoric stresses, involve a complex interplay of deformations from competing mechanisms including pore collapse and microcrack-microvoid development, which occur simultaneously allowing macroscopic pre-failure dilatation to occur even as pores continue to collapse. In addition, the strain-rate sensitivity of some porous rocks depends on the predominant deformation mechanism, e.g., the strain-rate sensitivity of shear and extensional failure is different from that of pore collapse, and the strain-rate sensitivity itself may be pressure dependent. This report summarizes the progress toward achieving a realistic rock constitutive theory that can be calibrated via standard laboratory experiments and is numerically *tractable* for massively parallel calculations using tens of millions of three-dimensional finite elements and loading conditions that involve ground shock and other non-quiescent processes. While Kayenta has achieved many of the stated objectives, there is still much to be accomplished. Current model-enhancement activities (to be documented in future reports) include pressure dependence of the extension/compression strength ratio, softening and failure (fracture), anisotropic jointed rock behavior (as observed in situ), and natural spatial variability resulting in localization.

Closing Remarks

APPENDIX A.
Parameterizing Kayenta

The following steps describe how to determine values for parameters used in Kayenta. In many cases, specialized parameterization software (e.g., **HYDROFIT, SHEARFIT,** etc.) was used to perform nonlinear regression to determine optimized parameter values. This supplemental software, which applies nonlinear least squares fitting is available from Arlo Fossum. Alternatively, nonlinear optimization is available via the "Solver" add-in of MS Excel.

STEP 1. **Use hydrostatic pressure vs. total volumetric strain data to obtain the nonlinear elastic bulk modulus parameters (b_0, b_1, and b_2) as well as the crush curve parameters** p_0, p_3, p_1, p_2. Hydrostatic data are used to obtain the nonlinear bulk modulus parameters in Eq. (4.9),

$$K = b_o + b_1 \exp\left(-\frac{b_2}{|I_1|}\right) \tag{A.1}$$

as well as the parameters in the crush curve, Eq. (4.69),

$$p_3 - \bar{\varepsilon}_v^p = p_3 e^{-(p_1 + p_2\bar{\xi})\bar{\xi}}, \text{ where } \bar{\xi} = \bar{X} - \bar{p}_0 = 3(\bar{p} - \bar{P}_E) \tag{A.2}$$

First express data as a column or space delimited table with the first column being total volume strain $\bar{\varepsilon}_v^{\text{tot}}$ and the next column $\bar{X} = 3\bar{p}$, where $\bar{p}$ is the pressure (positive in compression). Determine the parameters in Eq. (A.1) using Fossum's **HYDROFIT** program* (which assumes linear elasticity when $\bar{X} < \bar{p}_0$). The **HYDROFIT** program employs standard nonlinear regression fitting procedures [44] and includes parameter sensitivities [i.e., derivatives of Eq. (4.69) with respect to each parameter]. The input file for the **HYDROFIT** program contains one line with five values (initial guesses for the parameters p_3, p_1, p_2, p_0, b_0 *in that order*) and a second line that contains five integers, each having a value 1 or 0 to indicate whether that parameter is to be optimized (if not, its value is fixed). The peak inelastic volume strain, p_3, roughly equals the initial porosity. Refer to Fig. 4.14 for guidance on how to set initial guesses for the other crush parameters. The **HYDROFIT** program outputs optimized values for p_0, p_3, p_1, p_2, b_0, b_1, and b_2.

---

* **HYDROFIT** is available upon request. At present, this software presumes linear elasticity when $\bar{X} < \bar{p}_0$. If the data show nonlinear elasticity, as in Fig. A.1, **HYDROFIT** will provide only approximate parameter values. At present, fitting nonlinear parameters is not automated.
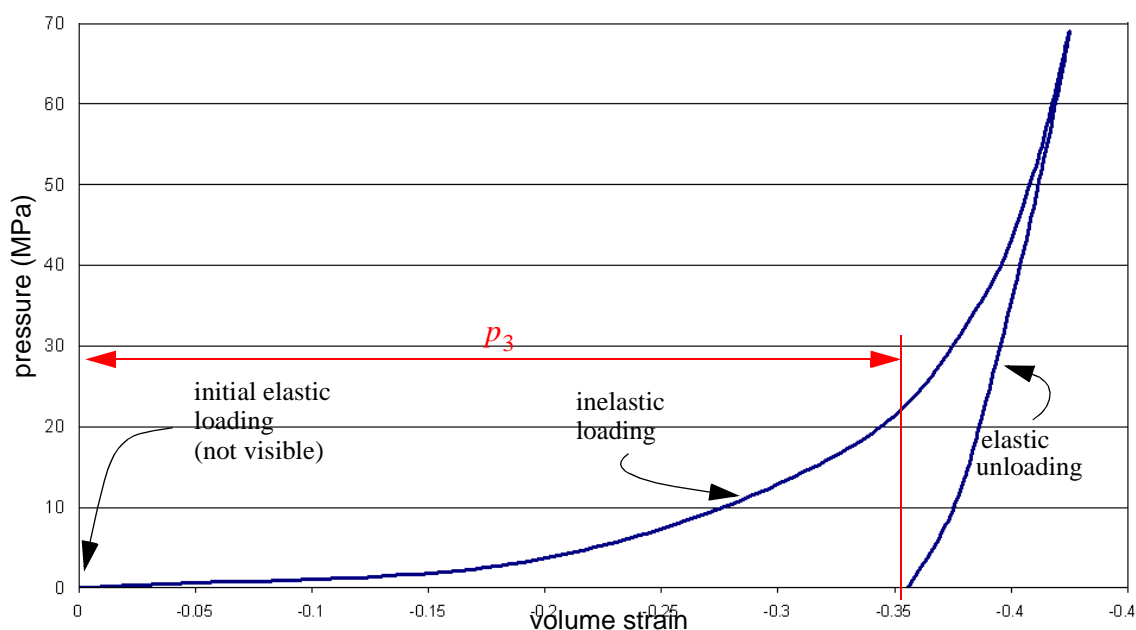
Figure A.1.   *Ideal hydrostatic parameterization data.*   The unloading portion is used to obtain the elastic bulk modulus parameters b_0, b_1, and b_2. With these parameters, the **HYDROFIT** program converts the loading portion of the data to a crush curve (see Fig. 4.14), and employs nonlinear regression to obtain the crush parameters p_0, p_3, p_1, and p_2. For this material (a ceramic powder, zircoa), the initial elastic loading curve is so small in comparison to the scale that it is not visible.
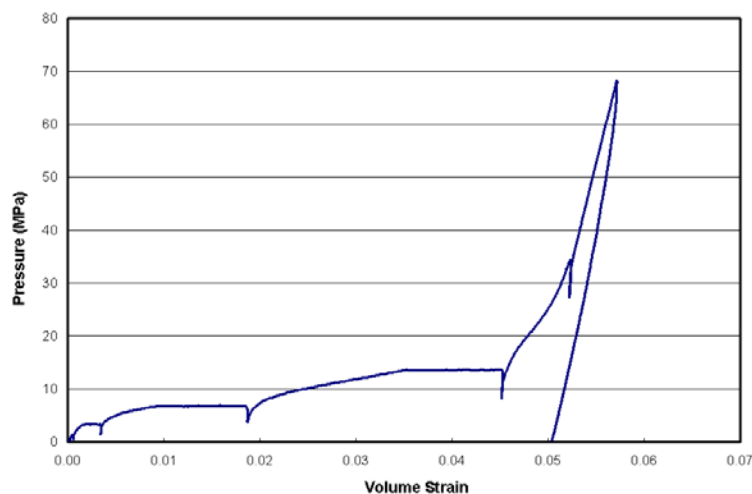
Figure A.2.   *Less-preferable hydrostatic parameterization data.*   Like the data for the material shown in Fig. A.1, this hydrostatic compression test (for frozen soil) was conducted nearly to full pore collapse, but the loading curve shows signs of material creep, which is not included in Kayenta.

A-2

STEP 2.**Use triaxial compression data to obtain the shear modulus parameters** g_0**,** g_1**, and** g_2. This step determines the parameters in Eq. (4.10),

$$G = g_o \left[\frac{1 - g_1 \exp(-g_2 J_2^{1/2})}{1 - g_1} \right] \tag{A.3}$$

Arrange the triaxial data as a two-column table, the first column being the axial strain ε_A and the second column being the stress difference $(\sigma_A - \sigma_L)$. Then use nonlinear least squares regression analysis to obtain the shear modulus parameters g_0, g_1, and g_2.
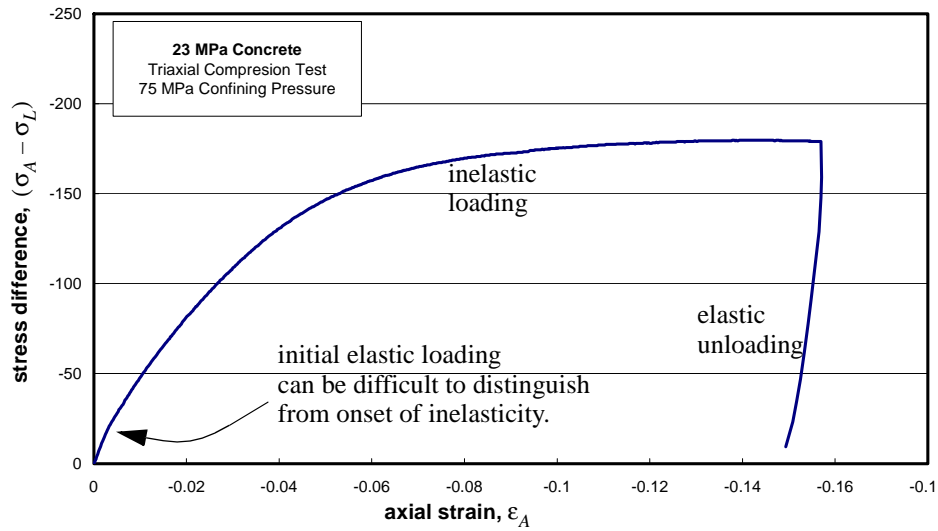
Figure A.3.   *Data representative of a triaxial compression parameterization test.* The slope of the unloading curve is the nonlinear tangent Young's modulus. Through standard moduli conversion formulas from linear elasticity, the previously determined bulk modulus parameters are used to obtain the elastic *shear* modulus parameters g_0, g_1, and g_2.

As illustrated in Fig. 3.3 in the main text, triaxial testing is typically performed as a two-stage process in which the material is first compressed hydrostatically to a given pressure. Then, during the second (triaxial) leg, the lateral stress is held fixed while the axial stress is varied. Only the elastic *unloading* data should be used for determining the nonlinear elastic shear modulus parameters. As explained on page 31, the plot of stress difference $(\sigma_A - \sigma_L)$ vs. axial strain ε_A will have a slope equal to Young's modulus E. Rather than directly using Young's modulus E as a user-specified material parameter, Kayenta requires the *shear modulus* G. Recall that the nonlinear elastic bulk modulus K was found previously in step 1. The **SHEARFIT** program computes the shear modulus G from K and E by using the standard linear elasticity formula, $G = \frac{3KE}{9K - E}$, cited in Eq. (4.15). If fitting to rock

data, Poisson's ratio, $\nu = (3K - E)/(6K)$, is typically in the neighborhood of 0.2 (this is a useful "sanity" check).

STEP 3. **(optional) maintain a record of *all* peak stress states ever measured for every available quasistatic load-to-failure experiment ever performed for the material of interest.** The softening threshold (peak limit) envelope is the boundary of any and *all* stress states quasistatically achievable for the material, including both elastically obtainable stress states and stress states that can be reached only through inelastic deformation. Unlike a yield surface, which is the boundary of *elastically* obtainable stresses (and which therefore will, in general, evolve as the microstructure is altered in response to inelastic deformation), the limit envelope is fixed in time (see Fig. 1.1 on page 6). All achievable yield surfaces (an infinite set) are contained within the *single* limit envelope. Characterizing the limit envelope requires numerous different experiments. Typically, each *individual* experiment has precisely one stress state at which the second stress invariant J_2 achieves a peak value. If the material softens before rupturing, the value of J_2 at failure might be lower than J_2^{peak}. It is the *peak* that is of interest, not the post-softening value at failure.

For every available quasistatic load-to-failure experiment, find the stress state at which J_2 is larger than for any of the other stress states in that experiment. Construct a table of data triplets $(\bar{I}_1^{@\text{peak}}, \sqrt{J_2^{\text{peak}}}, \bar{\theta}^{@\text{peak}})$, where $\bar{I}_1^{@\text{peak}}$ and $\bar{\theta}^{@\text{peak}}$ are the values of $\bar{I}_1$ and $\bar{\theta}$ at the stress state for which J_2 is at its peak value. The number of entries in your peak stress table will equal the number of experiments run to failure. The goal here is to gather sufficient data to parameterize both the Lode angle function $\Gamma(\bar{\theta})$ and the shear limit envelope in Eq. (4.39),

$$\boxed{F_f(I_1) = (a_1 - a_3 e^{-a_2 \bar{I}_1}) + a_4 \bar{I}_1}\ , \text{ where } \bar{I}_1 = -I_1 \quad \text{(shear limit function).} \quad \text{(A.4)}$$

STEP 4.**Use peak stresses from a family of triaxial compression tests to determine the shear failure envelope parameters a_1, a_2, a_3, and a_4.**

Recall that the F_f function represents a peak shear limit envelope in the meridional plane for which $\sqrt{J_2}$ is plotted against $\bar{I}_1$ for triaxial compression (TXC) stress states. Thus, the set of all stress states ever observed in TXC (Lode angle $\bar{\theta} = +30°$) must fall below the curve $\sqrt{J_2} = F_f(I_1)$, modulo experimental scatter. Stated differently, this curve defines boundary of all stress states that ever have been (or ever *can* be) observed in quasistatic TXC loading. A sufficient number of TXC experiments must be conducted under various confining pressures so that the bounding surface begins to take form. On other meridional planes (i.e., at other Lode angles), Kayenta presumes the bounding curve is adequately described by $\sqrt{J_2} = F_f(I_1)/\Gamma(\bar{\theta})$, which simply means that Kayenta presumes that the limit function at *non-TXC* Lode angles is simply a scalar multiple of the TXC function. Once the F_f function has been determined in this parameterization step, the peak stress data at other Lode angles will be used later to determine the Γ proportionality function.

Using only the TXC ($\bar{\theta} = 30°$) data create a scatter plot of all ever-achieved TXC values of $\sqrt{J_2}$ and $\bar{I}_1$. A scatter plot of all TXC stress data measured at various confining pressures might look somewhat as sketched below:

$$\sqrt{J_2} = F_f(I_1) = (a_1 - a_3 e^{-a_2 \bar{I}_1}) + a_4 \bar{I}_1$$
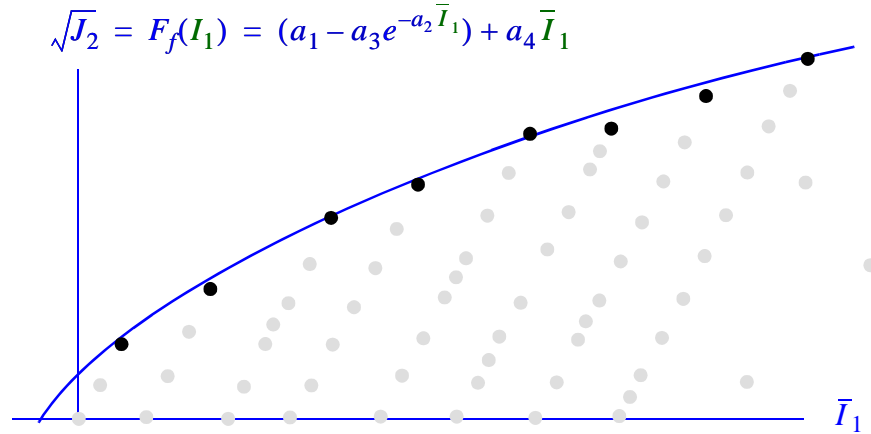
Figure A.4.   A family of TXC tests conducted to failure.   The boundary of data points defines the F_f function. All other (sub-peak) data points fall below this line. Plots like the are shown for various materials in Fig. 9.1.

In Fig. A.4, the *peak* data pairs (darkened dots) correspond to the $\bar{\theta}^{@\text{peak}} = 30°$ values from your table of peak-stress invariants collected in STEP 3. A suite of actual TXC experiments for porcelanite is shown in Fig. A.5, along with further

illustration of how discrete peak points from these experiments are transferred to a limit surface meridional plot for fitting to Eq. (A.4)
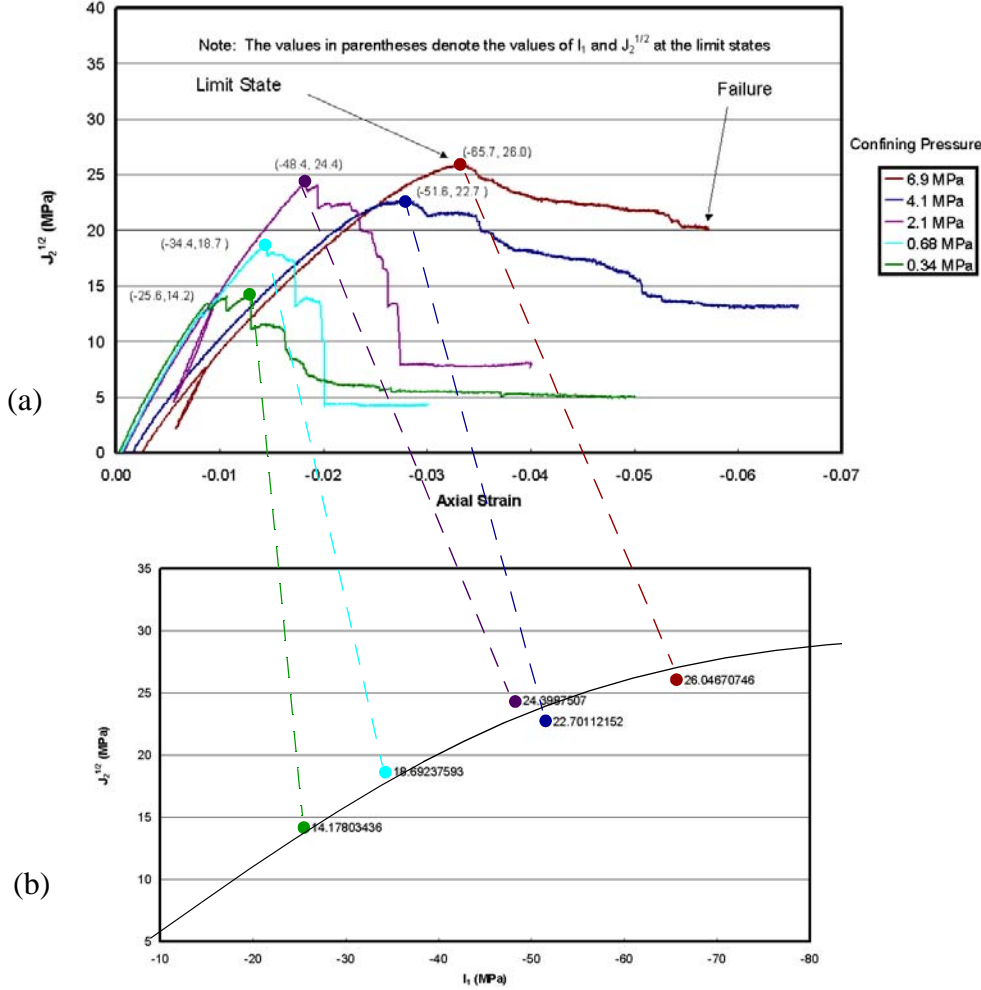
Figure A.5.   TXC stress-strain plots and extraction of their peak values to construct the meridional limit curve (data are for porcelanite).   (a) Each shear stress $\sqrt{J_2}$ vs. axial strain plot has exactly one peak value, as labeled. The value of I_1 at this peak is found by applying Eq. (3.28), $\bar{I}_1 = \sqrt{3}\bar{\tau} + 3\bar{\sigma}_L$ with $\bar{\tau} = \sqrt{J_2^{\text{peak}}}$ and $\bar{\sigma}_L$ equal to the lateral confining pressure for the test. (b) The peak states are transferred to a plot of $\sqrt{J_2}$ vs. $\bar{I}_1$ for fitting to the F_f meridional limit function.

Once enough TXC experiments have been conducted for a well-defined shear limit boundary to emerge, the next step is to determine values of a_1, a_2, a_3, and a_4 that best fit the F_f function to this boundary.

Given triaxial stress difference $\bar{\sigma}_A - \bar{\sigma}_L$ vs. axial strain $\bar{\varepsilon}_L$ data, Eqs. (3.28) and (3.29) show that value of J_2 at peak is given by $\sqrt{J_2^{\text{peak}}} = |\bar{\sigma}_A - \bar{\sigma}_L|^{\text{peak}} / \sqrt{3}$ and the value of I_1 (i.e., the trace of the stress) at peak equals $I_1^{@\text{peak}} = 3\bar{\sigma}_L + (\bar{\sigma}_A - \bar{\sigma}_L)^{\text{peak}}$, where $\bar{\sigma}_L$ is the (constant) lateral confining pressure. The $(\bar{I}_1^{@\text{peak}}, \sqrt{J_2^{\text{peak}}})$ data pairs from TXC experiments (i.e., those for which $\bar{\theta}^{@\text{peak}} = +30°$) may be fed into a nonlinear regression parameterization program, **SHEARFIT** (available upon request) to

optimize the parameters in Eq. (A.4). To use this program, create an input file containing, in the first line, your initial guesses for a_1, a_2, a_3, a_4 and, in the second line, four logical integers (0 or 1) to indicate whether or not to optimize on the corresponding parameter. Refer to Fig. 4.1(a) to help decide appropriate initial guesses. If the data suggest a linear envelope at high pressures, then your first guess for a_4 should be an approximation of the slope of this envelope. If in doubt, take $a_4 = 0.0$ (i.e., assume the data asymptote to a constant value as pressure goes to infinity). Eyeball the data to set your first guess for a_1 equal to the zero-pressure value of the linear asymptote line (extrapolate visually if necessary), set a_3 to equal a_1 minus your best estimate for the *actual* ordinate intercept of the low-pressure data (again, extrapolate if necessary). Finally, set a_2 to equal an estimate for the initial (low-pressure) slope of the data divided by a_3. Using these initial guesses, the **SHEARFIT** program applies nonlinear regression and outputs values for the a_1, a_2, a_3, and a_4 parameters.

BEWARE: In typical TXC experiments, all principal stresses are compressive, making it is possible that **SHEARFIT** will return a meridional fit to the *available* data that corresponds to a shear limit envelope that does *not* corral the origin (implying *nonphysically* that zero stress is "unachievable"). If this occurs, you might want to append your table of observed $(\overline{I}_1^{@\mathrm{peak}}, \sqrt{J_2^{\mathrm{peak}}})$ data with an entry $(-I_1^{\mathrm{limit}}, 0)$, where I_1^{limit} is your best estimate for the theoretical hydrostatic *tensile* strength of the material (therefore $-I_1^{\mathrm{limit}}$ is a *negative* number). Include this entry multiple times if necessary to force it to have greater weight in the nonlinear regression (or, preferably, perform more experiments to obtain a larger number of *real* data points at low values of I_1).

STEP 5. **Use peak stresses from a family of triaxial *extension* tests to determine the extension to compression ratio ψ.** As was done above for TXC tests, construct a table of $(\overline{I}_1^{\mathrm{peak}}, \sqrt{J_2^{\mathrm{peak}}})$ data pairs corresponding to peak attained stresses in triaxial *extension* (TXE). These are the data pairs in your peak data table from STEP 3 that correspond to $\overline{\theta}^{@\mathrm{peak}} = -30°$. For each of these TXE data pairs, compute

$$\psi = \frac{\sqrt{J_2^{\mathrm{peak\ in\ TXE}}}}{F_f(\overline{I}_1^{@\ \mathrm{peak\ in\ TXE}})} \tag{A.5}$$

where F_f is the TXC shear limit function parameterized in the previous step. Of course, each TXE experiment is likely to result in slightly different values for ψ. At present, Kayenta presumes that the TXE/TXC ratio ψ is constant. Therefore, set

the Kayenta parameter ψ equal to the average of each ψ computed using Eq. (A.5) for each available TXE experiment.

It is possible that the data might imply that the strength ratio ψ must vary with pressure. Kayenta provides a built-in non-adjustable pressure-dependent strength ratio option that is enabled by simply specifying the strength ratio to have the phony value of -1. Otherwise, Kayenta assumes that ψ is the same at *all pressures*. Thus, if the built-in pressure varying strength ratio proves to be inadequate, modeling errors must be managed by measuring the parameter ψ at a confining pressures in the neighborhood where Kayenta is likely to be applied. Similar statements can be made regarding any and all parameters used to define Kayenta's yield function.

Sometimes, it might be *impractical* — or overly expensive — to obtain TXE data. In this case, an engineering approach for *estimating* ψ presumes that it obeys the same coupling to the meridional profile slope as predicted in classical Mohr-Coulomb theory. Using Eq. (A.4) to set the TXC slope in Eq. B.19 in Appendix B, an estimate for the pressure-varying strength ratio is

$$\psi = \frac{1}{1 + \sqrt{3}[a_4 + a_2 a_3 e^{-a_2 \bar{I}_1}]} \qquad \text{(A.6)}$$

In the future, we hope to thoroughly explore the merits of this formula, which correlates the strength ratio with the TXC meridional slope. At present, Kayenta presumes the strength ratio is constant. If, however, the above correlation formula can be substantiated, then we will likely incorporate it into future releases, thereby possibly eliminating the need for a user-specified ψ altogether. Until then, you may evaluate the above formula at a value of $\bar{I}_1$ in the neighborhood where you plan to apply Kayenta to obtain a reasonable estimate for ψ.

STEP 6.**Determine the appropriate Lode function option `J3TYPE`.** Recall that Kayenta's function $\Gamma(\bar{\theta})$ defines the *shape* of the octahedral profile shape for Lode angles spanning the range from TXE ($\bar{\theta} = -30°$) to TXC ($\bar{\theta} = +30°$). Kayenta's parameter `J3TYPE` (see page 48) dictates the functional form to be used for the Γ function. Non-triaxial data are difficult to acquire. If no such data are available, you will need to use engineering judgement as to an appropriate choice for `J3TYPE`. This parameterization step aims to guide the choice in the happy circumstance that non-triaxial data *are* available.

As illustrated in Fig. 4.10, Kayenta's Γ function is defined to equal 1 in TXC and $1/\psi$ in TXE. Large values of Γ correspond to small shear strengths. In this model parameterization step, all available peak-state data obtained in *non-triaxial* loading paths are considered to help decide an appropriate choice for the `J3TYPE` option. Looping over your table (collected in STEP 3) of "all-observed" peak stress invariant triplets ($\bar{I}_1^{\text{peak}}, \sqrt{J_2^{\text{peak}}}, \bar{\theta}^{\text{peak}}$), especially those at non-triaxial states, create a new two-column table of ($\bar{\theta}, \Gamma$) data pairs, where

$$\Gamma = \frac{F_f(\bar{I}_1^{@\text{peak}})}{\sqrt{J_2^{\text{peak}}}} \tag{A.7}$$

By comparing a scatter plot of these ($\bar{\theta}, \Gamma$) data to the graphs in Fig. 4.10, an appropriate choice for `J3TYPE` should be more clear. To assist in the decision, it might be easier to instead scale the ordinate as shown in Fig. A.6. By overlaying data with the family of plots in Fig. A.6 an appropriate choice for `J3TYPE` should be apparent, as illustrated in Fig.A.7. If non-triaxial data are unavailable (a common problem), select `J3TYPE=1` if the material is judged to be moderately ductile; otherwise, select `J3TYPE=3`.
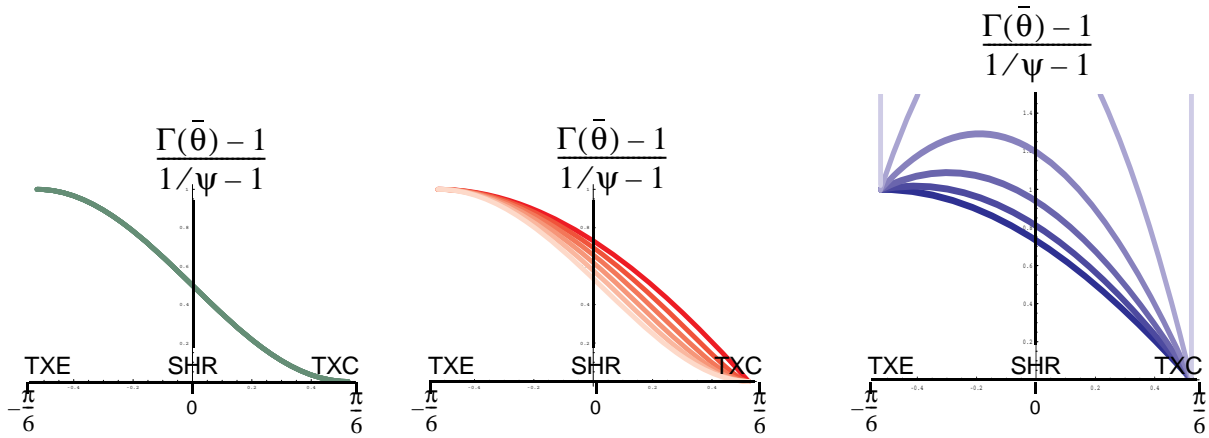
Figure A.6. *The Lode function information originally shown in Fig. 4.10 of the main report, now displayed with a transformed ordinate.* Knowing that $\Gamma = 1/\psi$ in TXE and $\Gamma = 1$ in TXC, it makes sense to scale the ordinate as shown so that, regardless of the value of ψ, the scaled ordinate equals 1 in TXE and 0 in TXC. With this scaling, all Gudehus Lode functions overlap; the others vary with ψ.
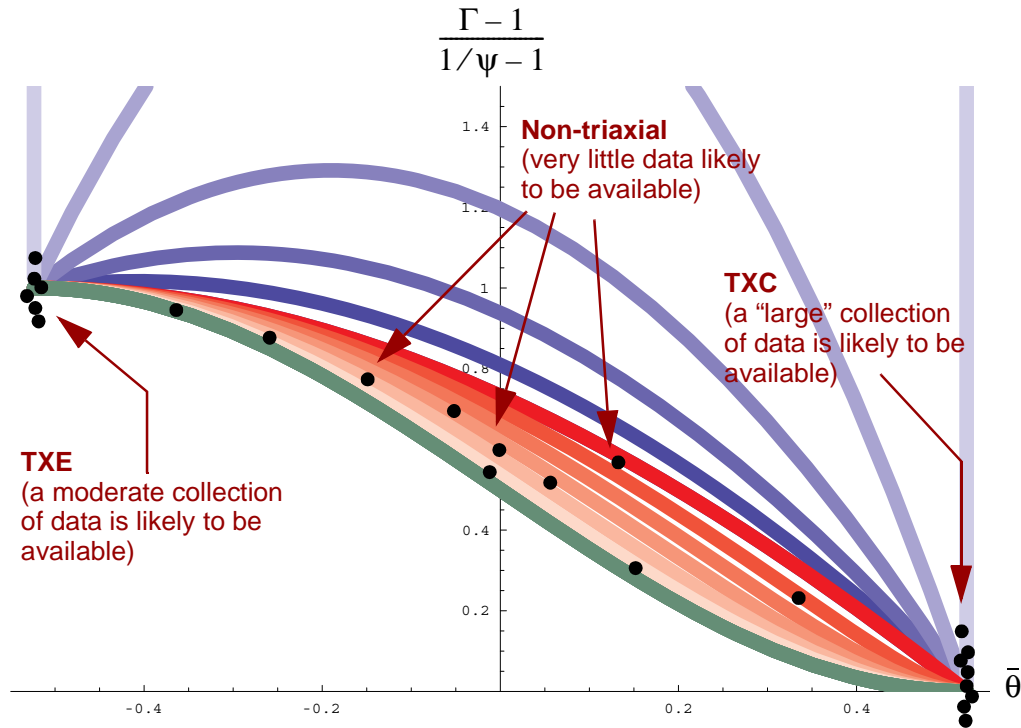
Figure A.7. *A sketch of how data might be distributed at non-triaxial states.* In this contrived example, most of the data at non-triaxial states falls in the **red** Willam-Warnke region and therefore **J3TYPE=2** would be appropriate for this material. In practice, data at non-triaxial Lode angles are rarely available. In this case, the user must resort to engineering judgement to decide which **J3TYPE** option to select.

STEP 7. **Hardening parameters.** In the previous steps, we determined Kayenta parameters that define the outer limit surface. No stress state outside this fixed (non-evolving) limit surface can be achieved through *any* load path. Consequently, the infinite set of all possible *yield* surfaces must be contained within this limit envelope. Unlike the limit surface, which bounds *all* possible stress states, the yield surface merely bounds the set of *elastically* obtainable stress states. Unlike the limit surface, a yield surface evolves (hardens) through time as a result of microstructural changes induced in the material under inelastic loading. The *initial* yield surface is typically much smaller than the limit surface (see Fig. 1.1 in the main text). Isotropic hardening permits the initial yield surface to expand on octahedral planes (by amounts that vary with pressure) up until the limit surface is reached. Kinematic hardening permits the yield surface to translate in stress space until the limit surface is reached. Both types of hardening may occur simultaneously.

As a rule, the amount of kinematic hardening relative to total stress is high at lower pressures. Therefore, kinematic hardening data are best inferred from unconfined compression tests. In the previous parameterization steps, we determined crush parameter values (p_0, p_1, p_2), elastic parameters $(b_0, b_1, b_2, g_0, g_1, g_2)$, the limit surface parameters $(a_1, a_2, a_3, a_4, \psi)$, and `J3TYPE`. Now these values should be used in a finite-element (or single cell driver) implementation of Kayenta, to obtain a simulated table of axial stress vs. volume strain to compare with available experimental data. The goal is to determine values for unknown Kayenta parameters through a systematic simulation sequence. As a first guess, set the "yet-to-be-determined" Kayenta parameters as follows:

- offset `RN`=N=0 (i.e. suppress hardening)
- kinematic hardening parameter `HC`=1e5
- shape parameter `CR`=R=10
- plastic potential function parameters for non-associativity `A2PF`==A2, `A4PF`==A4, `RKPF`=RK, `CRPF`=CR (i.e., tentatively assume associativity)
- joint spacing `RJS`=s=0.0
- rate sensitivity parameters `T1` through `T7` =0.0 (no rate sensitivity).

Run the finite-element code for unconfined compression and output axial stress vs. volumetric strain (`EVOL`). It is unlikely that this result will replicate observed unconfined compression data on the first try. We ultimately hope to assign values to the above parameters so that the volume strain will "turn around" as Fig. 9.6*(b)* (even though axial strain increases monotonically, the *volume* strain turns around because of the lateral bulking strains).
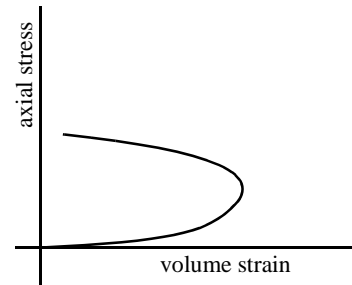
The phenomenological fitting functions employed in Kayenta are designed to extrapolate reasonably well into regions where data are not available, but these functions are also selected in part for computational tractability and they therefore serve only as approximations. Consequently, there will certainly be modeling error. Ideally, one should use regression fitting procedures to select Kayenta hardening parameters that minimize modeling error relative to available data. We have already described the programs "**HYDROFIT**" for regression optimization of the elastic parameters and **SHEARFIT** for finding the limit surface parameters, but no similar fitting software has yet been developed to determine the hardening parameters. Consequently, for these parameters, a more traditional exploratory manual search method must be used as described below.

In the following, we will be exploring adjustments of CR, RN, and HC to try to achieve a strain "turn around" at the correct (observed) strain and stress.

If no turn around is apparent in your simulation, try decreasing CR. Continue to decrease CR until turn around occurs. If you get no turn around, bring down the initial yield surface. The intercept on the ordinate on the meridional profile is located at $\sqrt{J_2} = a_1 - a_3$. Try increasing N to a value no larger than $a_1 - a_3$ (our initial guess of $N = 0$ presumed that the initial yield surface coincided with the shear limit surface. By setting N to a nonzero value, we are now permitting kinematic hardening). You will likely see "turn around" start to occur.

Next try changing HC. Increasing (say, doubling) HC will increase the strain value at which turn-around occurs. Lowering HC lowers the turn-around strain. If you continue to have trouble getting turn around, double check that you have correctly entered the previously determined (*known*) parameter values.

If the turn around stress is too high, try lowering HC.

Once shear-induced dilatation (turn-around) has been adequately modeled for unconfined TXC, go then to high-confinement data. Try changing CR (e.g., from 7 to 10 if computed peak strain is too large).

Go back to unconfined, and work on HC and RN.

Continue to go back and forth until you are satisfied with both confined and unconfined results.
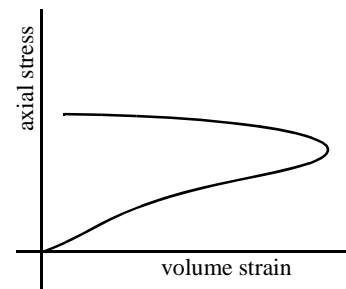
This concludes our guidance for parameterizing new materials to Kayenta. Further revisions of this manual will likely include additional tips and parameterization experiment suggestions.

APPENDIX B.
Nomenclature and Data Sets

This appendix contains three tables defining (1) model parameters, (2) plotable variables, and (3) other symbols or acronyms used internally within this manual. In each table, the first column shows the typeset symbol for the variable. The next column contains the ASCII string used for the variable in code input files and/or within the source code. In the SI units column, a "1" indicates that the variable is dimensionless. A "–" indicates that dimensions vary, while N/A means dimensions are not applicable. The defining equation (or page number) in the last column of the tables cites the location in this report where the quantity is defined or discussed.

Reminder: in mechanics, stress and strain are typically taken positive in tension. However, in applications, they are taken positive in compression. To manage this potentially confusing conflict of conventions, recall

$$\bar{x} \equiv -x$$ DEFINITION OF THE "OVER-BAR"   (B.1)

For example, I_1 denotes the trace of stress (positive in compression). Therefore, $\bar{I}_1 \equiv -I_1$ is positive in compression.

Model Parameters
(User Input)

Symbol or Acronym	ASCII Name	Name and meaning	SI units	defining equation
b_0	PROP(1) (B0)	Initial elastic bulk modulus (for intact material if modeling joints). The tangent bulk modulus is given by $$K = b_o + b_1 \exp\left(-\frac{b_2}{|I_1|}\right)$$	Pa	Eq. 4.9 Eq. A.1 Page B-30
b_1	PROP(2) (B1)	High pressure coefficient in nonlinear elastic (intact) bulk modulus function (see above formula). For linear elasticity, set $b_1=0$. For nonlinear elasticity, set b_1 so that the Bulk modulus K will asymptote to a value $b_0 + b_1$ at high pressures.	Pa	Eq. 4.9 Eq. A.1
b_2	PROP(3) (B2)	Curvature parameter in nonlinear elastic (intact) bulk modulus function (see above formula). For linear elasticity, set $b_2 = 0$. For nonlinear elasticity, set b_2 to a small value to transition rapidly from the low pressure bulk modulus to the high pressure modulus. Larger values of b_2 will result in a broader transition range.	Pa	Eq. 4.9 Eq. A.1
b_3	PROP(4) (B3)	Coefficient in nonlinear elastic bulk modulus to allow for plasticity-induced changes in the elastic properties. To neglect this effect, set $b_3 = 0$. When this parameter is nonzero, the elastic tangent bulk modulus is computed by $$K = f_K\left\{\left[b_o + b_1\exp\left(-\frac{b_2}{|I_1|}\right)\right] - b_3\text{Exp}\left(-\frac{b_4}{|\varepsilon_v^p|}\right)\right\}$$	Pa	Eq. 4.33
b_4	PROP(5) (B4)	Power in nonlinear elastic bulk modulus to allow for plasticity-induced changes in the elastic properties. To neglect this effect, set $b_4 = 0$. Otherwise, see above formula.	1	Eq. 4.33
g_0	PROP(6) (G0)	Initial elastic shear modulus (for intact material if modeling joints). The tangent shear modulus is computed by $$G = g_o\left[\frac{1 - g_1\exp(-g_2 J_2^{1/2})}{1 - g_1}\right]$$	Pa	Eq. 4.10 Eq. A.3
g_1	PROP(7) (G1)	Parameter used to define the elastic (intact) shear modulus at large shears (see above formula). Specifically, the shear modulus will asymptote to a value $g_0/(1 - g_1)$ as shear stress increases. Must be less than 1.0. For linear elasticity, set $g_1 = 0$. For the shear modulus to increase with shearing, set $0 < g_1 < 1$. For the shear modulus to decrease with shearing, set $g_1 < 0$.	1	Eq. 4.10 Eq. A.3

Symbol or Acronym	ASCII Name	Name and meaning	SI units	defining equation
g_2	PROP(8) (G2)	Curvature parameter in nonlinear elastic (intact) shear modulus function (see above formula). Must satisfy $g_2 \geq 0$. For linear elasticity, set $g_2 = 0$. For nonlinear elasticity small values of g_2 cause the shear modulus to transition *rapidly* from its initial value g_0 to its high shear value $g_o / (1 - g_1)$. Larger values of g_2 make this transition more gradual.	1/Pa	Eq. 4.10 Eq. A.3
g_3	PROP(9) (G3)	Coefficient in nonlinear elastic shear modulus to allow for plasticity-induced changes in the elastic properties. To neglect this effect, set $g_3 = 0$. When nonzero, the tangent shear modulus is computed by $$G = f_G \left\{ g_o \left[\frac{1 - g_1 \exp(-g_2 J_2^{1/2})}{1 - g_1} \right] - g_3 \mathrm{Exp} \left(-\frac{g_4}{\gamma_{\mathrm{eqiv}}^p} \right) \right\}$$	Pa	Eq. 4.34
g_4	PROP(10) (G4)	Power in nonlinear elastic shear modulus to allow for plasticity-induced changes in the elastic properties. To neglect this effect, set $g_4 = 0$. Otherwise, see above formula.	1	Eq. 4.34
	PROP(11) (RJS)	Joint spacing. Set this parameter to zero if the material has no geological (or rock-like) faults.	meter	
	PROP(12) (RKS)	Joint shear stiffness. Set this parameter to zero if the material has no geological (or rock-like) faults.	Pa/m	
	PROP(13) (RKN)	Joint normal stiffness. Set this parameter to zero if the material has no geological (or rock-like) faults.	Pa/m	
a_1	PROP(14) (A1)	Constant term in the fitting function for the meridional profile, $F_f(I_1) = a_1 - a_3 e^{-a_2 \bar{I}_1} + a_4 \bar{I}_1$, for the ultimate shear limit surface. Here, $\bar{I}_1 = -\mathrm{tr}\underset{\sim}{\sigma}$ and therefore $\bar{I}_1$ is three times the pressure. At zero pressure, $F_f(I_1) = a_1 - a_3$ while at high pressure (large $\bar{I}_1$), $F_f(I_1) \sim a_1 + a_4 \bar{I}_1$. Thus, a_1 is the vertical intercept of the linear *asymptote*, whereas $a_1 - a_3$ is the vertical intercept of the limit function *itself*. These parameters define the ultimate limit curve, at which the maximum possible hardening has occurred and softening is imminent. The *initial* onset of *yield* is described by $f_f(I_1) = F_f(I_1) - N$. Thus if fitting to data for yield *onset*, recognize that the constant term will be lower than a_1 by an amount N.	Pa	Eq. 4.39 Fig. A.4

APPENDIX B. Nomenclature and Data Sets

Symbol or Acronym	ASCII Name	Name and meaning	SI units	defining equation
a_2	PROP(15) (A2)	Curvature decay parameter in the fitting function for the meridional profile, $F_f(I_1) = (a_1 - a_3 e^{-a_2 \bar{I}_1}) + a_4 \bar{I}_1$. Keep in mind that $\bar{I}_1 = -3\bar{p}$, where $\bar{p}$ is pressure. Set $a_2 = 0$ for a linear meridional profile as in Mohr-Coulomb theory. Assign a_2 a large value to quickly asymptote to the high-pressure profile slope.	1/Pa	Eq. 4.39 Fig. A.4
a_3	PROP(16) (A3)	Parameter in the shear limit meridional fit function, $F_f(I_1) = (a_1 - a_3 e^{-a_2 \bar{I}_1}) + a_4 \bar{I}_1$.	Pa	Eq. 4.39 Fig. A.4
a_4	PROP(17) (A4)	High-pressure meridional slope parameter in the fit function, $F_f(I_1) = (a_1 - a_3 e^{-a_2 \bar{I}_1}) + a_4 \bar{I}_1$.	1	Eq. 4.39 Fig. A.4
p_0	PROP(18) (P0)	Value of I_1 at the onset of pore collapse for hydrostatic compression of virgin material. This parameter will be negative because I_1 is negative in compression. In the lexicon of traditional $p\text{-}\alpha$ crush models, this variable would equal $-3P_E$, where P_E is the elastic limit pressure in hydrostatic compression. In early (pre-2003) publications about Kayenta, this parameter is denoted X_o.	Pa	Eq. 4.68 Fig. 4.14 Eq. A.2 Page B-30
p_1	PROP(19) (P1)	One third of the slope of a porosity vs. pressure crush curve at the elastic limit. In early (pre-2003) publications about Kayenta, this parameter is denoted D_1.	1/Pa	Eq. 4.68 Fig.4.14 Eq. A.2
p_2	PROP(20) (P2)	Extra fitting parameter for hydrostatic crush curve data, used when the crush curve has an inflection point. In early (pre-2003) publications about Kayenta, this parameter is denoted D_2.	1/Pa^2	Eq. 4.68 Fig. 4.14 Eq. A.2
p_3	PROP(21) (P3)	Asymptote (limit) value of the absolute value of the plastic volume strain. This parameter is approximately equal to the initial porosity in the material and may be inferred from hydrostatic crush data. In early (pre-2003) publications about Kayenta, this parameter is denoted W.	1	Eq. 4.68 Fig. 4.14 Eq. A.2 p. 15 (footnote)

Symbol or Acronym	ASCII Name	Name and meaning	SI units	defining equation
R	`PROP(22)` `(CR)`	Shape parameter that allows porosity to affect shear strength. R equals the eccentricity (width divided by height) of the elliptical cap function, so it is the ratio a/b (not A/B) in Fig. 4.16. This parameter affects the stress level at which dilatation will occur in triaxial compression. If dilatation is occurring too soon, increase the value of R. Decreasing R will decrease the influence of porosity on shear strength and therefore enhance the effect of void space creation associated with crack growth. To replicate older classical pore collapse models (which initiate pore collapse only at a critical pressure, regardless of the level of shear stress), set R to a very small number.	1	Fig. 4.16 Eq. 4.71 pg. A-11 Page B-30
ψ	`PROP(23)` `(RK)`	TXE/TXC (triaxial extension to compression) strength ratio. Convexity of the yield surface requires that $1/2 \le \psi \le 2$ (or $7/9 \le \psi \le 9/7$ if using `J3TYPE=1`). Real materials generally satisfy $1/2 \le \psi \le 1$. To instruct Kayenta to automatically assign a pressure-dependent strength ratio according to Eq. B.19, enter "RK=–1.0".	1	page 48 Fig. 4.4 Eq. A.5
N	`PROP(24)` `(RN)`	Off-set parameter. Must be non-negative. Set $N = 0$ to suppress kinematic hardening. For problems with kinematic hardening, the backstress invariant $\sqrt{J_2^\alpha}$ will not be permitted to grow any larger than N. The initial yield surface is defined by $F_f^{\text{initial}}(I_1, N) = F_f(I_1) - N$, where F_f describes the shear limit surface (softening threshold). Roughly speaking, the shear strength can increase by an amount N before softening will commence.	Pa	Fig. 4.6 Eq. 4.40 page 64 pg. A-11
H	`PROP(25)` `(HC)`	Kinematic hardening parameter. Set $H = 0$ and $N = 0$ to suppress kinematic hardening. Otherwise, this parameter affects how "quickly" the yield surface evolves toward the ultimate shear failure surface.	Pa	Eq. 4.78 pg. A-11 Page B-30
I_1^{cut}	`PROP(26)` `(CTI1)`	Tensile cut-off in allowable value of the first stress invariant I_1. Value must be positive. If the first invariant (which is proportional to the negative of pressure) reaches this cut-off value, the isotropic part of the stress is replaced with this value. This parameter is available only temporarily to permit reasonable strength predictions in tension. Current enhancements of this model are focused on more physically rigorous tensile failure modeling. In principle, the yield function should limit achievable values of I_1. This option is available if the yield function is not cutting off strength at a tensile pressure low enough for the application at hand.	Pa	Page B-30

Symbol or Acronym	ASCII Name	Name and meaning	SI units	defining equation
—	`PROP(27)` `(CTPS)`	Principal stress tensile cut-off. If a predicted principal stress is found to exceed this value, then it is replaced with this value. See discussion regarding the state variable "CRACK" in the next table.	Pa	Page B-30
T_1	`PROP(28)` `(T1)`	Primary rate dependence parameter in the Duvaut-Lions overstress model. To specify a *constant* intrinsic material response time, set this user input equal to the characteristic response time. Use the other "T" parameters to enable dependence on strain rate and pressure. In the 2009 Kayenta builds, this parameter is interpreted differently when softening is allowed, and this alternative use of T1 is likely to change because softening is still in the research phase. Furthermore, the Duvaut-Lion use of T1 (and other T-parameters) is being updated and likely to change in future builds.	sec	Eq. 6.22 Page B-30
T_2	`PROP(29)` `(T2)`	Rate dependence parameter. See main text.	1/s	Eq. 6.22
T_3	`PROP(30)` `(T3)`	No longer used. Set to zero.	1	Eq. 6.22
T_4	`PROP(31)` `(T4)`	No longer used. Set to zero.	1/s	Eq. 6.22
T_5	`PROP(32)` `(T5)`	Rate dependence parameter. See main text.	Pa	Eq. 6.22
T_6	`PROP(33)` `(T6)`	Rate dependence parameter. See main text.	sec	Eq. 6.22
T_7	`PROP(34)` `(T7)`	Rate dependence parameter. See main text.	1/Pa	Eq. 6.22
—	`PROP(35)` `(J3TYPE)`	Integer-valued control parameter for specifying the desired type of 3rd-invariant yield surface: 1 - Gudehaus 2 - Willam-Warnke 3 - Mohr-Coulomb	1	page 48 Fig. A.7
a_2^{PF}	`PROP(36)` `(A2PF)`	Potential function parameter (=**A2** for associative). Assign this parameter in the same way you would assign a value to a_2, except that this parameter is used to generate the flow potential surface (i.e., the plastic strain rate will be normal to the flow potential surface). If a_2^{PF} is unspecified or zero, it will be automatically set equal to a_2.	1/Pa	page 51 Page B-30

Symbol or Acronym	ASCII Name	Name and meaning	SI units	defining equation
a_4^{PF}	`PROP(37)` `(A4PF)`	Potential function parameter (=**A4** for associative). Assign this parameter in a manner similar to a_4 except that this parameter will be used to generate the flow potential. If a_4^{PF} is unspecified or zero, it will be automatically set equal to a_4.	1	page 51 Page B-30
R^{PF}	`PROP(38)` `(CRPF)`	Potential function parameter (=**CR** for associative). Flow potential analog of the yield surface parameter R. If R^{PF} is unspecified or zero, it will be automatically set equal to R.	1	page 51 Page B-30
ψ^{PF}	`PROP(39)` `(RKPF)`	Potential function parameter (=**RK** for associative). Flow potential analog of the yield surface parameter ψ. If ψ^{PF} is unspecified or zero, it will be automatically set equal to ψ.	1	page 51
—	`PROP(40)` `(SUBX)`	Subcycle control parameter. If zero, Kayenta will select an appropriate subcycle step size. If **SUBX** is nonzero, then Kayenta's default subcycle increment will be multiplied by `10**SUBX` (ten raised to the power). If, for example, you want the code to decrease its subcycle size by a factor of 10, then set SUBX=–1. If you want the subcycle size altered by a factor "x", then set **SUBX** to the base ten log of "x" [$\log_{10} x = (\ln x)/(\ln 10)$].	1	—
—	`PROP(41)` `(DEJAVU)`	Not truly a user input. This is set equal to 1.0 when the input parameters have been checked (and altered for self consistency) by Kayenta's internal data check routine. To bypass data check (which is not advisable), the user may set DEJAVU=1.0. Otherwise, this parameter should be left unspecified (i.e. defaulted to zero)	1	N/A
	`PROP(42)` `(FSPEED)`	Parameter controlling the rate at which damage proceeds. Large FSPEED (>30) will result in a sudden loss of strength and stiffness, whereas small FSPEED (<5) will produce a more gradual softening process.	1	
	`PROP(43)` `(PEAKI1I)`	Theoretical initial tensile limit of I_1.		Fig. 5.2 Eq. 5.2
	`PROP(44)` `(STRENI)`	Initial high-pressure strength intercept.		Fig. 5.2 Eq. 5.3
	`PROP(45)` `(FSLOPEI )`	Failed high-pressure strength intercept.		Fig. 5.2 Eq. 5.1
	`PROP(46)` `(PEAKI1F)`	Theoretical failed tensile limit of I_1. If unspecified, defaults to zero (i.e., failed material has no tensile strength).		Fig. 5.2 Eq. 5.2

Symbol or Acronym	ASCII Name	Name and meaning	SI units	defining equation
	PROP(47) *(STRENF)*			Fig. 5.2 Eq. 5.3
	PROP(48) *(JOBFAIL)*	If zero, then the limit surface is treated as a non-hardening yield surface. If JOBFAIL is a nonzero integer, then material softening (loss of strength and stiffness) is applied. The JOBFAIL parameter specifies the approach to be used for softening. These options are under development. Therefore, consult with the model developers to determine allowed values of JOBFAIL.	1	page 44
	PROP(49) *(FSLOPEF)*	Initial slope of the *failed* TXC limit surface. If unspecified, defaults to a value appropriate to sand.	1	Fig. 5.2 Eq. 5.1
	PROP(50) *(FAIL-STAT)*	FAILSTAT is a control parameter available for verification testing. Setting it equal to 1.0 will stop the code at the onset of material failure when softening is enabled. Noting the stress state at this stopping point allows generating failure statistics that can be compared with the failure statistics specified in user input.	1	Fig. 8.14
	PROP(51) *(FREE01)*	*Not used -- control for research testing of new code.*		
	PROP(52) *(FREE02)*	*Not used -- control for research testing of new code.*		
	PROP(53) *(FREE02)*	*Not used -- control for research testing of new code.*		
	PROP(54) *(FREE02)*	*Not used -- control for research testing of new code.*		
	PROP(55) *(FREE02)*	*Not used -- control for research testing of new code.*		
	PROP(56) *(FREE02)*	*Not used -- control for research testing of new code.*		
	PROP(57) *(FREE02)*	*Not used -- control for research testing of new code.*		
	PROP(58) *(FREE02)*	*Not used -- control for research testing of new code.*		
	PROP(59) *(YSLOPEI)*	High-pressure slope of the initial limit surface.		Fig. 5.2 Eq. 5.4
	PROP(60) *(YSLOPEF)*	High-pressure slope of the failed limit surface. If unspecified, defaults to 0.0.		Fig. 5.2 Eq. 5.4

Other input parameters (available only in special builds).

When Kayenta is compiled with -D GEO_ORTHOTROPIC to include orthotropic joint sets, then there are the following additional parameters:

CKN = initial joint normal stiffness (stress/length)

VMAX = maximum joint closure (length)

SPACE = joint spacing (length)

SHRSTIFF = joint shear stiffness (stress/length)

each of which is appended with **01**, **02**, or **03** to indicate the joint normal direction. For example, SPACE02 is the spacing of joints whose normal points in the 2 direction.

When Kayenta is compiled with -D GEO_ANISOTROPIC to include up to four arbitrarily oriented joint sets, the relevant user parameters are the same as those listed above for orthotropic joints plus two inputs for specifying joint orientation:

STRIKE = strike angle of the joint (radian)

DIP = dip angle of the joint (radian)

With the generally anisotropic option, all joint parameter keywords are appended with **1**, **2**, **3**, or **4** to indicate the joint ID number. For example, SPACE2 is the spacing of joints in the second joint set.

Documentation of joints is available only in an unpublished memo (available to SNL on Web File Share under the keyword "GeoModel").

When Kayenta is compiled with -D GEO_EOS, thermodynamics of a true equation of state is enabled, requiring additional EOS input parameters such as reference density (RHO0), reference temperature (TMPR0), sound speed (SNDSP0), and other inputs that are typical of an equation of state. Contact the model developers to exercise this option.

Internal State Variables
(Plotable Output)

Symbol or Acronym	ASCII Name	Name and meaning	SI units	defining equation (or page)
κ	SV(1) [KAPPA] ELN EL	The value of I_1 at which the meridional yield profile first branches away from the crack failure surface and begins to morph into the cap function associated with porosity. Recalling that $\kappa = -\bar{\kappa}$, the internal state variable κ typically will be negative. As a rule of thumb: increasing the user-input parameter R will increase κ (and therefore decrease $\bar{\kappa}$). Recalling Fig. 4.16, κ is *not* the point at which the meridional profile has a zero slope — it is the *branching* location. The zero slope point is reached at a higher pressure. Isotropic hardening is controlled by the evolution of κ. In Kayenta physics source code, κ is denoted by ELN or by EL in the subcycling. Note: future builds of Kayenta are anticipated to replace the KAPPA output variable with the X variable in Fig. 4.5.	Pa	Fig. 4.5 Eq. 4.30 Fig. 4.16 Eq. 4.72
—	SV(2) [INDEX]	Indicator for the nature of plastic loading (this output is used primarily by code developers for debugging)	1	page 89
$\dot{\varepsilon}^{\text{equiv}}$	SV(3) [EQDOT]	L_2 (Frobenius) norm of input strain rate tensor. $\dot{\varepsilon}^{\text{equiv}} = \sqrt{\dot{\varepsilon}_{ij}\dot{\varepsilon}_{ij}}$.	1/s	page 89
I_1	SV(4) [I1]	First stress invariant (positive in tension).	Pa	Eq. 3.9 page 89
$\sqrt{J_2}$	SV(5) [ROOTJ2]	Square root of the second stress invariant $\sqrt{J_2}$ (always positive). This the equivalent shear stress in the material.	Pa	Eq. 3.10 Eq. 3.13 page 89
α_{11}	SV(6) [ALXX]	11 component of the backstress	Pa	page 63 page 52
α_{22}	SV(7) [ALYY]	22 component of the backstress	Pa	page 63 page 52
α_{33}	SV(8) [ALZZ]	33 component of the backstress	Pa	page 63 page 52
α_{12}	SV(9) [ALXY]	12 component of the backstress (= 21 component)	Pa	page 63 page 52
α_{23}	SV(10) [AXYZ]	23 component of the backstress (= 32 component)	Pa	page 63 page 52
α_{31}	SV(11) [ALXZ]	31 component of the backstress (= 13 component)	Pa	page 63 page 52

Symbol or Acronym	ASCII Name	Name and meaning	SI units	defining equation (or page)
G^α	`SV(12)` `[GFUN]`	Kinematic hardening decay function, equal to 1.0 initially and then decays down to 0.0 as the max allowable kinematic hardening (determined by the shift parameter N) is approached.	1	Eq. 4.81 page 63
γ^p_{eqiv}	`SV(13)` `EQP` `[EQPS]`	Equivalent uniaxial plastic shear strain (conjugate to $\sqrt{J_2}$). Specifically, $\gamma^p_{\mathrm{eqiv}} = \int \sqrt{2}\left\|\dot{\underset{\approx}{\gamma}}^p\right\| dt$, where $\dot{\underset{\approx}{\gamma}}^p$ is the deviatoric part of the plastic strain rate $\dot{\underset{\approx}{\varepsilon}}^p$.	1	Eq. 4.35
ε^p_v	`SV(14)` `[EQPV]`	Equivalent plastic volume strain: $\varepsilon^p_v = \int \mathrm{tr}\dot{\underset{\approx}{\varepsilon}}^p dt$.	1	page 89
κ_0	`SV(15)` `[EL0]`	Legacy output, not of interest to users equal to the calculated initial value for κ (the cap branch value of I_1). This is not really an internal state variable. It was originally introduced to prevent the cap from contracting past its initial value in response to pore expansion. Such behavior is now allowed but potentially unstable. Its value will remain constant throughout the calculation. Keep in mind: $\bar{\kappa}$ is typically positive and therefore $\kappa \equiv -\bar{\kappa}$ is typically negative. This output variable will be unused in future builds of Kayenta that replace the KAPPA state variable with the X variable in Fig. 4.5.	Pa	Fig. 4.16
h_κ	`SV(16)` `[HK]`	(Isotropic hardening parameter) Proportionality factor appearing in the relationship $\dot{\kappa} = \lambda h_\kappa$.	Pa^2	Eq. 4.75
$\varepsilon^{\mathrm{tot}}_v$	`SV(17)` `[EVOL]`	Total volume strain, $\int \mathrm{tr}\dot{\underset{\approx}{\varepsilon}} dt$.	1	page 89
$\sqrt{J^\alpha_2}$	`SV(18)` `[BACKRN]`	Square root of the second backstress invariant. This is like the equivalent shear stress, except applied to the backstress. The value of BACKRN is not permitted to exceed the user specified limit value of N	Pa	Eq. 4.81

Symbol or Acronym	ASCII Name	Name and meaning	SI units	defining equation (or page)
—	`SV(19)` `[CRACK]`	Flag indicating that the material has reached a stress at which softening (loss of load-carrying capability) *should* engage. **CRACK** is zero in non-softening regions. It equals 1.0 if a tensile cut-off (CTI1 or CTPS) has been reached. It equals 2.0 if the limit surface has been reached (i.e., when no further kinematic hardening can occur). If **CRACK** is nonzero, Kayenta has reached the limit of its applicability and all subsequent Kayenta predictions might be nonphysical. When **CRACK** becomes nonzero, Kayenta continues to run by holding the stress at its limit state rather than allowing the stress to drop as it should (i.e., Kayenta runs like a classical plasticity model after **CRACK** becomes nonzero). Kayenta never actually softens because doing so would result in mesh-dependent solutions without host-code intervention. For these types of problems, a more advanced beta version of Kayenta should be requested.	1	page 89
—	`SV(20)` `[SHEAR]`	Flag equal to 0.0 if the material response is elastic. Otherwise, if positive, the response is plastic. The value ranges from 0.0 if the trial stress rate is tangent to the yield surface to 1.0 if the trial stress rate is normal to the yield surface (i.e., pushing directly against it).	1	Fig. 7.1 page 89
f	`SV(21)` `[YIELD]` `F`	Value of the yield function	Pa^2	Eq. 4.46
$\bar{\theta}$	`SV(22)` `[LODE]`	Lode angle in degrees ranging from -30 in triaxial extension to +30 in triaxial compression. The Lode angle is frequently denoted β in other publications about Kayenta.	deg	Eq. 3.40 page 89
σ_{11}^L	`SV(23)` `[QSSIGXX]`	Internal Kayenta variable (quasistatic "low" stress)	Pa	Eq. 6.10
σ_{22}^L	`SV(24)` `[QSSIGYY]`	Internal Kayenta variable (quasistatic "low" stress)	Pa	Eq. 6.10
σ_{33}^L	`SV(25)` `[QSSIGZZ]`	Internal Kayenta variable (quasistatic "low" stress)	Pa	Eq. 6.10
σ_{12}^L	`SV(26)` `[QSSIGXY]`	Internal Kayenta variable (quasistatic "low" stress)	Pa	Eq. 6.10
σ_{23}^L	`SV(27)` `[QSSIGYZ]`	Internal Kayenta variable (quasistatic "low" stress)	Pa	Eq. 6.10
σ_{31}^L	`SV(28)` `[QSSIGZX]`	Internal Kayenta variable (quasistatic "low" stress)	Pa	Eq. 6.10
$\hat{\lambda}$	`SV(29)` `[DCSP]`	Plastic consistency parameter.	$\dfrac{1}{Pa \cdot s}$	Eq. 4.55 Eq. 4.85

Symbol or Acronym	ASCII Name	Name and meaning	SI units	defining equation (or page)
κ_L	SV(30) [QSEL]	Internal Kayenta variable (quasistatic "low" value of κ). In Eq. 6.15, q_L stands for any internal state variable. This is the particular instance for which $q_L = \kappa_L$, which is the quasistatic value of the isotropic hardening ISV.	Pa	Eq. 6.15
α_{11}^L	SV(31) [QSBSXX]	Quasistatic backstress. In Eq. 6.15, q_L stands for α_{ij}^L.	Pa	Eq. 6.15
α_{22}^L	SV(32) [QSBSYY]	Quasistatic backstress. In Eq. 6.15, q_L stands for α_{ij}^L.	Pa	Eq. 6.15
α_{33}^L	SV(33) [QSBSZZ]	Quasistatic backstress. In Eq. 6.15, q_L stands for α_{ij}^L.	Pa	Eq. 6.15
α_{12}^L	SV(34) [QSBSXY]	Quasistatic backstress. In Eq. 6.15, q_L stands for α_{ij}^L.	Pa	Eq. 6.15
α_{23}^L	SV(35) [QSBSYZ]	Quasistatic backstress. In Eq. 6.15, q_L stands for α_{ij}^L.	Pa	Eq. 6.15
α_{31}^L	SV(36) [QSBSZX]	Quasistatic backstress. In Eq. 6.15, q_L stands for α_{ij}^L.	Pa	Eq. 6.15
t^{grow}	SV(37) [TGROW]	Total time during which the material has been undergoing progressive damage. This output may be regarded as an "age of damage". As such, a color plot of this variable will reveal not only damaged material, but it also suggests the failure sequence.	s	Fig. 5.3
$1 - D$	SV(38) [COHER]	Coherence = 1 - damage. The value ranges from 1 for an intact material to 0 for fully failed material.	1	Fig. 5.3 Eq. 5.2

Other plot variables might be available if Kayenta is compiled with special options such as -D GEO_EOS. See the code output files for definitive lists of plotable output.

Other symbols
(used only in this report)

Symbol or Acronym	ASCII Name	Name and meaning	SI units	defining equation (or page)
C_{ijkl}		Fourth-order elastic stiffness tensor	Pa	Eq. 4.4
δ_{ij}	DELTA	Kronecker delta	1	Eq. 2.4
$\Delta\gamma^p_{ij}$	DEIJPL	Deviatoric plastic strain increment $= \left(\dot{\varepsilon}^p_{ij} - \frac{1}{3}\dot{\varepsilon}_{kk}\delta_{ij}\right)\Delta t$	1	—
$\Delta\varepsilon^p_v$	VOLPLAS	Plastic volume strain increment $= \dot{\varepsilon}^p_{kk}\Delta t$	1	—
	DFDSIG	Derivative of the plastic potential with respect to stress	—	—
t		time	s	—
Δt	DT	time increment	s	—
E		Young's modulus	Pa	Eq. 4.12
f_f		The part of the meridional yield profile function associated with microcracks; $f_f = F_f - N$	Pa	Fig. 4.6 Eq. 4.29
F_f	FF	Meridional shear limiter function	Pa	Eq. 4.39
f_c		The part of the meridional yield profile function associated with porosity; $f_c = \sqrt{F_c}$	1	Fig. 4.5 Eq. 4.29
F_c	FC	Meridional nominal yield function (Pelessone function)	1	Eq. 4.32 Eq. 4.30
ϕ	PHI	Friction angle (for Mohr-Coulomb theory)	1	Eq. B.3
ϕ	G	Flow potential function	Pa^2	Eq. 4.55
Γ	GAMMAP	Octahedral yield shape function (depends on J3TYPE)	1	page 48
$H^\alpha_{ij}, \underset{\approx}{H}$		Kinematic hardening modulus tensor	Pa	Eq. 4.80
HYD		Acronym: Hydrostatic loading. The stress is diagonal (no shears).		page 15
I_1	RI1	First stress invariant, $I_1 = \text{tr}\underset{\approx}{\sigma}$. This is positive in tension.	Pa	Eq. 3.9
$\bar{I}_1$		Negative of I_1. This is positive in compression	Pa	Eq. 3.9

Symbol or Acronym	ASCII Name	Name and meaning	SI units	defining equation (or page)
J_2	`RJ2`	Second stress invariant, $J_2 = \frac{1}{2}\mathrm{tr}\underset{\approx}{S}^2$ (never negative). Geometrically, $\sqrt{2J_2}$ equals the magnitude of the stress deviator, and it therefore equals the "length" of the projection of the pseudo stress vector in 3D Haigh-Westergaard (stress) space onto the octahedral-plane (i.e., $\sqrt{2J_2}$ is the Lode radius).	Pa^2	Eq. 3.10
J_2^{ξ}	`RELJ2ZP`	Second invariant of the shifted stress	Pa^2	page 10 Eq. 4.22
J_3	`RJ3`	Third stress invariant, $J_3 = \frac{1}{3}\mathrm{tr}\underset{\approx}{S}^3$. This is positive when the stress deviator is closer to TXE than to TXC.	Pa^3	Eq. 3.11
$\bar{J}_3$		Negative of J_3. This is positive when the stress deviator is closer to TXC than to TXE.	Pa^3	Eq. 3.11
J_3^{ξ}	`RELJ3ZP`	Third invariant of the shifted stress	Pa^3	page 10 Eq. 4.22
ν		Poisson's ratio	1	Eq. 4.12
p		Mean stress, $p = \frac{1}{3}\mathrm{tr}\underset{\approx}{\sigma} = \frac{I_1}{3}$. The mean stress is positive in compression. The *pressure* $\bar{p}$, which is positive in compression is the negative of the mean stress: $\bar{p} = -p$.	Pa	page 13
$\bar{p}$		Pressure = negative of mean stress, $\bar{p} = -\frac{1}{3}\mathrm{tr}\underset{\approx}{\sigma} = \frac{\bar{I}_1}{3}$	Pa	page 13 Eq. 3.12
Π		Porosity (unloaded).	1	Eq. 4.66
	`PONE`	Code parameter equal to 1.0	1	—
	`PTWO`	Code parameter equal to 2.0	1	—
	`PFOUR`	Code parameter equal to 4.0	1	—
$\underset{\approx}{R}$		Polar rotation tensor	1	Eq. 3.39 Eq. 4.3
ρ		mass density	$\mathrm{kg/m}^3$	
$\underset{\approx}{S}$		Stress deviator, $\underset{\approx}{S} = \underset{\approx}{\sigma} - \frac{1}{3}(\mathrm{tr}\underset{\approx}{\sigma})\underset{\approx}{I}$	Pa	Eq. 3.5
$\underset{\approx}{\sigma}$		The stress tensor.	Pa	Eq. 3.1

Symbol or Acronym	ASCII Name	Name and meaning	SI units	defining equation (or page)
SHR		Acronym: Shear loading (one principal value of the stress deviator is zero and the others are therefore negatives of each other). SHR applies even when all principal stresses are compressive — all that matters is the nature of the stress deviator.	N/A	page 20
TXE		Acronym: Triaxial extension: Two "lateral" principal stresses are equal and the distinct eigenvalue is more tensile than the lateral stresses. A stress state can be in TXE even when all principal stresses are compressive — the axial stress merely needs to be *less* compressive than the lateral stresses.	N/A	page 17
TXC		Acronym: Triaxial compression (two "lateral" principal stresses are equal and the distinct eigenvalue is more compressive than the lateral stresses)	N/A	page 17
$\underset{\approx}{T}$		The Hill tensor, defined to be the deviatoric part of $\underset{\approx}{S}^2$ and therefore given by $\underset{\approx}{T} = \underset{\approx}{S}^2 - \frac{2}{3}J_2\underset{\approx}{I}$	Pa	
T_{ijkl}		Plastic tangent stiffness tensor	Pa	Eq. 4.91
τ		Signed equivalent shear stress, $\tau = \text{sign}[\sqrt{J_2}, J_3]$. This equals $\pm\sqrt{J_2}$. It is positive when $J_3 \geq 0$, and negative when $J_3 < 0$.	Pa	Eq. 3.13
$\bar{\tau}$		Negative of τ. This is positive when the stress is closer to TXC, and negative when closer to TXE	Pa	Eq. 3.4
τ	TAU	Characteristic material response time	second	Eq. 6.4
$\bar{\theta}^\xi$	RLODE	Lode angle associated with the shifted stress tensor $\underset{\approx}{\xi} = \underset{\approx}{\sigma} - \underset{\approx}{\alpha}$ ($\bar{\theta}^\xi = 30°$ when $\underset{\approx}{\xi}$ is TXC and $\bar{\theta}^\xi = +30°$ when $\underset{\approx}{\xi}$ is TXE).	radian (or deg in plot output)	Eq. 3.40
$\sin 3\bar{\theta}^\xi$	SIN3BTAP	Sine of three times the Lode angle $\bar{\theta}^\xi$	1	Eq. 3.40
$\underset{\approx}{\xi}$	ZETA	Shifted stress tensor, $\underset{\approx}{\xi} = \underset{\approx}{\sigma} - \underset{\approx}{\alpha}$. When kinematic hardening is activated, the yield surface origin will be at $\underset{\approx}{\xi} = \underset{\approx}{0}$ instead of at the zero stress origin. The backstress tensor $\underset{\approx}{\alpha}$ represents the amount by which the origin has translated.	Pa	page 63

Datasets

This section cites parameters for some materials that have already been fit to Kayenta. Datasets undergo continual refinement as additional material data become available, so consult the model developers to obtain the latest values. This section concludes with simplified datasets for mimicing simpler classical theories (Von Mises plasticity, Mohr-Coulomb theory, etc.)

NOTE TO ALEGRA USERS: Kayenta must be run using the "Generic EOS". Appropriate EOS parameters are quoted at the bottom of each dataset.

Dataset for Salem Limestone

```
$ Kayenta parameters for Sidewinder Tuff
$ Units are SI
  B0 = 4.0e9          $Pa
  B1 = 6.5e9          $Pa
  B2 = 0.1e9          $Pa
  B3 = 0.0            $Pa
  B4 = 0.0            $Dimensionless
  G0 = 3.69e9       $Pa
  G1 = 0.0            $Dimensionless
  G2 = 0.0            $1/Pa
  G3 = 0.0            $Pa
  G4 = 0.0            $Dimensionless
  RJS = 0.0           $Meters
  RKS = 0.0           $Pa/Meter
  RKN = 0.0           $Pa/Meter
  A1 = 496.83e6     $Pa
  A2 = 6.293e-10    $1/Pa
  A3 = 481.08e6     $Pa
  A4 = 1.e-10         $Dimensionless
  P0 = -70.e6         $Pa
  P1 = 1.8e-11       $1/Pa
  P2 = 2.15e-19     $1/Pa^2
  P3 = 0.08           $strain
  CR = 15.0           $Dimensionless
  RK = 0.7            $Dimensionless
  RN = 0.0            $Pa
  HC = 0.0            $Pa
  CTI1 = 3.e6        $Pa
  CTPS = 1.e6        $Pa
  T1 = 0.0            $sec
  T2 = 0.0            $1/sec
  T3 = 0.0            $Dimensionless
  T4 = 0.0            $1/sec
  T5 = 0.0            $Pa
  T6 = 0.0            $sec
  T7 = 0.0            $1/Pa
  J3TYPE = 3          $Dimensionless
  A2PF = 0.0          $$$$$ default = A2 for normality
  A4PF = 0.0          $$$$$ default = A4 for normality
  CRPF = 0.0          $$$$$ default = CR for normality
  RKPF = 0.0          $$$$$ default = RK for normality

$model 2 generic eos
$ rho ref = 1870.              $ kg/m^3
$ tref = 298.                  $ K
$ ref sound speed = 2800.0   $m/s
$end
```

Dataset for Sidewinder Tuff

```
$ Kayenta parameters for Sidewinder Tuff
$ Units are SI
  B0 = 4.0e9         $Pa
  B1 = 6.5e9         $Pa
  B2 = 0.1e9         $Pa
  B3 = 0.0           $Pa
  B4 = 0.0           $Dimensionless
  G0 = 3.69e9       $Pa
  G1 = 0.0           $Dimensionless
  G2 = 0.0           $1/Pa
  G3 = 0.0           $Pa
  G4 = 0.0           $Dimensionless
  RJS = 0.0          $Meters
  RKS = 0.0          $Pa/Meter
  RKN = 0.0          $Pa/Meter
  A1 = 496.83e6      $Pa
  A2 = 6.293e-10     $1/Pa
  A3 = 481.08e6      $Pa
  A4 = 1.e-10        $Dimensionless
  P0 = -70.e6        $Pa
  P1 = 1.8e-11       $1/Pa
  P2 = 2.15e-19      $1/Pa^2
  P3 = 0.08          $strain
  CR = 15.0          $Dimensionless
  RK = 0.7           $Dimensionless
  RN = 0.0           $Pa
  HC = 0.0           $Pa
  CTI1 = 3.e6        $Pa
  CTPS = 1.e6        $Pa
  T1 = 0.0           $sec
  T2 = 0.0           $1/sec
  T3 = 0.0           $Dimensionless
  T4 = 0.0           $1/sec
  T5 = 0.0           $Pa
  T6 = 0.0           $sec
  T7 = 0.0           $1/Pa
  J3TYPE = 3         $Dimensionless
  A2PF = 0.0         $$$$ default = A2 for normality
  A4PF = 0.0         $$$$ default = A4 for normality
  CRPF = 0.0         $$$$ default = CR for normality
  RKPF = 0.0         $$$$ default = RK for normality

$model 2 generic eos
$ rho ref = 1870.          $ kg/m^3
$ tref = 298.              $ K
$ ref sound speed = 2800.0  $m/s
$end
```

Dataset for lab scale intact Climax Granite

```
$
$ Kayenta parameters for Lab-scale Intact Climax Granite
$
  B0 = 43.00e9    $Pa
  B1 = 750.0e9    $Pa
  B2 = 100.0e9    $Pa
  B3 = 0.0        $Pa
  B4 = 0.0        $Dimensionless
  G0 = 34.73e9    $Pa
  G1 = 0.0        $Dimensionless
  G2 = 0.0        $Pa
  G3 = 0.0        $Pa
  G4 = 0.0        $Dimensionless
  RJS = 0.0       $Meters (Joint spacing)
  RKS = 0.0       $Pa/Meter (Joint shear stiffness)
  RKN = 0.0       $Pa/Meter
  A1 = 1355.e6    $Pa
  A2 = 3.43e-10   $1/Pa
  A3 = 1328.e6    $Pa
  A4 = 3.82e-2    $Dimensionless
  P0 = -556.e6    $Pa
  P1 = 9.e-14     $1/Pa
  P2 = 0.         $1/Pa^2
  P3 = 0.05       $strain
  CR = 227.5      $Dimensionless
  RK = 0.72       $Dimensionless
  RN = 17.0e6     $Pa
  HC = 150000.e6  $Pa
  CTI1 = 30.e6    $Pa
  CTPS = 10.e6    $Pa
  T1 = 0.0        $sec
  T2 = 0.0        $1/sec
  T3 = 0.0        $Dimensionless
  T4 = 0.0        $1/sec
  T5 = 0.0        $Pa
  T6 = 0.0        $sec
  T7 = 0.0        $1/Pa
  J3TYPE = 3      $dimensionless
$ Flow potential parameters (for associativity, equate with yield parameters)
  A2PF = 0.0      $zero means will default to equal A2 (associative)
  A4PF = 0.0      $zero means will default to equal A4 (associative)
  CRPF = 0.0      $zero means will default to equal CR (associative)
  RKPF = 0.0      $zero means will default to equal RK (associative)

$model 2 generic eos
$ rho ref = 2635          $kg/m^3
$ tref = 298              $ K
$ ref sound speed = 17847 $m/s
$ end
```

Dataset for field scale jointed Climax Granite

```
$
$ Kayenta parameters for field-scale JOINTED Climax Granite
$
  B0 = 43.00e9    $Pa
  B1 = 750.0e9    $Pa
  B2 = 100.0e9    $Pa
  B3 = 0.0        $Pa
  B4 = 0.0        $Dimensionless
  G0 = 34.73e9    $Pa
  G1 = 0.0        $Dimensionless
  G2 = 0.0        $Pa
  G3 = 0.0        $Pa
  G4 = 0.0        $Dimensionless
  RJS = 0.06      $Meters (Joint spacing)
  RKS = 8.0e10    $Pa/Meter (Joint shear stiffness)
  RKN = 1.6e11    $Pa/Meter
  A1 = 1379.e6    $Pa
  A2 = 6.51e-11   $1/Pa
  A3 = 1328.e6    $Pa
  A4 = 0.0        $Dimensionless
  P0 = -556.e6    $Pa
  P1 = 9.e-14     $1/Pa
  P2 = 0.         $1/Pa^2
  P3 = 0.05       $strain
  CR = 227.5      $Dimensionless
  RK = 0.80       $Dimensionless
  RN = 17.0e6     $Pa
  HC = 150000.e6 $Pa
  CTI1 = 30.e6    $Pa
  CTPS = 10.e6    $Pa
  T1 = 0.0        $sec
  T2 = 0.0        $1/sec
  T3 = 0.0        $Dimensionless
  T4 = 0.0        $1/sec
  T5 = 0.0        $Pa
  T6 = 0.0        $sec
  T7 = 0.0        $1/Pa
  J3TYPE = 3      $dimensionless
$ Flow potential parameters (for associativity, equate with yield parameters)
  A2PF = 0.0      $zero means will default to equal A2 (associative)
  A4PF = 0.0      $zero means will default to equal A4 (associative)
  CRPF = 0.0      $zero means will default to equal CR (associative)
  RKPF = 0.0      $zero means will default to equal RK (associative)

$model 2 generic eos
$ rho ref = 2635          $kg/m^3
$ tref = 298              $ K
$ ref sound speed = 17847 $m/s
$ end
```

Dataset for 23MPa Concrete

```
B0 = 5.5e9              $Pa
B1 = 28.78e9            $Pa
B2 = 0.623e9            $Pa
B3 = 0.0                $Pa
B4 = 0.0                $Dimensionless
G0 = 1.9026e9           $Pa
G1 = 0.890513           $Dimensionless
G2 = 3.55e-9            $1/Pa
G3 = 0.0                $Pa
G4 = 0.0                $Dimensionless
RJS = 0.0               $Meters
RKS = 0.0               $Pa/m
RKN = 0.0               $Pa/m
A1 = 1255.7e6           $Pa
A2 = 1.93e-10           $1/Pa
A3 = 1248.2e6           $Pa
A4 = 0.0                $dimensionless
P0 = -1.067e8           $Pa
P1 = 7.66e-10           $1/Pa
P2 = 3.88e-20           $1/Pa^2
P3 = 0.1538             $Dimensionless(strain)
CR = 10.0               $Dimensionless
RK = -1.                $Dimensionless
RN = 3.0e6              $Pa
HC = 1.0e11             $Pa
CTI1 = 3e6              $Pa
CTPS = 1.e6             $Pa
T1 = 0.0                $Sec
T2 = 0.0                $1/Sec
T3 = 0.0                $Dimensionless
T4 = 0.0                $1/Sec
T5 = 0.0                $Pa
T6 = 0.0                $Sec
T7 = 0.0                $1/Pa
J3TYPE=2
A2PF = 0.0 $zero defaults to A2 (associative)
A4PF = 0.0 $zero defaults to A4 (associative)
CRPF = 0.0 $zero defaults to CR (associative)
RKPF = 0.0 $zero defaults to RK (associative)
SUBX = 0.0

$model 2 generic eos
$ rho ref = 2030.          $ kg/m^3
$ tref = 298.              $ K
$ ref sound speed = 4500.0   $ m/s
$end
```

Dataset for Conventional Strength Portland Concrete

```
B0 = 1.0954e10        $Pa
B1 = 0.0              $Pa
B2 = 0.0              $Pa
B3 = 0.0              $Pa
B4 = 0.0              $Dimensionless
G0 = 7.5434e9         $Pa
G1 = 0.0              $Dimensionless
G2 = 0.0              $1/Pa
G3 = 0.0              $Pa
G4 = 0.0              $Dimensionless
RJS = 0.0             $Meters
RKS = 0.0             $Pa/m
RKN = 0.0             $Pa/m
A1 = 4.26455e8        $Pa
A2 = 7.51e-10         $1/Pa
A3 = 4.19116e8        $Pa
A4 = 1.0e-10          $Dimensionless
P0 = -1.95520e8       $Pa
P1 = 1.2354e-9        $1/Pa
P2 = 0.0              $1/Pa^2
P3 = 0.065714         $Dimensionless(strain)
CR = 12.0             $Dimensionless
RK = -1.              $Dimensionless
RN = 0.0              $Pa
HC = 0.0              $Pa
CTI1 = 3.0e6          $Pa
CTPS = 1.0e6          $Pa
T1 = 0.0              $Sec
T2 = 0.0              $1/Sec
T3 = 0.0              $Dimensionless
T4 = 0.0              $1/Sec
T5 = 0.0              $Pa
T6 = 0.0              $Sec
T7 = 0.0              $1/Pa
J3TYPE=2
A2PF = 0.0 $zero defaults to A2 (associative)
A4PF = 0.0 $zero defaults to A4 (associative)
CRPF = 0.0 $zero defaults to CR (associative)
RKPF = 0.0 $zero defaults to RK (associative)
SUBX = 0.0


$model 2 generic eos
$ rho ref = 2250. $(kg/cubic meter)
$ tref = 298.
$ ref sound speed = 3056.0
$end
```

Datasets for mimicing classical (simplified) models

Kayenta is truly a unification of many simpler theories. By appropriately setting parameters, Kayenta can be made to exactly replicate results from simpler idealized theories, as illustrated below.
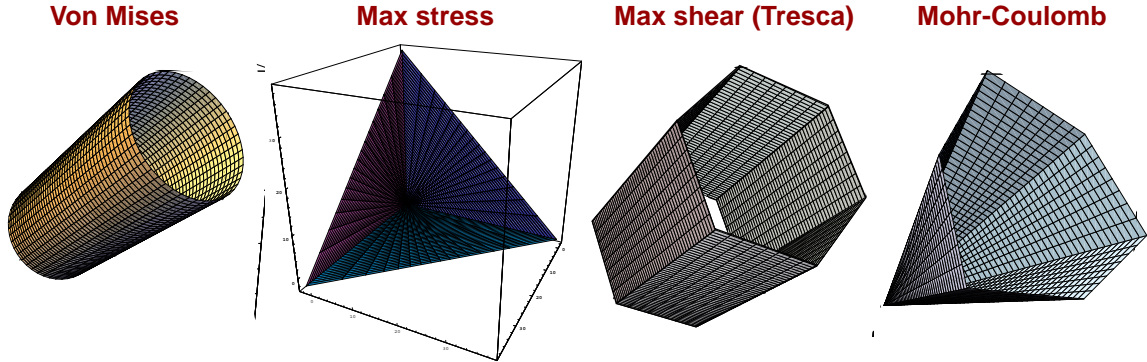
Von Mises **Max stress** **Max shear (Tresca)** **Mohr-Coulomb**

Figure B.1.   *Other yield surface shapes supported by Kayenta.*   The grid lines shown on these sketches correspond to lines of constant z and constant θ.

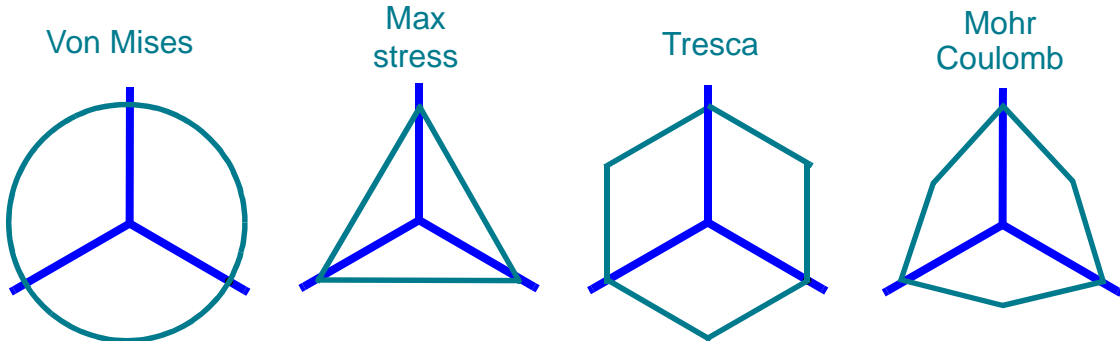Von Mises   Max stress   Tresca   Mohr Coulomb

Figure B.2.   *Classical simplified octahedral profiles.*   None of these models adequately describes rock failure surfaces, but the failure surfaces for real rocks sometimes share some qualitative features with these models, depending on the level of confining pressure. In these figures, the axes represent projections of the compressive principal stress axes onto the octahedral plane, taking stress to be positive in *tension*. For the max stress and Mohr-Coulomb models, the size of the octahedral profile increases with pressure. For all of these models, the meridional profile is a straight line.

In most finite-element codes, you can modify an existing data set (e.g., one for a real material) by simply redefining a material parameter *in a separate input line*, leaving the original value unchanged. By deviating from a correct input set to a "toy" input set in this way (rather than over-writing preferred values), you can retain a record of what the material parameters *should be*, thereby mitigating unintentional dissemination of physically bad input sets.

The following specialized input sets use an "aprepro" syntax to show where you need to provide values. Specifically, all required or computed values appear in braces {}. Specify numerical values wherever "`VALUE`" appears, and then ensure all other values in braces are computed as shown (they can be computed by hand or piped into aprepro).

Von-Mises material. Von Mises theory can be duplicated by using the following simplified set of Kayenta input values:

```
$
$ Kayenta parameters for replicating non-hardening Von-Mises plasticity
$ All parameters not listed are defaulted to zero.
$ Items in braces must be replaced with numbers
$
A1     = {yield_stress_in_shear = VALUE}
B0     = {linear_elastic_bulk_modulus = VALUE}
G0     = {linear_elastic_shear_modulus = VALUE}

J3TYPE = 1    $Use Gudehaus, which is capable of a circular octhedral profile
RK     = 1    $Set TXE/TXC ratio = 1.0 to make a circlular octahedral profile
P0     = -1.e99   $make yield in hydrostatic compression impossible
CTI1   = 1.e99   $ set pressure cut-off to "infinity"
CTPS   = 1.e99   $ set principal stress cut-off to "infinity"
CR = 0.001  $ minimize the size of the curved part of the cap
```

This list presumes that your implementation of Kayenta sets defaults for unlisted parameters.

Maximum Principal Stress failure. The very simplistic fracture criterion that initiates failure when the largest principal stress reaches a critical value can be modeled in Kayenta by using the following parameter set:

```
$ Kayenta parameters for duplicating a maximum principal stress criterion
$
${max_allowed_principal_stress = VALUE}
B0 = {VALUE}     $bulk modulus
G0 = {VALUE}     $shear_modulus
P0 = -1.e99      $ turn off the cap function
J3TYPE=3
A1={SQRT(3)*max_allowed_principal_stress}
A4={1/SQRT(3.0)}
RK = 0.5
A4PF = {1/SQRT(3.0)}
RKPF = 0.5
```

This list presumes that your implementation of Kayenta sets defaults for unlisted parameters.

Tresca. The simplistic criterion that a material fails when its largest shear stress reaches a critical value can be modeled by using the following Kayenta parameters:

```
$ User must specify values in braces
B0 = {bulk_modulus}
G0 = {shear_modulus}
P0 = -1.e99      $ turn off the cap function
J3TYPE=3
A1={2.0*yield_stress_in_shear/sqrt(3.0)}
RK = 1.0
RKPF = 1.0
```

This list presumes that your implementation of Kayenta sets defaults for unlisted parameters.

Mohr-Coulomb.

Classical Mohr-Coulomb theory for brittle failure can be derived from an idealization that the material contains a large population of equal sized cracks. Being all the same size, any given crack loaded in pure shear will fail (grow) if the resolved shear stress τ on the crack face exceeds a critical threshold value S_0. If a crack face is additionally subjected to a normal compressive stress $\bar{\sigma}_N$, then the applied shear τ needed to induce crack growth must be larger than S_0 by an amount $\tau^{\text{fric}} = \mu\bar{\sigma}_N$, where μ is the coefficient of friction. Stated differently, a given crack is *safe* from failure if

$$\tau - \tau^{\text{fric}} < S_0, \tag{B.2}$$

or, recalling that $\tau^{\text{fric}} = \mu\bar{\sigma}_N$,

$$\tau - \tan\phi\,\bar{\sigma}_N < S_0, \qquad \text{where} \qquad \tan\phi \equiv \mu \tag{B.3}$$

This criterion must be satisfied by *all cracks* in the material. Since Mohr-Coulomb theory arises from an idealization that the material contains a large population of cracks (uniformly random in orientation), a material is safe from failure under general stress states only if all points on the Mohr's diagram for the stress fall below the "failure line" defined by $\tau = S_0 + \tan\phi\,\bar{\sigma}_N$. Failure is therefore deemed to occur when the outer Mohr's circle first "kisses" the failure line. Working out the geometry of Fig. B.3, a circle of radius R, centered at $\bar{\sigma}_N = C$, will be tangent to the failure line if and only if

$$R = S_0\cos\phi + C\sin\phi \tag{B.4}$$

For the outer Mohr's circle,

$$R = \frac{\bar{\sigma}_1 - \bar{\sigma}_3}{2} \qquad \text{and} \qquad C = \frac{\bar{\sigma}_1 + \bar{\sigma}_3}{2} \tag{B.5}$$

or, removing the overbars (defined such that $\bar{\sigma}_k = -\sigma_k$),

$$R = \frac{\sigma_3 - \sigma_1}{2} \qquad \text{and} \qquad C = \frac{-(\sigma_3 + \sigma_1)}{2} \tag{B.6}$$

Substituting these into Eq. (B.4) gives

$$\boxed{\frac{\sigma_3 - \sigma_1}{2} = S_0\cos\phi - \frac{\sigma_3 + \sigma_1}{2}\sin\phi} \tag{B.7}$$

This is the Mohr-Coulomb failure criterion cast in terms of principal stresses. Eqs. (3.43a) and (3.43c) on page 27 of the main report imply
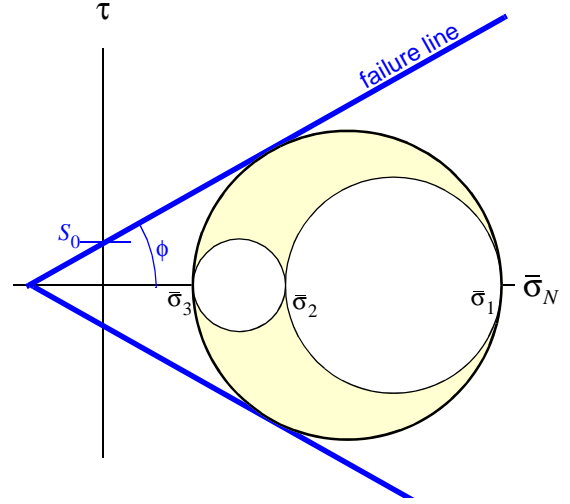

Figure B.3.   A stress at the limit state under Mohr-Coulomb theory.

$$\frac{\sigma_3 - \sigma_1}{2} = \sqrt{J_2}\cos\bar\theta \tag{B.8a}$$

$$\frac{\sigma_3 + \sigma_1}{2} = \frac{I_1}{3} - \frac{\sqrt{J_2}}{\sqrt{3}}\sin\bar\theta. \tag{B.9b}$$

Therefore, the stress invariant version of Eq. (B.7) is

$$\sqrt{J_2}\cos\bar\theta = S_0\cos\phi - \frac{I_1}{3}\sin\phi + \frac{\sqrt{J_2}}{\sqrt{3}}\sin\bar\theta\sin\phi, \tag{B.10}$$

or, solving for $\sqrt{J_2}$,

$$\sqrt{J_2} = \frac{S_0\cos\phi - \dfrac{I_1}{3}\sin\phi}{\cos\bar\theta - \dfrac{1}{\sqrt{3}}\sin\bar\theta\sin\phi}. \tag{B.11}$$

Recall from Eq. (4.39) that Kayenta's limit function F_f fits the *triaxial compression (TXC)* meridional profile to the following functional form

$$\sqrt{J_2} = a_1 - a_3 e^{-a_2\bar I_1} + a_4\bar I_1 \quad \text{in TXC } (\bar\theta = 30°) \tag{B.12}$$

In triaxial compression (TXC), the Lode angle is $\bar\theta = 30°$ so that

$$\cos\bar\theta = \cos 30° = \frac{\sqrt{3}}{2} \qquad \text{and} \qquad \sin\bar\theta = \sin 30° = \frac{1}{2} \tag{B.13}$$

Therefore, Eq. (B.11) specializes to TXC loading as

$$\sqrt{J_2} = \frac{2\sqrt{3}}{3 - \sin\phi}\left(S_0\cos\phi - \frac{I_1}{3}\sin\phi\right) \qquad \text{(Mohr-Coulomb in TXC)} \tag{B.14}$$

Being careful to note that $\bar I_1 = -I_1$, comparing this result with Eq. (B.12) implies that Kayenta's limit surface parameters for Mohr-Coulomb theory should be set as

$$a_1 = \left(\frac{2\sqrt{3}}{3 - \sin\phi}\right)S_0\cos\phi \tag{B.15a}$$

$$a_2 = 0 \tag{B.15b}$$

$$a_3 = 0 \tag{B.15c}$$

$$a_4 = \left(\frac{2\sqrt{3}}{3 - \sin\phi}\right)\frac{\sin\phi}{3} \tag{B.15d}$$

Therefore, the general Mohr-Coulomb criterion in Eq. (B.11) may be written in the form required for Kayenta as

$$\sqrt{J_2}\,\Gamma(\bar{\theta}) \,=\, f_f(\bar{I}_1)f_c(\bar{I}_1)\,,$$

where $f_f(\bar{I}_1) \,=\, a_1 + a_4\bar{I}_1\,,\qquad f_c(\bar{I}_1) \,=\, 1$

and $\Gamma(\bar{\theta}) \,=\, \dfrac{2\sqrt{3}}{3-\sin\phi}\left(\cos\bar{\theta} - \dfrac{\sin\phi\sin\bar{\theta}}{\sqrt{3}}\right)$ (B.16)

Naturally, **J3TYPE=3** is appropriate (see page 48). A classic Mohr-Coulomb material has no cap; to make the cap function f_c always equal 1, the cap and crush curve features should be disabled as described on page B-30. Classical Mohr-Coulomb theory is meant to apply to brittle rupture, so kinematic hardening should be disabled as described on page B-30. An appropriate value for the TXE/TXC strength ratio ψ must be determined by evaluating Eq. (B.11) in TXE where $\bar{\theta} \,=\, -30°$:

$$\sqrt{J_2} \,=\, \frac{2\sqrt{3}}{3+\sin\phi}\left(S_0\cos\phi - \frac{I_1}{3}\sin\phi\right) \qquad \text{(Mohr-Coulomb in \textbf{TXE})} \qquad \text{(B.17)}$$

The TXE/TXC strength ratio is then given by the ratio of the right-hand sides of Eqs. (B.17) and (B.14):

$$\psi \,=\, \frac{3-\sin\phi}{3+\sin\phi} \qquad\qquad \left[\text{The inverse relationship is} \quad \sin\phi = 3\left(\frac{1-\psi}{1+\psi}\right)\right] \qquad \text{(B.18)}$$

For this classical Mohr-Coulomb theory, the slope of the TXC meridional profile, $d\sqrt{J_2}/d\bar{I}_1$, equals a_4. Therefore, $\sin\phi$ may be eliminated from Eqs. (B.15d) and (B.18) to reveal that the TXE/TXC strength ratio is coupled to the slope of the TXC meridional profile according to

$$\psi \,=\, \frac{1}{1+\sqrt{3}A}\,, \quad\text{where}\quad A \equiv \left(\frac{\partial\sqrt{J_2}}{\partial\bar{I}_1}\right)_{\bar{\theta}=30°} \,=\, \frac{1}{\sqrt{6}}\left(\frac{dr}{d\bar{z}}\right)_{\bar{\theta}=30°} \qquad \text{(B.19)}$$

In other words, in Mohr-Coulomb theory, the strength ratio cannot be specified independently from the slope of the meridional profile. On page B-29, this relationship is applied to non-Mohr-Coulomb models to support a pressure varying strength ratio.

Incidentally, the Mohr-Coulomb Γ function in Eq. (B.16) may be written

$$\Gamma(\bar{\theta}) \,=\, \frac{\cos(\bar{\theta}-\bar{\theta}_0)}{\cos\left(\dfrac{\pi}{6}-\bar{\theta}_0\right)} \qquad \text{(B.20)}$$

where

$$\bar{\theta}_0 \,=\, -\mathrm{ArcTan}\left[\frac{\sin\phi}{\sqrt{3}}\right] \,=\, -\mathrm{ArcTan}\left[\sqrt{3}\left(\frac{1-\psi}{1+\psi}\right)\right] \qquad \text{(B.21)}$$

Here, $\bar{\theta}_0$ is the Lode angle at which the material has the lowest shear strength (i.e., the angle where the yield surface is closest to the origin).

Below, we show the skeleton required for setting Kayenta inputs to run classical Mohr-Coulomb theory. This input set also shows how to set parameters if you wish to run with non-associativity (where the flow potential function differs from the yield function only by having a different value for ϕ). Values for (a_1, a_2, a_3, a_4) and for (a_2^{PF}, a_4^{PF}) are set by using Eq. (B.15). Values for ψ and ψ^{PF} are set by using Eq. (B.18).

```
$ Kayenta parameters for duplicating a classical Mohr-Coulomb material
$ in BOTH the octahedral and meridional profiles.
$
$ Replace the four occurances of "VALUE" in this file with the appropriate
$ Mohr-Coulomb parameter. You may generate Kayenta input parameters
$ by using the command 'aprepro this_file output_file'. Preferably, if
$ your finite element code supports embedded aprepro directives, then
$ drop this file DIRECTLY into your finite element Kayenta input block.
$
$ {friction_angle = VALUE}     $angle "phi" in Kayenta Appendix B
$ {dilation_angle = VALUE}     $for associativity, this equals "phi"
$
$ {cohesion = VALUE}           $parameter "S_sub0" in Kayenta Appendix B
$                              $This equals yield stress in simple shear.


$ Let Aprepro compute some helper quantities
$          {scalef = 2.0*sqrt(3)/(3.0-sin(friction_angle))}
$          {scaleg = 2.0*sqrt(3)/(3.0-sin(dilation_angle))}
$
B0 = {VALUE}     $bulk modulus
G0 = {VALUE}     $shear modulus
J3TYPE=3         $Mohr-Coulomb octahedral option
A1 = {scalef*cohesion*cos(friction_angle)}
A2 = 0.0
A3 = 0.0
A4 = {scalef*sin(friction_angle)/3.0}
RK = {(3.0-sin(friction_angle))/(3.0+sin(friction_angle))}
A4PF = {scaleg*sin(dilation_angle)/3.0}
RKPF = {(3.0-sin(dilation_angle))/(3.0+sin(dilation_angle))}
P0 = -1.e99      $ turn off the cap and crush-curve features
CR = 0.001       $ prevent cap influence on shear response
```

This list presumes that your implementation of Kayenta sets defaults for unlisted parameters.

Pressure-varying strength ratio. If (unlike Mohr-Coulomb theory) the meridional profile is curved, then the user can set RK = –1 to instruct Kayenta to use Eq. (B.19) to assign a pressure-dependent strength ratio. As illustrated in Fig. B.4, this feature allows a smooth transition from a Mohr-Coulomb distorted hexagon (or triangle) at low pressures to a von Mises circle at high pressures.
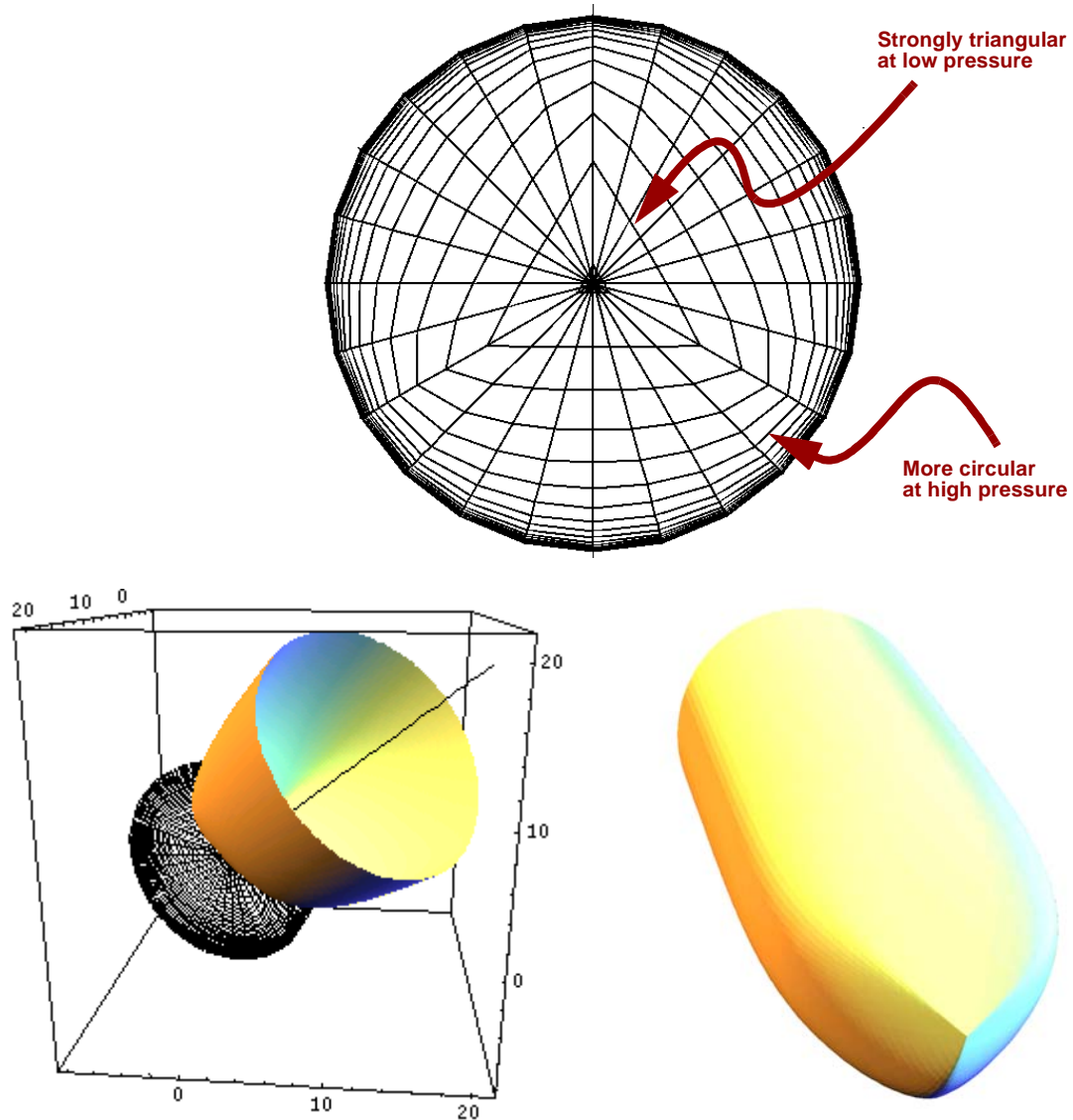
Figure B.4.   *Pressure varying strength ratio (enabled by setting RK=-1.0).*   At low pressure, this material (SiC-N) has a meridional slope nearly equal to $A = 1/\sqrt{3}$, for which Eq. (B.19) gives a strength ratio of 1/2, which is appropriate for a maximum principal stress failure criterion. At high pressures, the meridional slope approaches zero, for which Eq. (B.19) gives a strength ratio of 1, which (with J3TYPE=2) corresponds to a circular (von Mises) octahedral profile.

To conclude this appendix, sub-input sets are summarized for controlling various features of Kayenta.

Sub-input set for <u>linear</u> elasticity.

```
B1 = 0.0
B2 = 0.0
B3 = 0.0
B4 = 0.0
G1 = 0.0
G2 = 0.0
G3 = 0.0
G4 = 0.0
```

*Set **B0** to the constant bulk modulus and set **G0** to the constant shear modulus. To additionally disable any form of plasticity, set **A1** to a very large number and disable cut-offs as well as the cap and crush curve as described below.*

Sub-input set for "turning off" all rate dependence.

```
T1 = 0.0
T2 = 0.0
T3 = 0.0
T4 = 0.0
T5 = 0.0
T6 = 0.0
T7 = 0.0
```
*For LINEAR rate dependence, set **T1** to the material's characteristic response time and all other **T** parameters to zero.*

Sub-input set for disabling kinematic hardening.

```
HC=0.0
RN=0.0
```

Sub-input set for associativity.

```
CRPF=0.0
RKPF=0.0
A2PF=0.0
A4PF=0.0
```
This list presumes that your implementation of Kayenta sets defaults for unlisted parameters. If not, associativity requires that all parameters that end in "PF" be set equal to their yield parameter counterparts.

Sub-input set for disabling cap and crush curve.

```
P0    = -1.e99    $put the cap at infinity
P1 = 0.0
P2 = 0.0
P3 = 0.0          $set porosity to zero
CR = 0.001        $ minimize the size of the curved part of the cap
```

This list presumes that your implementation of Kayenta sets defaults for unlisted parameters. Kayenta's internal user-input processor and initializer will recognize these inputs as "cap disablers" and adjust the model appropriately.

Sub-input set for disabling tensile cut-off limits.

```
CTI1   = 1.e99   $ set pressure (I1) cut-off to "infinity"
CTPS   = 1.e99   $ set principal stress cut-off to "infinity"
```

This list presumes that your implementation of Kayenta sets defaults for unlisted parameters.

REFERENCES

[1] ALDRIDGE, D.F. (2002) Elastic wave radiation from a pressurized spherical cavity, <u>Sandia National Laboratories Report SAND2002-1882</u>, Albuquerque, NM.

[2] ARGUELLO, J.G., A.F. FOSSUM, D.H. ZEUCH and K.G. EWSUK. (2001) Continuum-based FEM modeling of alumina powder compaction. *KONA*, 19: 166-177.

[3] ARGYRIS,J.H., FAUST,G., SZIMMAT,J., WARNKE,E.P., and WILLAM,K.J. (1974) Recent developments in the finite element analysis of prestressed concrete reactor vessel, *Nuclear Engrg. Des.* **28**, p. 42-75.

[4] CARROLL, M. M. and HOLT, A.C. (1972) Static and dynamic pore-collapse relations for ductile porous materials. *J. Appl. Phys.* **43**, pp. 1626-1636.

[5] BAZANT, Z. P. and J. PLANAS (1998). **Fracture and Size Effect in Concrete and Other Quasibrittle Materials**. Boca Raton, FL, CRC Press LLC.

[6] BECKER, R. (2003) Lawrence Livermore National Laboratories, unpublished presentation materials.

[7] BLANFORD, M.L. (1998) Jas3d: A multi-strategy iterative code for solid mechanics analysis. Unpublished. Sandia National Laboratories.

[8] BORJA, RONALDO I., SAMA, KOSSI M., and SANZ, PABLO F. (2003) On the numerical integration of three invariant elastoplasticity constitutive models, *Comput. Methods Appl. Mech. Engr.* **192**, p. 1227-1258.

[9] BOSWELL, L.F. and CHEN,Z. (1987) A general failure criterion for plain concrete, *Int. J. Solids Struct.* **23**, p. 621-630

[10] BOUCHERON, E.A., K.H. BROWN, K.G. BUDGE, S.P. BURNS, D.E. CARROLL, S.K. CARROLL, M.A. CHRISTON, R.R. DRAKE, C.G. GARASI, T.A. HAILL, J.S. PEERY, S.V. PETNEY, J. ROBBINS, A.C. ROBINSON, R.M. SUMMERS, T.E. VOTH, and M.K. WONG (2002) ALEGRA: User Input and Physics Descriptions Version 4.2, <u>Sandia National Laboratories Report SAND2002-2775</u>, Albuquerque, NM.

[11] BRANNON, R.M. and W.J. DRUGAN (1993) Influence of non-classical elastic-plastic constitutive features on shock wave existence and spectral solutions, *J. Mech. Phys. Solids* **41**:2, p. 297-330.

[12] BRANNON, R.M. and M. K. WONG (1996) "MIG Version 0.0 Model Interface Guidelines: Rules to Accelerate Installation of Numerical Models Into Any Compliant Parent Code," <u>Sandia National Laboratories Report SAND96-2000</u>, Albuquerque, NM.

[13] BRANNON, R.M. (2004) Rotation and Reflection: a review of useful theorems associated with orthogonal tensors. http://www.mech.utah.edu/~brannon/public/rotation.pdf

[14] BRANNON, R. M. (2007). Elements of Phenomenological Plasticity: geometrical insight, computational algorithms, and applications in shock physics. **Shock Wave Science and Technology Reference Library: Solids I**, Springer-New York. 2: pp. 189-274.

[15] BRANNON, R. M., J. M. WELLS, and O.E. STRACK (2007). Validating theories for brittle damage. Metallurgical and Materials Transactions A: 2861-2868 doi:10.1007/s11661-007-9310-7

[16] Brannon, R.M. and S. Leelavanichkul (2009) Survey of four damage models for concrete, <u>Sandia National Laboratories Report SAND2008-xxxx</u> (in press), Albuquerque, NM.

[17] BROWN, A. A., J. CASEY, et al. (2003) Experiments conducted in the context of the strain-space formulation of plasticity. *Int. J. Plasticity* **19**, p. 1965-2005.

[18] DiGIOVANNI, A.A. and J.T. FREDRICH (2003) private communication, Sandia National Laboratories, Albuquerque, NM 87185, USA.

[19] DIENES, J. K., Q. H. ZUO, and J.D. KERSHNER (2006). Impact initiation of explosives and propellants via statistical crack mechanics. Journal of Mechanics and Physics of Solids 54(10): 2235-2240.

[20] DUVAUT, G. and J.L. LIONS (1972) Les Inequations en Mecaniquie et en Physique, Dunod, Paris.

[21] FARNSWORTH, G.V. and A.C. ROBINSON (2003) Improved Kinematic Options in ALEGRA, <u>Sandia National Laboratories Report SAND2003-4510</u>, Albuquerque, NM.

[22] FOSSUM, A.F. and R.M. BRANNON (2004) Unified compaction/dilation, strain-rate sensitive, constitutive model for rock mechanics structural analysis applications, *ARMA/NARMS 04-546*.

[23] FOSSUM, A.F. and R.M. BRANNON (2004) "The Sandia GeoModel: Theory and User's Guide" <u>Sandia National Laboratories Report SAND2004-3226</u>, Albuquerque, NM.

[24] FOSTER, C.D., R.A. REGUEIRO, A.F. FOSSUM, and R.I. BORJA (2004) Implicit numerical integration of a three-invariant, isotropic/kinematic hardening cap plasticity model for geomaterials, *submitted to Elsevier Science.*

[25] FREW, D.J., M.J. FORRESTAL, and W. CHEN (2001) A split Hopkinson Pressure Bar Technique to determine compressive stress-strain data for rock materials, *Experimental Mechanics,* **41**: 40-46.

[26] FUNG, Y.C. (1965) **Foundations of Solid Mechanics**, Prentice-Hall, Englewood Cliffs, NJ.

[27] GREENBERG, M.D. (1978) **Foundations of Applied Mathematics**, Prentice-Hall, Englewood Cliffs, NJ.

[28] GURSON, A.L. (1977) *J. Engng Mater. Technol.*, **99**, p. 2.

[29] HOFFMAN, E.L., C.A. LAVIN (2004) WISDM: Weapons Information System and Data Management, Version 2.2.0., Apr. 2002. <u>Sandia National Laboratories. Electronic. Sandia Network</u>.

[30] JAY, F. (1984), Ed., **IEEE Standard Dictionary of Electrical and Electronic Terms**, Institute of Electrical and Electronic Engineers, ANSI/IEEE Std. 100-1984.

[31] JIANG, J., PIETRUSZCZAK, S. (1988) Convexity of yield loci for pressure sensitive materials, *Comput. Geotech.* **5**, p. 51-63.

[32] JOHNSON, G.R. et al. (1994) User Instructions for the 1995 Version of the EPIC Code, <u>Alliant Techsystems, Inc., technical report</u>, Hopkins, Minnesota.

[33] JOHNSON, G.R. and T.J. HOLMQUIST: AIP Conf. Proc., 1994, vol. 309, pp. 981–84.

[34] KNUPP, P. and K. SALARI (2000) Code verification by the method of manufactured solutions, <u>Sandia National Laboratories Report SAND2000-1444</u>, Albuquerque, NM.

[35] KOTERAS, J.R. and A.S. GULLERUD (2002) **Verification of Computer Codes in Computational Science and Engineering**, Chapman & Hall/CRC.

[36] LUBLINER, J. (1990) **Plasticity Theory**, Macmillan, New York, NY.

[37] MATSUOKA, H., and NAKAI, T. (1974) Stress-deformation and strength characteristics of soil under three different principal stresses, *Proc. JSCE* **232**, p. 59-70.

[38] LADE, P.V., and DUNCAN, J.M. (1975) Elastoplastic stress-strain theory for cohesionless soil, *J. Geotech. Engrg. Div., ASCE* **101**, p. 1037-1053.

[39] LADE, P.V. (1977) Elasto-plastic stress-strain theory for cohesionless soil with curved yield surfaces, *Int. J. Solids Struct.* **13**, p. 1019-1035.

[40] LUBLINER, JACOB (1990) **Plasticity Theory**, MacMillian, New York.

[41] MALVERN, L.E. (1969) **Introduction to the Mechanics of a Continuous Medium**, Prentice-Hall, Englewood Cliffs, NJ

[42] NEEDLEMAN, A. and J.R. RICE (1978) *Mech. Mater.* **7**, p. 163.

[43] PELESSONE, D. (1989) A modified formulation of the cap model <u>Gulf Atomics Report GA-C19579, prepared for the Defense Nuclear Agency under Contract DNA-001086-C-0277</u>, January.

[44] PRESS, W.H., FLANNERY, B.P., TEUKOLSKY, S.A., VETTERLING, W.T. (1992) **Numerical Recipes in FORTRAN**, Cambridge University Press, Melbourne, Australia.

[45] PUCIK, T.A. (2004) Memorandum of Record, Material Model Driver, 11 April 2004, Pucik Consulting Services.

[46] PUCIK, T.A. (1993) "A case study of instability and nonuniqueness induced by nonassociated plastic flow", Unpublished Manuscript.

[47] RASHID, M (1993) Incremental kinematics for finite-element applications. *Int. J. Numerical Meth. in Engr.* **36**, no.23, pp. 3937-3956.

[48] ROACHE, P.J. (1998) **Verification and Validation in Computational Science and Engineering**, Hermosa publishers, Albuquerque, NM.

[49] SANDLER, I.S. and T.A. PUCIK (1994) Non-uniqueness in dynamic rate-independent non-associated plasticity, in G.Z. Voyiadjis, *et al.* (eds.) **Mechanics of Materials and Structures**, Elsevier Science B.V., New York, pp. 221-240.

[50] SANDLER, I.S. and D. RUBIN (1979) An algorithm and a modular subroutine for the cap model, *Int. J. Numer. & Anal. Meth. Geomech.* **3**, p. 173.

[51] SCHWER, L.E., Y.D. MURRY (1994) A three-invariant smooth cap model with mixed hardening, *Int. J. for Num. And Anal. Mech. In Geomech.* 18: 657-688.

[52] SCHWER, L. E. et al. (2006). Guide for verification and validation in computational solid mechanics, American Society of Mechanical Engineers, ASME V&V 10-2006.

[53] SENSEY, P.E., A.F. FOSSUM, & T.W. PFEIFLE (1983) Non-associative constitutive laws for low porosity rocks, *Int. J. for Num. and Analytical Meth. in Geomech.* **7**, pp. 101-115.

[54] SIMONS, D. (2003) Single-Element Load Paths to Complement ACTD V&V Problems 1&2, Northrop Grumman Information Technology unpublished presentation slides for ACTD V&V Working Group Meeting, Albuquerque, NM 17 April 2003.

[55] TAYLOR, L.M. and D.P. FLANNAGAN (1989) PRONTO 3D a three-dimensional transient solid dynamics program, Sandia National Laboratories Report SAND87-1912, Albuquerque, NM.

[56] TAYLOR, P.A. (2004) CTH Reference Manual: The Geo-Effective Stress (GEFFS) Model, Sandia National Laboratories Report SAND2004-5313, Albuquerque, NM.

[57] TELFORD, THOMAS (1993) CEB-FIB Model Code 1990, European Design Code, Lausanne, Switzerland

[58] WARREN, T.L., A.F. FOSSUM, and D.J. FREW (2004) Penetration into low strength (23 MPa) concrete: target characterization and simulations. *Int J. Impact Engr. (accepted).*

[59] WILLAM,K.J. and WARNKE,E.P. (1975) Constitutive model for the triaxial behavior of concrete, ISMES Seminar on Concrete Structures Subjected to Triaxial Stresses, Bergamo, Italy, p. 1-30.

[60] WOLFRAM, STEPHEN, **The Mathematica Book**, 4th Ed, Cambridge Univ. Press, 1999.

[61] WONG, M.K., J.R. Weatherby, C.D. Turner, A.C. Robinson, T.A. Haill, D.E. Carroll (2001) Physics Applications in the ALEGRA Framework, *First MIT Conference on Computational Fluid and Solid Mechanics*, June, 2001.

Distribution:

1	MS 0899	Technical Library
		9536 (electronic copy)